PolyPublie
Polytechnique Montréal

POLYTECHNIQUE MONTRÉAL
UNIVERSITÉ D'INGÉNIERIE

Titre: Title:	Fluidelastic Excitation of a Fuel Rod Bundle Subjected to Combined Axial-Flow and Jet Cross-Flow
Auteur: Author:	Ibrahim Ahmed Ibrahim Gadelhak
Date:	2022
Type:	Mémoire ou thèse / Dissertation or Thesis
Référence: Citation:	Gadelhak, I. A. I. (2022). Fluidelastic Excitation of a Fuel Rod Bundle Subjected to Combined Axial-Flow and Jet Cross-Flow [Thèse de doctorat, Polytechnique Montréal]. PolyPublie. https://publications.polymtl.ca/10581/

Document en libre accès dans PolyPublie
Open Access document in PolyPublie

URL de PolyPublie: PolyPublie URL:	https://publications.polymtl.ca/10581/
Directeurs de recherche: Advisors:	Njuki Mureithi
Programme: Program:	Génie mécanique

Ce fichier a été téléchargé à partir de PolyPublie, le dépôt institutionnel de Polytechnique Montréal
This file has been downloaded from PolyPublie, the institutional repository of Polytechnique Montréal

https://publications.polymtl.ca

POLYTECHNIQUE MONTRÉAL
affiliée à l'Université de Montréal

Fluidelastic Excitation of a Fuel Rod Bundle Subjected to Combined Axial-Flow and Jet Cross-Flow

IBRAHIM AHMED IBRAHIM GADELHAK
Département de génie mécanique

Thèse présentée en vue de l'obtention du diplôme de *Philosophiæ Doctor*
Génie mécanique

Novembre 2022

© Ibrahim Ahmed Ibrahim Gadelhak, 2022.

POLYTECHNIQUE MONTRÉAL
affiliée à l'Université de Montréal

Cette thèse intitulée :

Fluidelastic Excitation of a Fuel Rod Bundle Subjected to Combined Axial-Flow and Jet Cross-Flow

présentée par **Ibrahim Ahmed Ibrahim GADELHAK**
en vue de l'obtention du diplôme de *Philosophiæ Doctor*
a été dûment acceptée par le jury d'examen constitué de :

Aouni LAKIS, Ph.D. , président
Njuki MUREITHI, Ph.D. , membre et directeur de recherche
René KAHAWITA, Ph.D. , membre
Shudong YU, Ph.D. , membre externe

DEDICATION

To my family and all those who have believed in me...

ACKNOWLEDGEMENTS

First of all, I would like to express my sincere gratitude to my research supervisor, Professor Njuki Mureithi, for supervising my research dedicating both his time and experience throughout the entire period of this project. Thank you for believe in me since the beginning of this work, for your continuous support and encouragement, for patiently teaching and guiding me through these years. It was really an honor working with you.

My doctoral scholarship was sponsored by NSERC, the Canadian funding agency, and Framatome Inc. I am also thankful to Mr. Kostas Karazis, Mr. Brian Painter, and Mr. Gary Williams, on behalf of Framatome Inc., for providing the technical support during my Ph.D.

Appreciation also goes to the department technicians, Mr. Nour Aimene, Mr. Bénédict Besner, and Mr. Fabrice Danet for their kind help and advice in the preparation of experiments.

I am thankful to my FSI group members with whom I shared the office and many trips, discussions, coffees, equations... It would be impossible to list each one individually, but I would like to mention especially Loay Alyaldin, Sameh Darwish, and Abdallah Hadji. I am also grateful to all my friends in Montréal who helped me to have enjoyable and memorial stay.

I am particularly thankful to my family in Egypt for their belief in me and for supporting me during my Ph.D. journey despite being far away. I am sure this Ph.D. is an achievement for them as well.

Finally, I am most grateful to Aya, my wife, for her unconditional support and joyful companionship throughout the years I spent in Montréal. Aya deserves a lot of credit for completing this thesis.

RÉSUMÉ

Les vibrations induites par le flux (FIV*) dans les centrales nucléaires sont une préoccupation constante, notamment à cause de la demande de meilleures performances et efficacités thermiques quir remet en question les caractéristiques mécaniques, de flux et d'exposition à l'irradiation des conceptions de combustible. De par leur conception, certains réacteurs à eau pressurisée (REP) intègrent des caractéristiques de sécurité telles que des trous et des fentes d'accident de perte de réfrigérant primaire (APRP) dans les chicanes périphériques du cœur entourant les assemblages combustibles. Cela permet notamment une libération de l'accumulation de pression en cas d'APRP. Pendant le fonctionnement normal, le débit à travers les trous APRP était considéré comme minimal parce que le chemin d'écoulement de configuration à flux ascendant à travers l'espace annulaire entre le carottier et la plaque de chicane a été utilisé pour minimiser la chute de pression à travers la plaque de chicane. Cependant, ces usines conçues ont connu l'usure des combustibles par frottement dans le passé et encore plus récemment près des trous APRP de plaque de chicane.

L'objectif principal de ce projet de recherche est de comprendre l'effet d'écoulement axial combiné à un écoulement transversal à jet localisé sur la dynamique d'un faisceau de barres et de développer une stratégie de modélisation appropriée pour simuler cette dynamique; en particulier, lorsque le flux de jet est injecté à partir du trou APRP (c'est-à-dire un jet circulaire). Cet objectif sera atteint grâce à un programme de recherche comprenant des travaux expérimentaux et des modélisations analytiques. Dans le travail expérimental, une série de configurations d'écoulement de faisceaux de barres de plus en plus complexes seront testées. Le point de départ est une étude du comportement en stabilité d'un faisceau de barres monté élastiquement et soumis à un flux de jet pur (en l'absence d'écoulement axial). Un faisceau de barres avec des supports à 1-degrés de liberté (1-DDL) sera d'abord étudié; puis on remplace ce montage par des supports axisymétriques (c'est-à-dire à 2-DDL). Ensuite, une maquette reproduira les conditions de fonctionnement d'un assemblage combustible REP évalué fluidélastiquement en raison de l'écoulement croisé axial et à jet combiné. Un effet stabilisateur de l'écoulement axial sur l'instabilité induite par le jet sera étudié en détail dans le but de déterminer le mécanisme sous-jacent. Tout aussi important, les paramètres régissant l'instabilité fluidélastique (FEI*) des faisceaux de barres soumis à la fois à un écoulement transversal en jet pur et à un écoulement combiné seront

---

*FIV: Flow-induced vibration; FEI: Fluidelastic instability.

déterminés dans le but d'étendre les modèles théoriques d'instabilité fluidélastique existants au cas de l'écoulement en jet transversal et aux écoulements axial et à jet combinés.

De manière plus détaillée, les objectifs de ce travail sont : **O1** caractériser expérimentalement le comportement dynamique de faisceaux de barres soumis à un écoulement transverse de jet pur, **O2** mesurer les dérivées de stabilité fluidélastique et les retard de la réponse du fluide, **O3** développer un modèle semi-empirique quasi-stationnaire pour FEI induites par jets transverses, **O4** développer un modèle de vecteur propre généralisé pour prédire la forme modale d'un faisceau sous jets transverses, **O5** atténuer les vibrations induites par les jets transverses à l'aide d'un contrôle passif de cet écoulement, et **O6** caractériser expérimentalement et modéliser analytiquement la dynamique d'un faisceau de barres à une travée soumis à un jet en écoulement transverse (JITF*).

Trois installations expérimentales ont été conçues et construites. Le premier dispositif expérimental vise à étudier les vibrations induites par l'écoulement transversal du jet pour un faisceau de tiges en treillis carré 6x6 qui est supporté de manière flexible a fin de simuler une partie d'assemblage combustible REP, lequel est soumis à un écoulement de jet transversal pur. Le flux du jet est déplacé transversalement dans la section d'essai pour permettre d'étudier l'effet de stabilité du décalage entre les axes du jet et du faisceau de barres (c'est-à-dire l'excentricité du jet, ξ). Une deuxième configuration de faisceau de barres a été conçue. C'est un faisceau de barres 6x6 constitué de tiges flexibles axisymétriques pour étudier les vibrations biaxiales induites par l'écoulement du jet. Le deuxième appareil expérimental vise à mesurer les forces quasi-statiques et nonstationnaires pour le développement du modèle FEI induit par le jet. Une tige instrumentée avec un capteur de force à six axes est insérée dans un faisceau rigide 6x6 tandis que les tiges voisines sont instrumentées avec des jauges de contrainte pour mesurer les dérivées de force de couplage croisé. Dans l'appareil expérimental final, l'effet de l'écoulement axial sur le FEI induit par l'écoulement transversal du jet est considéré en concevant deux branches de la boucle de test, soit une pour l'écoulement axial et l'autre branche pour l'écoulement du jet. Un faisceau de maquettes RER à travée unique est conçu et fabriqué pour évaluer son comportement dynamique sous différentes configurations d'écoulement axial et d'écoulement croisé de jet. Les limites de stabilité mesurées sont aussi utilisées pour valider le modèle développé pour le FEI induit par JITF.

Les résultats des tests de la première configuration expérimentale montrent que l'écoulement transversal du jet pur provoque une instabilité fluidélastique dans la direction transversale. La vibration et l'instabilité du faisceau de tiges dépendent fortement de l'excentricité du jet

---

*JITF: Jet in transverse flow.

et de l'écart entre la buse et la première rangée (c'est-à-dire la distance de sécurité, H). Les vibrations transversales sont plus dominantes que celles dans le sens du jet. La vitesse critique diminue avec l'augmentation de la distance de recul du jet, puis s'inverse. Les résultats au niveau du flux montrent que l'excentricité variable du jet excitait le faisceau de tiges avec différents mécanismes. Les vibrations des tiges se sont produites avec le jet centré ainsi qu'avec le boîtier du faisceau de tiges et ont eu un phénomène de verrouillage/synchronisation. La vibration de grande amplitude observée dans le faisceau est atténuée à l'aide d'une nouvelle buse inspirée des requins. La performance de la buse inspirée du requin sur la vibration du faisceau de tiges est évaluée par rapport à un cas de référence de buse circulaire. Les résultats montrent que la vitesse d'écoulement critique du jet est retardée de 20% et on observe 80% de réduction d'amplitude par rapport à celles obtenues avec la buse circulaire. De plus, l'effet des diamètres d'écoulement de jet est étudié sur le faisceau de tiges axisymétriques pour obtenir **O4**. La principale découverte dans cet objectif est que la forme modale extraite est presque identique pour les buses avec un rapport d'accélération similaire (A_{Jet}/A_{Gap}). On peut notamment expliquer globalement que les zones d'écart d'écoulement à travers le faisceau changent à mesure que le diamètre de la buse augmente, mais les changements ne sont pas linéaires en raison de la correspondance géométrique entre l'emplacement de la buse et les tiges faisant face au flux du jet.

Les résultats de stabilité basés sur les dérivées de stabilité mesurées et le retard temporel du second appareil expérimental montrent que le modèle développé prédit la vitesse critique avec une erreur de 15%. La principale découverte des travaux théoriques selon laquelle les forces du fluide de jet sur la tige vibrante sont fonction de la tige est dérivée pour prendre en compte la caractéristique dynamique de la tige vibrante sous écoulement transversal à jet circulaire. De plus, les expériences FEI du faisceau à travée unique montrent que la vitesse critique d'écoulement transversal du jet augmente avec l'augmentation de la vitesse d'écoulement axial, introduisant un paramètre important, soit le rapport de vitesse, V_{Jet}/V_{Axial} pour quantifier la limite de stabilité de ce faisceau sous jet en écoulement transverse (JITF). Le FEI induit par le modèle JITF est développé et validé avec les résultats expérimentaux; les résultats du modèle montrent un accord avec la vitesse critique mesurée de l'écoulement transversal du jet avec une erreur absolue maximale de 12.5 % sur trois cas testés.

Dans l'ensemble, cette étude a démontré l'importance de l'instabilité fluidélastique en provoquant des amplitudes de vibration significatives dans les faisceaux de barres à combustible soumis à un écoulement croisé axial et de jet combiné. D'après les résultats obtenus dans ce projet, le potentiel de l'écoulement axial pour stabiliser la vibration du faisceau de la maquette REP et donc élever la limite de stabilité des faisceaux soumis à un écoulement croisé à jet pur est mis en évidence. Des recherches supplémentaires sont cependant nécessaires pour

valider cet effet stabilisateur de l'écoulement axial sous des paramètres d'écoulement de jet variés (D_{Jet}, H). Le travail de modélisation améliore la compréhension du mécanisme sous-jacent à l'instabilité induite par le jet. Un nouveau paramètre de la dérivée de la surface de la tige s'avère nécessaire pour simuler la caractéristique dynamique de barres à combustible vibrantes sous jet de trous APRP. Enfin, ce travail de recherche apporte des informations originales sur les limites de stabilité des faisceaux de barres soumis à jet pur et à jet en écoulement transverse (JITF). La stabilité de quoi résultats expérimentaux pourraient être utilisés pour concevoir des cœurs de réacteur efficaces et sûrs.

ABSTRACT

Flow-induced vibration (FIV) in nuclear power plants is a constant concern as the demand for better thermal performance and efficiencies challenges the mechanical, flow, and irradiation exposure characteristics of fuel designs. By design, certain pressurized water reactors (PWRs) incorporate safety features such as loss of coolant accident (LOCA) holes and slots in the core periphery baffles surrounding the fuel assemblies, providing relief from pressure build-up in the event of a LOCA. During normal operation, the flow rate through LOCA holes was thought to be minimal because the up-flow configuration flow path through the annulus between the core barrel and the baffle plate was used to minimize the pressure drop across the baffle plate. However, plants having these design features have experienced grid-to-rod fretting (GTRF) failure at the position of baffle plate LOCA holes in the past and again more recently.

The main goal of this research work is to understand the effect of a combined axial-flow and localized jet cross-flow on the dynamics of a rod bundle and to develop a proper modelling strategy to simulate these dynamics. Of particular interest is the case when the jet flow is injected from a LOCA hole (i.e. circular jet). This goal will be achieved through a research program comprising experimental work and analytical modelling. In the experimental work, a series of increasingly complex rod bundle-flow configurations are tested. The starting point is a study of the stability behaviour of a rod bundle mounted elastically under a pure jet cross-flow (in the absence of axial flow). A rod bundle with 1-DOF supports is firstly investigated and then this same bundle dimension is replaced with axisymmetric supports (i.e. 2-DOF). Thereafter, a mock-up PWR assembly is fluidelastically evaluated when subjected to combined axial-flow and jet cross-flow. The stabilizing effect of the axial flow on the jet-induced instability is studied in detail with the goal of determining the underlying excitation mechanism. Equally important, the parameters governing the fluidelastic instability (FEI) of rod bundles subjected to both pure jet cross-flow and combined flows are determined with the goal of extending existing fluidelastic instability theoretical models to the transverse jet flow case and then to the combined axial flow and jet-cross flow case.

On a more detailed level, the objectives of this work are: **O1** characterize experimentally the dynamical behavior of a rod bundle subjected to pure jet cross-flow, **O2** perform fluidelastic stability derivatives and time delay measurements, **O3** develop a semi-empirical quasi-steady model for FEI induced by jet cross-flow, **O4** develop a generalized eigenvector model to predict the mode shape of the array under jet cross-flows, **O5** proposed a passive mitigation

method for jet cross-flow induced vibrations, and **O6** characterize experimentally and model analytically the dynamics of a single-span flexible rod bundle subjected to a jet in transverse flow (JITF).

Three experimental facilities have been designed and built. The first experimental apparatus is used to study jet cross-flow induced vibration for a flexibly supported 6x6 square lattice rod bundle simulating part of a PWR fuel assembly subjected to a pure transverse jet flow. The jet flow is transversely injected into the test section by a specially designed jet flow injection and displacement mechanism to allow investigation of the stability effect of offset between the centerlines of the jet and rod array (i.e. jet eccentricity, ξ). The second rod bundle setup designed consists of a 6x6 rod bundle made of axisymmetric flexible rods to study bi-axial vibrations induced by the jet flow. The second experimental apparatus is used to measure the quasi-static and unsteady forces for the jet cross-flow induced FEI model development. An instrumented rod with a six-axis force sensor is inserted in the 6x6 rigid array while the neighboring rods are instrumented with strain gauges to measure the cross-coupling force derivatives. In the final experimental apparatus, the effect of axial flow on jet cross-flow induced FEI is considered by designing two branches of the test loop, one for the axial flow, and the other branch for the jet flow. A single-span PWR mock-up array is designed and fabricated to evaluate its dynamical behavior under different axial flow and jet cross-flow configurations. The measured stability boundaries are also used to validate a newly developed model for JITF-induced fluidelastic instability.

The test results from the first experimental setup show that pure jet cross-flow causes strong fluidelastic instability. The rod bundle vibration and instability depend strongly on the jet eccentricity and the gap between the nozzle and the first row (i.e. jet exit stand-off distance, H). The transverse vibrations are more dominant than those in the stream-wise direction. The critical velocity decreases with increasing stand-off distance and then reverses. The stream-wise results show that varying jet eccentricity excites the rod bundle with different mechanisms. The rod vibrations for the jet centered with the rod bundle case had a lock-in/synchronization phenomenon.

A new nozzle inspired by shark gills is shown to mitigate the observed large amplitude vibration in the array. The performance of the shark-inspired nozzle on the rod array vibration is evaluated versus the reference case of a plain circular nozzle. The results show that the critical jet flow velocity is delayed by 20% and vibration amplitude reduced by 80% compared to results obtained with the circular nozzle. The effect of jet flow diameter is investigated on the axisymmetric rod array. The results achieve **O4** by developing a generalized eigenvector model to predict the mode shape of the array under jet cross-flows. The main finding in

this objective is that the extracted mode shape is nearly identical for nozzles with a similar acceleration ratio (A_{Jet}/A_{Gap}). This is because the flow gap areas across the bundle change as the nozzle diameter increases. The changes are nonlinear due to geometrical matching between the nozzle location with the rods facing the jet flow.

The stability results based on the measured stability derivatives and time delay from the second experimental apparatus show that the newly developed model predicts the critical velocity within an error of 15%. The main finding from theoretical work is that the jet fluid forces on the vibrating rod are functions of the rod area derivative which accounts for the dynamic variation of the jet projected area on the first row rods.

The FEI experiments on the single-span array show that the critical jet cross-flow velocity increases with increasing the axial flow velocity, introducing an important parameter, velocity ratio, V_{Jet}/V_{Axial} to quantify the stability limit of this array under jet in transverse flow (JITF). A JITF induced FEI model is developed and validated with the experimental results. The model results show agreement with the measured critical jet cross-flow velocity with a maximum absolute error of 12.5% over the three tested cases.

Overall, this study demonstrated the importance of fluidelastic instability in causing significant vibration amplitudes in rod bundles subjected to combined axial flow and jet cross-flow. From the results obtained in this work, the potential of axial flow to stabilize the mock-up PWR array vibration and to increase the stability limit of arrays subjected to pure jet cross-flow is demonstrated. Additional research is, however, required to validate this stabilizing effect of axial flow for a wider range of jet flow parameters (D_{Jet}, H). The modeling work improves the understanding of the mechanism underlying jet-induced instability. A new parameter of the rod area derivative is found to be necessary to correctly model the dynamics of the vibrating rod under LOCA hole jetting. Finally, this research work provides original information on the stability boundaries of arrays subjected to pure jet cross-flow and jet in transverse flow (JITF). The stability and experimental results could be used to design efficient and fluidelastically safe reactor cores.

TABLE OF CONTENTS

DEDICATION iii

ACKNOWLEDGEMENTS iv

RÉSUMÉ v

ABSTRACT ix

TABLE OF CONTENTS xii

LIST OF TABLES xvi

LIST OF FIGURES xvii

LIST OF SYMBOLS AND ACRONYMS xxvii

CHAPTER 1 INTRODUCTION 1
- 1.1 Background 1
- 1.2 Problem Definition 5
- 1.3 Research Questions 7
- 1.4 Research Objectives 8
- 1.5 Thesis Outline 10

CHAPTER 2 LITERATURE REVIEW 12
- 2.1 Turbulent Jets 12
  - 2.1.1 Round Turbulent Jet 13
  - 2.1.2 Jet in Transverse Flow (JITF) 14
- 2.2 Flow Induced Vibration (FIV) Mechanisms 19
  - 2.2.1 Axial FIV Mechanisms 19
  - 2.2.2 Baffle Jetting FIV Mechanisms 23
- 2.3 Fluidelastic Instability (FEI) Theoretical Models 27
- 2.4 Unsteady Models 28
- 2.5 Quasi-steady Model 29
- 2.6 Quasi-Unsteady Model 32

CHAPTER 3 ARTICLE 1: JET CROSS-FLOW INDUCED VIBRATIONS IN ROD

BUNDLES. PART I: EXPERIMENTAL APPARATUS AND STREAM-WISE VIBRATION RESULTS . . . 35
3.1 Introduction . . . 36
3.2 Experimental setup and test parameters . . . 39
3.2.1 Parameter identification . . . 39
3.2.2 Test section design . . . 40
3.2.3 Test loop set-up . . . 44
3.2.4 Measurement systems . . . 46
3.2.5 Rod bundle map . . . 48
3.2.6 Test parameters . . . 48
3.3 Test results . . . 49
3.3.1 Dynamic behavior of fully flexible 6x6 rod bundle in stream-wise direction 49
3.3.2 Stability effect of stand-off distance on fully flexible 6x5 rod bundle . 58
3.4 Discussion . . . 60
3.5 Conclusions . . . 62

CHAPTER 4 ARTICLE 2: JET CROSS-FLOW INDUCED VIBRATIONS IN ROD BUNDLES. PART II: TRANSVERSE VIBRATION RESULTS AND EXCITATION MECHANISMS . . . 64
4.1 Introduction . . . 65
4.2 Experimental setup and test parameters . . . 67
4.2.1 Test loop set-up . . . 67
4.2.2 Test parameters . . . 68
4.3 Test results . . . 69
4.3.1 Dynamic behavior of fully flexible 6x6 rod bundle in the transverse direction . . . 70
4.3.2 Dynamic behavior of fully flexible 6x5 rod bundle in transverse direction 75
4.3.3 Dynamic behavior of fully flexible 6x4 rod bundle in transverse direction 80
4.4 Discussion . . . 81
4.5 Conclusions . . . 84

CHAPTER 5 ARTICLE 3: FLUIDELASTIC INSTABILITY (FEI) MODEL FOR A ROD BUNDLE SUBJECTED TO JET CROSS-FLOW . . . 86
5.1 Introduction . . . 87
5.2 Stability behavior of rod bundle subjected the jet cross-flow . . . 89
5.2.1 Test parameters . . . 89
5.2.2 FEI experimental results . . . 90

5.3 FEI model development 91
5.4 Experimental setup 95
5.4.1 Linear motor design and test section instrumentation 95
5.4.2 Test loop set-up 97
5.5 Test results 97
5.5.1 Quasi-static fluid force measurements 97
5.5.2 Time delay measurement 100
5.6 FEI model analysis results and model validation 103
5.6.1 Fluidelastic stability analysis 103
5.6.2 Stability effect of L_{Jet}/L_{Rod} 106
5.6.3 Stability effect of area derivative 107
5.7 Conclusions 109

CHAPTER 6 ARTICLE 4: PRINCIPAL COMPONENT ANALYSIS (PCA) OF ROD BUNDLE VIBRATION SUBJECTED TO JET CROSS-FLOW 111
6.1 Introduction 112
6.2 Methodology 115
6.2.1 Mathematical formulation 115
6.2.2 Experimental setup 116
6.3 Test results 120
6.3.1 Jet-induced vibration response 121
6.4 Stability boundary 128
6.5 Singular value decomposition (SVD) analysis 130
6.6 Principal component analysis (PCA) 133
6.6.1 PCA on rod bundle vibration for a single nozzle 133
6.6.2 PCA of rod bundle vibration and existence of generalized model . . . 137
6.7 Conclusions 140

CHAPTER 7 ARTICLE 5: MITIGATION OF JET CROSS-FLOW INDUCED VIBRATIONS USING AN INNOVATIVE BIOMIMETIC NOZZLE DESIGN INSPIRED BY SHARK GILL GEOMETRY 143
7.1 Introduction 144
7.2 Experimental design concept 148
7.2.1 Shark-inspired nozzle design 148
7.2.2 Experimental set up 150
7.2.3 Measurement system and image processing 150
7.2.4 Image processing algorithm 151

7.3 Results . . . 153
7.3.1 Circular nozzle jet cross- flow induced vibrations of rod bundle . . . 153
7.3.2 Jet cross-flow induced vibrations of rod bundle for 10-fin shark-inspired nozzle . . . 154
7.3.3 Jet cross-flow induced vibrations in rod bundle due to the shark-inspired nozzle with 15 fins . . . 155
7.4 Discussion . . . 156
7.5 Conclusions . . . 158

CHAPTER 8 ARTICLE 6: FLUIDELASTIC INSTABILITY OF A FUEL ROD BUNDLE SUBJECTED TO COMBINED AXIAL FLOW AND JET CROSS-FLOW . 159
8.1 Introduction . . . 160
8.2 Experimental setup . . . 165
8.2.1 Design and test parameters . . . 165
8.2.2 Flexible rod bundle and instrumentation . . . 165
8.2.3 Test section setup . . . 167
8.2.4 Test loop setup . . . 168
8.3 Test results . . . 169
8.3.1 Flow-induced vibration response of rod bundle subjected to purely axial flow . . . 169
8.3.2 Dynamics of rod bundle subjected to combined axial flow and jet cross-flow . . . 171
8.3.3 Axial flow damping tests . . . 177
8.4 JITF induced FEI model development . . . 179
8.5 FEI model analysis results and model validation . . . 185
8.6 Conclusions . . . 186

CHAPTER 9 GENERAL DISCUSSION . . . 189

CHAPTER 10 CONCLUSIONS AND RECOMMENDATIONS FOR FUTURE WORK 195
10.1 Contributions . . . 195
10.2 Limitations and Challenges . . . 197
10.3 Recommendations for Future Work . . . 197
10.4 Research Project Deliverables . . . 198

REFERENCES . . . 200

LIST OF TABLES

Table 2.1 Comparison of experimental values of round jet spread rate, β. 14

Table 2.2 Test parameters (Fujita et al., 1990). 26

Table 4.1 Stability constants (K) for three eccentricities with three stand-off distances. 83

Table 5.1 Steady drag and lift force coefficients (C_{D_0} & C_{L_0}) and derivatives of the lift coefficient ($C_L, y_k/D$) measured at $Re_{Jet} = 4\text{x}10^4$. 100

Table 6.1 PCA details for the five rods in the first row with the three tested jet diameters in the unstable vibration region. 137

Table 8.1 Damping ratio and frequency values of a single flexible rod versus axial flow velocity. 178

Table 8.2 Steady drag and lift force coefficients (C_{D_0} & C_{L_0}) and derivatives of the lift coefficient ($C_L, y_k/D$) measured at $Re_{Jet} = 4\text{x}10^4$, Gad-el Hak et al. (2022b). 184

LIST OF FIGURES

Figure 1.1	Cross section of pressure reactor vessel (U.S. NRC, 1980).	2
Figure 1.2	(a) down flow configuration flow path in a barrel-baffle region Hertrick et al. (1984), and (b) baffle jetting phenomena Hertrick et al. (1984).	3
Figure 1.3	Schematic drawing showing flow path through LOCA holes (blue arrows) (AREVA, 2017).	4
Figure 1.4	Jet flow parameters.	6
Figure 1.5	JITF with array configuration.	7
Figure 2.1	A sketch of flow regimes emanating from round jet (Lee et al., 2003).	13
Figure 2.2	A schematic drawing of jet in transverse flow (JITF).	15
Figure 2.3	Streamlines of shear layer vorticities along the symmetry plane of (a) top-hat and (b) parabolic jets.	17
Figure 2.4	Jet in transverse flow (JITF) flow regimes with respect to velocity ratio.	17
Figure 2.5	A sectional view of the JITF showing the jet trajectory.	18
Figure 2.6	Sketch of theoretical tube response with increasing cross flow velocity, (Nakamura et al., 2013).	20
Figure 2.7	Comparison of rod vibrations from Paidoussis' equation (Paidoussis, 1965), Burgreen' equation (Burgreen et al., 1958) and the experimental data conducted by Pavlica and Marshall (1966).	23
Figure 2.8	Baffle jetting parameters (Seki et al., 1986).	24
Figure 2.9	Comparison of measured (solid line) and calculated (densely dashed) values of the critical momentum flux, (a) 15x15 type and (b) 17x17 type, (Seki et al., 1986).	25
Figure 2.10	Dynamical behavior of a single tube in water subjected to (a) uniform flow, and (b) jet flow (Fujita et al., 1990).	26
Figure 2.11	(a) Stability effect of axial flow, and (b) stability effect of stand-off distance (H) on the stability constant (K), (Lee and Chang, 1990).	27
Figure 2.12	(a) cylinder array (b) the stability boundaries showing critical reduced velocity against mass ratio (Tanaka and Takahara, 1981).	29
Figure 2.13	Relative velocity diagram for a quasi-steady analysis.	30
Figure 2.14	Comparison between experimental data (Price et al., 1986) and the theoretical stability boundary for a single flexible cylinder in an in-line square array of rigid cylinders, with $P/D_{Rod} = 1.5$.	32

Figure 2.15 Transient variation of lift coefficient, δC_L(t) induced by a step displacement $Y(t) = Y_0 H(t)$: (a) $Y(t)$, (b) quasi-steady theory, (c) Price & Paidoussis model and (d) continuous variation of time delay as proposed in quasi-unsteady model (order 1) (Granger and Paidoussis, 1996). 33

Figure 2.16 Comparison of the stability boundaries for a single flexible tube between the quasi-steady model (dash), quasi-unsteady model with first order (line) and quasi-unsteady model with second order (dash-dot) in: (a) a rigid normal triangular array, and (b) a square in-line array (Granger and Paidoussis, 1996). 34

Figure 3.1 (a) Baffle-barrel design including LOCA holes,(AREVA, 2017) and (b) schematic drawing showing flow emanating from LOCA hole towards fuel rods. 38

Figure 3.2 Schematic drawings of the jet flow with the rod bundle:(a) side view, and (b) top view. 41

Figure 3.3 Jet flow displacement mechanism showing the main components: (1) nozzle, (2) moving plate, (3) threaded flange nut, (4) ultra-precision lead screw, (5) linear motion shaft, (6) linear ball bearing, (7) spring-loaded rotary shaft seal, (8) linear ball bearing and (9) hand wheel with the dial indicator. 43

Figure 3.4 Single flexible rod showing its support and the holes used to pass the strain gauge cables. 43

Figure 3.5 (a) Schematic drawing for the rod gap error due to the rod surface misalignment, and (b) 6x6 Flexible Rod bundle setup. 44

Figure 3.6 (a) Measured longitudinal gaps, and (b) measured transverse gaps. . 45

Figure 3.7 The main components of test loop set-up are labelled: (1) flow straightener, (2) barrel-baffle chamber, (3) displacement jet flow mechanism, (4) rod bundle, (5) water flow meter and (6) centrifugal pump. 45

Figure 3.8 Set of sequential image representing the rod bundle motion at ξ of $0.5P$ at jet velocity of 1.7 m/s. 46

Figure 3.9 (a) Eight instrumented rods with strain gauges, and (b) strain gauge calibration. 47

Figure 3.10 Rod bundle numbering. 48

Figure 3.11 Top sectional views of rod array for three jet eccentricities (a) ξ=0, (b) ξ=0.25P, and (c) ξ=0.5P and (e), (f) and (g) corresponding projected views from the nozzle, respectively. 49

Figure 3.12 Comparison of obtained stream-wise response from strain gauge and high-speed camera at $\xi = 0$. 50
Figure 3.13 Rod bundle vibrations in stream-wise direction for 6x6 configuration at $\xi = 0$. 51
Figure 3.14 PSD plots showing the dynamical behaviors of rod 301 within the first six tested jet velocities: (a) $V_{Jet} = 0.63$ m/s , (b) $V_{Jet} = 0.73$ m/s, (c) $V_{Jet} = 0.82$ m/s, (d) $V_{Jet} = 0.92$ m/s, (e) $V_{Jet} = 0.98$ m/s, and (f) $V_{Jet} = 1.05$ m/s. 52
Figure 3.15 Schematic drawings for jet flow: (a) free jet flow inside the nozzle, (b) jet flow through the gap between rods 301 & 401, (c) top view of the centred jet flow through the bundle, (d) first mode (varicose mode) of jet vortex arrays (Huang and Hsiao, 1999), and (e) second mode (sinuous mode) of jet vortex arrays (Huang and Hsiao, 1999). 53
Figure 3.16 Comparison of obtained stream-wise response from strain gauge and high-speed camera at $\xi = 0.25P$. 54
Figure 3.17 Rod bundle vibrations in stream-wise direction for 6x6 configuration at $\xi = 0.25P$. 54
Figure 3.18 Schematic drawing for flow paths in the bundle at $\xi = 0.25P$. 55
Figure 3.19 3D PSD plots showing the dynamical behaviors of rods: (a) rod 301, (b) rod 302 and (c) rod 303 at ξ=0.25P, respectively. 55
Figure 3.20 3D PSD plots showing the dynamical behaviors of rods: (a) rod 501, (b) rod 502 and (c) rod 503 at ξ=0.25P, respectively. 55
Figure 3.21 Comparison of obtained stream-wise response from strain gauge and high-speed camera at $\xi = 0.5P$. 56
Figure 3.22 Rod bundle vibrations in stream-wise direction for 6x6 configuration at $\xi = 0.5P$. 57
Figure 3.23 (a) Schematic drawing for flow paths in the bundle at $\xi = 0.5P$, and (b) PIV measurements for two parallel jets (Wang et al., 2016). . . . 57
Figure 3.24 3D PSD plots showing the dynamical behaviors of rods: (a) rods 401, (b) 402 and (c) 403 at ξ=0.5P, respectively. 58
Figure 3.25 Rod bundle vibrations in stream-wise direction for 6x5 configuration at $\xi = 0$. 59
Figure 3.26 Dominant response frequencies obtained from the power spectral density versus jet velocity in the two peaks of vibrations regions for rod 401 at $\xi = 0$. 59

Figure 3.27 Strouhal number at the peak at low flow velocities with varying stand-off distance at $\xi = 0$. 61

Figure 4.1 Jet flow parameters. 66

Figure 4.2 The main components of test loop set-up are labelled: (1) flow straightener, (2) barrel-baffle chamber, (3) displacement jet flow mechanism, (4) rod bundle, (5) water flow meter and (6) centrifugal pump. 68

Figure 4.3 Top sectional views of rod array for three jet eccentricities (a) ξ=0, (b) ξ=0.25P, and (c) ξ=0.5P and (e), (f) and (g) corresponding projected views from the nozzle, respectively. 69

Figure 4.4 Comparison of obtained transverse response from strain gauge and high-speed camera at $\xi = 0$. 70

Figure 4.5 Rod bundle vibrations in transverse direction for 6x6 configuration at $\xi = 0$. 71

Figure 4.6 PSD plots showing the dynamical behaviors of rod 401 at two velocities: (a) 1.05 m/s, and (b) 2 m/s. 71

Figure 4.7 Rod bundle vibrations in transverse direction for 6x6 configuration at $\xi = 0.25P$. 73

Figure 4.8 Dominant response frequencies obtained from the power spectral density functions versus jet velocity in the instability-induced vibrations region for three rods: (a) rod 401, (b) rod 402, and (c) rod 403. . . . 74

Figure 4.9 Rod bundle vibrations in transverse direction for 6x6 configuration at $\xi = 0.5P$. 74

Figure 4.10 Dominant response frequencies obtained from the power spectral density functions versus jet velocity in the instability-induced vibrations region for four rods: (a) rod 401, (b) rod 402, (c) rod 502 and (d) 403 at $\xi = 0.5P$. 75

Figure 4.11 Rod bundle vibrations in transverse direction for 6x5 configuration at $\xi = 0$. 76

Figure 4.12 (a) steady jet, (b) excited jet, (Narayanan, 1988). 77

Figure 4.13 Rod bundle vibrations in transverse direction for 6x5 configuration at $\xi = 0.25P$. 78

Figure 4.14 Rod bundle vibrations in transverse direction for 6x5 configuration at $\xi = 0.5P$. 79

Figure 4.15 PSD plots showing the dynamical behaviors of rod 401 with increasing jet velocity: (a) $V_{Jet} = 1.15$ m/s, (b) $V_{Jet} = 1.44$ m/s, and (c) dominant response frequencies of rod 401 versus jet velocity in the instability-induced vibrations region. 79
Figure 4.16 Rod bundle vibrations in transverse direction for 6x4 configuration at $\xi = 0$. 81
Figure 4.17 Rod bundle vibrations in transverse direction for 6x4 configuration at $\xi = 0.25P$. 82
Figure 4.18 Rod bundle vibrations in transverse direction for 6x4 configuration at $\xi = 0.5P$. 82
Figure 4.19 Threshold of instability-induced vibration for three jet eccentricities ($\xi = 0$, $0.25P$ and $0.5P$) tested with three rod bundles: (a) 6x6 rod bundle, (b) 5x6 rod bundle, and (c) 4x6 rod bundle. 83
Figure 5.1 (a) top sectional view of rod array for jet eccentricity of ξ=0.5P, (b) projected view from the nozzle at ξ=0.25P, and (c) side view of rod array with jet flow configuration. 90
Figure 5.2 The main components of FEI test loop set-up are labelled: (1) flow straightener, (2) barrel-baffle chamber, (3) displacement jet flow mechanism, (4) rod bundle, (5) water flow meter and (6) centrifugal pump. 91
Figure 5.3 FEI results for different arrays: (a) single rod, (b) 2x1 single row, (c) 3x1 single row, and (d) 6x6 fully flexible array. 92
Figure 5.4 (a) projected view from the nozzle, and (b) top view of the array with the nozzle. 93
Figure 5.5 (a) liner motor system components, and (b) test section instrumentation. 96
Figure 5.6 (a) comparison between sin wave, square wave, and 1/8 micro-steeping wave form, and (b) the motor response with 1/128 micro-step. 97
Figure 5.7 The main components of test loop set-up are labelled: (1) laser sensor, (2) displacement jet flow mechanism, (3) instrumented neighbouring rods, (4) linear motor system, (5) centrifugal pump and (6) flow meter. 98
Figure 5.8 Area change (red line) with rod displacement and its linear fitting (black line) for the three rods: (a) rod 301, (b) rod 401, and (c) rod 501. 99
Figure 5.9 Variation of the jet fluid force coefficients for the central rod with jet Reynolds number: (a) C_D, and (b) C_L. 99
Figure 5.10 Measured torque arm for rod 401 with its non-dimensional displacement. 100

Figure 5.11 Variation of the lift force coefficient of the three rods with their quasi-static displacements in the lift direction at $Re_{Jet} = 4\text{x}10^4$: (a) rod 301, (b) rod 401, and (c) rod 501. 101
Figure 5.12 (a) Fluid response due to sinusoidal rod motion, and (b) orbit plot showing the phase lag (φ). 102
Figure 5.13 (a) Extracted time delay (τ) versus V_{Jet}/fD, and (b) measured flow retardation parameter (μ) versus V_{Jet}/fD. 102
Figure 5.14 Variation of the eigenvalues (Re (λ) and Im (λ)) with reduced jet velocity for the single flexible rod and 2x1 flexible row: (a) and (c) for the single rod 401, and (b) and (d) for the two flexible rods 301 and 401.104
Figure 5.15 Variation of the eigenvalues with reduced jet velocity for the 3x1 flexible row: (a) Real part of λ, and (b) imaginary part of λ. 105
Figure 5.16 Rods response at $V_{Jet}/(f_w\ D) = 5.61$: (a) rod 301, (b) rod 401, and (c) rod 501. 105
Figure 5.17 Rods response at $V_{Jet}/(f_w\ D) = 5.76$: (a) rod 301, (b) rod 401, and (c) rod 501. 105
Figure 5.18 Phase portraits for rod 401 at two reduced jet velocities: (a) $V_{Jet}/f_w\ D = 5.61$, and (b) $V_{Jet}/(f_w\ D) = 5.76$. 106
Figure 5.19 (a) schematic showing a single span of fuel rods with LOCA hole, and (b) test rig used to calculate rod stiffness due to jet fluid force. 107
Figure 5.20 (a) variation of normalized rod stiffness ($K_e/K_{mid-point}$) with L_{Jet}/L_{Rod}, and (b) predicted reduced jet velocity as function of L_{Jet}/L_{Rod}. . . . 108
Figure 5.21 Variation of the eigenvalues with reduced jet velocity for two cases: (a) setting $\frac{\partial A}{\partial y}$=0, and (b) $e^{-i\omega\tau}\frac{\partial A}{\partial y}$ in the model. 108
Figure 6.1 (a) 2x2 inline square rod bundle in a jet cross-flow, and the rod bundle response with three phase difference (ψ): (b) $\psi = 0$, (c) $\psi = 20°$, and (d) $\psi = 40°$. 116
Figure 6.2 (a) single rods, and (b) 6x6 in-line square flexible rod bundle. 117
Figure 6.3 (a) Image processing technique, and (b) rod bundle vibration obtained by processing a series of images. 118
Figure 6.4 The main components of test loop set-up are labelled: (1) diverging rectangular transition section, (2) flow straightener, (3) empty chamber, (4) jet flow positioning mechanism, (5) rod bundle, (6) converging rectangular transition section, (7) centrifugal pump, (8) water flow meter, and (9) high-speed camera. 119

Figure 6.5 Three tested nozzles: (a) $D_{Jet} = 0.7$", (b) $D_{Jet} = 1.0$", and (c) $D_{Jet} = 1.3$". 120
Figure 6.6 Top sectional views and corresponding projected views from the nozzle for the three jet diameters: (a) and (b) for $D_{Jet} = 0.7$", (c) and (d) for $D_{Jet} = 1.0$", (e) and (f) for $D_{Jet} = 1.3$", respectively. 121
Figure 6.7 Rod bundle vibrations in transverse and stream-wise directions for $D_{Jet}/D = 1.6$. 122
Figure 6.8 Time traces, orbit plot, and PSD plots for Rod 401. 123
Figure 6.9 Time traces, orbit plot, and PSD plots for Rod 402. 123
Figure 6.10 Orbit plots for rod 401 for four jet velocities: (a) $V_{Jet} = 3.1$ m/s, (b) $V_{Jet} = 3.2$ m/s, (c) $V_{Jet} = 3.46$ m/s, and (d) $V_{Jet} = 3.6$ m/s, respectively. 124
Figure 6.11 Rod bundle vibrations in transverse and stream-wise directions for $D_{Jet}/D = 2.3$. 125
Figure 6.12 Time traces, orbit plot, and PSD plots for Rod 402. 125
Figure 6.13 Orbit plot of rod 402 with four jet velocities: (a) $V_{Jet} = 1.8$ m/s, (b) $V_{Jet} = 2.14$ m/s, (c) $V_{Jet} = 2.24$ m/s, and (d) $V_{Jet} = 2.34$ m/s, respectively. 126
Figure 6.14 Rod bundle vibrations in transverse and stream-wise directions for $D_{Jet}/D = 3.0$. 127
Figure 6.15 Time traces, orbit plot, and PSD plots for Rod 401. 127
Figure 6.16 Orbit plot of rod 402 with four jet velocities: (a) $V_{Jet} = 1.57$ m/s, (b) $V_{Jet} = 1.64$ m/s, (c) $V_{Jet} = 1.7$ m/s, and (d) $V_{Jet} = 1.75$ m/s, respectively. 128
Figure 6.17 (a) test section setup for the free decay test, and (b) experimental results for the free decay tests in air and water. 129
Figure 6.18 Threshold of unstable vibration for the tested bundle 6x6 with the three diameter ratios, D_{Jet}/D. 129
Figure 6.19 (a) Singular values σ_r, and (b) cumulative energy in the r modes for $D_{Jet}/D = 1.6$. 131
Figure 6.20 Truncated SVD of the rod bundle vibration at two ranks, $r = 2$ and 4 for $D_{Jet}/D = 1.6$. 132
Figure 6.21 Truncated SVD based on $r = 2$ for three diameter ratios: (a) $D_{Jet}/D = 1.6$, (b) $D_{Jet}/D = 2.3$, and (c) $D_{Jet}/D = 3.0$. 132
Figure 6.22 (a) Rod 402 vibration data with the original coordinate, and (b) principal component analysis (PCA) of rod 402 at test condition of $V_{Jet} = 2.14$ m/s, and $D_{Jet}/D = 2.3$. 135
Figure 6.23 (a) a schematic drawing showing the rotation angle, and (b) identification of mode shape based on θ. 135

Figure 6.24 3x3 reduced rod bundle mode shape with three diameter ratio (D_{Jet}/D): (a) $D_{Jet}/D = 1.6$, (b) $D_{Jet}/D = 2.3$, and (c) $D_{Jet}/D = 3.0$. 138

Figure 6.25 Absolute difference of rotation angles based on PC1 between individual and overall PCA eigenvectors. 140

Figure 6.26 Intersection regions between the three nozzles and the rod bundle. . . 141

Figure 6.27 Acceleration ratio of the jet flow associated with increasing the diameter ratio, D_{Jet}/D. 141

Figure 7.1 Modelling of bio–inspired nozzle. (a) shark anatomy, (b) ram ventilation concept corresponding to jet in cross flow, (c) drawing of a gill showing gill filaments (oxygen absorption), gill arch (supporting structure), and gill rakers, (d) schematic drawing of a portion of filaments and their secondary lamellae and also the countercurrent exchange system, (e) schematic drawing of shark-inspired nozzle, and (f) circular jet flow. 148

Figure 7.2 Three tested nozzle: (a) circular nozzle, (b) 10 fins shark-inspired nozzle, and (c) 15 fins shark-inspired nozzle. 149

Figure 7.3 Experimental set-up. 150

Figure 7.4 Test loop setup. 151

Figure 7.5 Camera set-up. 152

Figure 7.6 (a) processed images showing the detected circles by the code and the four-point boundary for each rod in the bundle, and (b) the time signals for two rods 302 and 402 during one second at V_{Jet}= 2 m/s for 15 fins shark-inspired nozzle. 152

Figure 7.7 Rod bundle vibrations using the circular nozzle. 154

Figure 7.8 (a) PSD plot for Rod 401 at V_{Jet} = 1.45 m/s, and (b) PSD plot for Rod 401 at V_{Jet} = 1.75 m/s. 154

Figure 7.9 Rod bundle vibrations using 10 fins shark-inspired nozzle. 155

Figure 7.10 Rod bundle vibrations using 15 fins shark-inspired nozzle. 156

Figure 7.11 Comparison of rod 402 response with three different nozzles. 156

Figure 7.12 Comparison of critical jet velocity and momentum from the three tested nozzles. 157

Figure 8.1 Baffle-barrel design including LOCA holes,(AREVA, 2017). 162

Figure 8.2 (a) schematic drawing of jet in cross-flow (JITF), (b) sectional view of the JITF showing the jet trajectory. 164

Figure 8.3 (a) sectional view of 3x1 flexible row configuration for jet eccentricity of ξ=0.25P, (b) sectional view of 6x5 fully flexible bundle configuration for jet eccentricity of ξ=0.25P, and (c) top view of rod array. 166
Figure 8.4 6x5 fully flexible rod bundle setup. 166
Figure 8.5 (a) jet flow displacement mechanism, (b) assembled test section frame. 167
Figure 8.6 (a) assembled test section with panels, (b) setup of the rod bundle inside the test section. 168
Figure 8.7 The main components of test loop setup are labelled: (1) cross-flow pump, (2) cross-flow meter, (3) axial flow pump, (4) axial flow meter, (5) flow straightener, (6) main test section, (7) displacement jet flow mechanism, (8) data acquisition system. 169
Figure 8.8 Axial flow induced vibrations for two arrays: (a) 3x1 flexible row, (b) 6x5 fully flexible bundle. 170
Figure 8.9 3D power spectral densities (PSDs) plots for rod 401 in the stream-wise direction (x), and the transverse direction (y): (a) 3x1 flexible row, (b) 6x5 fully flexible bundle. 170
Figure 8.10 RMS response and dominant response frequencies of 3x1 rod bundle for three tested axial flow velocities: (a) and (b) for V_{Axial} = 1 m/s, (c) and (d) for V_{Axial} = 1.5 m/s, and (e) and (f) for V_{Axial} = 2.0 m/s. 172
Figure 8.11 3D PSD plots in the stream-wise direction of rod 401 with the three axial flow velocities cases: (a) V_{Axial} = 1.0 m/s , (b) V_{Axial} = 1.5 m/s, and (c) V_{Axial} = 2.0 m/s. 173
Figure 8.12 3D PSD plots in the transverse direction of rod 401 with the three axial flow velocities cases: (a) V_{Axial} = 1.0 m/s , (b) V_{Axial} = 1.5 m/s, and (c) V_{Axial} = 2.0 m/s. 173
Figure 8.13 Orbit plots for three rods for the V_{Axial} = 1.0 m/s case at V_{Jet} = 2.6 m/s: (a) rod 301, (b) rod 401, and (c) rod 501. 174
Figure 8.14 Orbit plots for three rods for the V_{Axial} = 1.5 m/s case at V_{Jet} = 2.8 m/s: (a) rod 301, (b) rod 401, and (c) rod 501. 174
Figure 8.15 Orbit plots for three rods for the V_{Axial} = 2 m/s case at V_{Jet} = 3.5 m/s: (a) rod 301, (b) rod 401, and (c) rod 501. 174
Figure 8.16 RMS response for four rods in 6x5 fully flexible rod bundle for V_{Axial} = 1.0 m/s, (b) corresponding 3D PSD plots in the stream-wise direction of rod 401, and (c) corresponding 3D PSD plots in the transverse direction of rod 401. 176

Figure 8.17 RMS response for four rods in 6x5 fully flexible rod bundle for V_{Axial} = 1.5 m/s, (b) corresponding 3D PSD plots in the stream-wise direction of rod 401, and (c) corresponding 3D PSD plots in the transverse direction of rod 401. 176
Figure 8.18 RMS response for four rods in 6x5 fully flexible rod bundle for V_{Axial} = 2 m/s, (b) corresponding 3D PSD plots in the stream-wise direction of rod 401, and (c) corresponding 3D PSD plots in the transverse direction of rod 401. 176
Figure 8.19 (a) Stability boundaries of jet cross-flow velocity with axial flow velocity for the two tested arrays, and (b) jet in transverse flow (JITF) flow regimes with respect to velocity ratio (VR= V_{Jet}/V_{Axial}). 177
Figure 8.20 Free decay test setup. 178
Figure 8.21 Free decay tests: (a) in still water, (c) at V_{Axial} = 1.5 m/s, and FRF fit of experimental data: (b) in still water, and (d) at V_{Axial} = 1.5 m/s. 179
Figure 8.22 (a) projected view from the nozzle, (b) top view of the array with the nozzle, (c) schematic drawing showing the JITF with the array, and (d) variation of the incidence angle with the velocity ratio (VR). . . . 180
Figure 8.23 (a) Measured phase difference (φ) between the rod motion and the lift force, and (b) extracted time delay (τ) versus V_{Jet}/fD, (Gad-el Hak et al., 2022b). 184
Figure 8.24 Extracted flow retardation parameter (μ) versus V_{Jet}/fD, (Gad-el Hak et al., 2022a). 185
Figure 8.25 Variation of the eigenvalues (Re (λ) and Im (λ)) with jet velocity for the three axial velocities cases: (a) and (d) for V_{Axial} = 1.0 m/s, and (b) and (e) for V_{Axial} = 1.5 m/s, (C) and (f) for V_{Axial} = 2.0 m/s. . . 187
Figure 8.26 JITF induced FEI model validation for the three axial flow cases: (a) effect of the flow retardation parameter (μ) on the stability limits, and (b) effect of the cross-coupling force terms on the stability limits. . . 187
Figure 9.1 Flowchart of the research conducted. 190

LIST OF SYMBOLS AND ACRONYMS

3D	Three dimensions
A_{Gap}	Gap flow area
A_{Jet}	Cross-sectional area of the nozzle
C_D	Drag force coefficient
C_f	Added-fluid damping matrix
C_L	Lift force coefficient
C_s	Structure damping matrix
CVP	Counter-rotating vortex pair
D_{Jet}	Jet diameter
D_{Jet}/D	Jet-to-rod diameter ratio
D	Rod diameter
E	Young's modulus of elasticity
f	Rod frequency
FEI	Fluidelastic instability
FIV	Flow-Induced Vibration
g	Inter-rod gap = P-D
GTRF	Grid-to-rod fretting
H	Stand-off distance
I	Rectangular moment of inertia
IAEA	International Atomic Energy Agency
JICF	Jet in cross-flow
JITF	Jet in transverse flow
K	Stability constant
K_f	Added-fluid stiffness matrix
K_s	Structure stiffness matrix
L	Rod length
L_{Jet}	Location of applied jet flow
LOCA	Loss-of-coolant accident
m	Rod mass per unit length including added mass
m_f	Added-fluid mass
m_s	Structural rod mass
M_f	Added-fluid mass matrix
M_s	Structure mass matrix

MR	Momentum ratio
NRC	Nuclear Regulatory Commission
P	Pitch
P/D	Pitch-to-diameter ratio
PLA	Polylactic acid
PCA	Principal component analysis
PWR	Pressurized water reactor
RMS	Root mean square
Re_{Jet}	Jet Reynolds number
SVD	Singular value decomposition
Str_{Jet}	Strouhal number based on the jet diameter and the average jet velocity
TIV	Turbulence induced vibration
V_{Jet}	Average flow velocity discharge from the nozzle
VIV	Vortex induced vibration
VR	Velocity ratio
ZEF	Zone of established flow
ZFE	Zone of flow establishment
α	Angle of attack
β	Jet spread rate
δ	Logarithmic decrement
ζ	Damping ratio
θ	Incidence angle of jet flow/rotation angle
λ	Eigenvalue
μ	Flow retardation parameter/dynamic viscosity
ξ	Jet eccentricity
ρ	Fluid density
τ	Time delay
υ	Kinematic viscosity
ϕ	Phase
ψ	Phase difference
ω	Angular frequency

CHAPTER 1 INTRODUCTION

1.1 Background

Nuclear energy can significantly contribute to providing the world with a high-powered and clean energy system, which not only supplies a zero-carbon and abundant electricity, but also mitigates climate change and strengthens energy security. The growing understanding of the effects of greenhouse gas emissions on global worldwide temperature has focused efforts towards investigating the long term environmental and safety feasibility of nuclear power plants. Nuclear fuel rods are key components of nuclear reactors. Due to the high energy density of the fuel contained therein, maintaining the structural integrity of the fuel rods is imperative. Fuel failures could have harmful effects on plant operation, and influence on the public acceptance of nuclear power. It is thus important to fully understand the behavior of nuclear fuel during both normal and accident conditions such as a loss of coolant accident (LOCA).

Fuel cladding is a key barrier for containing fission radioactive products. It is essential for this barrier to be robust and remain unbroken during its lifetime. Fuel failures characterize the deterioration of this barrier, which can be detected by monitoring the activity of fission product such as iodine isotopes:^{131}I/^{133}I in the primary coolant (IAEA, 2015). The failures can contribute to increase plant radiation levels during reactor operation and radioactive waste to the environment after removal of these damaged fuel rods. Nuclear fuel should be adequately robust not only to ensure safe operation under normal condition, but also to resist any transient or accident events.

Flow-induced vibration (FIV) is a potential cause of fuel rod failures in nuclear reactor cores. Pressurized water reactor (PWR) fuel rods are arranged in a square lattice array, named a fuel assembly. The latter is characterized by the number of rods in each array, which is typically 17 x17 fuel assembly in the Westinghouse company design (U.S. NRC, 2016). In order to prevent fuel rod burnout and fuel melting, coolant flow must be guided along fuel rods with sufficient flow velocity to prevent bulk boiling at any point in the core. Since the fuel assemblies have a square geometry and the core barrel is circular (see Figure 1.1), a large amount of the coolant would bypass the fuel assemblies and pass through the gap around the periphery of the core. Baffle plates are therefore introduced to guide the coolant flow through the core and establish the new boundary around fuel assemblies as shown in Figure 1.1. These baffle plates are fixed and aligned with the core barrel by using horizontal plates, called formers which also act as stiffeners, as shown in Figure 1.2a.

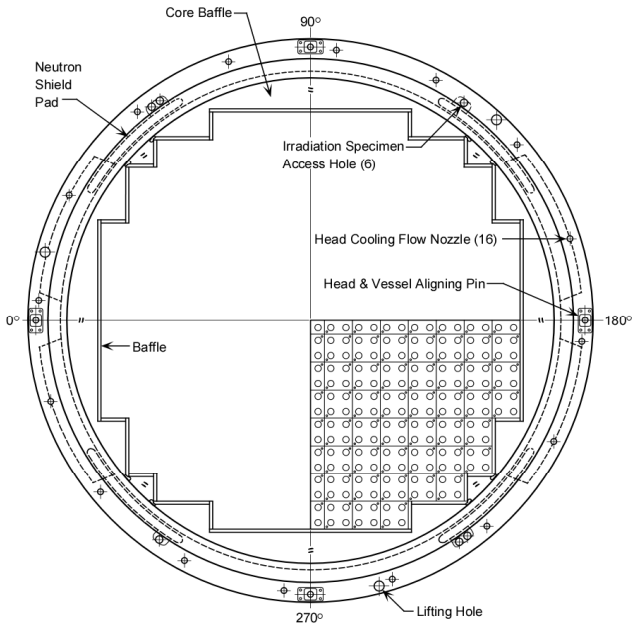

Figure 1.1 Cross section of pressure reactor vessel (U.S. NRC, 1980).

In practical terms, around 1.84% of total core flow is bypassed in the core barrel-baffle region through small holes in the formers to provide internal cooling for the baffles (U.S. NRC, 1980). Thus, a significant pressure difference is generated between the ascending coolant flow and the descending flow in the barrel-baffle region along the baffle plates as shown in Figure 1.2a. This pressure difference can lead to high jet cross flow emitting through any defective joints between the baffle plates. This phenomenon, called the *baffle jetting*, is shown in Figure 1.2b. This jet can rush the fuel rods either tangentially, developing corner baffle jets, or perpendicularly, developing central baffle jets.

NRC Circular No. 80-17 reported that during the period 1971-1975, corner baffle jetting caused damage to six fuel rods in assemblies adjacent to the baffle in different nuclear plants around the world. Moreover, ten fuel rods were damaged at the Swedish Plant, Ringhals Unit 2 in 1979 due to central baffle jetting; indicating that central baffle jetting has a greater impact on fuel failure than corner baffle jetting. Recently, several failure cases were observed due to baffle jetting. The Slovenian Nuclear Energy Administration reported, in 2013, that baffle jetting caused damage to fuel rods in three fuel assemblies in the Krško nuclear power plant. Furthermore, two fuel rods were suffered excessive damage during the North Anna power plant refuelling in 2014 (Licensee Event Report No. 50- 339/2014-002-00). The damaged fuel rods were found with top springs dislodged and fuel pellets were able to leak from the fuel rod. Fuel pellet loss occurred because of baffle jetting induced rod vibrations, moreover, seven fuel pellets were not found in the reactor core. It was suspected that were ground into

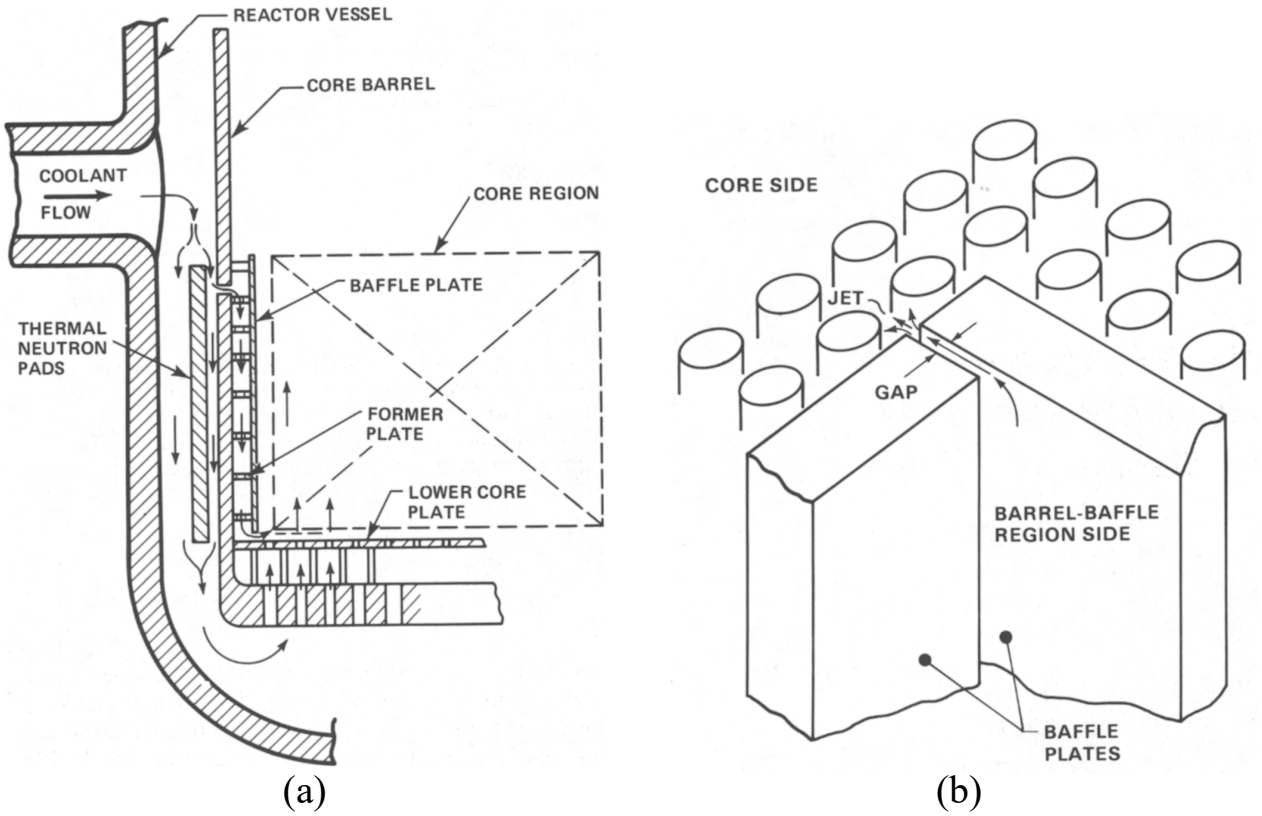

Figure 1.2 (a) down flow configuration flow path in a barrel-baffle region Hertrick et al. (1984), and (b) baffle jetting phenomena Hertrick et al. (1984).

fine particles.

Several corrective actions have been taken since initial observation of the baffle jetting problem. One of these suggested actions was reducing the gap size of defective joints by performing mechanical peening on the baffle joints, which would reduce the emanating flow. However, subsequent incidents of baffle jetting-induced fuel rod failures were late observed, thus the peening operation was not always effective to diminish the gap. The ultimate solution to prevent baffle jetting in a reactor is eliminating the differential pressure by converting the bypass flow direction from a down ward to an up ward configuration. This modification can be achieved by plugging existing core barrel holes (see Figure 1.2a) and adding appropriate new holes in the top former baffle plate to allow bypassed flow to come from inside the reactor and continue flowing upwards parallel to the primarily coolant flow along the baffle plates. This modification has successfully contributed to reduce the number of fuel assemblies affected by this failure mechanism as reported by Kitlan Jr et al. (1991).

In the hypothetical case of a loss of coolant (LOCA) event in a reactor, the hydrodynamic

pressure would increase significantly across the baffle plates. In order to mitigate the occurrence of this pressure rise, the baffle plates in the reactor core are designed with flow holes (LOCA Holes) as shown in Figure 1.3, which would safely release the pressure build up across the baffle plate during a LOCA event. The flow rate through LOCA holes is supposed to be minimal during normal operation due to the effect of up conversion on reduction of the differential pressure. However the fretting failure of fuel assemblies near baffle plate LOCA holes has been observed in some plants, IAEA (2015). Thus, the circular-jet-induced vibrations of fuel rods during normal operation could lead to grid-to-rod fretting (GTRF).

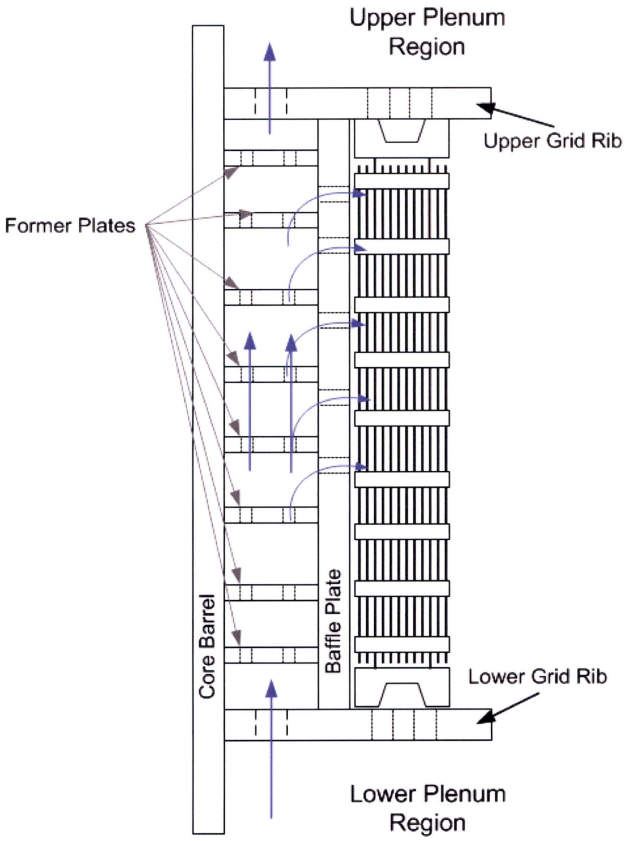

Figure 1.3 Schematic drawing showing flow path through LOCA holes (blue arrows) (AREVA, 2017).

PWR fuel assemblies consist of fuel rods subjected to combined axial and jet-cross flows. Concerning the excitation mechanisms of fuel rod vibrations, cross flow induced higher vibrations than that induced by purely axial flows owing to randomly fluctuations of pressure exerting on the surface of the fuel rods (Paidoussis, 1981). For cross flow, fluidelastic instability (FEI) is the most destructive excitation mechanism and can cause catastrophic rod failure. This instability is typical of self-excited vibration in that it results from the coupling

between the rod motion and fluid dynamic forces. Additionally, resonance vibrations can occur by coincidence of the natural frequency of fuel rod with the frequency of flow periodicity. These excitation mechanisms can contribute to grid-to-rod fretting (GTRF) which could potentially lead to release of fission products in the primary coolant flow. Consequently, FIV analysis of the fuel assemblies plays a key role in setting safety margins.

Uniform cross-flow induced vibrations in tube bundles have been extensively investigated in the literature (Chen, 1984, Paidoussis et al., 2010). Throughout these studies, the fundamental mechanisms underlying a tube bundle excitation are well understood, especially, fluidelastic instability phenomena. However, for the phenomenon of baffle jet induced vibrations, there is considerable difficulties to full understand the problem of flow-induced vibrations due to the non-uniformity of jet flow. The jet velocity is non-uniform in the jet cross section; therefore, the jet velocity that impinges on the fuel rods is related to jet flow parameters, including jet location relative to the rod bundle, jet-to-rod diameter ratio and the offset between the centerlines of jet and rod. Evidently, the stability behavior of the rod bundle is strongly depended on the jet parameters.

A few studies have been conducted to investigate the effect of jet parameters on the rod bundle vibration subjected to planar jet (Fujita et al., 1990, Lee and Chang, 1990, Seki et al., 1986). However, the research on round jet induced vibration is still limited in the literature on flow-induced vibrations. Compared to the baffle jet, the flow complexity of a round jet, due to its axisymmetric shear layer, highlights the difficulty of the resulting flow-induced vibration problem. The major aspects of the problem are described in the following section.

1.2 Problem Definition

Examples of fail-safe features of some designs of pressurized water reactor are the LOCA holes in the baffle plates surrounding the fuel assemblies, which are meant to release pressure build up in the hypothetical case of a loss of coolant accident (LOCA) event in a reactor. During normal operation, on the other hand, a localized jet cross-flow is emitted from the LOCA holes due to the pressure differences across the baffles. This jet flow could induce vibrations for fuel assemblies located near to these holes, which might lead to fuel failures. The stability behaviour of fuel rods subjected to combined axial flow and jet cross-flow is still not be fully covered in the literature and has many unknown aspects due to the complexity of the resulting combined flow.

Jet flow parameters are defined to identify the location of rod array relative to the jet flow

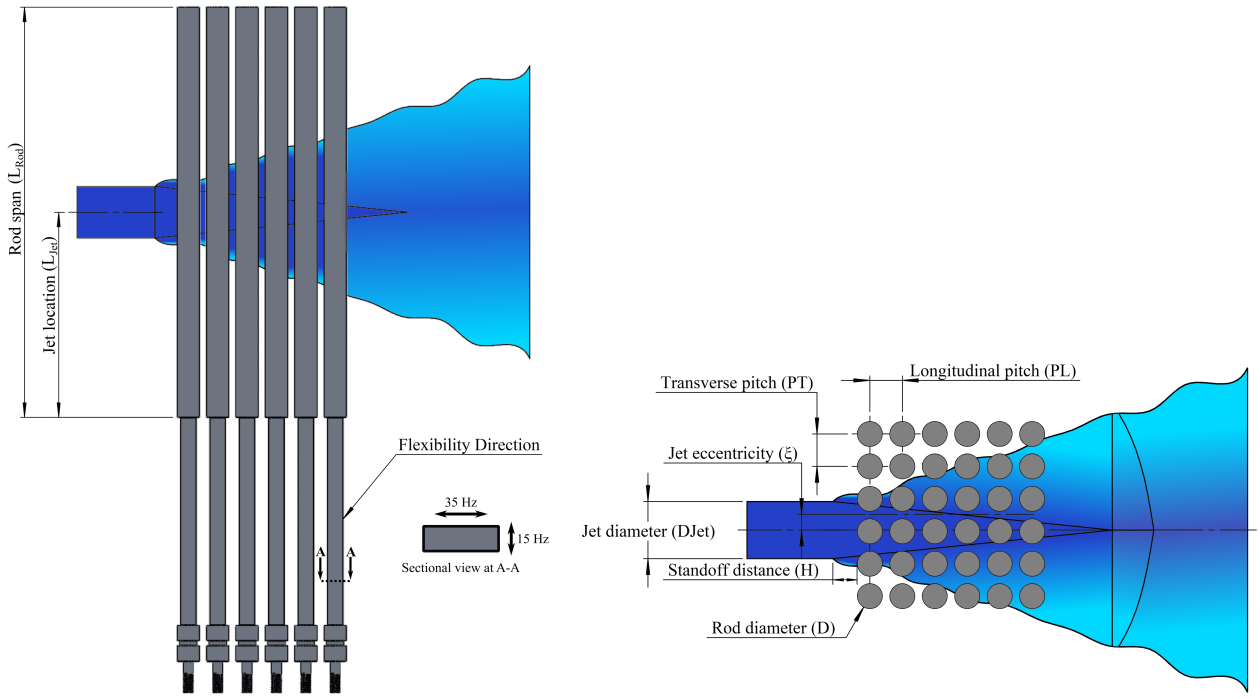

Figure 1.4 Jet flow parameters.

centerline since the flow velocity is not uniform across the rod bundle. Figure 1.4 presents a schematic of the side and top views of a rod array, showing the geometrical and jet flow parameters in the bundle subjected to pure jet cross-flow. In the present work, these key problem parameters are defined as follows:

1. Jet eccentricity (ξ): jet centerline offset from array centerline.
2. Standoff distance (H): gap between the first row and the jet exit.
3. Jet location parameter (L_{Jet}/L): jet centerline elevation relative to rod span.
4. Jet-to-rod diameter ratio (D_{Jet}/D).
5. Flexibility direction: Stream-wise (1 dof), transverse (1 dof) or combined stream-wise/transverse (2 dof) motion relative to jet-flow.

Two parameters, velocity ratio (VR) = V_{Jet}/V_{Axial} and incidence angle (θ), are added for the jet in transverse flow (JITF) case as shown in Figure 1.5.

In attempting to overcome the pressure build up in the baffle-barrel region while still maintaining operating conditions far away from that critical conditions for fluidelastic instability,

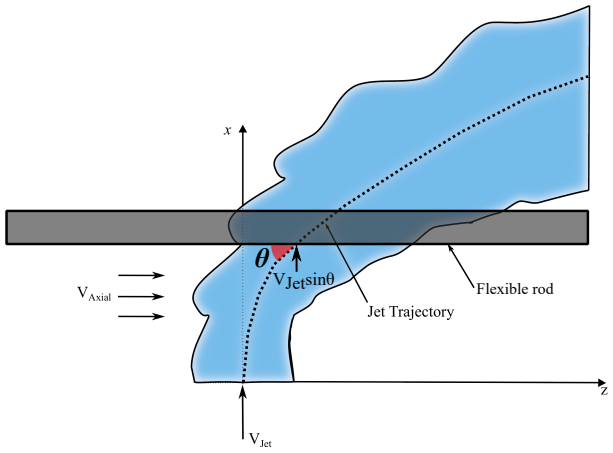

Figure 1.5 JITF with array configuration.

the stability maps for rod bundle subjected to round jet cross-flow in addition to external axial flow would be a very valuable piece of additional data to the flow-induced vibration problems. Using these maps, precise and correct guidelines would be available for the design of the baffle plates having LOCA holes.

The primary objective of the present research project is to investigate and quantify the problem of fluidelastic instability of rod bundles subjected to a jet cross-flow combined with a parallel axial flow. To fully comprehend the whole system, this could be explored in two steps: first, investigate the influence of pure jet cross-flow on rod bundle vibration, and then consider the effect of combined flow.

1.3 Research Questions

The research problem presented in the previous section is concisely presented in specific research questions. The questions can be divided into mainly six issues, which some of them have a few sub-issues. These issues are organized as follows:

Q1: What are the fundamental mechanisms underlying the excitation of fuel rods subjected to a pure circular jet cross-flow?

Q2: How do the main jet flow parameters (H,ξ,D_{Jet},L_{Jet}) affect the stability of a rod bundle and what is the effect of rod flexibility direction (stream-wise, transverse, axisymmetric) on the rod array response?

Q3: Does there exist a generalized eigenvector model that can predict the rod bundle vibration in jet flows (different D_{Jet})?

Q4: In the case where instability occurs, (i) how can the jet cross-flow effect be theoretically modelled to predict the instability threshold? (ii) How can the model developed for pure jet cross-flow be adapted to predict fluidelastic instability of a fuel rod bundle subjected to combined axial flow and jet cross-flow?

Q5: What is the effect of combined axial flow and jet cross-flow on the stability behavior of rod bundle?

Q6: If a large vibration amplitude is happened, is there a way to mitigate rod array vibration?

1.4 Research Objectives

The general goal of this research is to understand the effect of a combined axial flow and localized cross-flow on the dynamics of a PWR fuel assembly mock-up and to develop a proper modelling strategy to simulate the dynamics. This goal will be achieved through a series of experiments in three independent test loops and a combination of analytical modelling. The research objectives are the following:

O1: Characterize experimentally the dynamical behavior of a rod bundle subjected to pure jet cross flow.

- **O1-1**: Design and fabricate a test section having dimensions as close as possible to represent the real fuel assembly.
- **O1-2**: Design and build test loop to investigate the dynamical behavior of rod bundles in jet cross-flow.
- **O1-3**: Determine the flexibility direction of the rod array that could be most susceptible to instability by testing separately the effect of jet cross-flow on stream-wise and transverse direction vibrations.
- **O1-4**: Generate stability maps of the rod bundle as a function of jet flow parameters.

O2: Determine experimentally the fluidelastic stability derivatives and time delay parameters.

- **O2-1**: Design and fabricate a test section to measure the lift and drag force coefficients on a rod within the rod bundle.
- **O2-2**: Design a mechanism to move statically the rod in order to measure lift and drag forces as functions of rod position.

O2-3: Perform dynamic tests to determine the phase delay associated with the rod velocity.

O3: Develop a semi-empirical quasi-steady model for FEI induced by jet cross-flow.

O3-1: Develop model to capture the dynamic features of the vibrating rod in jet flow.

O3-2: Validate the stability threshold predicted by the model against that obtained from the experiments.

O4: Develop a generalized eigenvector model to predict mode shape of array under jet cross-flows.

O4-1: Design an axisymmetric rod bundle to simulate the actual case of nuclear fuel rods in cores.

O4-2: Test the array under different nozzle diameters and collect the experimental vibration data.

O4-3: Build a model for all data sets using a principal component analysis (PCA), and compare the generalized eigenvector model results with each mode shape obtained from the tested nozzle.

O5: Propose and test a method to mitigate jet cross-flow induced vibrations using a passive flow control of jets.

O5-1: Design a new nozzle using a biomimicry approach.

O5-2: Test and evaluate the performance of the biomimetic nozzle versus the circular nozzle on the stability behavior of rod array.

O6: Characterize experimentally and model analytically the dynamics of a single-span flexible rod bundle subjected to combined axial flow and jet cross-flow.

O6-1: Design and fabricate a test section to study the dynamics of rod bundle under combined axial flow and jet cross-flow.

O6-2: Design and build a test loop having two branches, one for each type of flow.

O6-3: Test the mock-up array under different axial and jet cross-flow conditions to investigate the fluidelastic behavior of the array under the jet in transverse flow (JITF).

O6-4: Adopt the developed model for jet cross-flow induced FEI to take into account the effect of axial flow, and validate the developed theoretical model for jet in transverse flow (JITF) induced FEI.

The following paragraph explains the full structure of the dissertation.

1.5 Thesis Outline

The contents of the dissertation are divided into ten chapters. Chapter 1 gave a general overview of the problem and the objectives of the research. Chapter 2 presents a literature review, focusing on the main features of turbulent jet flow in addition to flow-induced vibration (FIV) mechanisms associated with axial flow and jet cross-flow. Finally, the theoretical models used in predicting instability threshold are retrieved from a literature study. This chapter is divided into three parts:

2.1. Free turbulent jets and jet in transverse flow (JITF). This section gives a theoretical background of the turbulent jet flow.

2.2. Flow-induced vibrations of rod bundles in axial and cross flows. This section describes mechanism underlying rod bundle vibrations in axial and cross flow.

2.3. Theoretical models for FEI of tube arrays subjected to uniform cross-flow.

Chapters 3 and 4 present the experimental work conducted to investigate and quantify the problem of fluidelastic instability of rod bundles subjected to a jet cross flow in stream-wise and transverse directions respectively. Two jet flow parameters, stand-off distance (H) and jet eccentricity (ξ), are investigated on each vibration direction. Stability maps are generated for the unstable cases as function of jet flow parameters (H and ξ). The work in this chapter marks the achievement of **Objective 1**.

Fluidelastic instability occurs mainly in the transverse direction. Thus, modelling the rod bundle instability in this direction is the next step to understand the mechanism underlying rod bundle fluidelastic excitation. Chapter 5 presents experimental and theoretical work to model the instability of flexible fuel bundle in pure jet cross-flow. A theoretical model is developed based on a quasi-steady approach. A new formulation of the fluidelastic forces as functions of the projected rod area derivative is our finding to account for variation of the projected area relative to the LOCA hole. The model results are then validated versus the experimental critical velocities. The work in this chapter achieves both **Objective 2** and **Objective 3**.

After understanding the fluidelastic behavior of the rod bundle instability both experimentally and analytically, a new set of axisymmetric flexible rods is fabricated to increase system complexity and simulate the real case of fuel rods in reactor cores. Chapter 6 presents experimental and theoretical work to answer the research question (**Q3**) on the existence of generalized eigenvector models to predict rod bundle mode shapes under jet cross-flows. A series of FEI experiments are conducted with three different nozzles and the rod array response is tracked using a high speed camera. An image processing algorithm is developed to extract the stream-wise and transverse vibrations, and the rod motion trajectory through thousands of captured frames. Singular value decomposition (SVD) and principal component analysis (PCA) are applied on the rod bundle vibration in the unstable region to reduce the dimensionality effect of the vibration data and gain insight into the directionality of rod vibration through rotation angles. The work in this chapter achieves **Objective 4**.

Fluidelastic instability by jet cross-flow resulted in large vibration amplitudes reaching 60% of the inter-rod gap (g). As a countermeasure passive control of jet flows could be used to enhance the mixing rate of the jet flow with the surrounding flow which would, in turn, reduce the jet flow-induced vibrations. A biomimetic nozzle inspired by the shark gill slits structure is proposed and designed to convert jet linear momentum into angular momentum (i.e vortices) is presented in Chapter 7. The performance of the shark-inspired nozzle is then evaluated versus the plain circular nozzle. The biomimetic nozzle results show a significant effect by delaying the critical jet velocity and reducing the vibration amplitude. The work in this chapter achieves **Objective 5**.

The last step in this research is to characterize experimentally and model analytically the dynamics of a PWR assembly mock-up subjected to a combined axial flow and jet cross-flow. Chapter 8 presents the test loop used to investigate the stability behavior of the single-span mock-up array under jet cross-flow while also subjected to a primary axial flow. The effect of two flows, pure axial flow and jet in transverse flow (JITF), on the dynamical behavior of the mock-up bundle is investigated. Moreover, a model of JITF induced fluidelastic instability is developed by implementing the effect of axial flow on jet cross-flow. A stability analysis is carried out and the theoretical results are compared with the experimental stability boundaries for the model validation. The work in this chapter achieves **Objective 6**.

Finally, Chapter 9 presents a general discussion of the results, while Chapter 10 provides the conclusions of the study and recommendations for future work.

CHAPTER 2 LITERATURE REVIEW

The primary goal of this research is to investigate the flow-induced vibrations in pressurized water reactor (PWR) fuel assembly simulating its behavior during normal operation under LOCA hole jetting. PWR fuel consists of long small diameter (approximately 0.43 in.) rods arranged in a normal square array pattern supported at multiple axial locations with so-called spacer grids. The fuel rods are subjected to external axial flow and also, at certain location along the span, a jet cross-flow normally directed to fuel rods at LOCA holes locations in the baffle.

The review of literature related to the research problem is organized in the following manner. The first part of the review gives a summary of the flow characteristics of the round jet flow and jet in transverse flow (JITF), including their structures and features. The second part is a review of the excitation mechanisms of the rod bundle in axial flow and baffle jetting (i.e. planar jet). Theoretical models that are used in predicting instability for rod bundle in uniform cross flow are reviewed in the last part.

The remainder of this chapter is structured as follows: Section 2.1 introduces jet flow behavior starting with a description of the different flow zones resulting from round jet in subsection 2.1.1 and introducing the combined flow behavior of round jet flow in axial flow in subsection 2.1.2. Section 2.2 introduces the mechanisms of FIV, with subsection 2.2.1 summarizing the mechanisms of axial FIV, while subsection 2.2.2 discusses the mechanisms of baffle jetting cross-flow. Section 2.3 reviews the theoretical models used to predict the critical flow velocity for tube array subjected to uniform cross flow.

2.1 Turbulent Jets

A free jet is defined as a pressure-driven unrestricted flow of a fluid into a quiescent environment whose boundary is sufficiently distant from the jet. The jet boundary that is created as interface with the surrounding fluid cannot sustain a pressure difference across it, thus a free shear layer is developed along the jet boundary. This shear layer generates turbulence and mixing with the surrounding fluid, resulting in entrainment of the surrounding fluid into the jet stream. As a result, the jet mass flow increases gradually along the downstream direction, increasing the jet cross section and spreading the jet. The jet centerline velocity decreases in turn with downstream distance in order to conserve momentum. A free jet, in other words, is the flow produced by a continuous source of momentum.

2.1.1 Round Turbulent Jet

A round jet is created when an axisymmetric source of momentum emits into a stagnant environment. The flow presents two regions: the zone of flow establishment (ZFE) and the zone of established flow (ZEF) as shown in Figure 2.1. In the ZFE, a potential core region develops where there is no decay in longitudinal or radial velocity components inside the potential core. The centerline velocity in this region is the same as the entrance jet velocity. Shear flow begins at the potential core boundary and extends to the jet boundary. In the ZEF, the centerline velocity begins to decay in proportion to the axial distance (x) and shear layers combine from both sides in this interaction region.

The major differences between plane and round jets are: (i) the potential core length, and (ii) the radial spreading. In the round jet flow, the flow has higher potential than that of the plane jet (Lee et al., 2003). Furthermore, the shear flow layer is formed in three dimensions in round jet flow, whereas it is formed in two dimensions when flow is injected from a slot (i.e. planar jet).

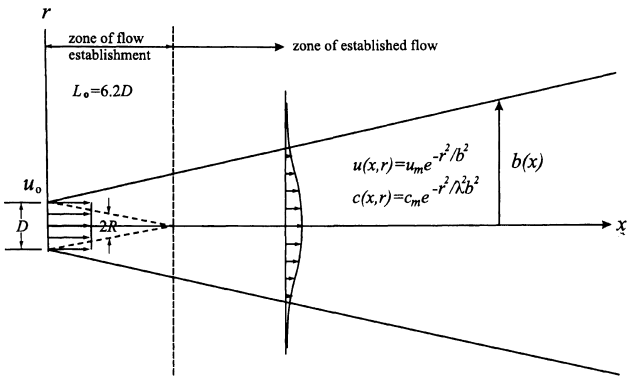

Figure 2.1 A sketch of flow regimes emanating from round jet (Lee et al., 2003).

Several studies including (Abramovich et al., 1984, Albertson et al., 1950, Kuethe, 1935, Rajaratnam, 1976) carried out research and highlighted the flow structure of round jets. The mean velocity profile is found to attain self-similarity beyond the potential core:

1. In the zone of flow establishment (ZFE), $x \leq 6.2\mathrm{D}_{Jet}$;

$$\begin{aligned} u(x,r) &= u_0 exp[-\frac{(r-R)^2}{b}]; r > R \\ u(x,r) &= u_0, r \leq R \end{aligned} \tag{2.1}$$

where $R(x)$ is the half-width of the potential core, $b(x)$ is the width of the mixing layer,

$u(x,r)$ is the jet velocity, u_0 is the outlet jet velocity and r is the radial distance from the center line (see Figure 2.1).

2. In the zone of established flow (ZEF), $x > 6.2D_{Jet}$, the jet velocity profiles are self-similar:

$$u(x,r) = u_m exp[-\frac{r^2}{b^2}], u_m = 6.2u_0(\frac{x}{D_{Jet}})^{-1} \tag{2.2}$$

where (x,r) are stream-wise and radial coordinates, and $u_m(x)$ is the centerline maximum velocity.

3. The turbulent round jet spreads linearly according to the relation:

$$b = \beta x \tag{2.3}$$

The jet spread rate for a round jet has been determined experimentally in several studies as listed in Table 2.1.

Table 2.1 Comparison of experimental values of round jet spread rate, β.

Reference	Jet spread rate, β
Albertson et al. (1950)	0.114
Wygnanski and Fiedler (1969)	0.114
Papanicolaou and List (1988)	0.108

The geometrical characteristics of the nozzle play a key role in shaping the exit velocity profiles. For instance, when the nozzle has a large contraction ratio, the developed velocity distribution is more constant over the cross-section and is commonly called a top-hat profile.

2.1.2 Jet in Transverse Flow (JITF)

Combined axial flow and localized jet cross-flow, also known as jet in cross-flow (JICF) in this work referred as jet in transverse flow (JITF), describes a jet of fluid that emits from a nozzle and interact with the cross-flow. The main flow features of JITF have been addressed in numerous experiments and simulations as reviewed by Margason (1993). Mixing is induced and accompanied by a complex three-dimensional flow topology and entrainment phenomena as depicted by the coherent structures in the schematic in Figure 2.2. The resulting interaction that occurs between the two flows creates a complex set of flow structures and vortex systems. Based upon the experimental observations by Fric and Roshko (1994),

four principal types of vortical structures created due to interaction between the jet and axial flow. These structures can be classified as: shear layer vortices, counter-rotating vortex pair (CVP), horseshoe vortex system and wake vortices as shown in Figure 2.2.

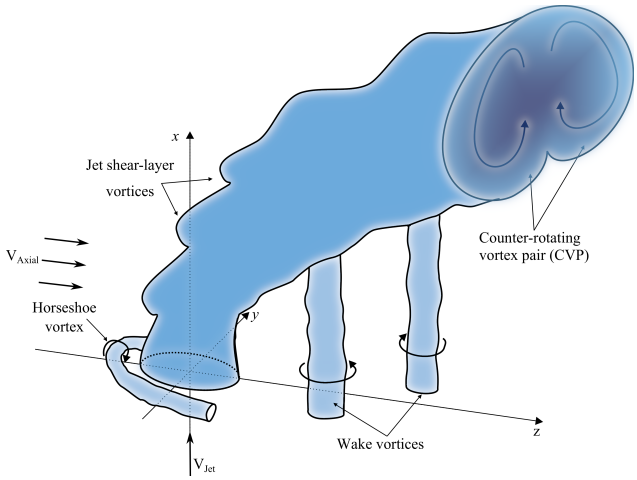

Figure 2.2 A schematic drawing of jet in transverse flow (JITF).

When the jet cross-flow encounters the axial flow, two counter-rotating vortices are formed that appear to originate from inside the nozzle, and continue far downstream of the jet nozzle exit following the deflected jet path. Along the wall upstream of the jet nozzle exit, a horseshoe vortex system is generated. Downstream of the jet exit, periodic upright wake vortices generate between wall vortices and the counter rotating vortex pair. In the following sections, the flow parameters that utilized to describe the behavior of JITF are summarized and the coherent structures for each vortex system also described.

Flow Similarity Parameters

Similarity parameters allow for the reduction of variables and simplicity comparison of various investigations. The flow behavior of the jet in transverse flow depends on fluid parameters between jet and transverse flow and geometrical aspects. For this reason, similarity parameters are defined to categorize the structure of JITF. The major characteristics of the developing flow are dependent on the velocity ratio (VR) between the mean velocities of jet flow V_{Jet} and the transverse flow V_{Axial}:

$$VR = \frac{V_{Jet}}{V_{Axial}} \tag{2.4}$$

This velocity ratio is useful to define the flow structure for configurations where jet and axial flow fluid have the same densities and the jet exit flow velocity profile is close to a

top-hat profile. If, however, the jet velocity profile is parabolic, this similarity parameter is insufficient to classify the resulting flow regimes. For that purpose, the velocity ratio has been extended to take into account the velocity profile leading to the introduction of a corresponding parameter, the momentum ratio (MR):

$$MR = \int \frac{\rho_{Jet} V_{Jet}^2 dA}{\rho_{Axial} V_{Axial}^2 dA} \tag{2.5}$$

where A is the area of the jet exit, ρ_{Jet} and ρ_{Axial} are the fluid densities of the jet and the axial flow fluid, respectively.

New et al. (2006) visualized experimentally, using laser-induced fluorescence, the effect of top-hat and parabolic jet velocity profiles on the development of the shear layer vortices, for momentum ratios (MRs) ranging from 2.3 to 5.8. The results showed that the thicker shear layer accompanying a parabolic JITF could delay the development of leading-edge and lee-side vortices (i.e. shear layer vortices) when compared to the top-hat JITF at the corresponding MR as shown in Figure 2.3. Consequently, there was an increase in jet penetration and a reduction in the near-field entrainment of axial flow fluid by a parabolic JITF. Furthermore, because the leading-edge and lee-side vortices in a parabolic JITF are less coherent, they are more likely to break up randomly into smaller-scaled vortices.

Cambonie and Aider (2014) experimentally studied the effect of low values of velocity ratio (VR) on the JITF topology. They found that the JITF topology has three different flow regimes:(i) swept topology, (ii) deformed classical JITF topology and (iii) classical JITF topology. The transition values for each region are presented in Figure 2.4. The ratio VR = 1.25 is a transition value between partially detached JITF and fully detached JITF.

The Reynolds number is another governing parameter that influences the development of turbulent structures in the interaction region. Two Reynolds numbers, the jet Reynolds number and the axial flow Reynolds number were defined to characterize their effect on the range of turbulent structures in the interaction region. The jet Reynolds number is based on the jet velocity and jet diameter and is defined as:

$$Re_{Jet} = \frac{\rho_{Jet} V_{Jet} D_{Jet}}{\mu} \tag{2.6}$$

It was found suitable to define the axial flow Reynolds number based on the jet diameter. It is expressed as:

$$Re_{Axial} = \frac{\rho_{Axial} V_{Axial} D_{Jet}}{\mu} \tag{2.7}$$

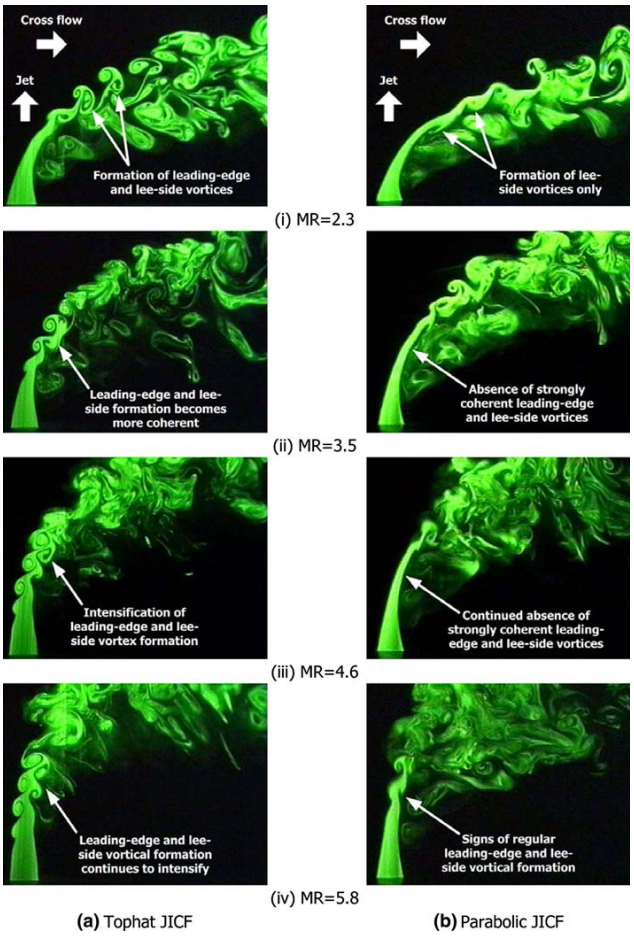

Figure 2.3 Streamlines of shear layer vorticities along the symmetry plane of (a) top-hat and (b) parabolic jets.

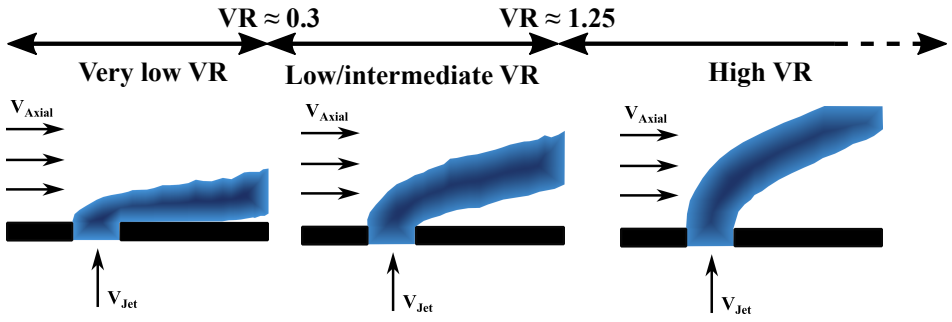

Figure 2.4 Jet in transverse flow (JITF) flow regimes with respect to velocity ratio.

Callaghan (1948) experimentally studied the effect of the jet Reynolds number, density ratio and velocity ratio on the penetration of a circular air jet with different jet diameters. It was observed that the jet Reynolds number had a negligible influence on the jet trajectory. However, it was found that the jet penetration was strongly correlated with both velocity

and density ratios.

Jet Trajectory

The jet trajectory has been considered as one of the major characteristics of the jet in transverse flow. The trajectory defines the deflection path of the jet in the transverse flow direction as shown in Figure 2.5. The predicted jet trajectory is critically important information for the flow configuration in a reactor core under a LOCA event since it determines how far the jet can penetrate before being deflected by the axial flow. The jet trajectory has long been at the core of many experimental measurements and analytical studies (Broadwell and Breidenthal, 1984, Keffer and Baines, 1963, Smith and Mungal, 1998). The jet centerline trajectory has been defined by the locus of the maximum velocity measured on the plane of symmetry. It is clearly recognized that the penetration of jet into the transverse flow is mainly correlated with the velocity ratio. Many experimental data can be scaled by using power-law form (Broadwell and Breidenthal, 1984):

$$\frac{x}{VR.D_{Jet}} = A(\frac{z}{VR.D_{Jet}})^B \tag{2.8}$$

where A and B are constants determined from the experiments and $VR{=}V_{Jet}/V_{Axial}$ is the velocity ratio. Pratte and Baines (1967) found A = 2.05 and B = 0.28 for ratio VR from 5 to 35.

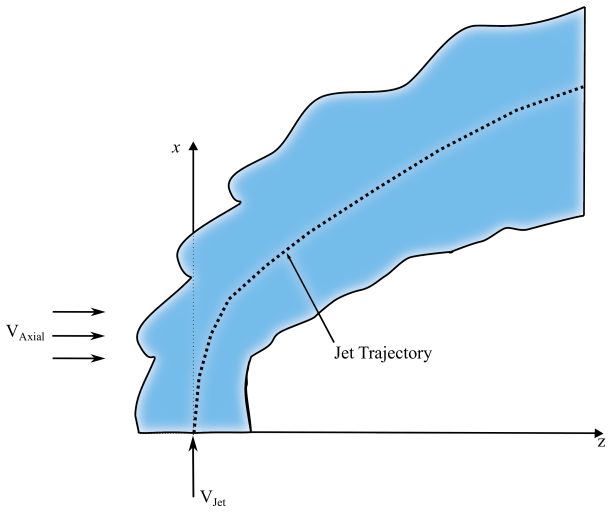

Figure 2.5 A sectional view of the JITF showing the jet trajectory.

Coelho and Hunt (1989) investigated the two proposed mechanism responsible for the deflec-

tion of the jet namely; pressure drag and entrainment mechanisms. The first one is assumed the flow around the jet and is the same as in the case of a bluff body; thus the drag force acts to deflect the jet, while the entrainment process occurring between the jet and surrounding fluid bends the jet in the latter mechanism. They concluded that the pressure drag mechanism effect is negligible compared to the effects of entrainment on the deflection of the jet. The majority of the entrainment into the jet takes place in the counter-rotating vortex pair where the formation of large vortices leads to enhance mixing (Yuan et al., 1999). All resulting vorticity structures of a JITF can contribute as excitation sources of the fuel assembly during a LOCA jetting.

2.2 Flow Induced Vibration (FIV) Mechanisms

A key aspect of this research is experimentally investigating the flow-induced vibrations in pressurized water reactor (PWR) cores; focusing attention on a flexible rod bundle subjected to external water flow in the axial direction in addition to localized jet cross flow owing to LOCA hole jetting. This is the flow configuration found in the nuclear reactor cores of interest. Consequently, a literature review of flow-induced rod vibration mechanisms in an axial flow is discussed in Section 2.2.1, while Section 2.2.2 gives a description of the mechanisms of baffle jetting cross-flow induced vibrations.

2.2.1 Axial FIV Mechanisms

Flow induced vibrations (FIVs) can be classified, depending on its nature as proposed by Weaver (1976), into three main groups, namely forced vibrations, self-controlled vibrations and self-excited vibrations. By coupling characteristics of a fluid flow to the dynamical behaviour of a structure, it is then possible to identify FIV. The response of the structural components has been modeled based on the three excitation mechanisms described below:

1. Turbulence induced vibration (TIV): the structure is excited by the random pressure fluctuation due to turbulent flow around the structure surface. These fluctuations can be caused locally by the fluid itself (near field turbulence) or produced due to far field turbulence, for instance, the turbulence induced by the spacer grids supporting the fuel rods. This phenomenon is the principal excitation mechanism in axial flow situations. TIV is considered as a forced vibration.

2. Vortex induced vibration (VIV): Karman vortex shedding is often generated downstream of structures subjected to cross flow. This induces periodic pressure fluctuations on the structure surface that may lead to vibrations. Resonance vibrations may

occur if the vortex shedding frequency is synchronized with the natural frequency of the structure. VIV is classified as a self-controlled mechanism.

3. Fluidelastic Instability (FEI): fluidelastic instability depends on the coupling between flow-induced dynamic forces and the motion of the structure. When the energy from the fluid dynamic forces is higher than the energy dissipated by damping, instability occurs. FEI is a self-excited vibration.

Depending on the flow velocity, the final dynamical behavior of the structure can be the superposition of several mechanisms as shown in Figure 2.6. Hence, it is not always easy to specify the cause of the vibrations.

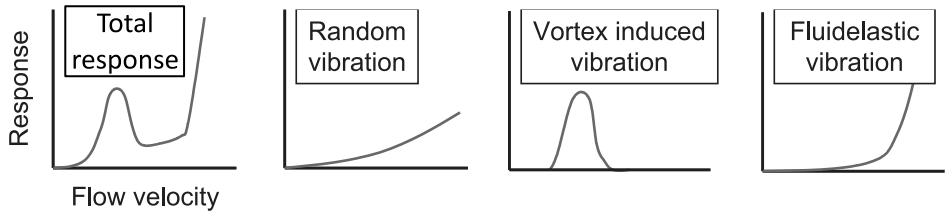

Figure 2.6 Sketch of theoretical tube response with increasing cross flow velocity, (Nakamura et al., 2013).

Figure 2.6 shows that for typical cross-flow induced vibrations, there are three major sources of vibration excitation. For external axial flow conditions, vortex shedding usually does not contribute to the tube response. Flow induced vibrations are mainly initiated owing to the occurrence of pressure fluctuations in the boundary layer. Of the possible types of excitations, fluidelastic instability has the greatest destructive potential as indicated by the high response in Figure 2.6.

The PWR fuel rods in a fuel assembly are commonly considered to be a group of identical cylinders arranged in a square lattice, through which a single liquid phase fluid passes. The dynamical behaviour of both solitary cylinders and clusters of cylinders subjected to external axial flow has been investigated extensively by Chen (1985) and Paidoussis and Curling (1985) among others. It was experimentally found that the cylinder response can be divided into two flow velocity regions delimited by the threshold limit of velocity called the critical flow velocity. If the mean axial flow velocity exceeds this critical flow velocity, the cylinder may undergo fluidelastic instabilities (FEIs) such as divergence, which is a non-oscillatory instability, followed at higher flow velocities by flutter. Whereas, below this critical flow velocity, the sub-critical vibration is caused by random pressure fluctuations due to flow turbulence. For external axial flow conditions, the critical flow velocities for fluidelastic

instabilities are generally much higher than for cross flow conditions, (Nakamura et al., 2013). These two excitation mechanisms will be covered in more details in the following two subsections.

Turbulence Induced Vibration (TIV)

Sub-critical vibration amplitudes associated with axial flow turbulence, are typically very small as less than 10^{-2} to 10^{-1} of a cylinder radius, (Paidoussis and Curling, 1985). Vibrations of such small amplitude would generally be ignored. However they must be carefully estimated due to the extremely close spacing of fuel rods in fuel assemblies (e.g., fuel rod diameter = 0.43 in. and spacing between cylinders is 0.138 in.). For such spacings, even very small amplitude vibrations may cause impact either between the fuel rods or between the fuel rod and imperfect supports. This could lead to wear and fretting damage of the fuel elements.

Paidoussis (1966a,b) studied the dynamics of a solitary flexible slender cylinder immersed in axially flowing fluid both theoretically and experimentally. The dynamical analysis showed that small flow velocities having damping effect on the free motions of the cylinder, while for sufficiently high flow velocities, fluidelastic instabilities may occur; both buckling (divergence) and oscillatory instabilities (flutter). However, at low flow velocities (sub-critical flow regime), cylinders in axial flow are under forced excitation by the random pressure fluctuations in the turbulent axial flow acting on the cylinder surfaces. Several studies were conducted to formulate the equations to predict the amplitude of the random vibration of a rod due to turbulent axial flow. A brief summary of these equations will be given below.

The earliest expression was proposed by Burgreen et al. (1958) based on their experimental data. The amplitude of vibration was correlated as function of a number of system parameters, including the flow velocity, fluid density, hydraulic diameter, etc. The empirical equation was given as:

$$(\frac{y_{pp}}{D_h})^{1.3} = 0.83x10^{-10}k(\frac{\rho V^2 L^4}{EI})^{1/2}(\frac{\rho V^2}{\mu\omega}) \tag{2.9}$$

where, k is an end fixity factor ($k = 5$ for simply supported rods) and y_{pp} the maximum (peak-to-peak) amplitude.

Later, Paidoussis (1965) proposed an empirical equation based on the available experimental data reported by Burgreen et al. (1958), Quinn (1962), Rostrom (1964) who had measured the vibration response of a single rod and its response in rod bundles having different flow channel cross section area and varying boundary conditions of the rod. The proposed equation was

written as:

$$\frac{y_{0.5pp}}{D} = \alpha^{-4}\frac{(v^2 Re_h \varepsilon^2)^{4/5}}{1+2u^2}\frac{\beta^{2/3}}{1+4\beta}10^{-5} \tag{2.10}$$

where, $y_{0.5pp}$ is the maximum value of half the peak to peak amplitude, α is dimensionless eigenvalue of the rod, v is dimensionless flow velocity, equal to $(\mathrm{m}_a/EI)^{0.5}V_{Axial}L$ and Re_h is the Reynolds number based on hydraulic diameter.

$$\begin{aligned} &\beta = \frac{m_f}{m_f + m_s} \\ &\alpha = \pi \ \text{ for a simply-supported rod} \\ &\alpha = 4.73 \ \text{ for a fixed-fixed rod} \end{aligned} \tag{2.11}$$

The results showed that Paidoussis' equation had a good agreement with the experimental results except for the case of the cantilever rod. This was attributed to the wake forces generated at the free end of the rod which were not included in the proposed equations.

Pavlica and Marshall (1966) carried out experiments to compare between the semi-empirical equations developed by Burgreen et al. (1958) and Paidoussis (1965). The authors investigated experimentally the effect of the viscosity term on the rod vibrations by changing the water temperature. The experimental results showed that the Paidoussis correlation agreed well with experimental data for high viscosity (70°F) as shown in Figure 2.7. However, the correlation was found to predict values about 250% higher than Paidoussis values.

Fluidelastic Instabilities (FEIs)

Paidoussis (1973) analysed the stability of a flexible cylinder subjected to axial flow by studying the effect of increasing axial flow on the free motion of the cylinder which was carried out theoretically and also investigated experimentally. The effects of boundary conditions, pinned-pinned and cantilevered were investigated theoretically and experimentally. The theoretical results showed that the cylinder first loses stability by buckling in its first mode and then by flutter in its second and third modes. The critical dimensionless velocity for the onset of buckling instability (v_b) was 3.137 for pinned-pinned cylinder, while this velocity reduced to 2.04 in case of cantilevered cylinder. However, at higher dimensionless velocity, $v_c = 6.48$ flutter instability was indicated by the model. The experimental results confirmed the model's capability to predict critical velocities in the case of the cantilevered cylinder. However, experimental results for pinned-pinned cylinders had an acceptable agreement with theory. This was attributed to imperfections in the cylinders and the supports that introduced non-linear effects. The critical velocity for buckling instability is very high; for

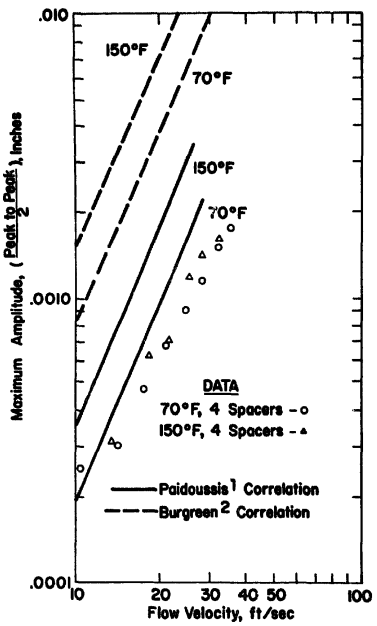

Figure 2.7 Comparison of rod vibrations from Paidoussis' equation (Paidoussis, 1965), Burgreen' equation (Burgreen et al., 1958) and the experimental data conducted by Pavlica and Marshall (1966).

instance, for a hollow steel cylinder of half inch diameter, 1/64 in. wall-thickness and 48 in. long, in water flow, the predicted buckling velocity $V_b = 55.7$ m/s.

It may be concluded that, for PWR reactor cores where the maximum flow velocity is approximated 6 m/s, the velocity is much lower than the range of critical velocities for fluidelastic instabilities. Consequently, the fuel assemblies cannot undergo instabilities during steady state conditions, in which the fuel rods are subjected to a purely axial flow. However, in the case of LOCA hole jetting, the combined jet cross-flow and axial flow may induce instability at lower velocity than that of pure axial flow case. It is this latter case that is of concern for the reactor.

2.2.2 Baffle Jetting FIV Mechanisms

In comparison with the research conducted on fluidelastic instability of tube arrays subjected to uniform transverse flow, only a few researchers have discussed the excitation mechanisms of flow induced vibrations due to baffle jet phenomena. The non-uniformity of the cross flow emanating from the narrow (baffle) gaps draws the attention to additional parameters for the jet flow including, the gap size and the location of jet flow with respect to rod span. However, the modeling of the resulting non-uniform flow needs consideration. Seki

et al. (1986) performed experiments to develop an analytical model to predict the instability threshold for fuel rod vibrations subjected to transversal baffle jetting. The experiments were conducted on a 4x5 rigid array with different test parameters including, gap size, fuel rod spacing, effect stand-off distance and distance between the centerlines of the jet and rod array as shown in Figure 2.8. The authors examined the effect of test parameters on the fuel rod vibrations by measuring the pressure distribution around large diameter cylinders; the large diameter (3 x reactor rod diameter) was chosen for practical convenience. The fluid flow velocity distribution, on the other hand, was measured from the baffle gap between two prototypical size fuel rods by using the laser Doppler velocimeter (LDV). Results were compared to those obtained from the theoretical formulas. The comparison showed that the decay of the measured centerline velocity had good agreement with that calculated by theoretical equations for a free planar jet.

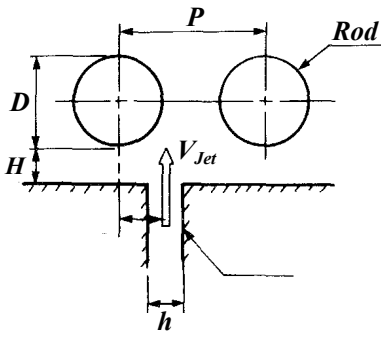

Figure 2.8 Baffle jetting parameters (Seki et al., 1986).

The force exerted on the test rods was obtained by integrated circumferentially the pressure distribution around the rods. This force was normalized in the form of a force coefficient C_f and its direction (θ) resulting in the following expressions:

$$\begin{aligned} C_f &= 0.032h(1-\frac{g}{5.37})[-3H+4(\xi-7.15)+12] \\ \theta &= \frac{150h+40}{70}[-60(H-1.5)+40(\xi-7.15)+70]f(g) \text{ for } H \geq 1.5 \text{ mm} \\ \theta &= \frac{150h+40}{70}[40(\xi-7.15)+70]f(g) \text{ for } H > 1.5 \text{ mm} \end{aligned} \tag{2.12}$$

$$\begin{aligned} f(g) &= -0.72g+3.58 \text{ for } g \geq 3.58 \text{ mm} \\ f(g) &= 1.0 \text{ for } g > 1.5 \text{ mm} \end{aligned} \tag{2.13}$$

The flow velocity distribution is measured in the large diameter rod model and is compared

to the prototypical rod diameter model to estimate the scaling factor of conversion for the measured force. A correlation was developed to evaluate the critical momentum flux. The validation of the proposed correlation was performed by Nuclear Fuel Industries Ltd. using two life-sized fuel assembly, 15 x15 and 17 x17 configurations with range of baffle gap (0.1-0.4) mm. The comparison between the experimental results and the calculated values of the critical momentum flux indicates that the model agrees with measured values as shown in Figure 2.9.

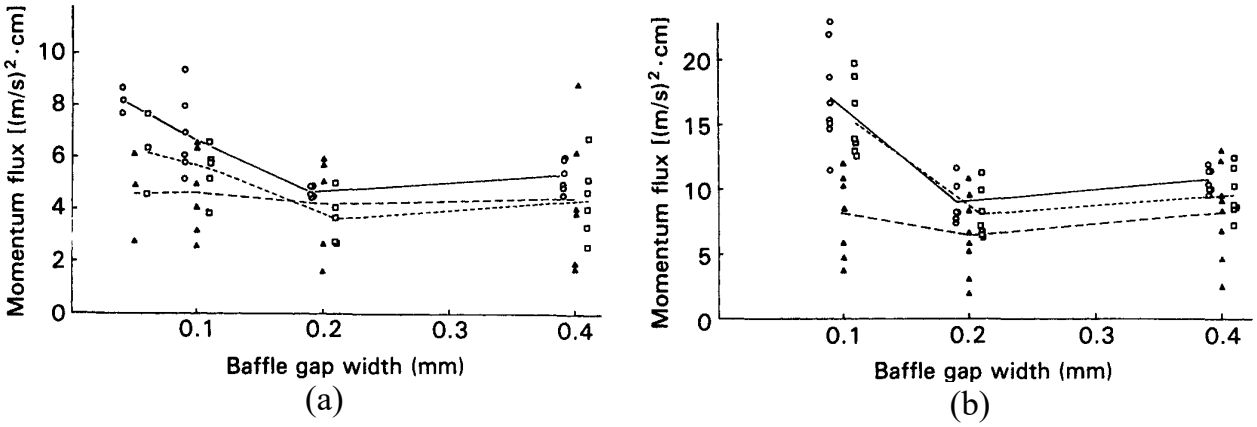

Figure 2.9 Comparison of measured (solid line) and calculated (densely dashed) values of the critical momentum flux, (a) 15x15 type and (b) 17x17 type, (Seki et al., 1986).

Fujita et al. (1990) extended the study on the baffle jet induced vibrations by considering the effects of jet eccentricity, rod damping, rod natural frequency, jet length relative to the rod span and gap size. In addition to varying the jet velocity, the experiments were conducted with two test fluids, air and water. Moreover, three tube array configurations were studied, 7x6, 7x5, 7x1 in-line arrays and also a single rod. Table 2.2 shows the main test parameters.

Similarly to the case of a uniform cross flow, the tube array in a jet cross-flow experienced fluidelastic instability in addition to vortex shedding. However, the experimental results for a single tube subjected to a uniform cross flow showed that it was fluidelastically stable as shown in Figure 2.10(a), while jet flow induced FEI was found for a single tube having different eccentricities with the jet flow as shown in Figure 2.10(b). Clearly, the jet eccentricity parameter has a significant influence on the tube vibratory behavior.

The authors observed that the tubes underwent instability when the jet momentum ($V_{Jet}^2 h$) exceeded a certain critical value. This is the instability threshold jet momentum. Consequently, it was proposed that the threshold of unstable vibration could be determined by the following two equation:

Table 2.2 Test parameters (Fujita et al., 1990).

Items	Explanation
Tube array (inline)	7x6, 7x5, 7x1, 1
Number of spans	Single span
Diameter of tube, D	16 mm
Gap, h	0.1-168 mm
Pitch to diameter ratio, P/D	1.325
H	2.4 mm
ξ	0, 5.7, 8.0, 10.6 mm
Rod material	Aluminum
Fluid	Water or air

$$\frac{\sqrt{V_{Jet}^2 h}}{fD^{3/2}} = 6(\frac{m\delta_0}{\rho D^2}) \text{ fitted with different tube mass per unit length, } m.$$
$$\frac{\sqrt{V_{Jet}^2 h}}{fD^{3/2}} = 5(\frac{m\delta_0}{\rho D^2}) \text{ fitted with different fluid density, } \rho. \tag{2.14}$$

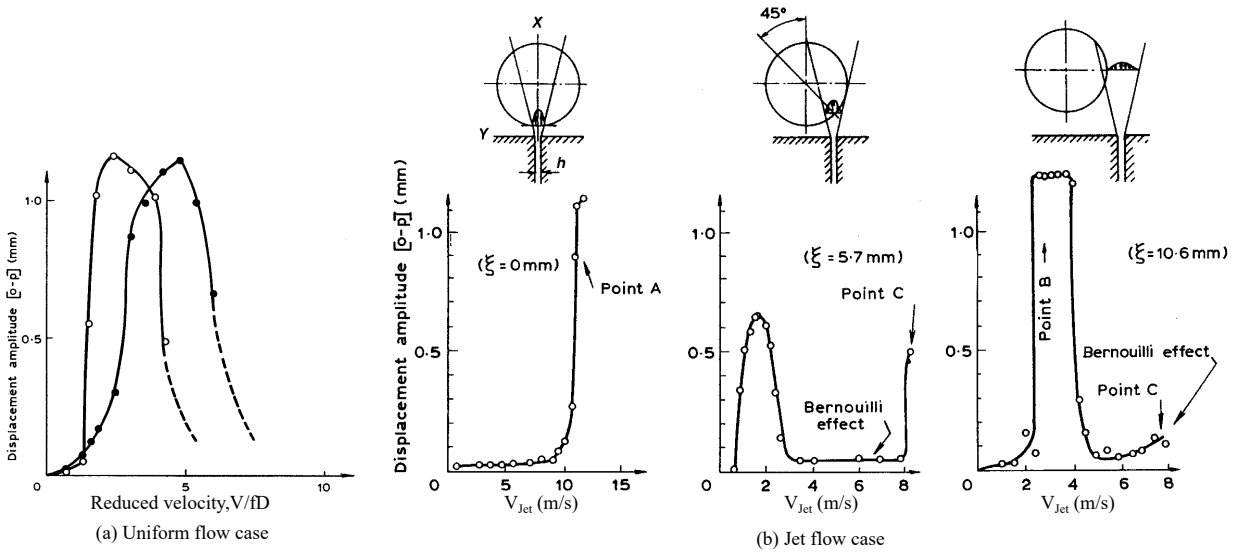

Figure 2.10 Dynamical behavior of a single tube in water subjected to (a) uniform flow, and (b) jet flow (Fujita et al., 1990).

where m is the mass per unit length of the tube including fluid added mass, δ_0 the logarithmic decrement of damping in fluid, and ρ the fluid density.

Lee and Chang (1990) further studied experimentally the effect of axial flow velocity and the jet stand-off distance on the instability of a rod array. The experiments were performed

with two inline square arrays, 4x4 and 4x5, having a pitch-to-diameter ratio of 1.32. Rod vibration due to FEI was observed beyond a critical jet velocity. However, when the authors considered the effect of both axial flow and jet flow, the instability occurred but at higher jet velocity than that found in case of pure jet cross-flow. This indicates that the axial flow had a stabilizing effect as shown in Figure 2.11(a). On the other hand, shorter stand-off distance had a destabilizing effect as shown in Figure 2.11(b). The following instability threshold equation was provided to predict critical flow velocity:

$$\frac{V_{Jet}}{fD} = K\sqrt{(\frac{D}{h})(\frac{m\delta_0}{\rho D^2})} \tag{2.15}$$

The instability of rod arrays subjected to jet cross flow was characterized by low stability constant ($1.53 \leq \mathrm{K} \leq 2.18$ at $H/D = 0.8$) compared to uniform flow. It was found that the stability constant is dependent on the normalized stand-off distance (H/D) as follows:

$$K = 1.9(H/D) + 0.1 \tag{2.16}$$

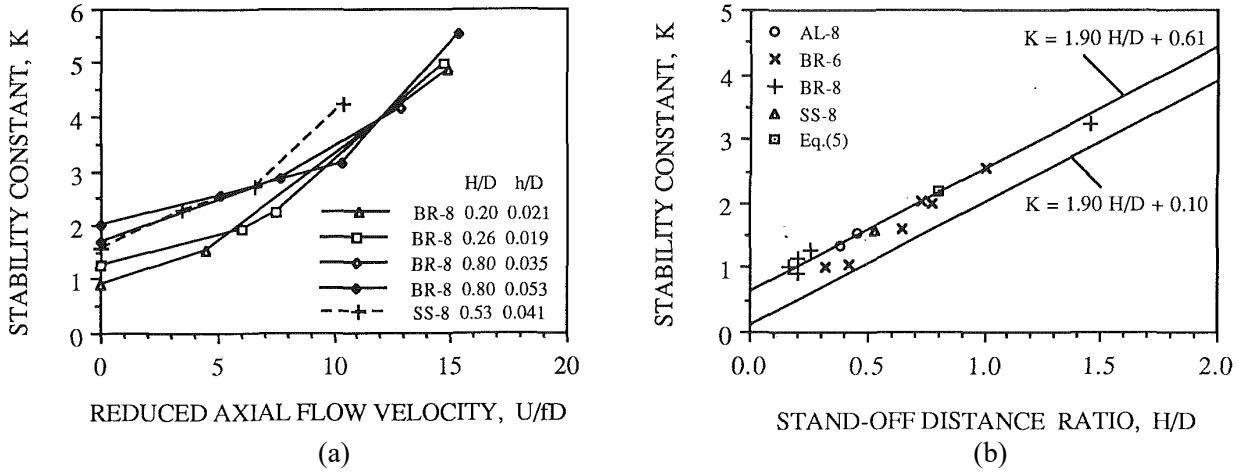

Figure 2.11 (a) Stability effect of axial flow, and (b) stability effect of stand-off distance (H) on the stability constant (K), (Lee and Chang, 1990).

2.3 Fluidelastic Instability (FEI) Theoretical Models

It is of greatest interest to identify the fundamental mechanisms governing FEI. To this end, a number of theoretical models have been developed to predict the instability threshold in tube bundles. Due to the mutual feedback interaction between the moving cylinder and the resulting fluid forces, it is inadequate to model the fluid forces on cylinder as though in

its static position. Careful considerations of the effect of cylinder motion in the theoretical models ensures an accurate prediction of the critical velocity to initiate FEI. This, however, significantly increases the complexity of these models. Chen (1987) classified the FEI models based on motion-dependent fluid forces into three categories: quasi-static, quasi-steady and unsteady flow theories. This section will outline the physical assumptions that are used to derive mathematical equations for the existing models; quasi-(un) steady models, and general unsteady models.

2.4 Unsteady Models

Tanaka and Takahara (1981) developed the unsteady model by measuring the unsteady fluid forces on an in-line square array with spacing ratio $P/D = 1.33$. The authors performed an experimental study in which a central tube in an in-line tube array was excited harmonically and the fluid forces acting on the adjacent tubes were measured. The fluid forces acting on the central tube O in the array are assumed to be functions of its own motion as well as that of the motions of the four neighbouring tubes only, namely tubes U, R, L and D as shown in Figure 2.12a. Thus, assuming linear fluid dynamics and using assumptions based on array symmetry, the fluid forces per unit length acting on the cylinder O were written as follows:

$$F_x = \frac{1}{2}V^2[C_{xOx}x_O + C_{xLx}(x_L + x_R) + C_{xLy}(y_L - y_R) + C_{xUx}x_U + C_{xDx}x_D] \tag{2.17}$$

$$F_y = \frac{1}{2}V^2[C_{yOy}y_O + C_{yLx}(x_L - x_R) + C_{yLy}(y_L + y_R) + C_{yUy}y_U + C_{yDy}y_D] \tag{2.18}$$

where example, C_{xLy} means the x-direction force induced by the left cylinder (L) vibrating in the y-direction.

The unsteady lift and drag forces were measured over a range of Reynolds numbers and reduced velocities. These fluid forces were used to complete the array equation of motion. A stability analysis was performed by solving the resulting eigenvalue problem for increasing flow velocity. A vanishing of the real part of one of the eigenvalue marked the critical flow velocity. The authors found a discontinuity in the stability boundary for values of mass-damping parameters in the range of ($50 \leq \mathrm{m}/\rho\mathrm{D}^2 \leq 500$) as shown in Figure 2.12b, concluding that the instability mechanisms below and above this range are different. The comparison between the theoretical boundary from Tanaka and Takahara's model with their experimental results showed the model predicted precisely the system stability. However, the number of measured parameters related to force coefficients required for this model is considerably high.

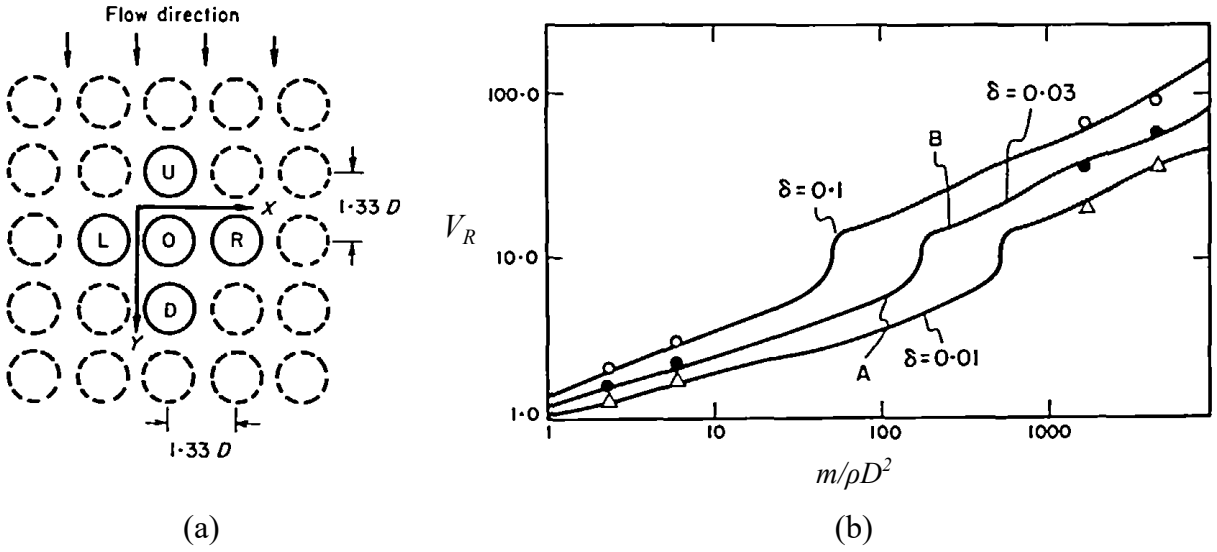

Figure 2.12 (a) cylinder array (b) the stability boundaries showing critical reduced velocity against mass ratio (Tanaka and Takahara, 1981).

Chen (1981, 1983a,b) found that there are two basic mechanisms underlying fluidelastic instability: (i) negative fluid-damping mechanism, and (ii) fluidelastic-stiffness mechanism. The first mechanism is governed by fluid damping, which the second depends fluidelastic cross-coupling forces. The damping mechanism is associated with fluid forces having a phase difference with the tube displacement, therefore the force would have a component in-phase with the tube velocity. The fluid damping force is proportional to the tube velocity and when the flow velocity exceeds a certain value, the modal damping becomes negative and the system becomes unstable. A single flexible tube can only undergo instability by this mechanism. The second instability mechanism requires at least two degrees-of-freedom, thereby it is related to the fluid cross-coupling terms of neighbouring tube vibrations; it is also called the *"displacement mechanism"*. The dominant fluid force is proportional to the relative displacements of the tubes. The fluidelastic force may affect natural frequencies as well as modal damping. As the flow velocity increases, the fluidelastic force may reduce the modal damping. When the damping of a mode vanished, the tubes become unstable.

2.5 Quasi-steady Model

In the quasi-steady model the relative velocity of the flow approaching an oscillating cylinder is modified to take into account the effect of the cylinder motion. This leads to the introduction of the relative velocity vector with respect to the cylinder. The resultant lift and drag forces are reoriented to become normal and parallel, respectively, to this relative velocity

vector, as shown in Figure 2.13.

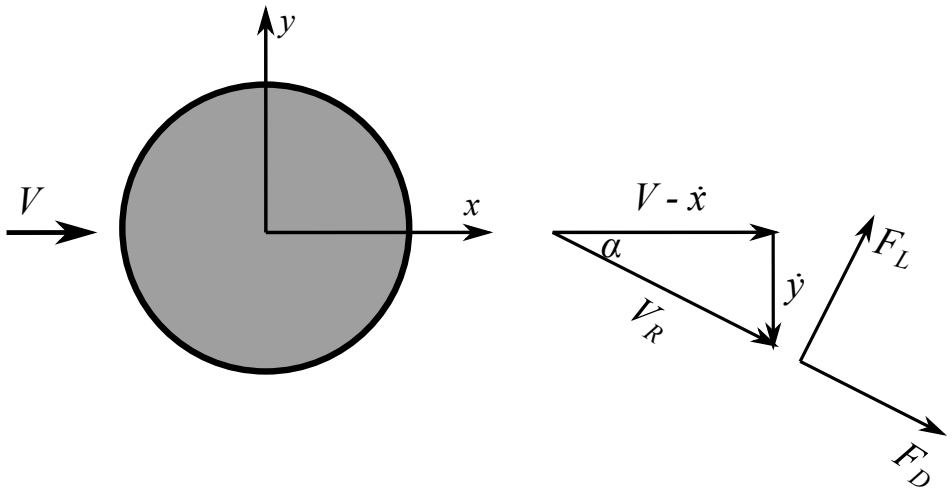

Figure 2.13 Relative velocity diagram for a quasi-steady analysis.

As the cylinder vibrates, the relative velocity V_R oscillates as well. Price and Paidoussis (1983) linearlized C_L and C_D for cylinder i in a double row of cylinders by using an angle of attack α which is obtained by the approximation $\alpha \approx \dot{y}/V$. As an example, the drag coefficient for cylinder i, C_{D_i}, which is a function of the adjacent cylinder dispalceemnts $(x_{i\pm1}, y_{i\pm1})$ and α is expressed as follows:

$$\begin{aligned} C_{D_i} = [&C_{D0_i} + x_{i-1}(C_{D_i x_{i-1}}) + y_{i-1}(C_{D_i y_{i-1}}) + x_i(C_{D_i x_i}) + y_i(C_{D_i y_i}) \\ &+ x_{i+1}(C_{D_i x_{i+1}}) + y_{i+1}(C_{D_i y_{i+1}}) + \alpha_i(C_{D_i \alpha_i})] \end{aligned} \tag{2.19}$$

where C_{D0_i} is the equilibrium drag coefficient of cylinder i and, for example, $C_{D_i x_{i+1}} = \partial C_{D_i} / \partial x_{i+1}$.

Price and Paidoussis (1984, 1986) further incorporated a time delay (τ) between the tube motion and the fluid response to improve the quasi-static model, which was introduced as the time required for the mean flow to pass one tube row downstream. By following an approach similar to that of Simpson and Flower (1977), this time lag effect is incorporated into the quasi-static model, resulting in frequency-dependent terms which are of a non-quasi static type (i.e. quasi-steady model). The authors proposed a constant time delay (τ) expression in the form:

$$\tau = \frac{\mu D}{V} \tag{2.20}$$

where μ is the flow retardation parameter assumed to be of order 1, D is the tube diameter,

and V is the approaching velocity. For example, the effect of this flow retardation on the drag coefficient C_{D_i} for cylinder 'i' becomes:

$$C_{D_i} = C_{D0_i} + \sum_{k=i-1}^{i+1} \{gx_k \frac{\partial C_{D_i}}{\partial x_k} + gy_k \frac{\partial C_{D_i}}{\partial y_k}\}; \quad g = e^{-\lambda\tau} \tag{2.21}$$

Price and Paidoussis (1986) used the model to analyze the stability of a single flexible cylinder in a rigid array and obtained, for values of $V_p/(f_n D) \geq 10$, the following expression for the critical flow velocity for the onset of instability in the lift direction:

$$\frac{V_c}{f_n D} = \frac{4am\delta/\rho D^2}{-C_D - \mu D(\partial C_L/\partial y)} \tag{2.22}$$

and for the drag direction:

$$\frac{V_c}{f_n D} = \frac{4am\delta/\rho D^2}{-2C_D - \mu D(\partial C_D/\partial y)} \tag{2.23}$$

where a is the ratio of reference gap velocity to free stream velocity, $V_{pitch}/V_{freestream}$.

The authors also investigated the effects of the damping and stiffness mechanisms by comparing the stability boundaries for a fully flexible array to those for a single flexible tube in a rigid array. It was concluded that instability for mass-damping parameters less than 300 is mainly due to the damping mechanism, while for mass damping parameters above 300 the stiffness mechanism is predominant. The theoretical stability boundaries obtained from Price and Paidoussis (1986) were compared with the available experimental data for a single flexible cylinder in an inline square rigid array. It can be seen from Figure 2.14 that the developed model is in reasonably good agreement with experiment.

Since the quasi-steady approach is the central point of interest in the current study, it is important to clarify the quasi-static theory assumption which is the measurement of force coefficients on a statically displaced tube. This assumption is valid, however, when the frequency of periodic components in the near wake associated with vortex shedding is significantly higher than the natural frequency of the structure (Price and Paidoussis, 1984). Blevins (1977) claimed the ratio between the vortex shedding frequency and the structural frequency should be 2. This means the reduced velocity (V/fD) should be greater than 10 (i.e. Strouhal number of 0.2) for a circular cylinder in uniform flow. However, for closely packed arrays (i.e. fuel assemblies), Strouhal numbers of up to 1.0 may be obtained, leading to the criterion of $V/fD > 2$ for the quasi-static theory to be valid.

Previous studies have demonstrated the validity of the quasi-steady theory in predicting the

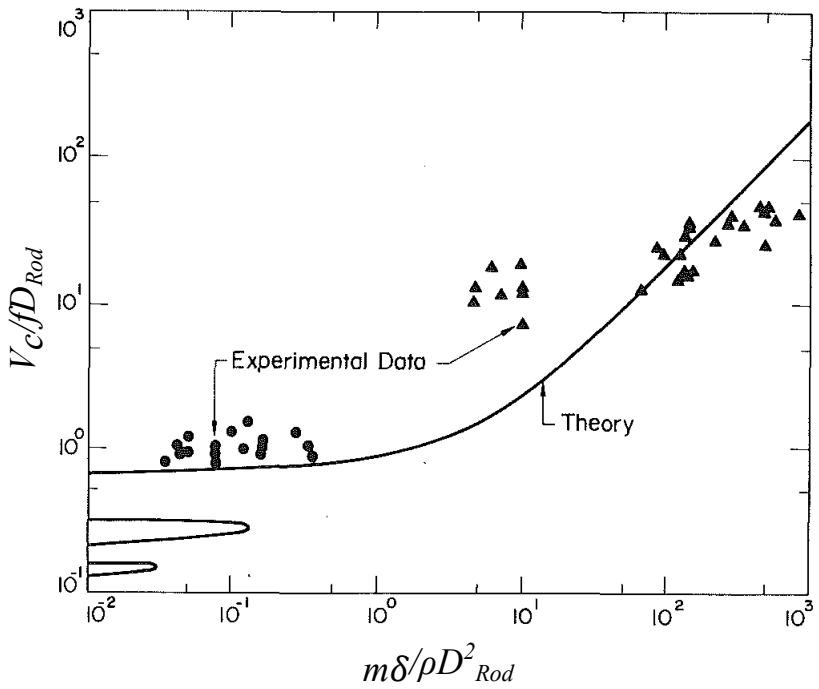

Figure 2.14 Comparison between experimental data (Price et al., 1986) and the theoretical stability boundary for a single flexible cylinder in an in-line square array of rigid cylinders, with $P/D_{Rod} = 1.5$.

stability boundary of arrays in single-phase flow, besides that, Yu et al. (2004) extended the use of the quasi-steady approach in predicting the fluidelastic instability of a cylindrical wire in the shear layer of a two dimensional jet. It was found in the experiments that the wire is unstable and induced to vibrate if initially mounted in a shear layer with sufficiently high flow velocity and velocity gradient (G), while the wire is stable in uniform cross flow. The fluid forces were normalized based on the Reynolds number and the shear flow velocity gradient. The developed model results agreed well with the experimental results. The results also showed that the shear parameter (K=GD/V), and hence the lift coefficient C_L are crucial to the fluidelastic instability of a circular cylinder in shear flow.

The quasi-steady approach is chosen in the current study because earlier work on single-phase flow and shear flow suggests that it is more achievable in terms of experimental effort and agreement with experimental data.

2.6 Quasi-Unsteady Model

Granger and Paidoussis (1996) developed a quasi-steady model to take into account the unsteady effects which were previously neglected in the theoretical model of Price and Paidoussis

(1984), formulating the quasi-unsteady model. The authors considered the model of a single flexible tube in a rigid array, in which the instability could occur owing to the damping mechanism only. They solved the continuity and Navier-Stokes equations to predict the fluid response to an impulse motion of the cylinder. They concluded that due to the impulse motion of the tube, a finite layer of small vortices is generated on the cylinder surface. They attributed the time delay between the cylinder vibration and fluid force response to the time required for reorganization of the flow in these layers of vortices, which is a function of flow velocity. This led to a model of unsteady effects in the fluid dynamic forces representing an effect of memory in the flow, instead of using the simple time delay function. The comparison between three theories that are used in the literature to model the time delay is illustrated in Figure 2.15. Price and Paidoussis (1984) had assumed in their model that the time delay was a constant time shift while the quasi-unsteady model considered the retardation associated with reorganization of the flow in the vorticity layer.

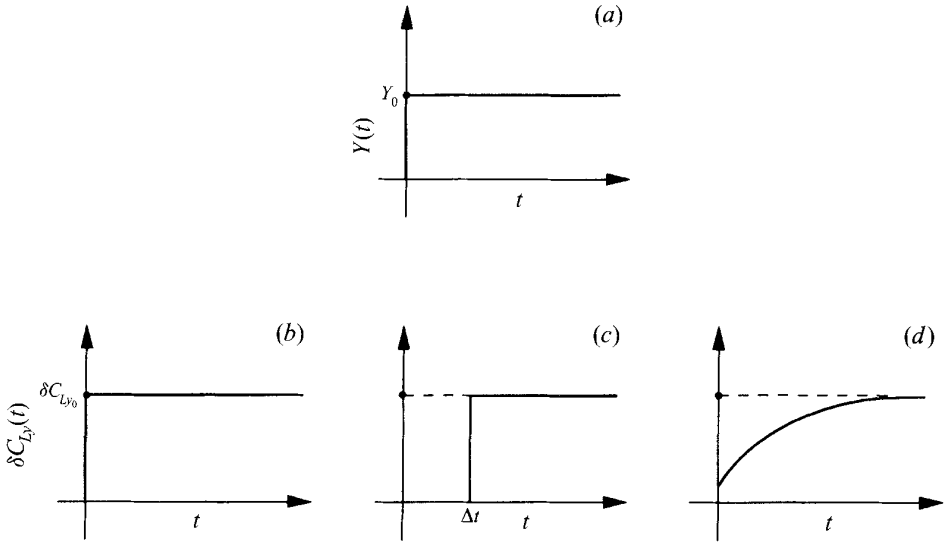

Figure 2.15 Transient variation of lift coefficient, δC_L(t) induced by a step displacement $Y(t) = Y_0 H(t)$: (a) $Y(t)$, (b) quasi-steady theory, (c) Price & Paidoussis model and (d) continuous variation of time delay as proposed in quasi-unsteady model (order 1) (Granger and Paidoussis, 1996).

Granger and Paidoussis (1996) also compared the results obtained from the quasi-unsteady model to experimental data and to stability boundaries obtained from the Price & Paidoussis model as presented in Figure 2.16. This comparison proved that the quasi-unsteady model is a clear improvement on Price & Paidoussis' approach, leading to a more reasonable agreement with experimental results and providing refined insights into the physical mechanisms responsible for fluidelastic instability. The memory effect of the time delay was modeled us-

ing either a first-order or second order equation. The agreement between the quasi-unsteady stability boundaries and the experimental data was improved by increasing the order of the function for the memory effect, as seen in Figure 2.16.

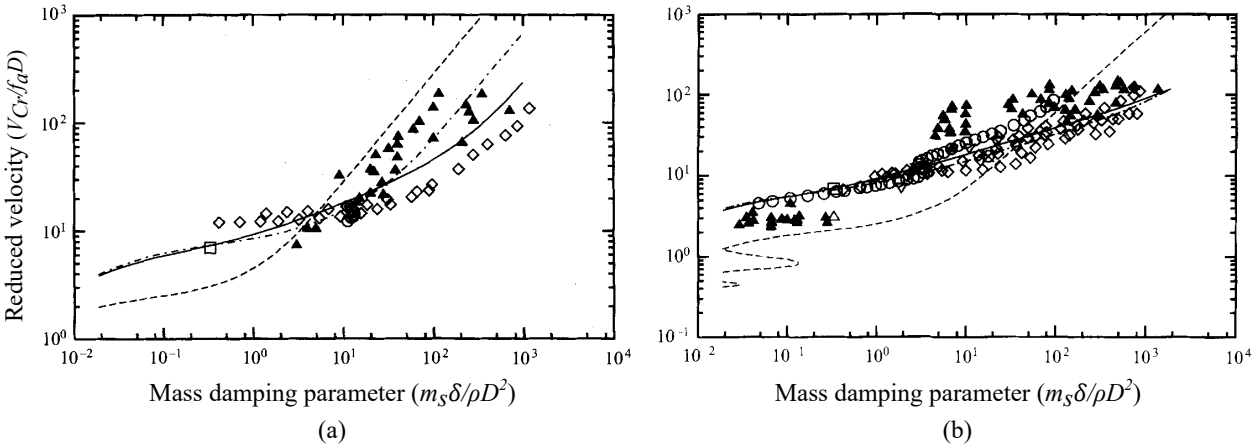

Figure 2.16 Comparison of the stability boundaries for a single flexible tube between the quasi-steady model (dash), quasi-unsteady model with first order (line) and quasi-unsteady model with second order (dash-dot) in: (a) a rigid normal triangular array, and (b) a square in-line array (Granger and Paidoussis, 1996).

CHAPTER 3 ARTICLE 1: JET CROSS-FLOW INDUCED VIBRATIONS IN ROD BUNDLES. PART I: EXPERIMENTAL APPARATUS AND STREAM-WISE VIBRATION RESULTS

Gad-el-Hak, I, Mureithi, N, Karazis, K, and Williams, G.

This article was submitted to "Nuclear Engineering and Design" on 23rd November 2021, it is accepted on 6th November 2022.

Summary

This chapter presents experimental data for rod bundle vibration due to jet cross-flow. Rod bundles of size, 6x6, and 6x5 are tested under pure jet cross-flow having $D_{Jet}/D = 2.6$. Two jet-flow parameters, stand-off distance (H) and jet eccentricity (ξ) are investigated to understand their effects on the stability boundaries of the arrays. The rod arrays are flexible in the stream-wise direction relative to the jet flow. This work is performed to answer the research questions (**Q1**, **Q2**) and to achieve the objective (**O1**).

Graphical Abstract

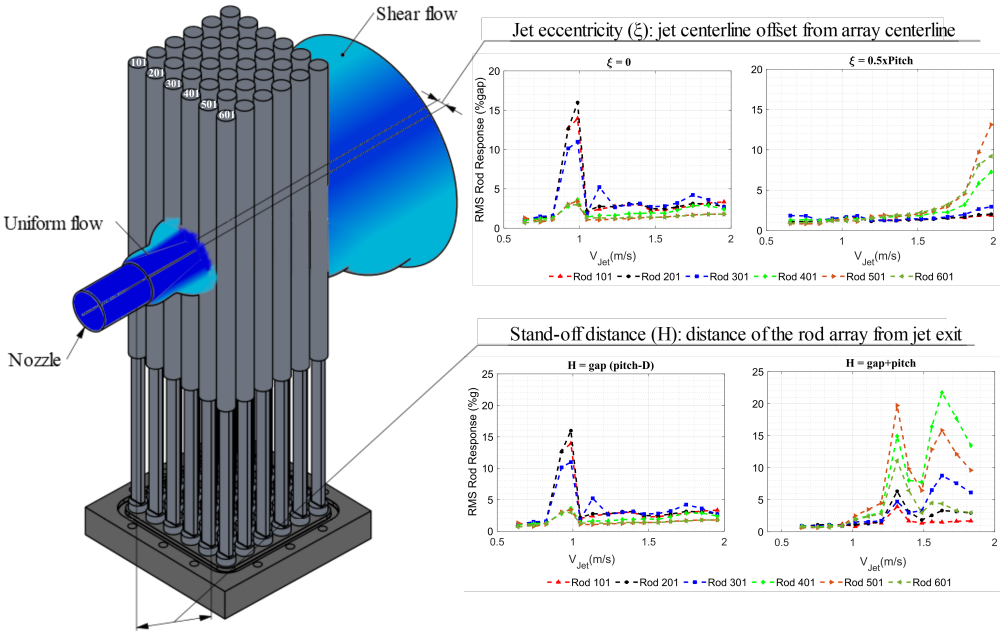

Abstract

Jet cross-flow induced vibration of fuel assemblies has recently been observed in some reactors that have fail-safe features for pressure release in the event of a loss of coolant accident (LOCA). The generated pressure in the barrel-baffle region during LOCA is mitigated by discharging the flow through LOCA holes and slots normally to the primary axial coolant flow inside the core. However, the jet flow injected through the LOCA holes and slots can induce vibration in the fuel assembly near the baffle before being mixed with the axial flow, and subsequent it can cause grid-to-rod-fretting (GTRF). In this paper, experimental investigations were performed to characterize the jet cross-flow induced vibration of fuel rods by performing fluidelastic instability (FEI) tests on flexible rod bundles. The effect of the stream-wise which is called "stand-off distance", is studied by the changing number of rows in the tested bundle. Furthermore, an offset between the centerlines of the jet and the bundle (jet eccentricity) which means the transverse direction on the jet centerline, is changed to show its effect on rod bundle vibration. An experimental test facility was designed to give the capability to study different jet eccentricities to examine their stability effects. The stream-wise results show that varying jet eccentricity excited the rod bundle with different mechanisms. The rods vibrations occurred with the centred jet with rod bundle case had a lock-in/synchronization phenomenon, where the resonant peak is observed. While, the excitation mechanism is switched to turbulence-induced vibrations by moving the jet flow by 0.25 of pitch. However, the aligned jet-rod case showed a fluidelastic instability phenomenon at relatively high jet velocity. On the other hand, the two resonant peaks are obtained when the rod bundle moved away from the jet flow (i.e larger stand-off distance).

Keywords: PWR fuel rods, LOCA, Fluid-structure interaction, Jet cross-flow induced vibrations, Fluidelastic instability tests, Image processing.

3.1 Introduction

In nuclear reactors, flow induced vibration (FIV) of fuel rods within fuel assemblies has been the center of attention to ensure that the safety of nuclear power plants is not compromised during normal and accident conditions such as a loss-of-coolant accident (LOCA). Some pressurized water reactor reactor (PWR) designs have fail-safe features to release pressure build-up in the event of a loss-of-coolant accident (LOCA). The features include holes and slots in the baffles that peripherally surround the core as shown in Figure 3.1. The flow emanating from LOCA holes and slots serves to equalize the pressure across the baffle plates. During normal operation, however, these reactors have experienced grid-to-rod fretting in

some of the fuel assemblies due to their proximity to the LOCA holes as reported in a review issued by the International Atomic Energy Agency (IAEA) on fuel failures in water-cooled reactors (IAEA, 2015).

Cross-flow induces vibrations higher than those induced by purely axial flows owing to the lower turbulence of external axial flow on the surface of the fuel rods (Paidoussis, 1981). In extreme cases, the fuel rods may undergo fluidelastic instability resulting in violent and destructive vibrations. Flow periodicities induced by shear layer oscillations may also potentially cause strong resonance oscillations. These undesirable vibrations and instabilities are responsible for grid-to-rod-fretting (GTRF) and wear of the fuel rod cladding. Consequently, FIV analysis of the fuel assemblies in proximity to LOCA holes during normal conditions plays a key role to set safety margins of the operating conditions of reactors.

Jet cross-flow, especially for assemblies neighbouring baffle plates in reactors, can have a significant impact on fuel rod fretting. Grid-to-rod fretting was previously observed in PWRs at peripheral core positions due to baffle jetting. Fuel failure from baffle jetting occurred in PWRs having a down flow baffle barrel design as noted by U.S. NRC (1980). In this design, a small portion of the total primary coolant flow is diverted into the region surrounding the reactor core, in the direction opposite that of flow through the core. Some of this flow passes through defect gaps between adjacent baffle plate joints owing to the differential pressure existing between the ascending coolant flow through the core and the descending flow providing internal cooling for the baffles. The direction of the jet is transverse to the fuel rods, causing them to vibrate and impact against their supports. The root cause of failure was improper joining of the baffle plates. The failure became rare following various modifications, including a change in coolant flow behind the baffle plate, which reduces the differential pressure across the plates as reported in Kitlan Jr et al. (1991). Another corrective action was the modification of peripheral fuel assemblies that were placed in baffle joint positions. Framatome developed special anti-fretting clips to prevent rod vibration and damage resulting from baffle plate leakage cross-flow. The clips can be attached to peripheral rods of assemblies in sites known to be susceptible to baffle jetting.

Compared to research on fluidelastic instability of tube arrays subjected to uniform transverse flow, only a few researchers have addressed the problem of baffle jet (planar jet) cross-flow induced FEI. Fujita et al. (1990) performed experiments on a tube array subjected to a transverse narrow-gap jet flow. In addition to varying the flow velocity, the effects of jet eccentricity, stand-off distance, tube damping, and jet width were also quantified. As in the case of a uniform cross-flow, a jet cross-flow was also found to lead to FEI of the tube array. Other excitation mechanisms considered include vortex shedding, the Coanda effect, and the

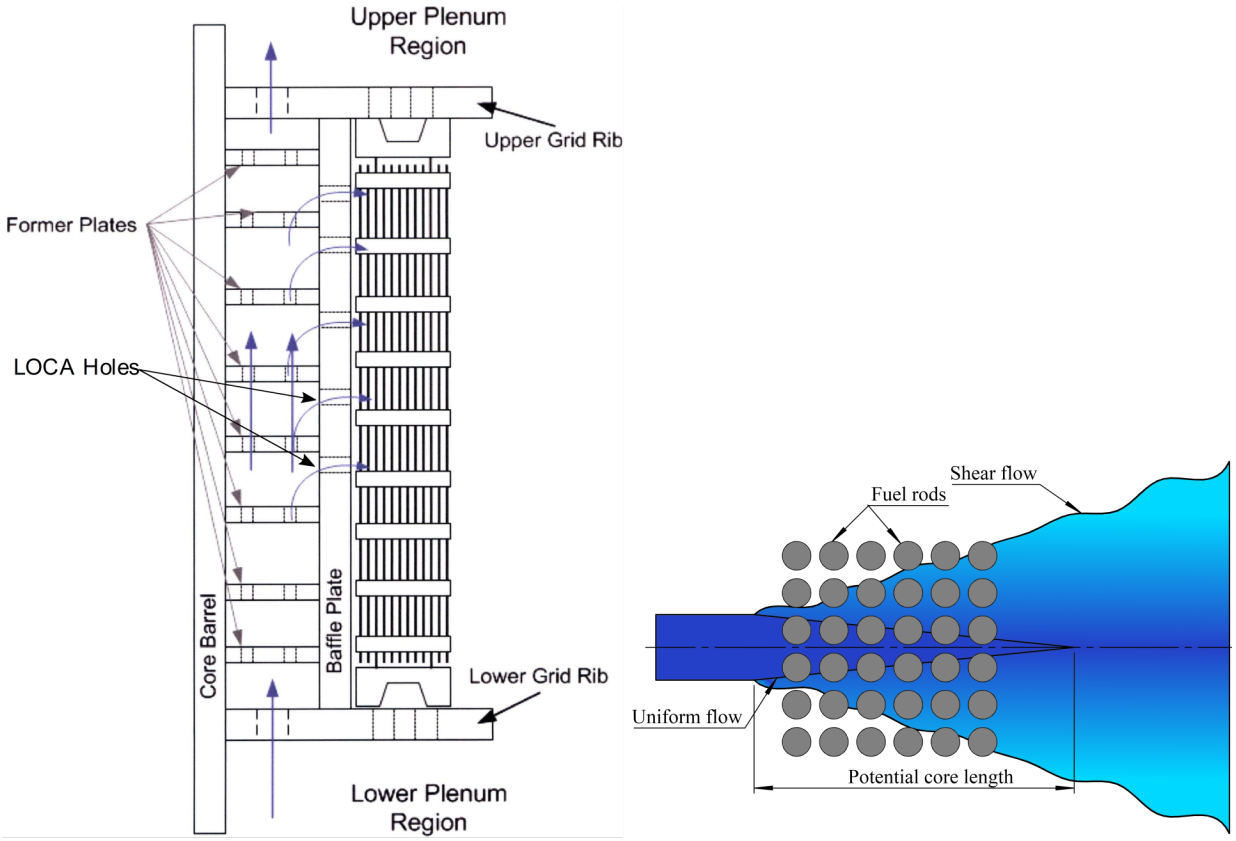

(a) (b)

Figure 3.1 (a) Baffle-barrel design including LOCA holes,(AREVA, 2017) and (b) schematic drawing showing flow emanating from LOCA hole towards fuel rods.

Bernoulli effect due to the interaction between the wall and the first row tubes. The jet momentum was found to be the parameter that best quantified the instability threshold. A single tube subjected to a jet flow was also found to undergo instability (unlike the case of a single tube in uniform flow which remains fluidelastically stable). Lee and Chang (1990) presented an experimental study of the jet-flow induced vibration of a rod array. The effect of the axial velocity and the stand-off distance on the critical instability velocity was also reported. Large amplitude rod vibrations, akin to FEI, were observed above a critical velocity. Increasing the axial flow velocity was found to have a stabilizing effect. On the other hand, shorter stand-off distances had a destabilizing effect. As is done for tube arrays in uniform cross-flow, researchers developed a stability criterion based on a relation between the reduced velocity and the rod mass-damping parameters. A rather low stability constant ($1.53<K<2$) was found compared to the uniform flow case. The stability constant was also found to depend on the stand-off distance.

By comparing the flow issuing from a narrow slot (baffle jet) and that from a circular hole (LOCA hole), two main differences appear. On one hand, a circular jet can penetrate deeper into the surrounding fluid compared to a plane jet (Lee et al., 2003), which means that several fuel rods in an assembly may be subjected to LOCA jetting induced vibrations relative to the case of baffle jetting. On the other hand, the exit velocity from round holes changes in three dimensions leading to the growth of jet shear layers in both stream-wise and radial directions. The circular jet-induced vibration of rod bundles has never been investigated experimentally or numerically. The resulting flow complexity, due to its axisymmetric shear layer, highlights the difficulty of the resulting flow-induced vibration problem.

Framatome in collaboration with Polytechnique Montreal has developed an experimental test program to investigate the dynamical behavior of fuel rods subjected to combined axial and jet cross flows. The work reported here addressing the question of fluidelastic instability in rod bundle subjected to a localized jet cross-flow is the first step. The research is motivated by the need to quantify the risk of fluidelastic instability excitations that could occur in fuel assemblies in proximity to LOCA holes. In order to release the pressure build-up in the baffle-barrel region while still maintaining operating conditions far away from the critical conditions for FEI, the stability maps for rod bundles subjected to round jet cross-flow would be valuable additional data to the flow induced vibration problems. The maps can inform guidelines for the design of fuel assemblies in proximity to LOCA holes and baffle plates having LOCA holes.

3.2 Experimental setup and test parameters

The main goal of this study is to investigate the fundamental mechanisms underlying rod bundle excitation by understanding rod bundle behavior in a transverse jet flow in the absence of axial flow. This can be achieved by obtaining the rod vibration response as the jet flow velocity is increased up to the condition of FEI. However, the rod vibration is strongly affected by jet flow parameters and system dynamical parameters, thus identifying the physical parameters of the problem is necessary to design a test facility capable of studying these parameters. The FEI experiments are performed in the Fluid-Structure Interaction Laboratory at Polytechnique Montréal.

3.2.1 Parameter identification

The flow-induced vibration problem of interest should be defined in three dimensions since the injected flow from a round jet spreads in a conical form from the injection location

as shown in Figure 3.2. Since the flow velocity is not constant over the rod bundle, it is necessary to define jet flow parameters to identify the location of any rod in the array relative to the jet flow centerline. Evaluating the jet flow parameter contributions to flow-induced vibrations is important to understanding different aspects of the problem. Figures 3.2a and 3.2b present the schematic side and top views, respectively, showing the geometrical and jet flow parameters in the bundle. The jet flow and dynamical parameters are also identified in the figure:

- Jet eccentricity (ξ): jet centerline offset from array centerline.
- Standoff distance (H): gap between the first row and the jet exit.
- Jet location parameter (L_{Jet}/L): jet centerline level relative to rod span.
- Flexibility direction (stream-wise or transverse): orientation of flat plate rod-support relative jet flow which determines main vibration direction (stream-wise or transverse directions).

Having defined the physical system parameters the next step is designing a test section with dimensions as close to the real reactor as possible to make the experiments more useful in practice. This is a particularly challenging task due to the densely packed fuel rod bundle configurations in reactors.

3.2.2 Test section design

The resulting problem has many parameters and it is difficult to study their effects on the rod vibration due to experimental limitations. Thus a trade-off is needed to select the most effective parameters. The geometric dimensions of the designed rod bundle are kept the same as in the fuel assemblies. The jet flow in the experiments is always directed at the middle of the rod span, thus $L_{jet}/L = 0.5$. The jet-to-rod diameter ratio (D_{Jet}/D) has evidently a significant effect on the rod array vibration. However, we have decided to keep this parameter constant during the tests as a first step towards identifying and understanding the main excitation mechanisms governing vibrations in the rod bundle. The jet-to-rod diameter ratio is set at 2.3 for the FEI tests. The jet eccentricity (ξ) and standoff distance (H) are varied in the tests to study their effects on the stream-wise and transverse rod bundle stability. The test section consists of three main components:

- Barrel-baffle chamber.

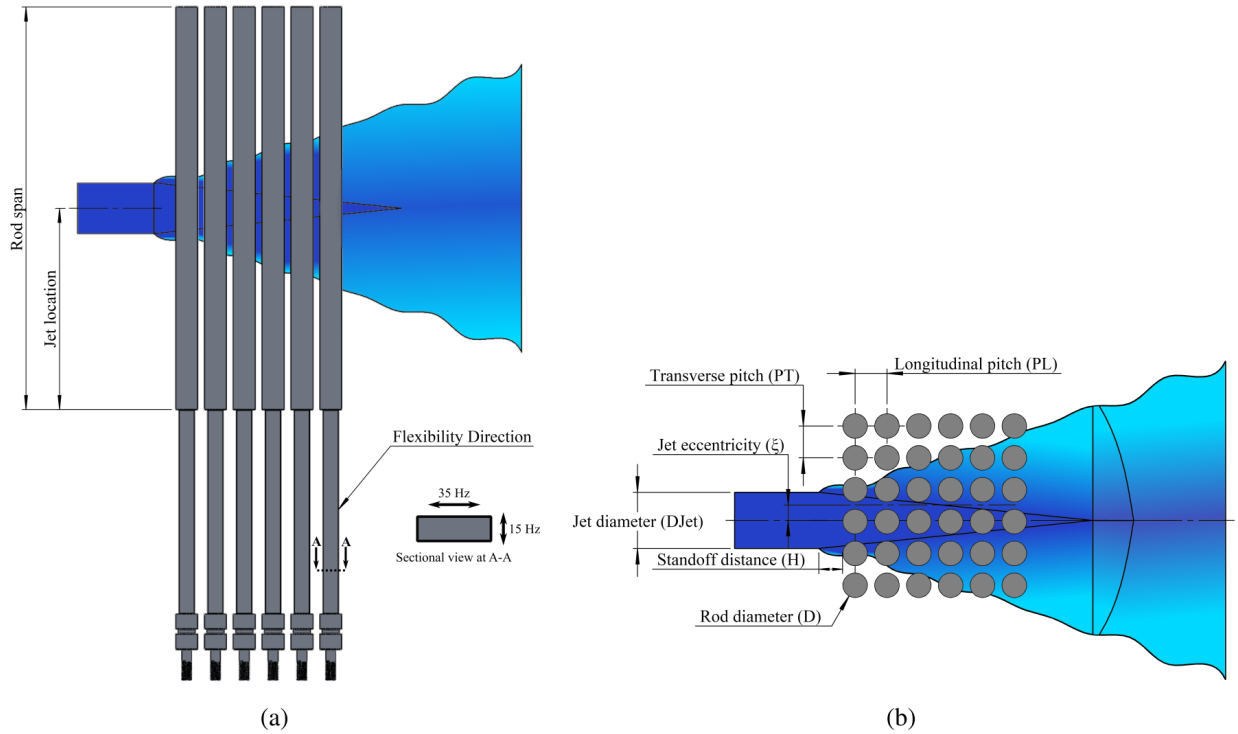

Figure 3.2 Schematic drawings of the jet flow with the rod bundle:(a) side view, and (b) top view.

- Jet flow displacement mechanism.
- Flexible rod bundle.

Barrel-baffle chamber

In the reactor core, the jet flow is introduced from the barrel-baffle region through the LOCA hole. Simulating this flow condition is considered in the test section design by introducing an empty chamber upstream of the rod bundle before the oncoming flow enters the nozzle. The main function of this chamber is to provide a fully developed jet velocity profile by minimizing the turbulence at the nozzle inlet. In addition, a discharge valve is installed at the chamber bottom to discharge the water from the test section.

Jet flow displacement mechanism

The rod bundle vibration response is significantly dependent on the jet eccentricity as observed by Fujita et al. (1990). Accordingly, it is important to study the eccentricity effect on the circular jet cross-flow induced vibrations. A specialized displacement mechanism is

designed to move the jet flow and introduce an offset with the rod bundle centerline. As shown in Figure 3.3, this mechanism consists of a 3D printed nozzle fixed on an aluminum plate which is secured by a threaded flange nut manufactured from delrin acetal plastic to reduce friction and operating with minimal backlash. The plate is driven by an ultra-precision lead screw having an accuracy of 0.6 microns per inch of travel distance. In order to restrict the rotational motion from the lead screw into translation motion, a polished linear motion shaft is used. To reduce the generated friction in the motion shaft which also reduces the force required to move the jet flow, a corrosion-resistant linear ball bearing is attached to the moving plate and coupled with the linear motion shaft.

Preventing water leakage while the nozzle moves inside the test section was a challenging task in the displacement mechanism design. The concept used in centrifugal pump sealing is incorporated in the current design. A spring-loaded rotary shaft seal from Svenska Kullagerfabriken (SKF) is installed in contact with the circumference of the rotating lead screw. To easily rotate the lead screw, a corrosion-resistant linear ball bearing is installed between the housing and the lead screw. This specialized displacement mechanism can move the nozzle 0.1 in. per turn with a total travel distance of 0.75 inches. Measuring the jet eccentricity precisely is the main priority in this setup. A hand wheel with a dial indicator is mounted on the lead screw to precisely change the position of the nozzle relative to the array centerline. One turn of the hand wheel is divided into 12 main partitions corresponding to 0.1/12 in. major increment of travel distance.

Flexible rod bundle

LOCA holes are distributed in nuclear reactor cores circumferentially with a ratio of six to eight rods per LOCA hole. Thus, the flexible rods are arranged in a square lattice with a pitch ratio (P/D) of 1.32 to form a 6x6 configuration. The rods are fabricated with a diameter of 0.43 in., the same as reactor fuel rod diameter. In order to control the frequency and vibration direction of the bundle, the rods are mounted on flat plates which act as asymmetric linear springs which vibrate the rod in the lower stiffness direction at a nominal frequency of 15 Hz (see Figure 3.2a). In the normal direction, the frequency is 35 Hz. The total rod span immersed in the test section flow is 7.925 inches. Figure 3.4 shows the fabricated single flexibly supported rod.

Rod bundle gap measurements

Before installing the rod bundle in the test section, verification of the inter-rod gaps is necessary for this densely packed bundle. The very small gap of 0.138 in. (3.5 mm) made

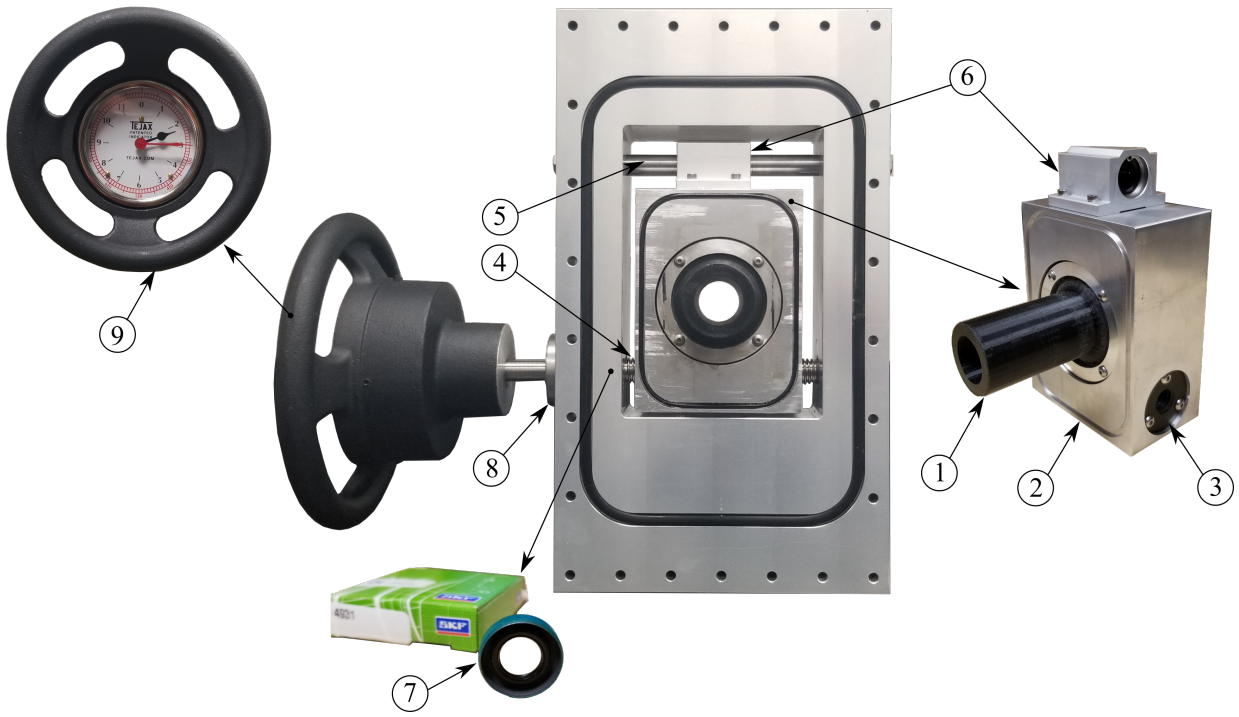

Figure 3.3 Jet flow displacement mechanism showing the main components: (1) nozzle, (2) moving plate, (3) threaded flange nut, (4) ultra-precision lead screw, (5) linear motion shaft, (6) linear ball bearing, (7) spring-loaded rotary shaft seal, (8) linear ball bearing and (9) hand wheel with the dial indicator.

Figure 3.4 Single flexible rod showing its support and the holes used to pass the strain gauge cables.

the rod bundle assembly complicated since a very small misalignment of 0.025 mm between the bottom rod surface and the mounting plate makes the rod incline with an angle of 0.13°. However, this small angle causes a rod offset of 0.74 mm from the equilibrium position which gives gap errors up to 20% as shown in Figure 3.5a. Thus, the machining tolerance plays a key factor for this rod bundle setup. In order to minimize the gap error, set screws (2-56) are passed through the mounting plate normal to each bottom rod surface to adjust the rod gaps and also the flexibility direction of the rods. After bundle assembly, high precision measurements were performed for each gap in the bundle using gauge blocks from KURODA Precision Industries Ltd. as shown in Figure 3.5b. Since precision width blocks have a resolution of 0.001 in., the distance between rods is determined precisely by passing the

blocks between the rods without causing static deflection. Figures 3.6a and 3.6b show the measured inter-rod gaps in the longitudinal and transverse directions, respectively.

(a) (b)

Figure 3.5 (a) Schematic drawing for the rod gap error due to the rod surface misalignment, and (b) 6x6 Flexible Rod bundle setup.

3.2.3 Test loop set-up

All fabricated test section components are assembled on a sturdy structure to eliminate any extraneous vibrations that could come from the structure. Figure 3.7 shows the final test loop with the test array installed in the test section. The test apparatus was used to perform fluidelastic tests on the rod bundle with different jet parameters. A 2 HP centrifugal pump is used to pump the water through the test section. Before the flow enters the tested rod bundle, it first passes through a flow straightener (label 1 in Figure 3.7) to minimize any turbulence that may come from pipe fittings. The flow then enters the barrel-baffle chamber. In the jet displacement mechanism, the uniform flow is converted into a jet flow through the nozzle to be finally injected into the flexible rod bundle.

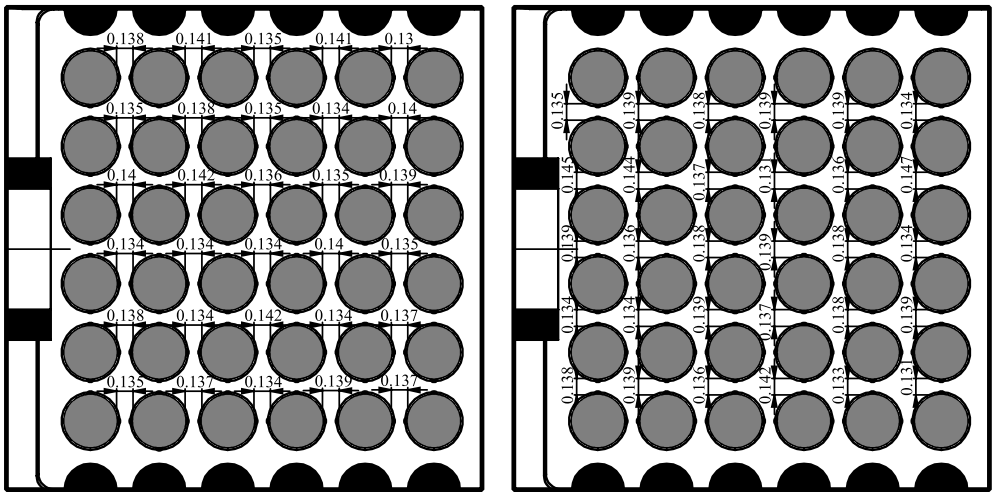

(a) (b)

Figure 3.6 (a) Measured longitudinal gaps, and (b) measured transverse gaps.

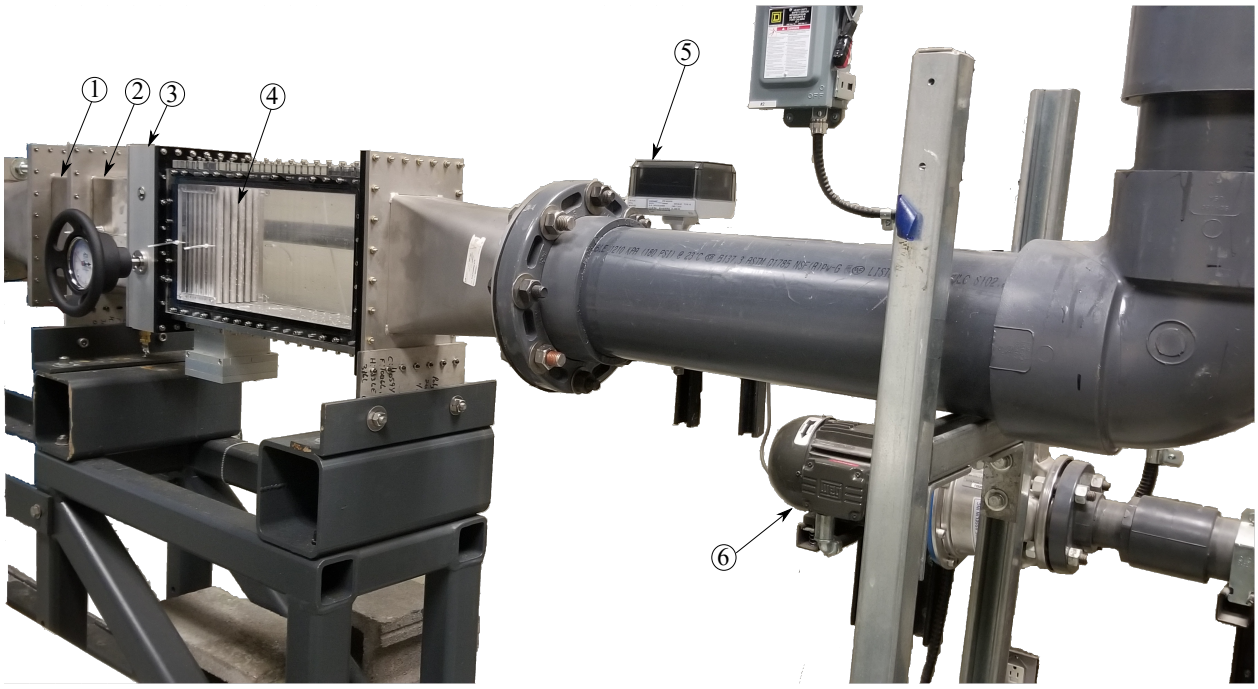

Figure 3.7 The main components of test loop set-up are labelled: (1) flow straightener, (2) barrel-baffle chamber, (3) displacement jet flow mechanism, (4) rod bundle, (5) water flow meter and (6) centrifugal pump.

3.2.4 Measurement systems

The objective of the experiments is to study the vibrations of the rod bundle under flow conditions leading to the onset of fluid-elastic instability. The main effort has been directed towards the development and implementation of a system to measure the time-dependent displacement of the rod bundle subjected to various jet cross-flow velocities to give clear insight into how each rod in the bundle behaves in jet flow.

Using a high-speed digital camera (Motion BLITZ Cube 4, MIKROTRON), sequential images of the rod bundle response are captured as the rods are excited by the jet cross-flow at a specific velocity. The camera speed can reach 1000 frames per second (fps) while recording at 1280 (H) x 1024 (V) resolution. At 1000 fps, the maximum full-resolution recording time is 3.24 seconds. However, the camera can record for longer time durations for reduced resolution and image speed. The camera is oriented toward the top acrylic panel, thereby the viewing plane of the camera is normal to the axis of the rods. A series of unprocessed images, captured at a high frame rate (ten times the rod frequency), represent the rod bundle motion at different jet flow velocities: one movie, consisting of 6,673 frames (about 66.73 seconds), is recorded for a specified mean jet flow velocity for a 6x6 rod bundle frame size. An image processing algorithm is developed in MATLAB to detect and thus track the center of each rod in the raw image series to obtain the rod bundle vibration at each jet flow velocity. A high-speed image sequence showing the rod bundle response for a short time duration of 0.04 sec. including the detected circles of the rods (red circles) from the detection and tracking algorithm is shown in Figure 3.8.

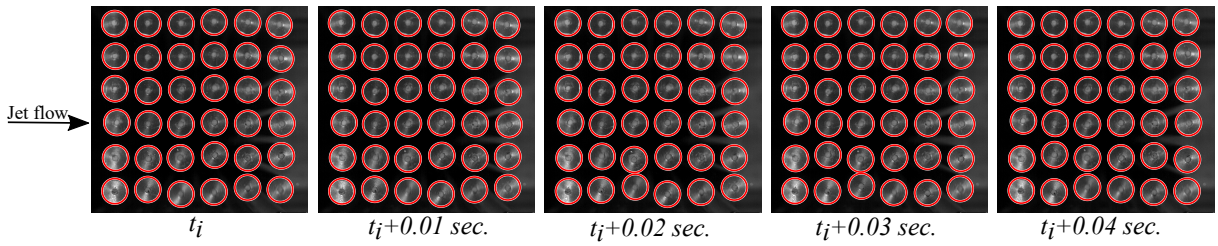

Figure 3.8 Set of sequential image representing the rod bundle motion at ξ of $0.5P$ at jet velocity of 1.7 m/s.

In the field of flow induced vibrations in steam generator tube array, Catton et al. (2004) used a high-speed camera to measure the vibrations of a sub-group tubes within a large array of fifteen flexibly mounted tubes; the subgroup size was five tubes in a normal square array and seven tubes in a normal triangular array. The authors claim that the selected subgroup patterns are representative of these arrays based on symmetry considerations; the subgroups

were also compatible with a unit cell in a computational model. In their experiments, the camera speed was 120 frames per second to capture the range tube frequencies tested; 12, 16, and 20 Hz for a recording time period of 5 seconds.

In the present work, the jet flow is, however, not symmetric in the test section. The frame size of the image must therefore capture all the rods in the bundle. A comparison between the rod response obtained from the high-speed camera with a more accurate measuring system with a higher sampling frequency is needed to justify and prove the efficiency of the proposed measuring system with a high-speed camera. Consequently, eight rods are instrumented with strain gauges as shown in Figure 3.9a for measurement comparison. The gap between the rods is 3.5 mm, therefore the strain gauges were selected to capture small displacements of the rod tip and operate linearly over the gap. To achieve this, the strain gauges (CEA-13-062UW-350) are bonded on both sides of the flat plates. The selected strain gauges are calibrated to determine the factor needed to convert strain to tip displacement; the relation between the obtained strain and tip displacement is linear as shown in Figure 3.9b. M-Coat B and M-Coat F sealing products are used to insulate the strain gauges.

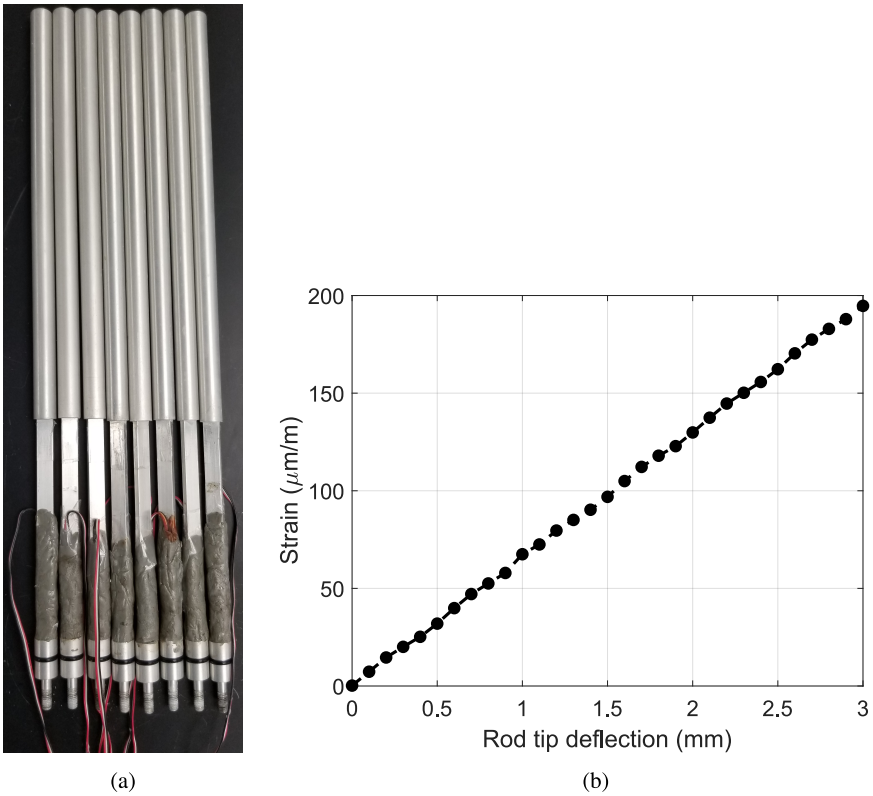

Figure 3.9 (a) Eight instrumented rods with strain gauges, and (b) strain gauge calibration.

3.2.5 Rod bundle map

The image processing algorithm provides the time-dependent displacement for the 36 rods in the bundle, thus a proper numbering method of these rods is needed. The rods in the tested bundle are identified by their column number followed by their row number. For example, rod 401 is located in column number 4 and row number 1 as shown in Figure 3.10.

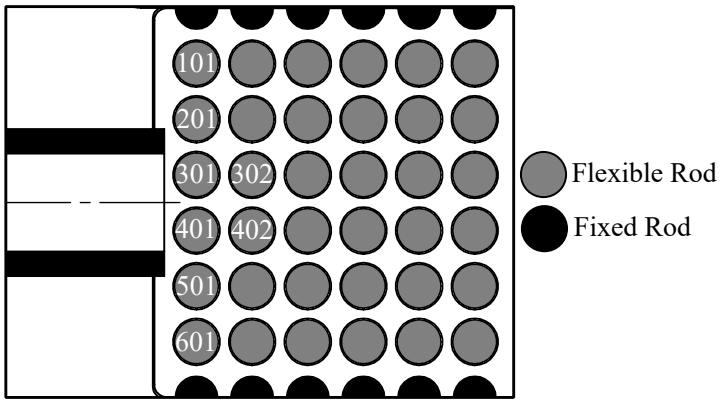

Figure 3.10 Rod bundle numbering.

3.2.6 Test parameters

Two jet flow parameters are studied; jet eccentricity (ξ) and standoff distance (H). The stability effects of three jet eccentricities is investigated. The three eccentricities are:

- $\xi = 0$, which represents jet flow aligned with the rod array, as shown in Figures 3.11a and 3.11b.
- $\xi = 0.25P$, corresponding to a jet flow offset by a quarter spacing (P) as shown in Figures 3.11c and 3.11d.
- $\xi = 0.5P$, corresponding to a jet flow aligned with the rod centerline, as shown in Figures 3.11e and 3.11f.

The stand-off distance is varied by removing a row of rods in the bundle to increase this distance. However, the resultant number of rows is still in the recommended range to measure the array instability threshold (Weaver and El-Kashlan, 1981). The response of the rod bundle is obtained for increasing jet cross-flow velocity up to the onset of fluidelastic instability for each jet eccentricity.

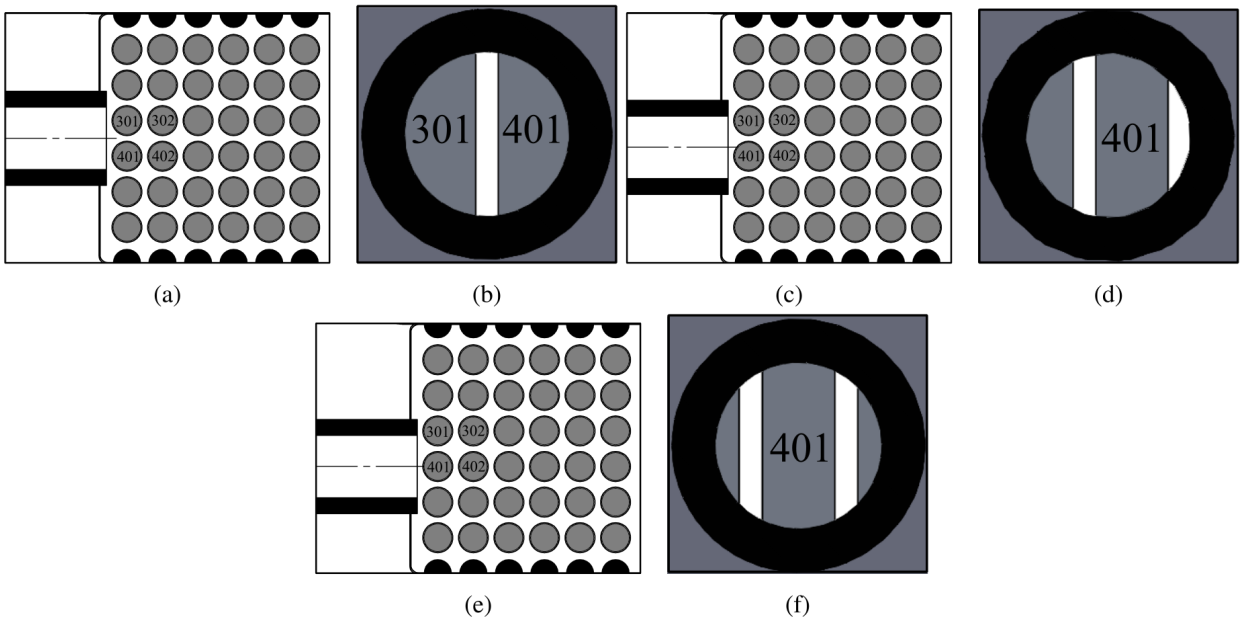

Figure 3.11 Top sectional views of rod array for three jet eccentricities (a) ξ=0, (b) ξ=0.25P, and (c) ξ=0.5P and (e), (f) and (g) corresponding projected views from the nozzle, respectively.

3.3 Test results

The fully flexible 6x6 rod bundle is tested with the circular jet cross-flow to investigate the effect of jet eccentricity on the stability behavior in the stream-wise direction. Three eccentricities are investigated, $\xi = 0$, $0.25P$, and $0.5P$. Moreover, the effect of the stand-off distance on the rod bundle stability is investigated by changing the number of rows in the tested bundle.

3.3.1 Dynamic behavior of fully flexible 6x6 rod bundle in stream-wise direction

Dynamic behavior for jet eccentricity $\xi = 0$

The eight instrumented rods are installed in columns five and six in the middle rows of the bundle. The sampling frequency of the acquired strain signal is 1000 samples per second. Sequential images are captured at 100 frames per second for the same jet velocity to compare the responses obtained from the two measuring systems. The rod bundle is tested in the range of jet velocities 0.6 m/s to 2.0 m/s. The jet velocity is defined as the average velocity of flow from the nozzle. The RMS response from these eight rods is compared first with that obtained from image processing to verify the quality of the images. The rod tip RMS

response is expressed as a percentage of the inter-rod gap (g=P-D). Figure 3.12 shows the comparison between the RMS response from the image processing (dashed lines) and the strain gauge (solid lines). The maximum deviation between the two systems is less than one percent of the inter-rod gap (g) at the maximum vibration amplitude. In addition the response trend is predicted very well by the image tracking method.

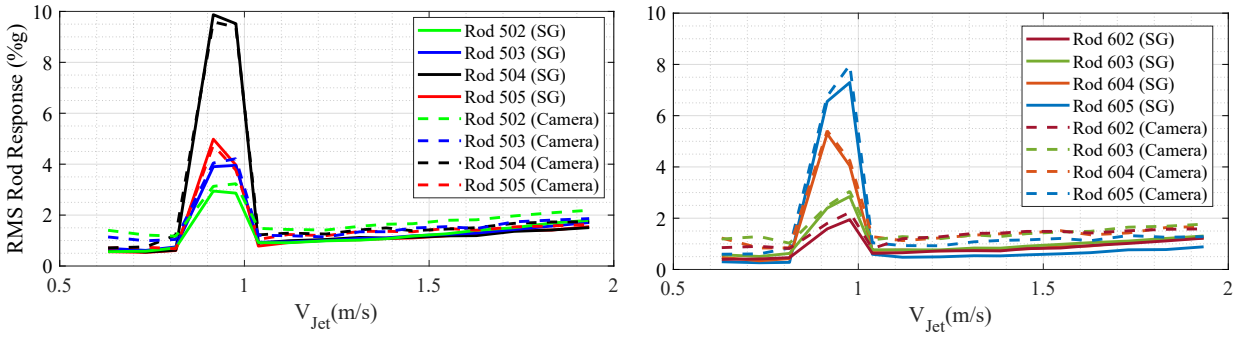

Figure 3.12 Comparison of obtained stream-wise response from strain gauge and high-speed camera at $\xi = 0$.

After verifying the high-speed camera results, the relationship between the RMS vibration amplitude and the jet flow velocity for each row in the bundle is illustrated in Figure 3.13. The rod bundle vibration sharply increases and subsequently decreases within a jet velocity range (0.82 to 1.05). This could be related to a vortex shedding phenomenon. The strong hydrodynamic coupling in this densely packed bundle leads to nearly identical response trends in the different rows. The second row response is the highest one in the bundle due to large static deflection in the stream-wise direction. Rod 301 also shows a second peak. The downstream rows from the jet flow vibrated with relatively lower amplitude than the first two rows. This is attributed to the entrainment process of the surrounding water into the jet flow while the jet penetrates further in the test section. However, the last row response increased slightly up to 13%g; this may be due to the vortex shedding generated in the wake of the rod bundle as observed computationally for the in-line 6x6 square tube array having a pitch-to-diameter ratio of 1.5 in uniform flow by Zhao et al. (2015). Figure 3.14 shows the response spectra for rod 301 at the first six velocities covering the response during the first peak. The rod frequency in still water is 12.25 Hz. The first frequency peak in Figure 3.14a corresponds to the rod frequency in water, however, the second frequency peak at 13.25 Hz, may be due to shear layer oscillations. The second frequency peak is still present for increasing jet flow velocity, up to 0.82 m/s. Above this velocity, lock-in occurs at a single frequency of 12.75 Hz. With increasing flow velocity, this single peak moves by 0.25 Hz with an increment of jet velocity of 0.06 m/s. A Strouhal number is calculated for this frequency

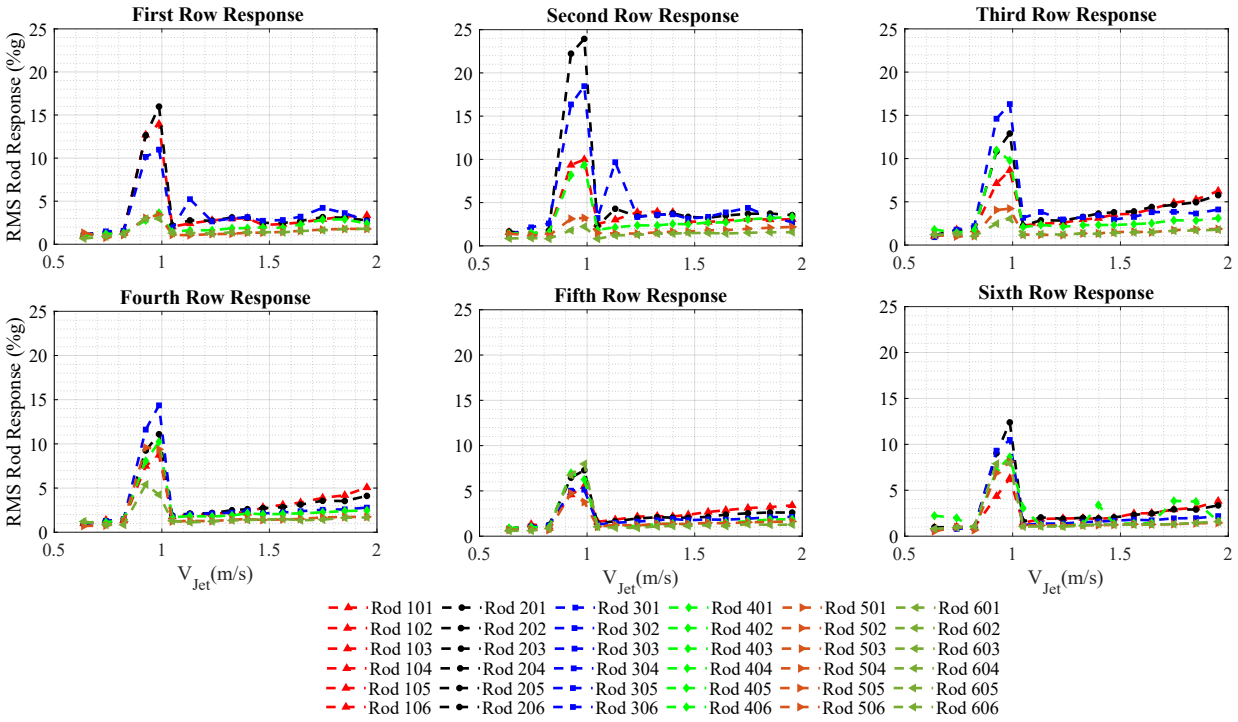

Figure 3.13 Rod bundle vibrations in stream-wise direction for 6x6 configuration at $\xi = 0$.

based on jet diameter (D_{Jet}) and the average jet velocity (V_{Jet}) as defined in the following equation:

$$Str_{Jet} = fD_{Jet}/V_{Jet} \tag{3.1}$$

The Strouhal number within the lock-in region is 0.33 ($Str_{Rod} = 0.15$). This value is close to the jet preferred excitation mode which occurs in the stream-wise direction. Boulanger et al. (1997) conducted experiments on PWR fuel rods with local jets injecting from small gaps (0.5 mm, 1 mm, 5 mm and 12 mm) having a height of 0.54 m. Early vibratory peaks were observed in the tested cases with the jets centred on the inter-rod gap ($\xi = 0$). The Strouhal numbers based on the fuel rod diameter were 0.24, 0.17, 0.26 for the jet widths = 0.5 mm, 1 mm, 5 mm, respectively.

The cross sectional area of flow passage is converted from circular (see Fig. 3.15a) at the nozzle exit to an approximately rectangular slot through the bundle as illustrated in Figure 3.15b, due to the proximity of the rod bundle to the nozzle and also the jet alignment with the rod bundle centerline. The injected jet flow through the narrow gap (3.5 mm) creates a shear flow layer bordering the surrounding fluid which leads to formation and breakup of vortex rings due to Kelvin–Helmholtz (K-H) instability as depicted schematically in Figure 3.15c. The first mode (varicose mode) of the jet vortex array contains symmetric vortices

as shown in Figure 3.15d. However, the second mode (sinuous mode) has non-symmetric vortices as shown in Figure 3.15e. The first mode, with symmetric vortex shedding, induces the stream-wise vibrations because the excitation force is in the flow direction.

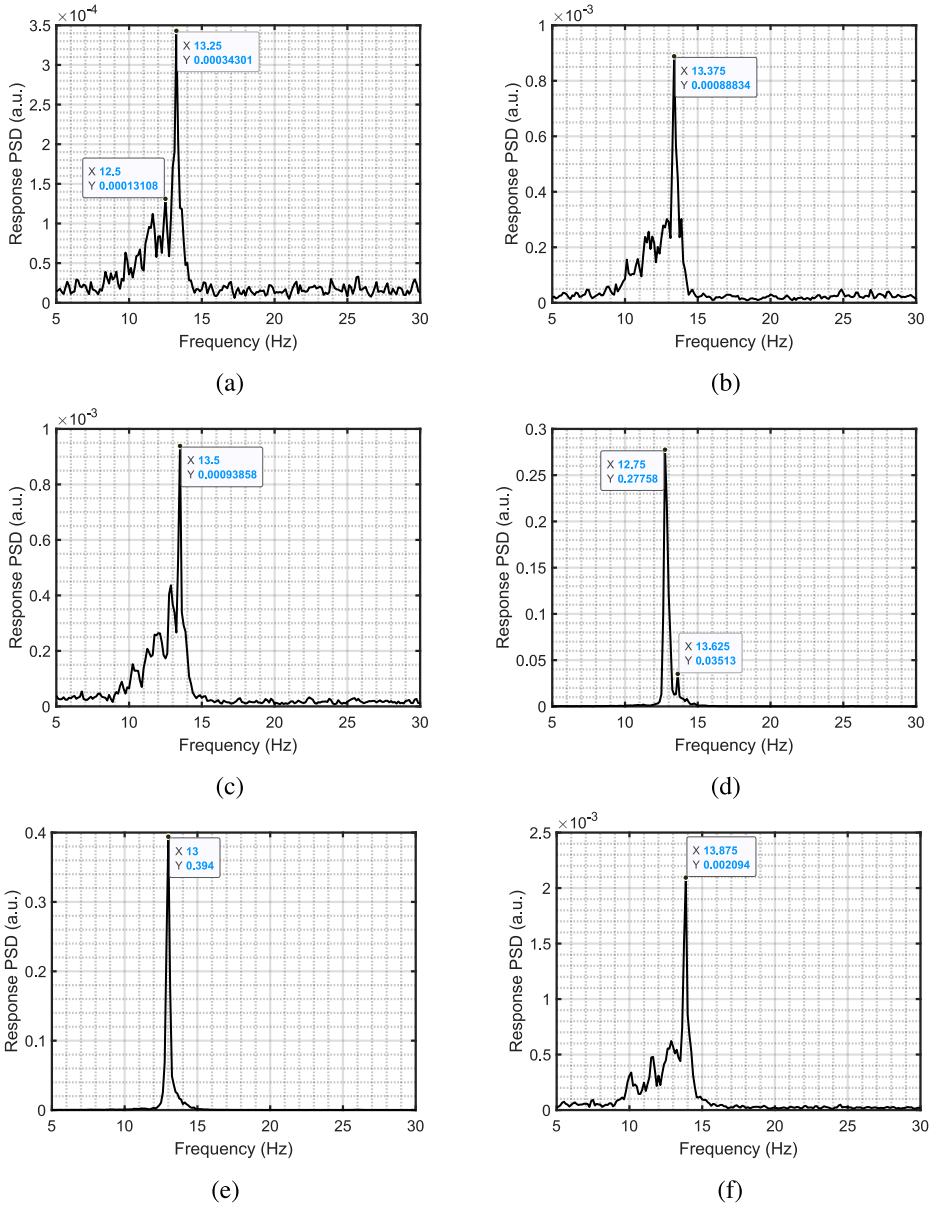

Figure 3.14 PSD plots showing the dynamical behaviors of rod 301 within the first six tested jet velocities: (a) $V_{Jet} = 0.63$ m/s , (b) $V_{Jet} = 0.73$ m/s, (c) $V_{Jet} = 0.82$ m/s, (d) $V_{Jet} = 0.92$ m/s, (e) $V_{Jet} = 0.98$ m/s, and (f) $V_{Jet} = 1.05$ m/s.

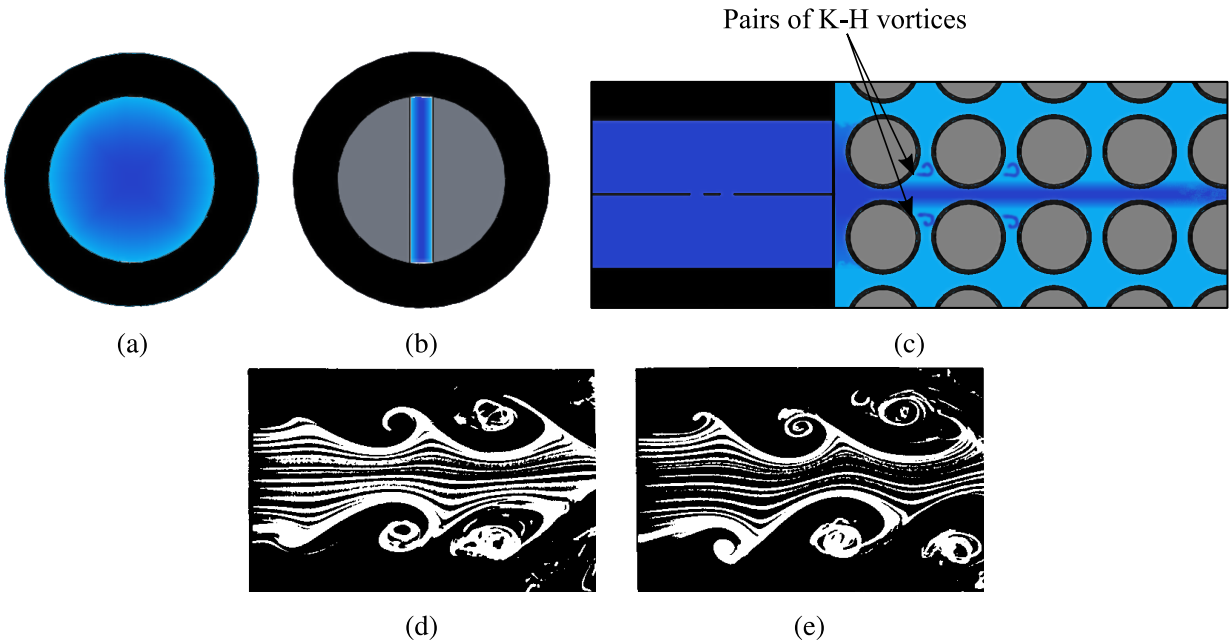

Figure 3.15 Schematic drawings for jet flow: (a) free jet flow inside the nozzle, (b) jet flow through the gap between rods 301 & 401, (c) top view of the centred jet flow through the bundle, (d) first mode (varicose mode) of jet vortex arrays (Huang and Hsiao, 1999), and (e) second mode (sinuous mode) of jet vortex arrays (Huang and Hsiao, 1999).

Dynamic behavior for jet eccentricity $\xi = 0.25P$

The jet flow is moved by $0.25P$ to study the effect of an asymmetric jet location on the rod bundle vibration. Figure 3.16 shows a comparison of the rod response obtained by the two measuring systems used in this study. The maximum deviation is $0.5\%g$ at the maximum vibration amplitude. Figure 3.17 shows the stream-wise vibrations for the six rows in the bundle. The vibration amplitude in this case increased gradually with the jet flow velocity. The magnitudes of these vibrations are of the order of $10\%g$. Based on the number of columns, the first half of the rod bundle has smaller vibrations than the downstream columns. This could be due to the asymmetric flow condition relative to the nozzle around rod 401 as shown in Figure 3.18, whereby one side of rod 401 would be exposed to a higher velocity than the other side which deflects the jet flow towards columns 5 & 6. This phenomenon is the well known *Coanda effect* or wall-attachment effect.

Our claim could be verified based on the response power spectral densities (PSDs) for two columns in each half of the rod bundle. Figures 3.19 and 3.20 show PSDs for rods in column number 3 and 5 in the first three rows, respectively. The PSD magnitude for column 5 rods is more than ten times higher than that for column 3 due to the jet flow switching to columns

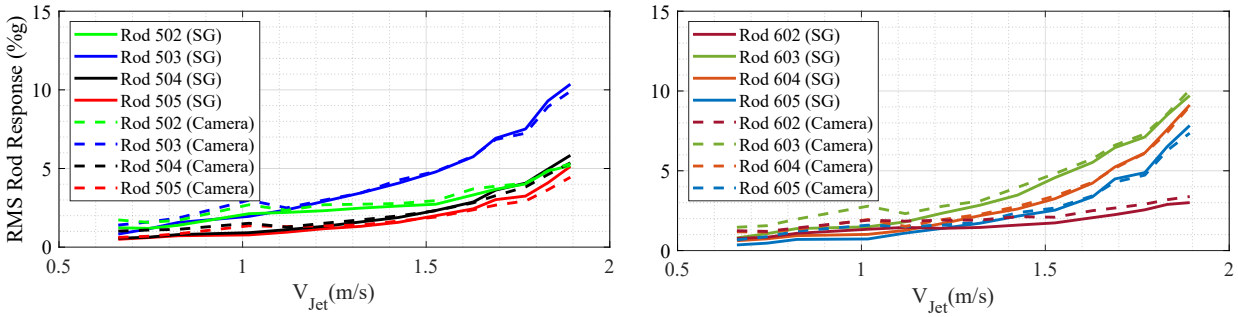

Figure 3.16 Comparison of obtained stream-wise response from strain gauge and high-speed camera at $\xi = 0.25P$.

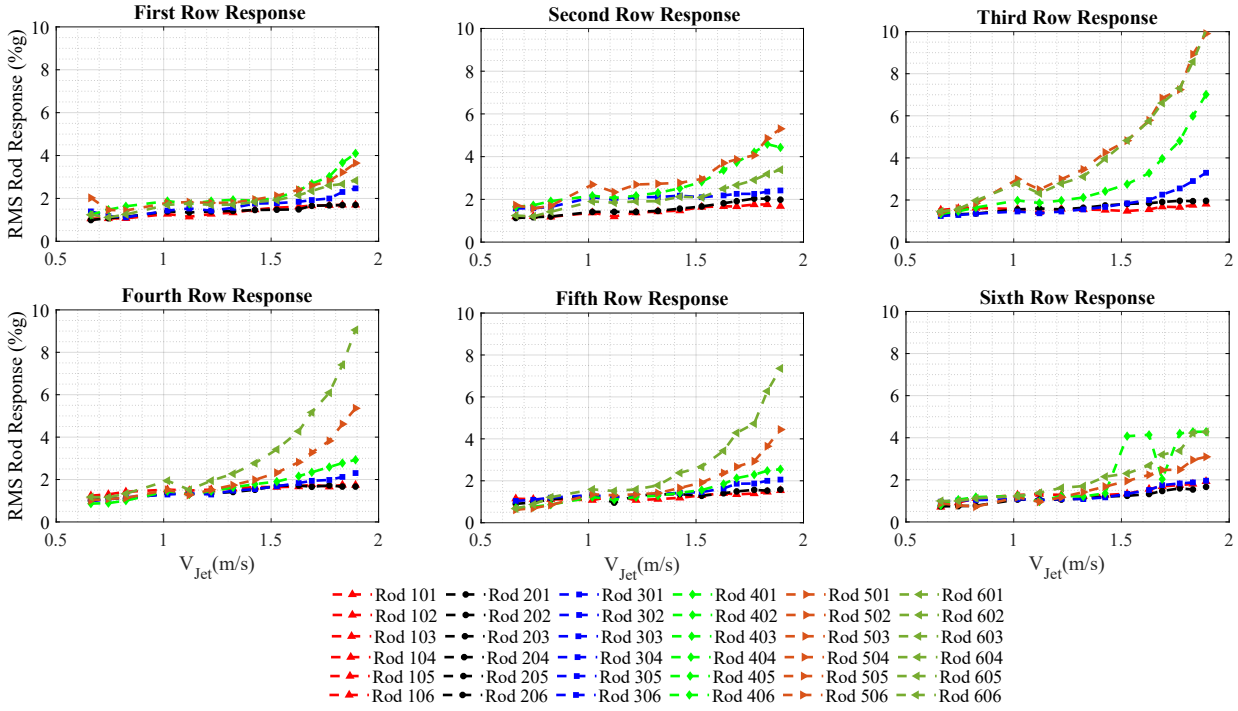

Figure 3.17 Rod bundle vibrations in stream-wise direction for 6x6 configuration at $\xi = 0.25P$.

4, 5 and 6 in the bundle. In addition, a wider bandwidth of the frequency spectrum of rod response in column number 3 could be caused by higher turbulence intensity at the jet flow boundary located near this column.

To conclude, the excitation for this configuration ($\xi = 0.25P$) is attributed to turbulence-induced vibrations because of the measured wide band power spectral densities (PSDs) of the rod bundle vibration. The turbulence is generated in the bundle by the asymmetric condition relative to the nozzle as shown in Figure 3.18; the presence of the two rods 301 and

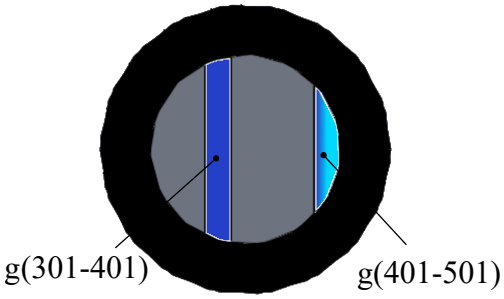

Figure 3.18 Schematic drawing for flow paths in the bundle at $\xi = 0.25P$.

401 which are not symmetric with the nozzle splits the main flow into two different streams through the two gaps.

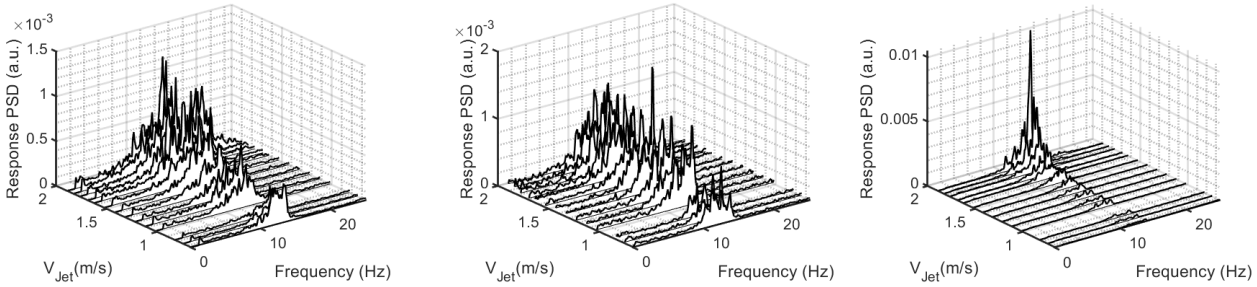

(a) (b) (c)

Figure 3.19 3D PSD plots showing the dynamical behaviors of rods: (a) rod 301, (b) rod 302 and (c) rod 303 at ξ=0.25P, respectively.

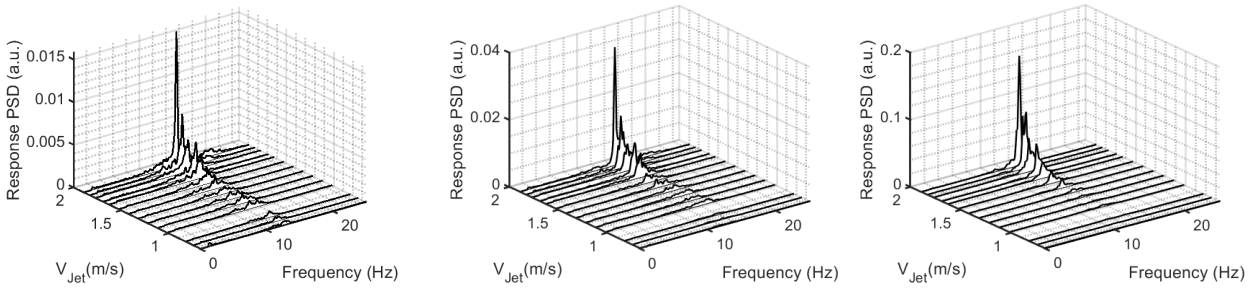

(a) (b) (c)

Figure 3.20 3D PSD plots showing the dynamical behaviors of rods: (a) rod 501, (b) rod 502 and (c) rod 503 at ξ=0.25P, respectively.

Dynamic behavior for jet eccentricity $\xi = 0.5P$

FIV tests are performed with the jet flow aligned with the rod centerline by moving the nozzle towards rod 401. Figure 3.21 shows a comparison of the vibration responses for the two measurement methods. The maximum deviation is $0.5\%g$ at the maximum vibration amplitude. The rod bundle vibrations are plotted in Figure 3.22. The vibration amplitudes in this case, increase gradually with jet flow velocity up to $V_{Jet} = 1.8$ m/s. The flow turbulence is the dominant excitation mechanism for this velocity range. For $V_{Jet} > 1.8$ m/s, the rate of change suddenly increases resulting in high vibration amplitudes, and indicating fluidelastic instability.

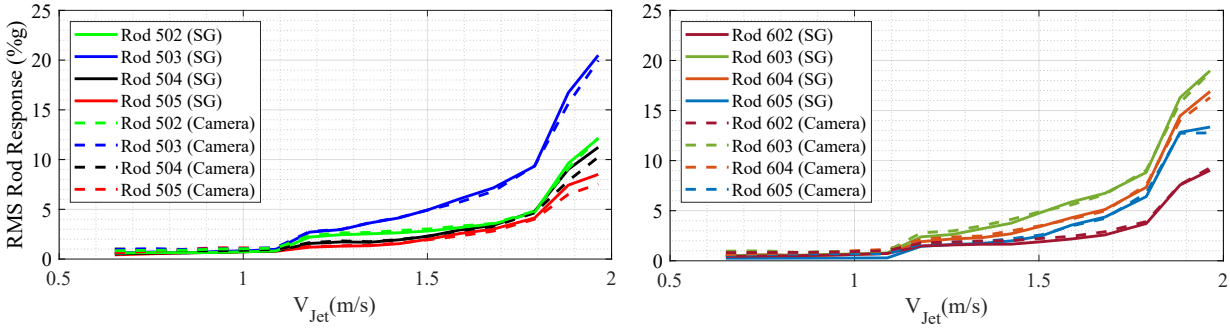

Figure 3.21 Comparison of obtained stream-wise response from strain gauge and high-speed camera at $\xi = 0.5P$.

The cross sectional area of the flow passage changes from circular at the nozzle exit to two symmetric slots through the bundle as illustrated in Figure 3.23a, due to the alignment the jet flow with the rod 401 centerline. As a result, this case features a jet flow configuration that is similar to that of two parallel jets. Wang et al. (2016) performed particle image velocimetry measurements of the water jet flow emanating from two parallel slots. The slots had dimensions close to our setup; the slot width (a) was 5.8 mm and the spacing between the two jets was 17.8 mm, which corresponds to the pitch of 14.4 mm in the tested bundle. Figure 3.23b shows the PIV results for a jet velocity of 0.75 m/s. The injected jet flow from the two gaps created three main flow regions; converging (flow A and B in Figure 3.23b), merging (flow C in Figure 3.23b) and combined regions. The converging region extends from the jet's exit point and ends at the merging point as illustrated in Figure 3.23b. The two jets approach each other within the merging region, and beyond this region ($y/a > 12.3$), the jets behave as a single combined jet. The jets are deflected and a recirculating zone is generated due to the convergence of the two jets in the converging region. Moreover, the minimum flow velocity is located inside the recirculating region. The first two rows in the bundle are

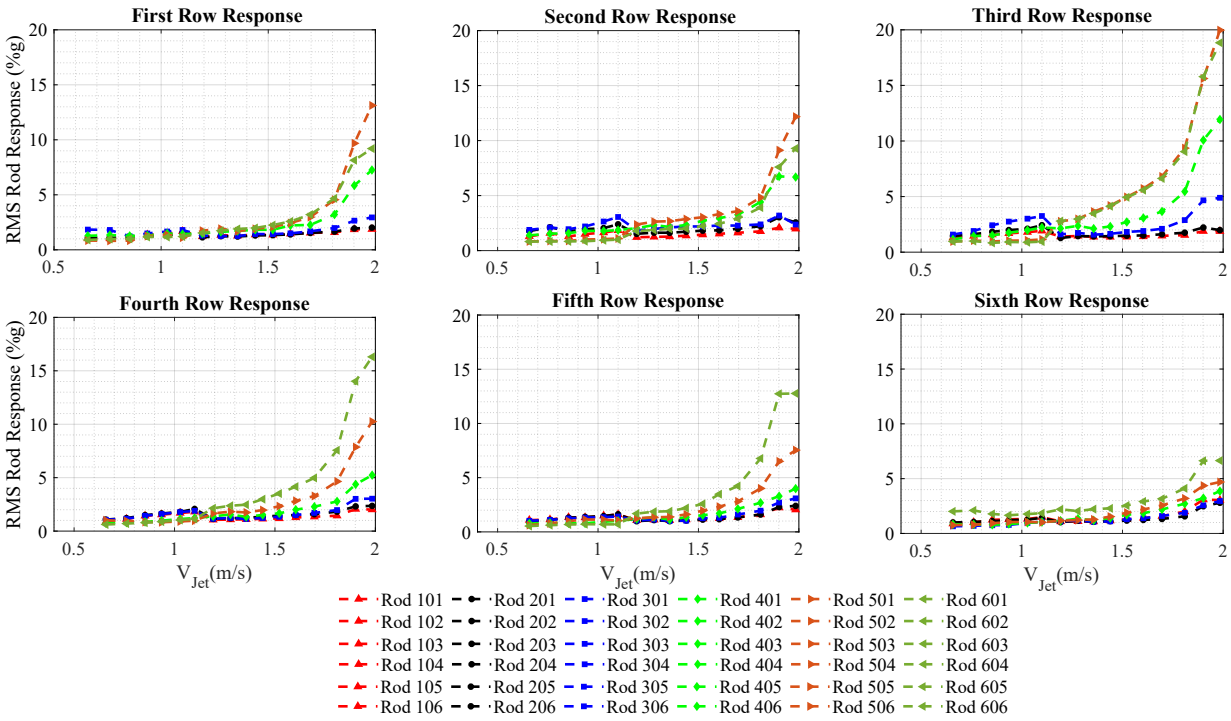

Figure 3.22 Rod bundle vibrations in stream-wise direction for 6x6 configuration at $\xi = 0.5P$.

located in the recirculating region and and as a result the response for these rows is lower than that in the third row which is located in the combined flow zone. Plotting the power

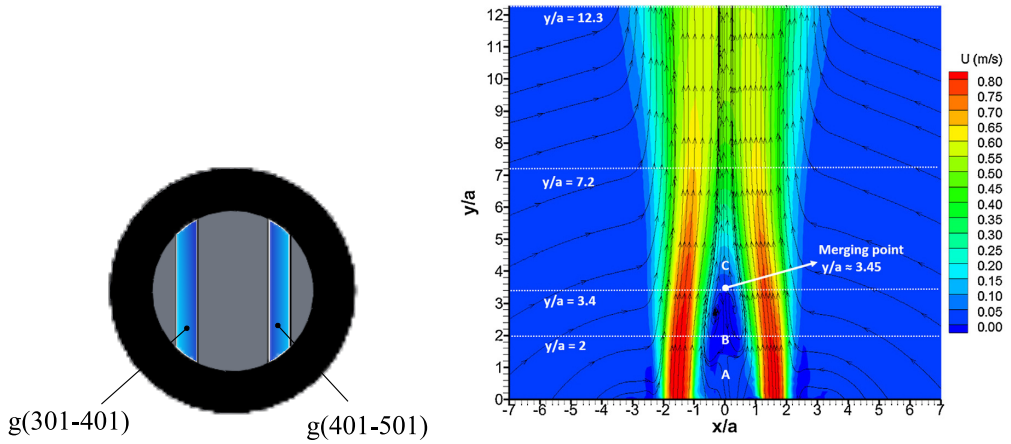

(a) (b)

Figure 3.23 (a) Schematic drawing for flow paths in the bundle at $\xi = 0.5P$, and (b) PIV measurements for two parallel jets (Wang et al., 2016).

spectrum densities for rods 401, 402, and 403, which reflect the dynamics of rods located in either the recirculating or combined regions, supports our arguments for this aligned jet-rod

case. Figures 3.24a, 3.24b and 3.24c show the power spectral density (PSD) plots for the rods 401, 402, 403, respectively. It is seen from these figures that for higher velocities there are two dominant frequencies; 14 and 20.5 Hz in the first two rows. The 20.5 Hz frequency, however, disappears when the rod is located further downstream in the third row due to the presence of two rods (401 and 402) in the recirculating zone. This confirms our claim that the rod 403 has a higher PSD amplitude than the other two rods because of the merging of the two plane jets at that location in the bundle where the instability occurred.

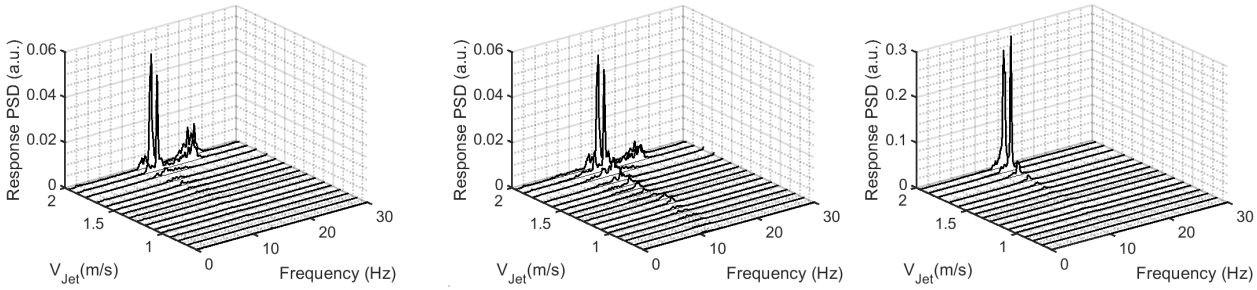

Figure 3.24 3D PSD plots showing the dynamical behaviors of rods: (a) rods 401, (b) 402 and (c) 403 at ξ=0.5P, respectively.

3.3.2 Stability effect of stand-off distance on fully flexible 6x5 rod bundle

The stability effect of the standoff distance on the stream-wise rod bundle vibrations was also investigated. This was done by removing the first row of rods to increase the standoff distance from 0.138 in. to 0.706 inches. The 6x5 rod bundle was tested with the jet eccentricity (ξ) equals to 0. The rod bundle vibration was obtained using a high speed camera with a speed resolution of 150 frames/sec. Figure 3.25 illustrates the relationship between the RMS displacement amplitude of the rod tip and the jet flow velocity for the five rows in the bundle. The dynamical behavior was obtained by increasing the jet flow velocity from a low value of 0.6 m/s until large amplitude of vibrations was observed. The first peak of vibration for this configuration which has a standoff distance of 0.706 in. occurs at a jet flow velocity of 1.2 m/s, whereas the first peak for the bundle having the shortest standoff distance (0.138 in.) occurred at 0.8 m/s (see Figure 3.13). The threshold of the first peak is higher because of the mixing and entrainment process that occurs for longer stand-off distance before the jet flow reaches the first row in the bundle, lowering the approach velocity. Furthermore, the second peak response initiated at 1.5 m/s reaching a maximum RMS vibration amplitude of 20%g with a jet velocity increment of 0.1 m/s.

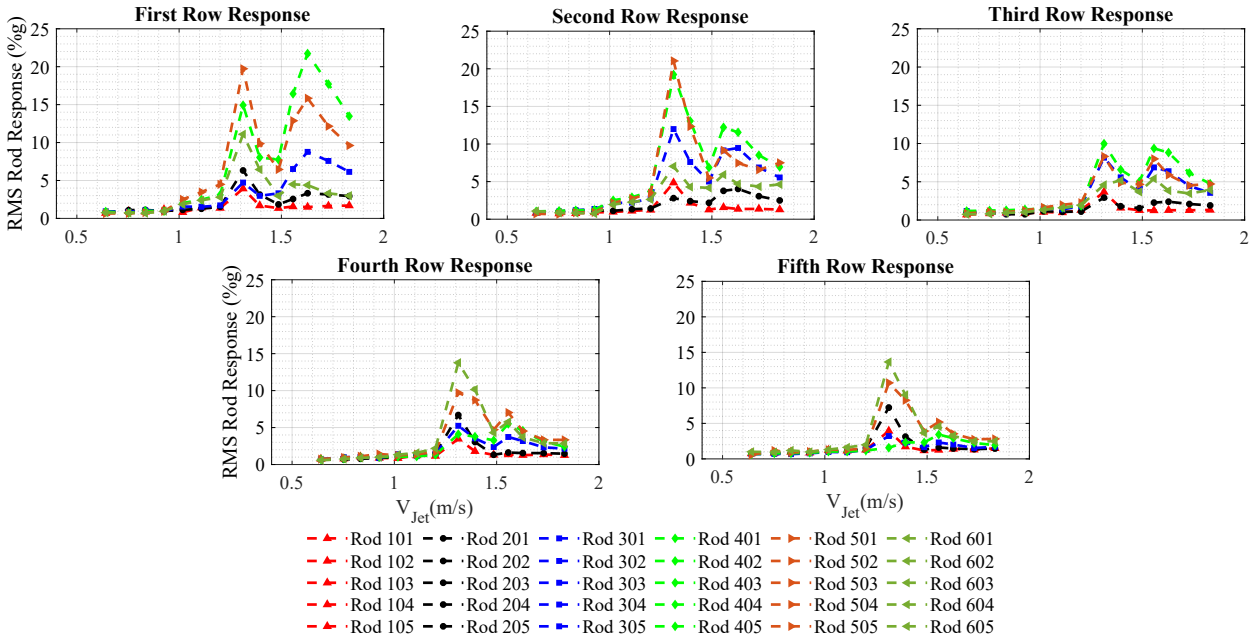

Figure 3.25 Rod bundle vibrations in stream-wise direction for 6x5 configuration at $\xi = 0$.

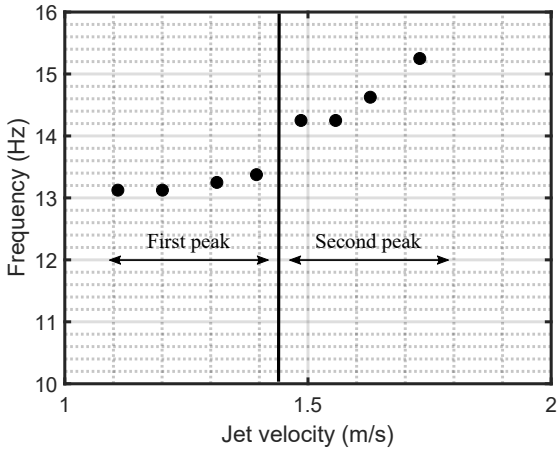

Figure 3.26 Dominant response frequencies obtained from the power spectral density versus jet velocity in the two peaks of vibrations regions for rod 401 at $\xi = 0$.

It is seen from Figure 3.26 that the vibration response can be divided into two regions: (i) V_{Jet} from 1.2 to 1.5 m/s and (ii) V_{Jet} from 1.5 to 1.87 m/s. The dominant frequency in the first region is almost constant at 13.25 Hz, which is consistent with what was found for tests with the shortest stand-off distance bundle. The similarity in the frequency value might be due to the lock-in phenomenon since the jet is squeezed through only one gap, at the rod

array centerline, generating stream-wise vortices. The average Strouhal number (Str_{Jet}) for the first peak is 0.265 which is very close to that observed by Crow and Champagne (1971) for the forcing frequency of jet flow which corresponds to a Strouhal number of 0.3. They found this particular frequency dominated the jet *preferred mode*. However, the second peak of vibrations shows a linear relation between jet velocity and frequency. The ratio corresponds to a Strouhal number (Str_{Jet}) of 0.22. da Silva and Metais (2002) analyzed the dominant Strouhal number for the vortex dynamics of the forced round jet with two types of forcing; flapping and variflap excitations. The latter is a combination of a varicose (axisymmetric) excitation and of a flapping excitation. They found two frequencies ($Str_{Jet} = 0.38$ and $Str_{Jet} = 0.19$), respectively, associated with the varicose and the flapping excitations. This could explain the observed response for the longer stand-off distance bundle. Thus, the second peak in the rod array vibration corresponds to a switched in the excitation mode from the varicose to the jet flapping excitation mode which occurs in the larger gap before the jet enters the rod bundle.

3.4 Discussion

The experimental results for the stream-wise vibrations showed that rod bundles subjected to jet cross-flow have resonant peaks at low jet velocities and unstable vibrations at relatively high jet velocities. The unstable vibrations that occurred in the jet-rod aligned case ($\xi = 0.5P$) resemble a fluidelastic instability phenomenon. The Strouhal numbers for the resonance vibrations vary according to the stand-off distance between the rod bundle and the jet. The Strouhal number is calculated based on jet diameter (D_{Jet}) and the average jet velocity (V_{Jet}) as defined in the following equation:

$$Str_{Jet} = fD_{Jet}/V_{Jet} \tag{3.2}$$

Figure 3.27 shows the effect of the stand-off distance (H) on the Strouhal numbers for the resonant peak at low jet velocities. At the stand-off distance of 0.138 in., Str_{Jet} is equal to 0.33. This value is close to that of the jet preferred excitation mode which acts in the stream-wise direction. However, for two new resonant peaks observed at longer stand-off distances, a Strouhal number of 0.265 for the first peak is found, while the second peak occurs at the Strouhal number $Str_{Jet} = 0.22$. It is possible that the two Strouhal numbers occur as a result of switching from one jet mode to another due to the large gap in this arrangement which allows for jet mode transitions.

From the FIV test for the jet-rod aligned case, the rod bundle undergoes instability at a

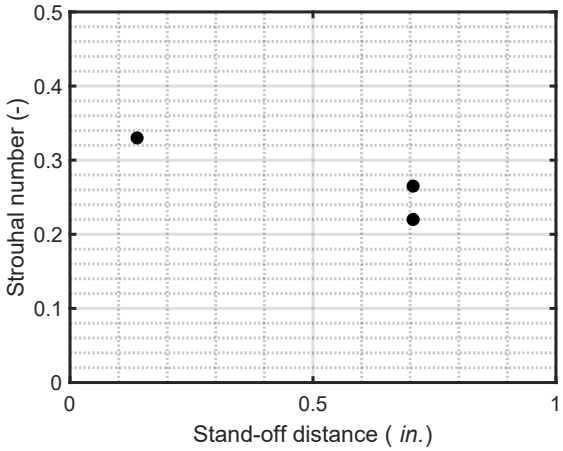

Figure 3.27 Strouhal number at the peak at low flow velocities with varying stand-off distance at $\xi = 0$.

critical jet velocity. Above this stability threshold, the fluid energy in the jet, which is proportional to the jet momentum, overcomes the energy dissipated by rod damping, resulting in high amplitude vibrations. The stability equation for the jet cross-flow, as previously stated by Seki et al. (1986) for baffle jetting, can be expressed by the following formula, which is derived similarly to the case of baffle jet (2D jet):

$$\rho A_{Jet} V_{Jet}^2 = K^2 f^2 D m l \delta_0 \tag{3.3}$$

where ρ = fluid density, A_{Jet} = cross-sectional area of the nozzle, V_{Jet} = average flow velocity discharge from the nozzle, K = stability constant, f = rod frequency in still water, D = rod diameter, m = rod mass per unit length including added mass of water, L = rod length and δ = logarithmic decrement. Equation 3.3 can be arranged in non-dimensional form as follows:

$$\frac{V_{Jet}}{fD} = K\sqrt{\frac{m\delta_0}{\rho D^2}\frac{D}{D_{Jet}}\frac{L}{D_{Jet}}} \tag{3.4}$$

A stability map is generated to identify the stability threshold as a function of four non-dimensional parameters; the reduced velocity (V_{Jet}/fD), the mass damping parameter ($m\delta_0/\rho D^2$), the reduced jet diameter (D/D_{Jet}) and the rod span to jet diameter ratio (L/D_{Jet}). The logarithmic decrement of damping is measured by performing a free decay test in water for a single flexible rod. The stability constant (K) in equation 3.4 is determined to be 12.34 for this case of $\xi = 0.5P$. For the other jet eccentricities ($\xi = 0$, $\xi = 0.25P$) tested the bundle was found to be fluidelastically stable in the jet velocity range tested.

3.5 Conclusions

Some PWR fuel bundles have encountered grid-to-rod fretting failure in the region of baffle plate LOCA holes. Investigating the excitation mechanisms of circular jet-induced vibrations of rod bundles is still a challenge in the field of fluid-structure interaction. This study aimed to understand rod bundle response to a circular jet flow and to determine the important parameters affecting the rod bundle vibrations. A specialized test facility was designed to investigate the stability effect of jet centerline offset from array centerline (jet eccentricity). A rod bundle with a LOCA hole that has a prototypical nuclear reactor geometry was used to evaluate the dynamical behaviour of the rod bundle.

Stream-wise rod bundle vibration was studied using asymmetric stiffness rods to identify the stability effect of jet eccentricity (ξ). The $\xi = 0$ case was also tested to investigate the effect of the stand-off distance between the first row and the exit flow from the nozzle. The experiments confirmed existence of two periodic phenomena. The first is attributed to a lock-in as found in uniform flow; the Strouhal number (Str_{Jet}) for this phenomenon corresponds to the jet preferred mode which means that small rod vibrations that occur at the beginning due to turbulence, provide feedback excitation to the varicose mode. The second periodicity may be due to the switch from the varicose to the jet flapping excitation mode.

The fluidelastic behavior of two rod bundles was also obtained using a high-speed camera and strain gauges. The stability effect of three jet flow eccentricities has been investigated. The experimental results showed that:

- Jet eccentricity significantly affects the dynamical behavior of the rod array.
- Turbulence-induced vibration is the dominant excitation mechanism for the case of $\xi = 0.25P$ due to the lowest RMS response, in addition to a wide band spectral response for this configuration.
- A lock-in phenomenon occurs when the jet is aligned with the rod bundle centerline. The occurrence of lock-in is attributed to the stream-wise vortex excitation from the jet flow.
- The dynamical behavior for $\xi = 0.5P$ is similar to fluidelastic instability in the uniform flow case. Above a specific jet velocity, the rod bundle vibrate sinusoidally with a frequency close to the rod natural frequency.

The longer term objective of this research is to determine the stability threshold for fluidelastic instability in fuel assemblies in proximity to LOCA holes that may occur during normal

operation. Stability maps have been obtained from FEI tests conducted on a unidirectionally stream-wise flexible rod bundle. Consequently, further experiments investigating transverse rod bundle vibration are needed to complete our findings and stability maps.

CHAPTER 4 ARTICLE 2: JET CROSS-FLOW INDUCED VIBRATIONS IN ROD BUNDLES. PART II: TRANSVERSE VIBRATION RESULTS AND EXCITATION MECHANISMS

Gad-el-Hak, I, Mureithi, N, Karazis, K, and Williams, G.

This article was submitted to "Nuclear Engineering and Design" on 23rd November 2021, it is accepted on 6th November 2022.

Summary

This chapter gives experimental data for rod bundle vibration due to jet cross-flow. The rod bundles, 6x6, 6x5, and 6x4, are tested under pure jet cross-flow having $D_{Jet}/D = 2.6$. Two jet flow parameters, stand-off distance (H) and jet eccentricity (ξ) are investigated to understand their stability effects on the stability boundaries of arrays. The rod arrays are flexible in the transverse direction to the jet flow. This work is performed to answer the research questions (**Q1**, **Q2**) and to achieve the objective (**O1**).

Graphical Abstract

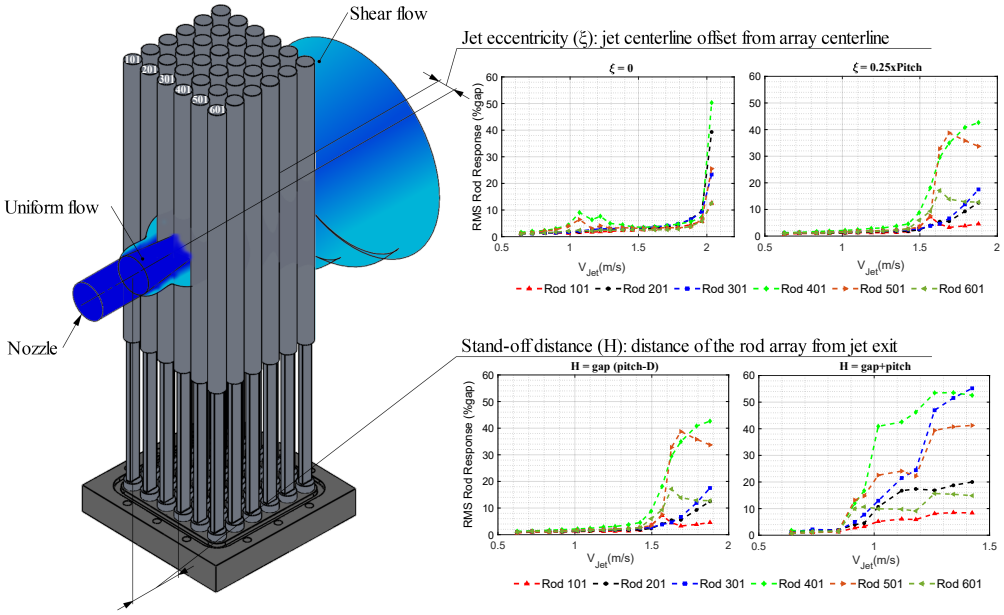

Abstract

Jet cross-flow in fuel assemblies has recently led to grid-to-rod fretting (GTRF) in reactors with fail-safe features, for the event of a loss of coolant accident (LOCA), including LOCA holes and slots. The findings in Part I of the paper showed that the stream-wise response behavior of the rod bundle was strongly dependent on the jet eccentricity and stand-off distance. These two parameters were defined to identify the location of the rod bundle centerline with respect to the jet centerline.

The experimental investigation was extended to identify the direction in which the instability is most critical. The present Part II of the paper discusses the effect of both jet eccentricity and stand-off distance on the stability of transverse rod bundle vibrations and the underlying excitation mechanisms. This is achieved by adjusting the flexible rods to vibrate in the direction normal to the jet flow. The results show that jet cross-flow causes fluidelastic instability in the transverse direction. The rod bundle vibration and instability depends strongly on the jet eccentricity. The transverse vibrations are more dominant than those in the stream-wise direction. The critical velocity decreases with increasing stand-off distance and then reverses. This stand-off distance behavior in the transverse direction is opposite of that found for stream-wise vibrations.

Keywords: PWR fuel rods, LOCA, Fluid-structure interaction, Jet cross-flow induced vibrations, Fluidelastic instability tests, Image processing.

4.1 Introduction

Grid-to-rod fretting (GTRF) is the dominant mechanism leading to fuel rod leakage in pressurized water reactors (PWRs) worldwide as reported by IAEA on fuel failures in water-cooled reactors (IAEA, 2015). The major root causes of these failures have been identified as deficient fuel rod support in the assembly due to improper design and/or fabrication defects, as well as fuel rod vibration caused by axial and cross flows in the assembly. The vibrations induced by cross-flow are usually more significant than those caused by axial flow. Rods in cross-flow reach fluidelastic instability (FEI) at a much lower velocity compared to those exposed to axial flow (Paidoussis, 1981). PWR Fuel rods are mainly subjected to external axial flow. However, some plants have fail-safe LOCA features where the flow is injected through LOCA holes and slots in the baffles that peripherally surround the core. Flow through the penetrations (LOCA Holes and slots) enters along a path perpendicular to fuel rods. This corresponds to jet cross-flows. The cross-flow interacts with axial flow producing a mixed flow or jet in transverse flow (JITF). The rods in peripheral assemblies, closet to the LOCA

holes/slots, may be subjected to pure jet cross-flow before the jet flow is deflected by axial flow. These rods may thus undergo fluidelastic instability in extreme cases which may lead to grid-to-rod fretting (GTRF) of the fuel rod. Furthermore, resonance oscillations may be caused by flow periodicities, due to jet and shear layer oscillations. LOCA holes and slots are proposed to discharge the high pressure generated in the barrel-baffle region in the case of LOCA event. Consequently, flow induced vibration analysis of the fuel assemblies can play a key role to ensure fuel reliability during normal operation and during any transient or accident events.

Fluidelastic behavior of tube arrays subjected to uniform cross-flow has been investigated by researchers for many years (Paidoussis et al., 2010, Price, 1995). The instability has been found to occur mostly in the direction transverse to the flow, depending also on tube array configuration, pitch-to-diameter ratio and number of flexible tubes in an array (Nakamura and Mureithi, 2017).

In Part I of this two-part paper, stream-wise fluidelastic instability was discussed. The measured vibration response of the rod array with jet eccentricity indicated the possibility of stream-wise fluidelastic instability for the jet-rod aligned case ($\xi = 0.5P$). However, the jet-gap aligned case ($\xi = 0$) showed a resonance behavior similar to vortex induced vibrations (VIV). For this reason, the transverse instability in jet cross-flow should also be studied for the same tested parameters, jet eccentricity and stand-off distance, as done for stream-wise direction. Figure 4.1 shows the key jet flow parameters. The jet-to-rod diameter ratio and jet location with respect to rod span are kept the same as in the stream-wise FIV tests in order to compare the stream-wise and transverse instability boundaries.

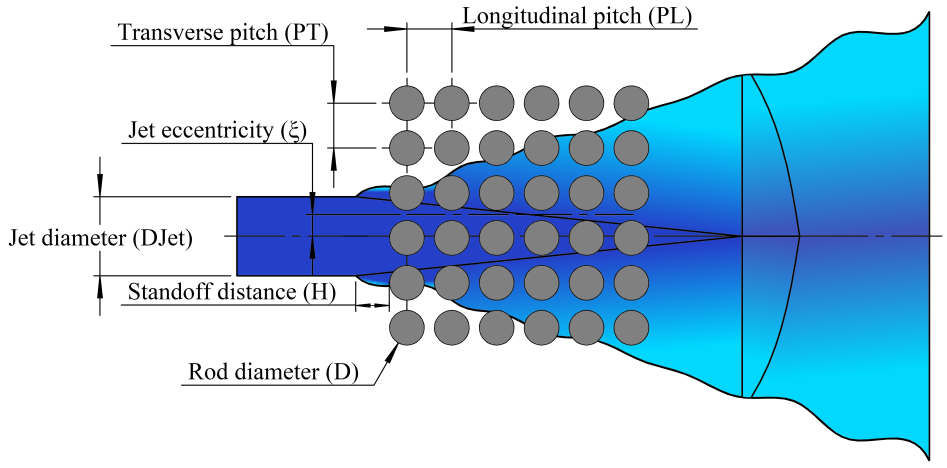

Figure 4.1 Jet flow parameters.

In contrast to the number of studies available in the literature that are dedicated to the fluidelastic instability of tube arrays subjected to uniform flow, only a few studies have been committed to the topic of instability induced by jet cross-flow injected from a small gap (2D jet). Fujita et al. (1990) tested a tube array subjected to a gap jet cross-flow and with axisymmetrically flexible tubes. A biaxial accelerometer was placed inside the tubes to detect the dominant vibration direction of the tube array. A single flexible tube became unstable in the stream-wise and transverse directions, while in the uniform flow case, the tube is dynamically stable. In addition, the dynamic behavior of single flexible tube was dependent on jet eccentricity. The jet-rod aligned case undergoes stream-wise instability without resonance vibration, whereas the jet-gap centered case exhibited a VIV lock-in phenomenon before instability, as found for stream-wise vibrations in Part I of our two-part paper series. Moreover, the dominant vibration direction was found to depend on the gap flow width; for a large gap width (uniform flow case), the tube array vibrated predominantly in the transverse direction whereas for small gap width (jet flow case), stream-wise vibration was more significant. To conclude, the jet cross-flow induced vibration behavior is more complex than in the uniform flow case. This is due to the circular jet flow added parameters including jet diameter, jet eccentricity, stand-off distance and injection point along the rod span.

In this second part of the paper, experimental results are reported which demonstrate the stability effects of jet eccentricity and stand-off distance on transverse rod bundle vibration. The requirement to evaluate the risk of fluidelastic instability excitations in PWR reactor fuel assemblies during normal operation prompted the extended research effort presented in Part II of our paper. The threshold for FEI in both directions is provided as the output from this research. The stability maps for jet cross-flow induced instability in a square rod bundle, simulating the fuel assembly in reactors, could be used as a guideline for designing reactor cores with LOCA holes.

4.2 Experimental setup and test parameters

4.2.1 Test loop set-up

The jet cross-flow induced vibration was investigated using a water tunnel. A 6x6 fully flexible rod bundle was fabricated from aluminum rods. The rods vibrate in one-degree with a fundamental frequency of 15 Hz in air. The fabricated rod bundle had the same dimensions of the fuel assemblies to make the experimental results more practical. The more detailed test section design for test loop was described in Part I. Figure 4.2 shows the main components of

the test loop used to investigate the fluidelastic behavior of the rod bundle with different jet parameters. The flow delivered from the pump is passed through a flow straightener (label 1) to filter any turbulence coming from pipe fittings. The next section accumulates the flow in an empty chamber (label 2) similar to the barrel-baffle region in the reactor pressure vessels. The flow streamline is squeezed through the nozzle (label 3) to form the jet flow which is directed to the flexible rod bundle (label 4).

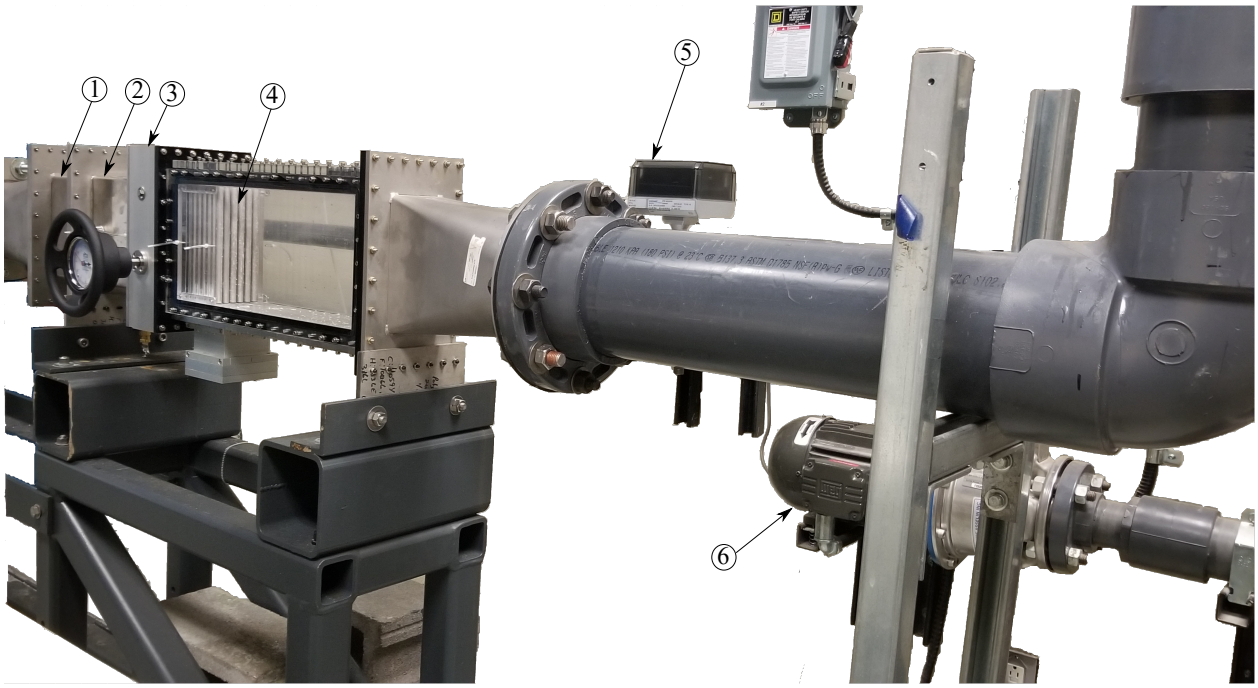

Figure 4.2 The main components of test loop set-up are labelled: (1) flow straightener, (2) barrel-baffle chamber, (3) displacement jet flow mechanism, (4) rod bundle, (5) water flow meter and (6) centrifugal pump.

4.2.2 Test parameters

Two jet flow parameters are studied; jet eccentricity (ξ) and jet standoff (H) distance. The rod bundle stability behavior is investigated for three jet eccentricities as follows:

- $\xi = 0$ corresponds to the jet flow aligned with the rod array, as shown in Figures 4.3a and 4.3b.
- $\xi = 0.25P$ corresponds to the jet flow offset by a quarter of spacing (P), as shown in Figures 4.3c and 4.3d.

- $\xi = 0.5P$ corresponds to the jet flow aligned with the rod centerline, as shown in Figures 4.3e and 4.3f.

The standoff distance is varied by removing a row of rods in the bundle to increase this distance. The response of the tested bundles is obtained by increasing the jet flow velocity up to the onset of fluidelastic instability for each jet eccentricity.

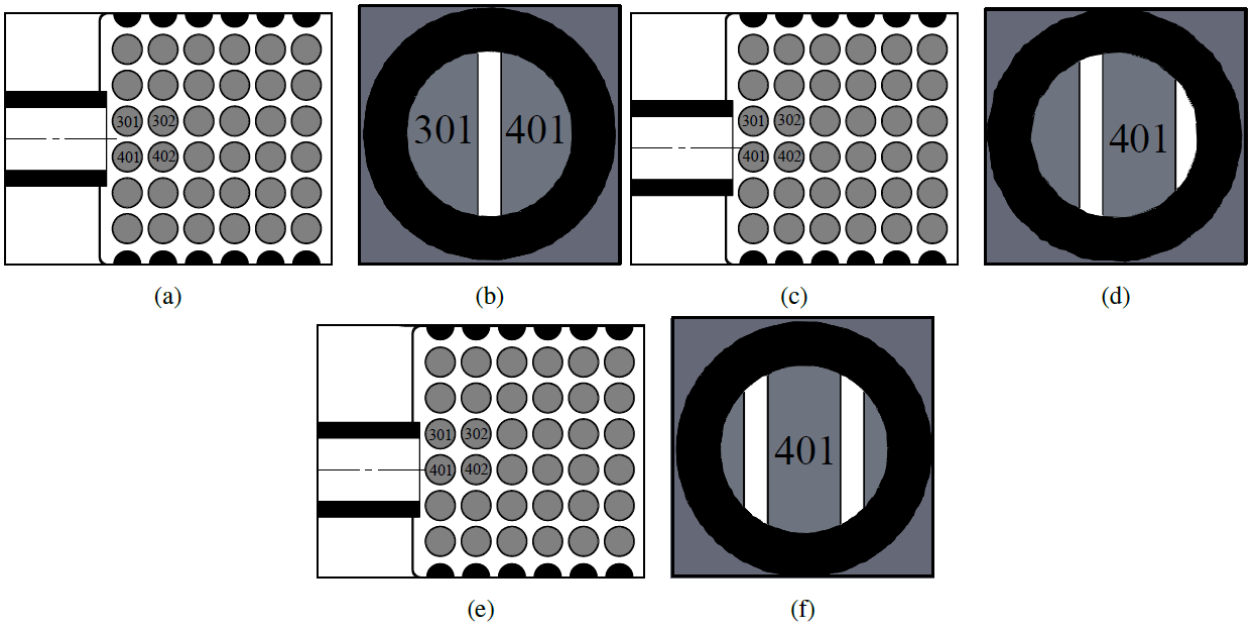

Figure 4.3 Top sectional views of rod array for three jet eccentricities (a) ξ=0, (b) ξ=0.25P, and (c) ξ=0.5P and (e), (f) and (g) corresponding projected views from the nozzle, respectively.

4.3 Test results

The 6x6 rod bundle is tested with the circular jet cross-flow to determine the effect of jet eccentricity on bundle response and stability in the transverse direction. Moreover, different rod bundles, 6x6, 6x5, and 6x4, were tested to evaluate the effect of the stand-off distance on rod bundle response and stability in the transverse direction. Each bundle was tested with the three aforementioned jet eccentricities.

4.3.1 Dynamic behavior of fully flexible 6x6 rod bundle in the transverse direction

The transverse direction dynamics of the fully flexible (6x6) rod bundle are presented in the following subsections. Results for the three jet eccentricities are compared. The rod bundle is tested in the same range of jet velocity as in stream-wise direction to identify the direction of dominant vibration.

Dynamic behavior for jet eccentricity $\xi = 0$

The eight strain-gauge instrumented rods are located in the first two rows in the middle of the bundle. The strain data serve as reference for comparison with the responses from the image processing. Verification of the high-speed camera results is presented in Figure 4.4. The maximum deviation in the response obtained from image processing (dashed lines) with that from strain gauges (solid lines) is less than 1.6 %g. The RMS vibration amplitudes of

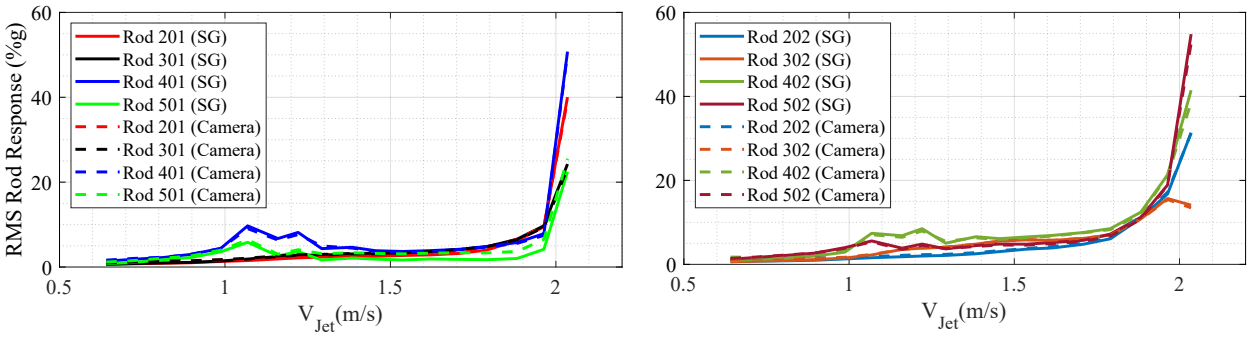

Figure 4.4 Comparison of obtained transverse response from strain gauge and high-speed camera at $\xi = 0$.

the 36 rods are obtained with increasing jet flow velocity as presented in Figure 4.5. The jet cross-flow induced vibrations are higher in the transverse direction (maximum amplitude of 55%g) compared with vibrations found in the stream-wise direction (maximum amplitude of 25%g). In addition the transverse vibrations are induced by instability at a high jet velocity in contrast to forced vibrations in the stream-wise direction. The first small peak (10%g) at low velocities near 1 m/s may come from the synchronization of the rod frequency with the periodicity in the jet flow as observed for stream-wise vibrations (see Part I) for the same jet eccentricity. However, the bundle becomes unstable at 2 m/s and the maximum vibration amplitude in the first three rows increases sharply to 55%g. Fluidelastic instability is confirmed by the sinusoidal motion and a corresponding sharp frequency peak at this

velocity as shown in Figure 4.6. The last three rows vibrate with relatively small amplitudes due to the decrease of jet momentum as the flow propagates through the bundle.

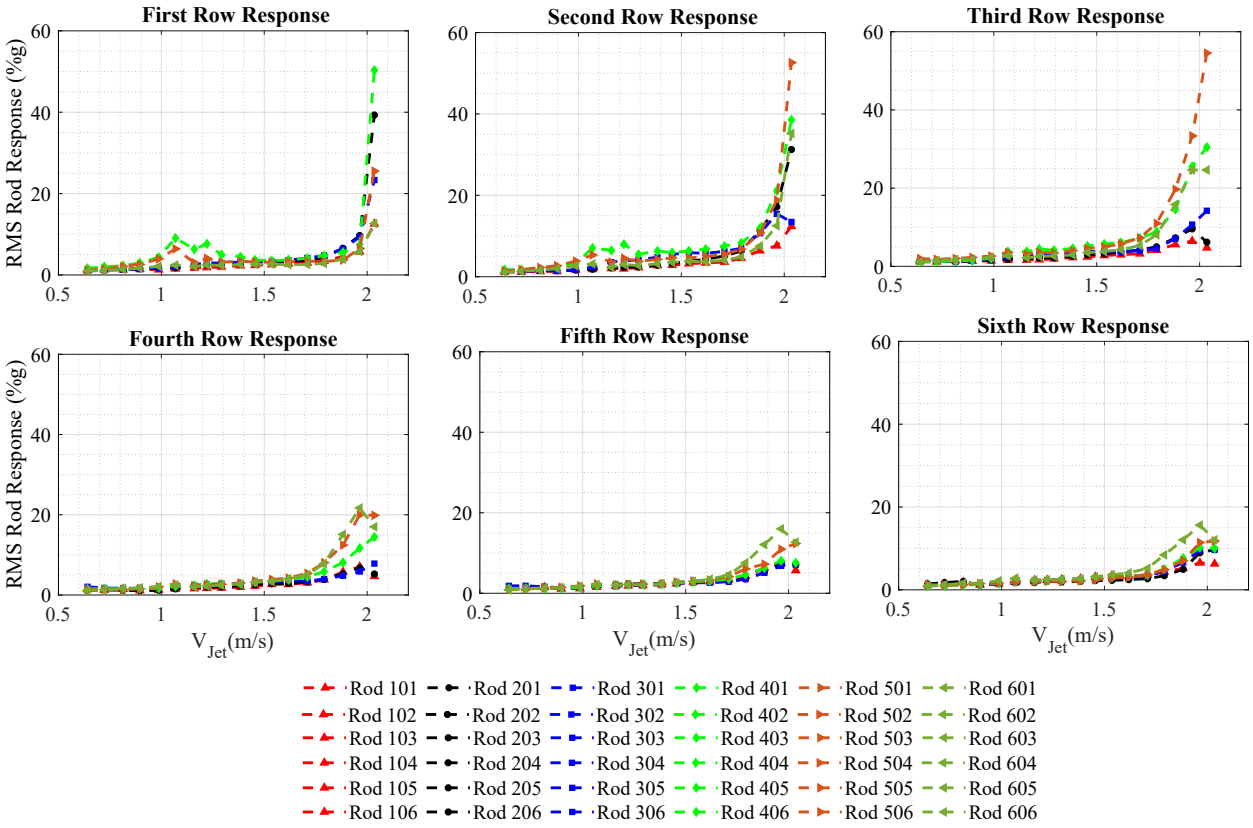

Figure 4.5 Rod bundle vibrations in transverse direction for 6x6 configuration at $\xi = 0$.

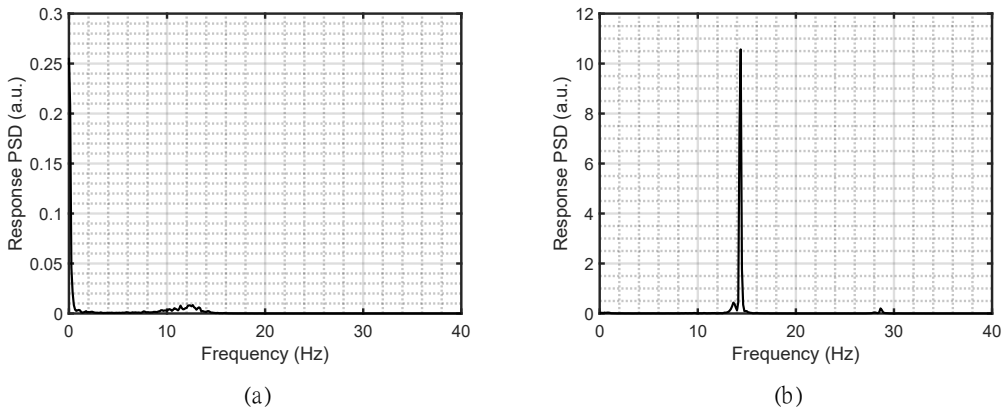

Figure 4.6 PSD plots showing the dynamical behaviors of rod 401 at two velocities: (a) 1.05 m/s, and (b) 2 m/s.

Dynamic behavior for jet eccentricity $\xi = 0.25P$

In this section, the asymmetric condition of jet velocity through the two gaps adjacent to column four is investigated by moving the nozzle $0.25P$. Figure 4.7 shows the vibrational behaviour for the 36 rods in the tested bundle. For this case, instability-induced large amplitude vibrations occurred at a lower jet velocity, $V_{Jet} = 1.5$ m/s, compared to that observed for $\xi = 0$. The destabilizing effect for this configuration could be attributed to the sensitivity of the lift forces generated around column number 4 because one side of rods experience higher velocities than the other side (see Part I) at static condition. As the rods vibrate, the asymmetric gap variation strongly influences the derivatives of the fluidelastic forces. The maximum response occurred in the first three rows in the bundle, reaching approximately $60\%g$. The bundle stability behavior could be divided into two regions: (i) V_{Jet} from 1.5 to 1.62 m/s and (ii) V_{Jet} from 1.68 to 1.87 m/s as shown in Figure 4.8. In the first region, the dominant frequency is 12.6 Hz which is approximately the natural frequency of a single flexible rod in the bundle. In addition, small peaks observed in the first two rows, come from some flow periodicity which is generated near the jet flow. However, these peaks disappear in the third row due to developing flow as shown in Figure 4.8. In the second region, the rods vibrate with a higher frequency near 14.375 Hz for the three rods 401, 402, and 403. The increase in frequency is due to a fluid-added stiffness (K_f) effect at higher flow velocities in these very confined gaps (0.138 in.) as shown in the coupled equations of motion (Equation 4.1). The matrix $[K_f]$ terms come from derivatives of the lift coefficient with rod displacement.

$$[M_s + M_f]\ddot{\vec{y}}(t) + [C_s + C_f]\dot{\vec{y}}(t) + [K_s + K_f]\vec{y}(t) = 0; \quad \vec{y} = [y_1, y_2...., y_k]^T \tag{4.1}$$

where y is the transverse rod displacement, $[M_f]$, $[C_f]$, $[K_f]$ are the added-mass, added-damping and added-stiffness matrices of the fluid, respectively. $[M_s]$, $[C_s]$, $[K_s]$ are the mass, damping, and stiffness matrices of the structure, respectively. A quasi-static approximation of the fluid lift force (per unit area) acting on a rod (i) may be expressed in the approximate linear form:

$$F_{y_{ii}} = \frac{1}{2}{V_{Jet}}^2 \left[C_{L_{i0}} + \frac{\partial C_{Li}}{\partial y_i} y_i \right] \tag{4.2}$$

where C_L is the lift force coefficient. The resulting fluid-added stiffness is:

$$K_{f_{ii}} = -\frac{1}{2} V_{Jet}^2 \frac{\partial C_{Li}}{\partial y_i} y_i \tag{4.3}$$

Test results reported by Price and Paidoussis (1986) show that $\frac{\partial C_{Li}}{\partial y_i} < 0$ for a square geometry tube array in uniform flow. This implies a positive fluid-added stiffness proportional to jet flow velocity (squared). A similar stiffness effect seems reasonable for the jet-array system although the exact fluid-stiffness value would be expected to be different.

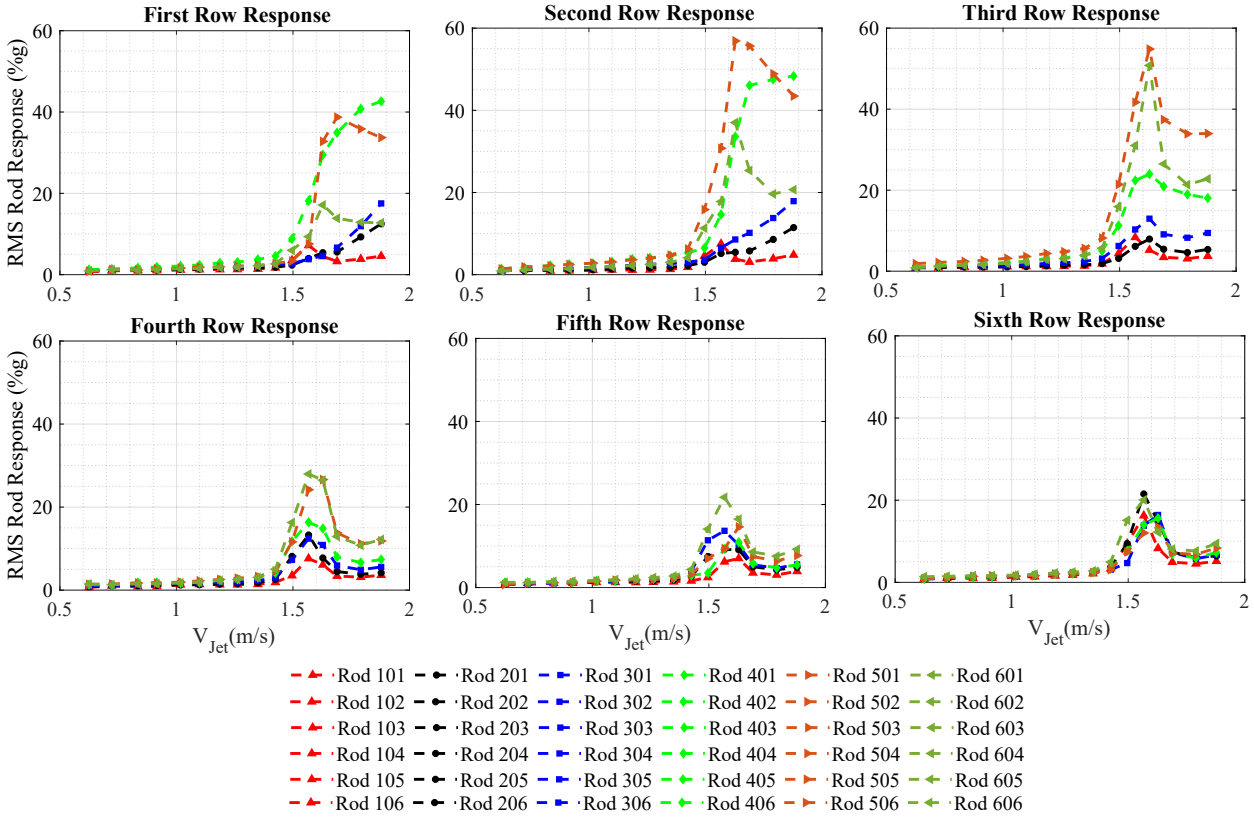

Figure 4.7 Rod bundle vibrations in transverse direction for 6x6 configuration at $\xi = 0.25P$.

Dynamic behavior for jet eccentricity $\xi = 0.5P$

The fluidelastic behavior of the bundle is also investigated when the jet is located at the centerline of rod 401. The rod bundle vibration is presented for each row in Figure 4.9. Large amplitude vibrations started at $V_{Jet} = 1.62$ m/s. However, the response does not increase sharply with jet velocity in the first two rows because of the proximity of these rows to the jet centerline, which is exposed to larger jet momentum (inducing drag). On the other hand, the RMS displacement amplitude increases abruptly in the third and fourth rows at the critical jet velocity of 1.62 m/s. Rod 402 vibrates with lower amplitude than rod 401 due to its location in the second row (the recirculating zone of two parallel jets as shown in Part I). The flow-induced vibrations could be divided into two types for: (i) V_{Jet}

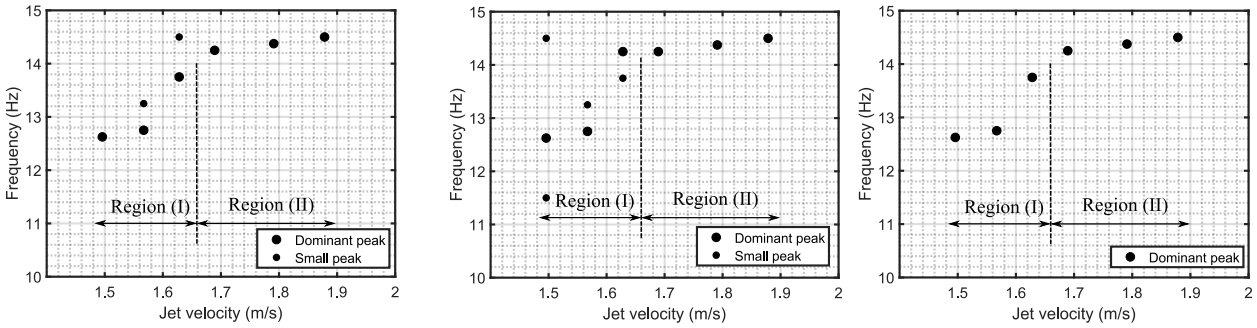

Figure 4.8 Dominant response frequencies obtained from the power spectral density functions versus jet velocity in the instability-induced vibrations region for three rods: (a) rod 401, (b) rod 402, and (c) rod 403.

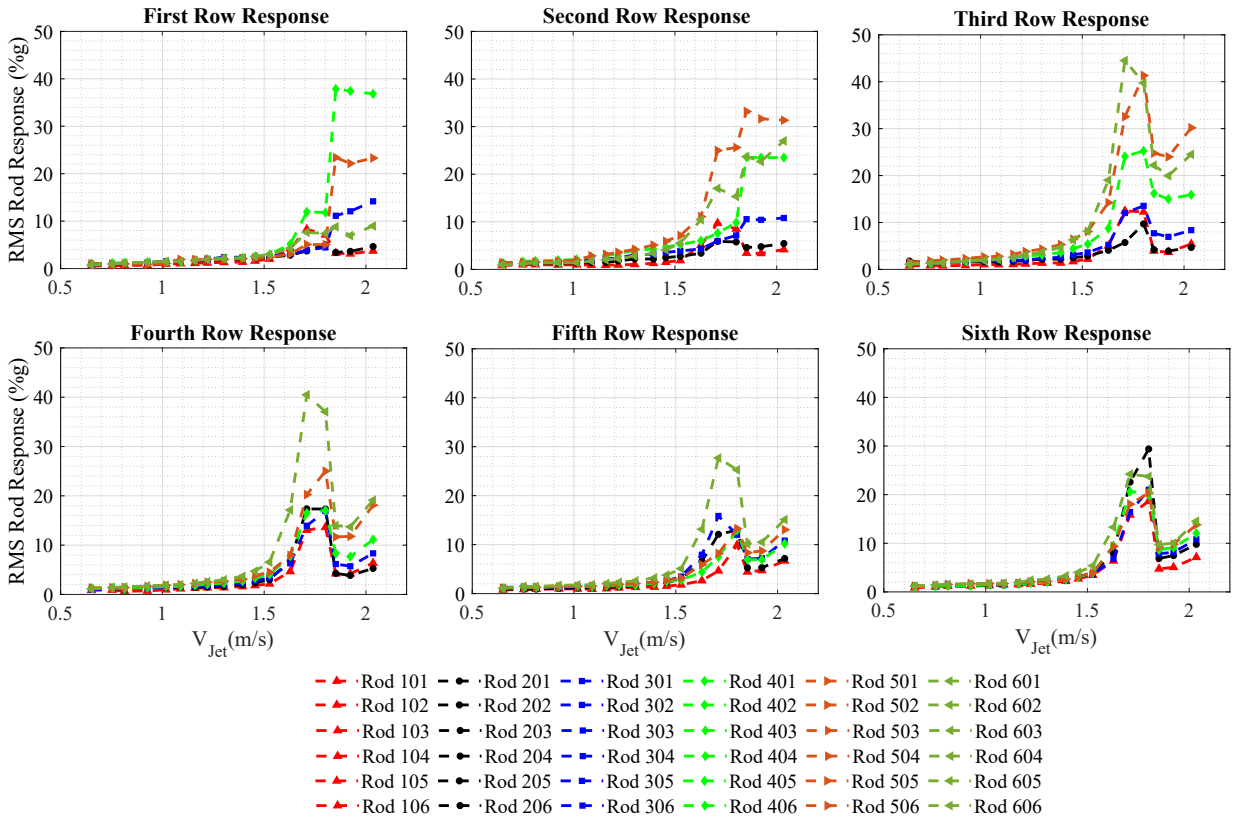

Figure 4.9 Rod bundle vibrations in transverse direction for 6x6 configuration at $\xi = 0.5P$.

from 1.62 to 1.8 m/s and (*ii*) V_{Jet} from 1.85 to 2.04 m/s. In the first range of velocities, the dominant vibration occurred firstly at 12.625 Hz which is the rod frequency without added

stiffness from the jet flow. In addition, small peaks that appeared in the dynamics of rod 402 as shown in Figure 4.10b, may be due to shear layer oscillations which are generated from disturbance of the jet flow by rod 401. However, these peaks are not found for the adjacent rod in the same row; rod 502 as shown in Figure 4.10c. Rod 403 in the third row vibrated with one dominant frequency around the rod natural frequency which is why the third row response is more significant. In the second region where rod responses are obtained in the jet velocity range of 1.85 to 2.04 m/s, the rod frequency goes up from 12.6 to 15.9 Hz by the effect of added stiffness from fluid flow. As result, the response amplitude is decreased at the switching point in the last four rows as illustrated in Figure 4.9. The response in these rows then increases slightly with jet velocity by a mechanism similar to vortex-induced vibrations as inferred from the response PSDs. A small peak having a lower frequency near 13.75 Hz accompanied the dominant rod frequency as shown in Figure 4.10d. The downstream rows may be excited due to the vorticity originating from the upstream vibrating tubes because of the jet centerline aligned with column number 4. While the vibrations of the middle four rods in the two rows nearest to jet flow are maintained and a single peak is clearly presented in this range, it seems that fluidelastic instability is the dominant excitation mechanism for the first two rows. To summarize, the excitation mechanism of jet flow varies from row to row and apparently from rod to rod within the same row.

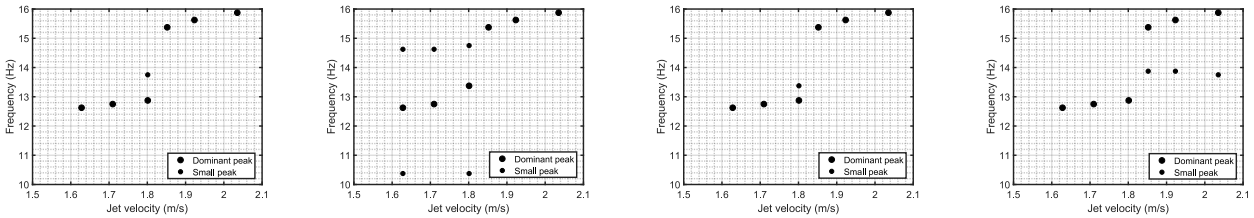

Figure 4.10 Dominant response frequencies obtained from the power spectral density functions versus jet velocity in the instability-induced vibrations region for four rods: (a) rod 401, (b) rod 402, (c) rod 502 and (d) 403 at $\xi = 0.5P$.

4.3.2 Dynamic behavior of fully flexible 6x5 rod bundle in transverse direction

The comparison between stream-wise and transverse vibrations occurring in a fully flexible 6x6 bundle with the tested jet eccentricities highlighted the importance of investigating the stability effect of standoff distance on the transverse vibrations. This is achieved by removing the first row to increase the standoff distance from 0.138 in. to 0.706 in. and testing the 6x5

rod bundle with the three jet eccentricities ($\xi = 0$, $0.25P$ and $0.5P$).

Dynamic behavior for jet eccentricity $\xi = 0$

Figure 4.11 shows the relationship between the RMS displacement amplitude of the rod tip and the jet flow velocity for the five rows in the rod bundle. FEI behavior is obtained by increasing jet flow velocity from a low value of 0.6 m/s as in the 6x6 rod bundle until the onset of fluidelastic instability. The onset of FEI for this configuration, which has a standoff distance of 0.706 in., occurs at a jet flow velocity of 1.24 m/s, whereas the onset for the bundle having the shortest standoff distance (0.138 in.) occurred at approximately twice this jet flow velocity (2 m/s). Furthermore, the instability of this bundle is violent and reaches maximum RMS vibration amplitude of 60%g from 5%g for a jet velocity increment of 0.08 m/s. This behavior is more destructive than that attained in the experiments using the shortest standoff distance (see Figure 4.5). Two excitation mechanisms control the vibration

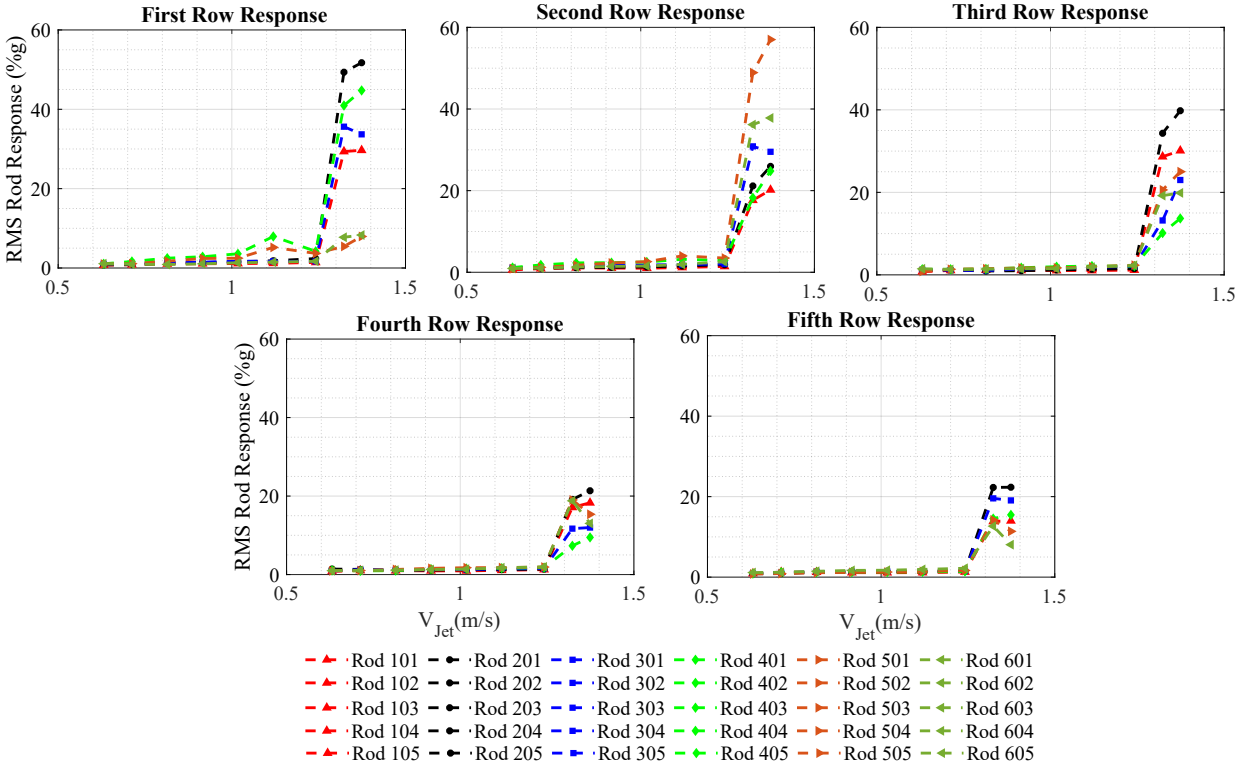

Figure 4.11 Rod bundle vibrations in transverse direction for 6x5 configuration at $\xi = 0$.

in this bundle; turbulence excitation at low jet velocities and fluidelastic instability above 1.24 m/s. Increasing the gap between the nozzle and the first row has two contradictory effects on generated fluid forces; the average jet velocity is decreased by mixing process

with the surrounding fluid while on the other hand, the projected area from the jet profile is enlarged with increasing standoff distance. Crow and Champagne (1971) observed that introducing perturbations at specific frequencies excites the large eddies in a round jet which increases the mixing rate and thus entrains more fluid from the surrounding fluid. However, the projected area on the exposed rods is not constant during FEI because it is function of the amplitude and frequency of the rod bundle vibration. When the rods start to vibrate, the jet cross-section is amplified as shown in Figure 4.12. Thus, a larger portion of the rods is exposed to fluid forces. This amplification mechanism of the excited jet could be responsible for the reduction in the critical jet velocity to almost half of that obtained with the shortest standoff distance.

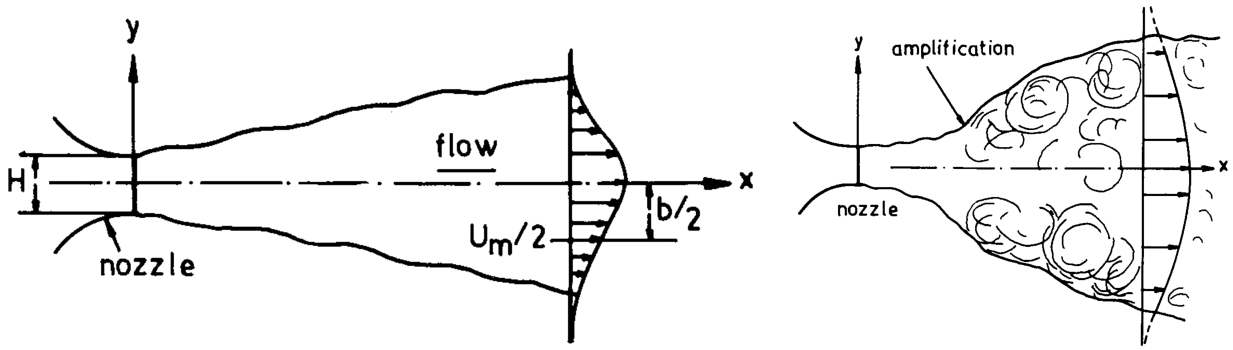

(a) (b)

Figure 4.12 (a) steady jet, (b) excited jet, (Narayanan, 1988).

Dynamic behavior for jet eccentricity $\xi = 0.25P$

The asymmetric condition of the jet velocity through the bundle is also investigated versus the standoff distance by moving the nozzle $0.25P$. Figure 4.13 presents the relationship between the RMS displacement amplitude and the jet flow velocity for the five rows in the bundle. The vibration response of the bundle started to be significant at a lower jet flow velocity 0.85 m/s, whereas the critical jet flow velocity for the bundle having the shortest standoff distance (0.138 in.) occurred at approximately 1.5 m/s (see Figure 4.7), twice the jet flow velocity obtained for the present configuration. Furthermore, the instability of this bundle occurs in a more gradual manner than that found with $\xi = 0$. Above the critical velocity, the rods vibrated at a single frequency. This frequency changed from 13.125 Hz to 14 Hz at higher velocity due to the effect of fluid added stiffness. Vibration amplitudes were highest in the first two rows; the maximum response reaches approximately $55\%g$, while the response in the last three rows goes down to $10\%g$ since the jet flow energy is dissipated

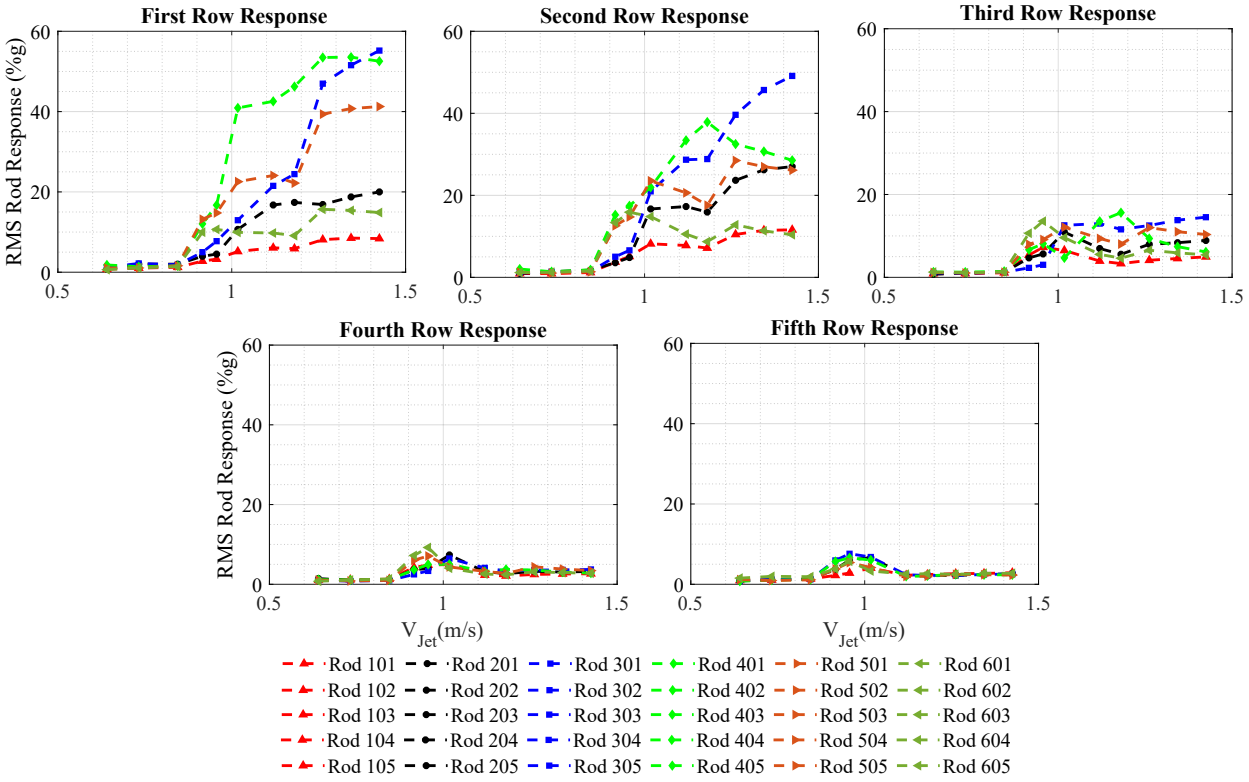

Figure 4.13 Rod bundle vibrations in transverse direction for 6x5 configuration at $\xi = 0.25P$.

faster than in the case $\xi = 0$ when the jet is centered with the gap; in the latter case the jet flow could propagate further downstream thus exciting more rows (see Figure 4.11).

Dynamic behavior for jet eccentricity $\xi = 0.5P$

In this section, the FEI behavior of the 6x5 bundle is obtained while the jet flow is centered with rod 401. Figure 4.14 shows the rod bundle vibration for each row. The rod tip displacements increased sharply with jet velocity above 0.92 m/s. The rod 401 frequency also increased from 13.1 Hz to 14.9 Hz with increasing jet velocity in the instability-induced vibration range as shown in Figure 4.15. The bundle excitation is mainly due to two mechanisms; synchronization with flow periodicity and fluidelastic instability. At $V_{Jet} = 1.15$ m/s, the rod frequency reaches 14.1 Hz. As a result, the rod displacement remains constant for rod 401 or decreases by increasing effect of frequency for rod 502. In the velocity range 0.92 to 1.44 m/s, the downstream rods were excited by the vortices originating from the upstream vibrating tubes because of the ideal condition to produce vortices in this case ($\xi = 0.5P$). Another observation of interest is that the 6x5 bundle exhibits the same behavior as in the

6x6 bundle for $\xi = 0.5P$.

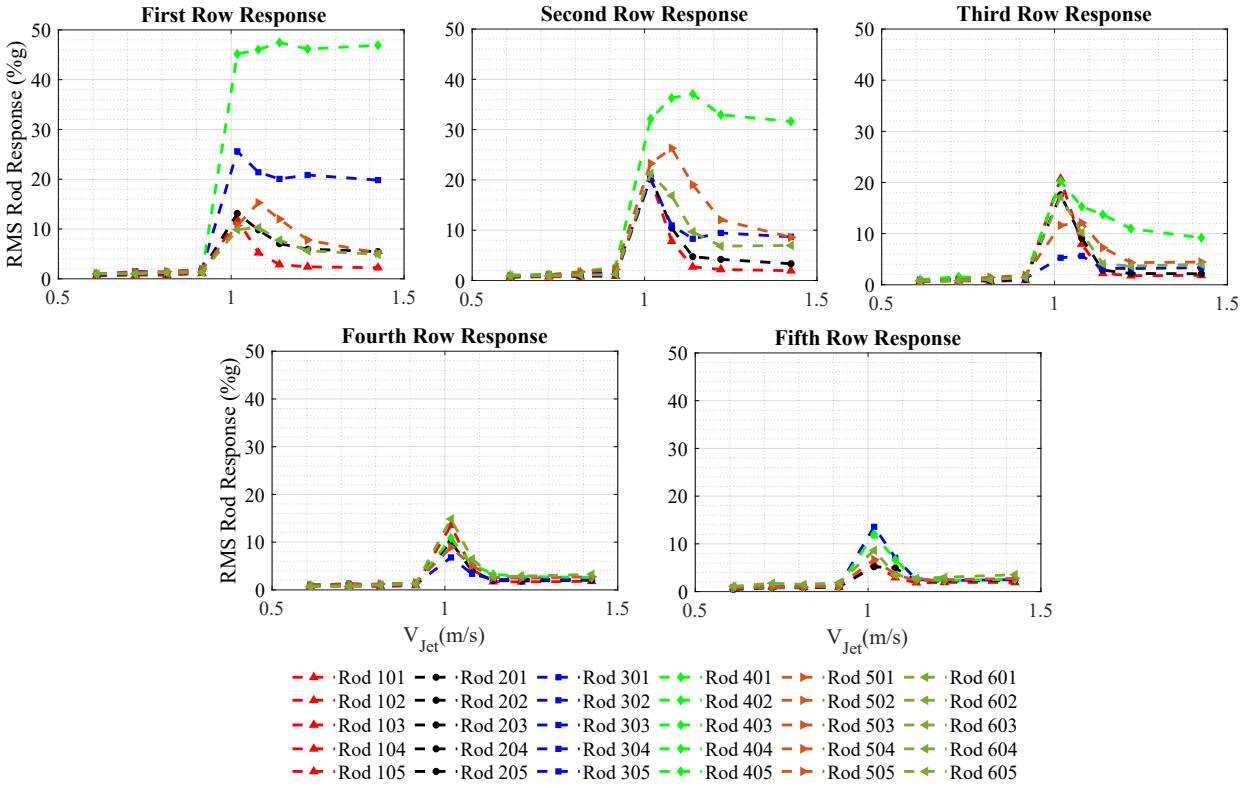

Figure 4.14 Rod bundle vibrations in transverse direction for 6x5 configuration at $\xi = 0.5P$.

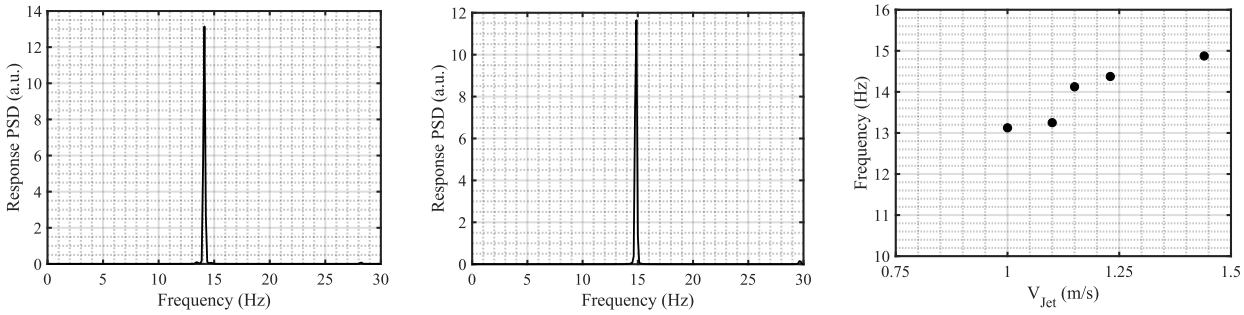

(a) (b) (c)

Figure 4.15 PSD plots showing the dynamical behaviors of rod 401 with increasing jet velocity: (a) $V_{Jet} = 1.15$ m/s, (b) $V_{Jet} = 1.44$ m/s, and (c) dominant response frequencies of rod 401 versus jet velocity in the instability-induced vibrations region.

4.3.3 Dynamic behavior of fully flexible 6x4 rod bundle in transverse direction

The interesting observation of the destabilizing effect of the standoff distance, which is contradictory to the expectation that moving the bundle away from the nozzle should reduce the critical jet velocity leads us to investigate the effect of larger standoff distance on the rod bundle vibration. Thus, a 6x4 fully flexible rod bundle is tested with the three eccentricities; $\xi = 0$, $0.25P$, and $0.5P$.

Dynamical behavior for jet eccentricity $\xi = 0$

Figure 4.16 illustrates the relationship between the rod tip displacement amplitude of the 24 rods in the array and the jet flow velocity. The bundle lost its stability above 1.22 m/s resulting in violent vibrations. The response increases sharply in the first row from $5\%g$ to $50\%g$ with a jet velocity increment of 0.06 m/s. With increasing jet velocity, the vibration amplitude increased to $70\%g$. This is the highest amplitude obtained comparing to the response from the shorter standoff distances. Increasing the standoff distance reduces the drag effect from the jet flow which allows the rods to vibrate with the largest amplitudes. The vibration in the downstream rows also occurs with a relatively significant amplitude ($40\%g$).

Dynamic behavior for jet eccentricity $\xi = 0.25P$

The stability effect of an eccentricity $\xi = 0.25P$ is also investigated to determine how the dynamic behavior changes with the asymmetric condition of jet flow in the bundle. The FEI behavior is presented in Figure 4.17 for each row. The critical velocity for this configuration increases again with increasing standoff distance, and the instability occurs at 1.22 m/s. This suggest that increasing the stand-off distance from the nozzle exit which allows the shear layer to develop thus increasing mixing which reduces the average jet velocity. The effect of decreasing jet velocity is thus more dominant than the effect of increase in projected area in this case.

Dynamic behavior for jet eccentricity $\xi = 0.5P$

The final test is conducted with the jet directed at rod 401. The rod tip displacements are tracked with a high-speed camera and the response obtained from image processing is shown in Figure 4.18. The onset velocity of FEI is 1.0 m/s in the first three rows while the last row is excited mainly by flow turbulence. The stabilizing effect of the eccentricity $\xi = 0.5P$

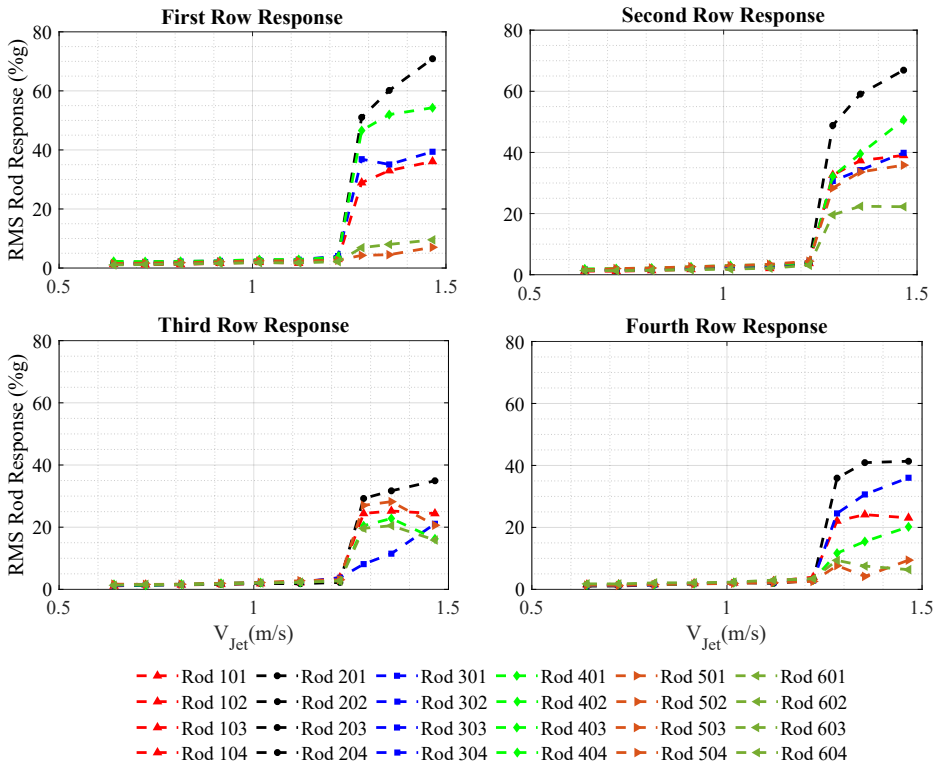

Figure 4.16 Rod bundle vibrations in transverse direction for 6x4 configuration at $\xi = 0$.

appears as was observed in the case of $\xi = 0.25P$ due to the mixing process in the region between the nozzle and the bundle.

4.4 Discussion

Fluidelastic instability of the rod bundle causes large amplitude vibrations which are dominant in the direction transverse to the jet flow. The stability boundary equation for the jet cross-flow induced vibration was previously defined in Part I as follows:

$$\rho A_{Jet} V_{Jet}^2 = K^2 f^2 D m l \delta_0 \tag{4.4}$$

where K = stability constant, f = rod frequency in still water, D = rod diameter, m = rod mass per unit length including added mass of water, L = rod length and δ = logarithmic decrement. Equation 4.4 can be expressed using non-dimensional parameters as follows:

$$\frac{V_{Jet}}{fD} = K\sqrt{\frac{m\delta_0}{\rho D^2}\frac{D}{D_{Jet}}\frac{L}{D_{Jet}}} \tag{4.5}$$

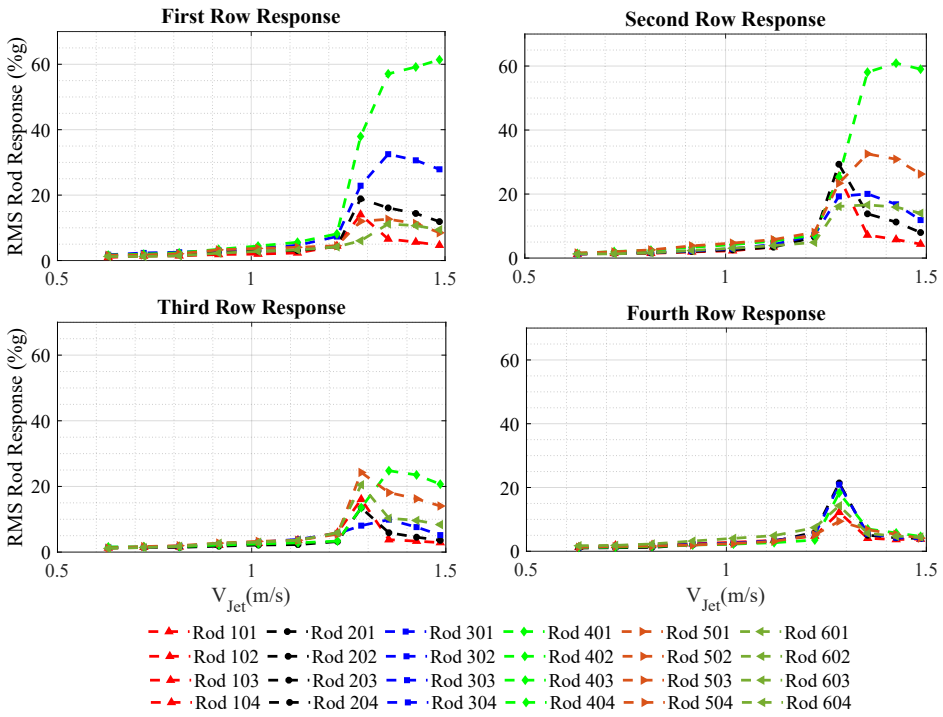

Figure 4.17 Rod bundle vibrations in transverse direction for 6x4 configuration at $\xi = 0.25P$.

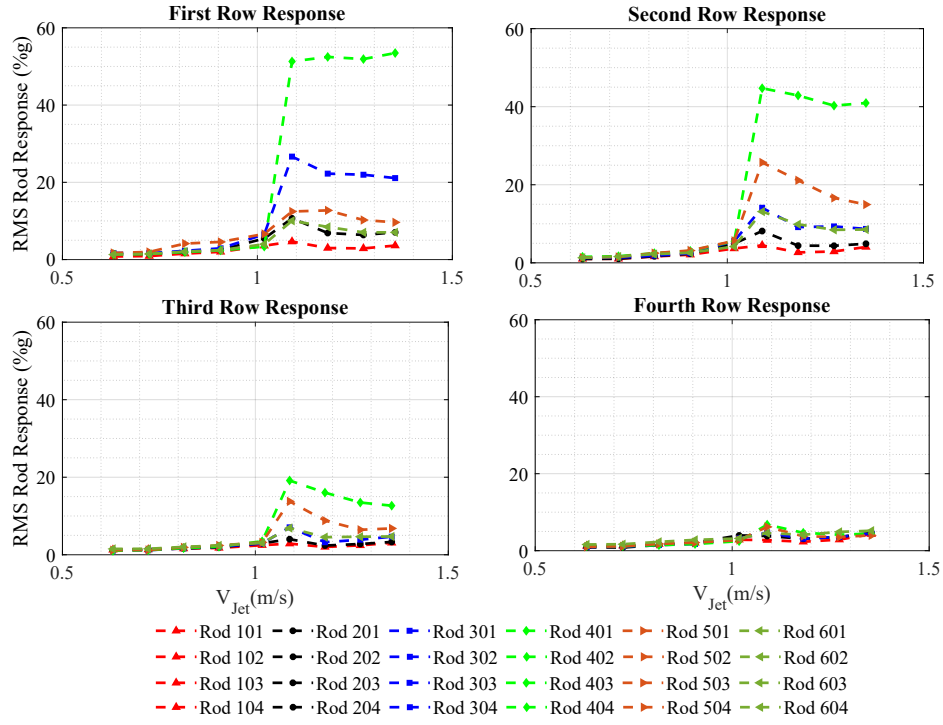

Figure 4.18 Rod bundle vibrations in transverse direction for 6x4 configuration at $\xi = 0.5P$.

Stability maps are generated to identify the stability threshold as a function of four non-dimensional parameters: the reduced velocity (V_{Jet}/fD), the mass damping parameter ($m\delta_0/\rho D^2$), the reduced jet diameter (D/D_{Jet}) and the rod span to jet diameter ratio (L/D_{Jet}). Figure 4.19 summarizes the experimental values of stability threshold obtained by varying jet eccentricity and stand-off distance. The stability constant (K) in Equation 4.5 is determined to show the stability effect of each parameter on the array as shown in Table 4.1. Regarding the stability effect of jet eccentricity, the bundle is relatively more stable with $\xi = 0$ because of lower jet interaction with the rods; the jet passes ideally through one gap at the center of the bundle. On the contrary, the case of $\xi = 0.25P$ undergoes fluidelastic instability earlier than the other cases for 6x6 and 6x5 rod bundles. Asymmetric flow conditions around the rods make this case very sensitive to transverse vibrations. The $\xi = 0.5P$ case splits the circular jet into two equal parallel plane jets emanating through the two gaps, aligned with the jet, on both sides of the rod. Derivatives of fluidelastic forces are less sensitive to transverse vibration than in the case $\xi = 0.25P$.

Table 4.1 Stability constants (K) for three eccentricities with three stand-off distances.

Rod bundle configuration	$\xi = 0$	$\xi = 0.25P$	$\xi = 0.5P$
6x6 (H/P=0.243)	13.44	10.21	10.5
6x5 (H/P=1.243)	8.50	5.83	6.30
6x4 (H/P=2.243)	8.36	8.36	7.0

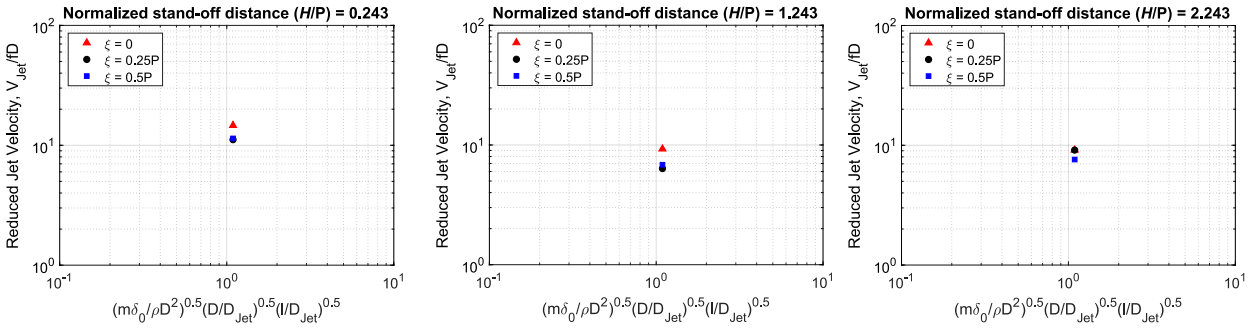

(a) (b) (c)

Figure 4.19 Threshold of instability-induced vibration for three jet eccentricities ($\xi = 0$, $0.25P$ and $0.5P$) tested with three rod bundles: (a) 6x6 rod bundle, (b) 5x6 rod bundle, and (c) 4x6 rod bundle.

4.5 Conclusions

Recently, jet cross-flow induced vibrations has been investigated to understand fuel rod dynamics in PWR reactor cores that have LOCA holes in baffle plates. The main purpose of the jet penetrations is to minimize the pressure generated in the barrel-baffle zone during LOCA events. However, during normal operation, these plants have experienced grid-to-rod fretting failure near LOCA holes. Flow induced vibration studies are therefore necessary to ensure fuel reliability during normal operating.

In Part I of the paper, stream-wise vibrations of rod bundles were investigated while varying two parameters, jet eccentricity and stand-off distance. The test facility used to test different rod bundles with different tested parameters was described in detail along with the design challenges for this closely packed array highlighted. The study here is mainly conducted to investigate the transverse vibrations and their excitation mechanisms and to compare with those obtained for stream-wise vibrations to identify the more unstable direction. The rod bundles are tested in the transverse direction using asymmetric stiffness rods with the same test parameters as in the stream-wise direction to make for direct comparison.

The stability effect of the stand-off distance shows interesting behavior of rod array vibration. In the transverse direction, increasing the gap has a destabilizing effect at first and then a stabilizing effect. The fluid forces acting on rods exposed to jet flow are functions of the velocity and the projected area of the jet. Two mechanisms are simultaneously active: the first is a decrease in velocity in the stream-wise direction of the jet, while the second is an increase in the cross-sectional area of the jet. The second mechanism takes over for wider gaps, causing the critical velocity to increase. However, this parameter had a different effect in the stream-wise direction. The critical velocity decreased with increasing stand-off distance between the nozzle and the first row facing the jet flow.

The fluidelastic behavior of three rod bundles is obtained using a high-speed camera and strain gauges. Each bundle is tested with varying jet eccentricity parameter. Stability effect of three eccentricities is investigated. The experimental investigations obtained in this study showed that:

- Jet eccentricity significantly affects the rod array response.
- The case of $\xi = 0.25P$ has the lowest critical velocities. Rod motion in asymmetric velocity field might have a large effect on fluidelastic forces which leads to instability at low values of jet velocity.
- The bundle with $\xi = 0$ lost stability at a higher critical jet velocity than the other two

cases. In this case, the jet flow is mainly squeezed through one gap; exposing one side of the rods to higher jet flow while the other side is submerged in the surrounding fluid, resulting in less interaction between the jet and the rods.

- The effect of the offset $\xi = 0.5P$ on the dynamical behavior of the rod bundle is more complex. The bundle vibrations occurred at a critical velocity near that for the case $\xi = 0.25P$. However, the amplitude increases in each row with the same pattern while raising the jet velocity, which preserves the unstable response in the first two rows while decreasing and then increasing the response in the other rows. The downstream rods may be excited by the vortices produced by the upstream vibrating rods.

CHAPTER 5 ARTICLE 3: FLUIDELASTIC INSTABILITY (FEI) MODEL FOR A ROD BUNDLE SUBJECTED TO JET CROSS-FLOW

Gad-el-Hak, I, Mureithi, N, and Karazis, K.

This article was submitted to "Journal of Fluids and Structures" on 28th June 2022, is accepted pending revision on 1st October 2022. This is the revised version.

Summary

This chapter presents a theoretical and experimental frame work to understand the instability of arrays under jet cross-flow. Experimental tests are carried out with four different arrays (single flexible rod, 2 flexible rods, 3 flexible rods, and fully flexible array) at $\xi = 0.25P$ and $D_{Jet}/D = 3.0$. The array with 3 flexible rods as well as the fully flexible array shown to be fluidelastically unstable, whereas the two smaller arrays are shown to be stable. A theoretical model based on the quasi-steady approach that also includes the rod area derivative is proposed to predict the dynamics (stability/instability) of the rod arrays. The model results show that the area derivative is important for the accurate prediction of the instability threshold. This work is performed to answer the research question (**Q4**) and to achieve the objectives (**O2** and **O3**).

Graphical Abstract

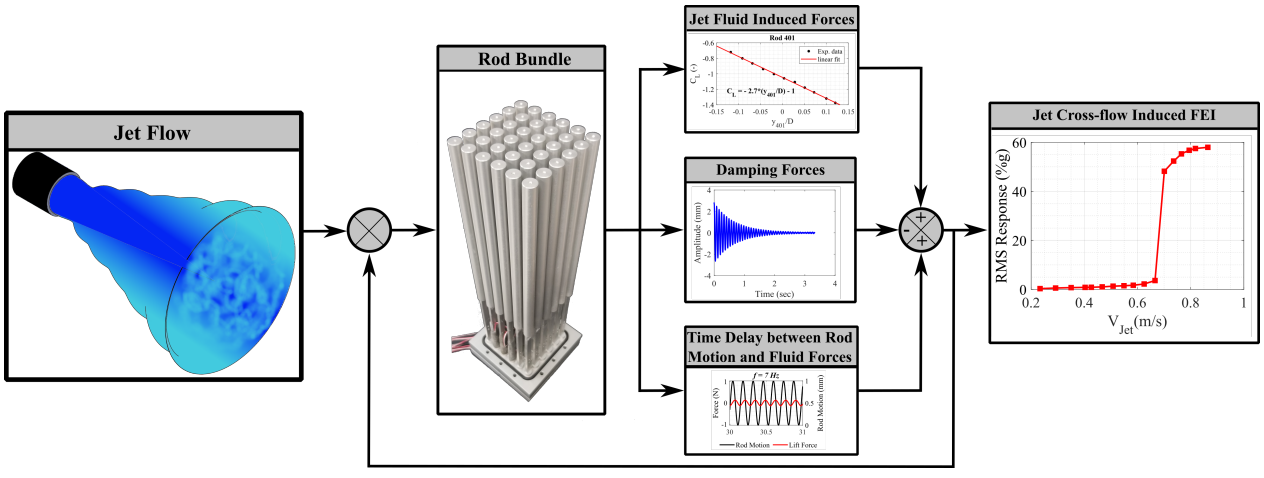

Abstract

Jet flow emanating from loss of coolant accident (LOCA) holes in the baffle plates of some pressurized water reactors (PWRs) was found responsible for flow induced vibration in nuclear fuel bundles. This could cause fretting wear of the fuel rods at the spacer grid location. Fluidelastic instability (FEI) is the most critical flow-induced vibration mechanism. This paper presents a theoretical framework to model the fluidelastic instability of a flexible fuel bundle in jet cross-flow.

A few stability boundary correlations based on the Connors equation were developed for baffle jetting (i.e. 2D jet) problem in PWRs. Except for these correlations, no theoretical model accounting for fluid-structure interaction under jet cross-flow has been reported. A theoretical model is developed here based on a quasi-steady approach. A new formulation of the fluidelastic forces as functions of the projected rod area derivative is proposed to account for variation of the projected area through LOCA hole (i.e. circular jet).

The theoretical work highlights the need of determining the jet fluid response (i.e. time delay) due to the rod response and the fluidelastic forces in the PWR mock-up array (i.e. closely packed arrays) under jet cross-flow. The theoretical model results are validated by experimental results of tested arrays. The developed model is found to be capable of differentiating between the stable and unstable arrays. Moreover, the model predicts the critical jet velocity of unstable vibration with an error of 15%.

Keywords: PWR fuel rods, LOCA, Fluidelastic instability model, Jet fluid force measurements, Jet cross-flow induced vibrations, Quasi-steady model.

5.1 Introduction

Flow-induced vibration (FIV) in nuclear power plants is a constant concern as the demand for better thermal performance and efficiencies challenges the mechanical, flow and irradiation exposure characteristics of fuel designs. Some PWRs are built with safety features such as loss of coolant accident (LOCA) holes and slots in the core periphery baffles enclosing the fuel assemblies, which relieve pressure build-up in the event of LOCA. During normal operation, some of these reactors have experienced grid-to-rod fretting fuel rods due to injected flows from LOCA holes. Thus, the fuel rods are exposed to the resulting combined axial and transverse jet flow conditions at multiple axial positions where LOCA holes are located. However, the fuel rods may potentially undergo fluidelastic instability (FEI) in extreme cases which could cause excessive vibration. Theoretical and experimental research on this problem remains quite limited.

Uniform cross-flow induced vibrations in tube bundles have been extensively investigated in the literature. Research on fluidelastic instability (FEI) has led to an in-depth understanding of the fundamental mechanisms governing it (Chen, 1984). A single flexible tube undergoes instability via the 1-dof negative damping mechanisms; this mechanism has only been found for flexibility transverse to the flow direction. Cross-coupling between neighboring tubes in the array can also lead to instability via the stiffness controlled mechanism (Paidoussis et al., 2010). Theoretical models of varying complexity have also been developed to predict FEI. The earliest study (i.e. jet-switching model) was presented by Roberts (1962) to model fluidelastic instability for both single and double rows of cylinders in uniform cross-flow. Roberts observed that instability occurred principally in the stream-wise direction; hence, his analysis was limited to predicting the stream-wise instability and importantly, the model fails to predict instability in the transverse direction. In the model, slight misalignment between two adjacent cylinders in a row is necessary in developing the wake dynamics and the jet switching instability. Thus, he assumed that the flow downstream of two adjacent cylinders could be represented by two wake regions, one larger than the other, with a classic jet-flow between them. The main constraints of Roberts's model are that the flow separation from the cylinder occurs at the minimum gap between the tubes centers (at 90 degrees) and also that the cylinder wakes are regions of constant pressure. Additionally, the flow upstream of the separation points and in the jet region was considered to be inviscid. The other models range from the purely analytical (Yetisir and Weaver, 1993a,b) and the semi-analytical flow channel model (Lever and Weaver, 1986, Shinde et al., 2018) to the unsteady models (Chen, 1987, Tanaka and Takahara, 1981). The semi-empirical quasi-static model (Connors, 1970) was developed to evaluate a stability constant (K) by introducing the stability constant between two main parameters, reduced critical velocity and mass damping parameter. Of particular interest here is the class of quasi-steady (Price and Paidoussis, 1986) models which depend on experimentally measured stability derivatives and drag coefficients. In the quasi-steady model, fluid force velocity dependence is accounted for by introduction of a time delay or phase lag parameter. From the foregoing, it is clear that FEI of tube arrays subjected to uniform flow is well understood and existing models work reasonably well. This work provides a valuable contribution for the case of jet-induced FEI.

In comparison with the research conducted on fluidelastic instability of tube arrays subjected to uniform transverse flow, only a few researchers (Fujita et al., 1990, Lee and Chang, 1990, Seki et al., 1986) have discussed 2D jet flow induced vibrations due to baffle jetting. However, in the studies, basic correlations based on Connors equation were presented by fitting the experimental results with their models to calculate the stability constant. There is, however, lack of theoretical models for jet cross-flow induced vibration.

Circular jet cross flow induce vibration has been experimentally investigated in in-line arrays simulating fuel rods under LOCA hole jetting by Gad-el Hak et al. (2021). The authors found that the stability threshold of the tested arrays is depending on offset between the jet centerline and array centerline (i.e. jet eccentricity, ξ). The lowest critical velocity for the tested arrays was observed when ξ was 25% of pitch. A destabilizing effect of this jet eccentricity could be used as safety limit for arrays subjected to circular jet cross-flow. Developing a theoretical model to predict the instability for this array-jet configuration is necessary to investigate the mechanism underlying jet-induced fluidelastic instability.

Framatome in collaboration with Polytechnique Montreal has developed a research program to understand the fluidelastic excitation behavior and mechanism of rod array subjected to jet cross-flow. The work reported here consists of FEI model development, and experimental work to measure model input parameters in addition to the instability threshold. Thereby, two experimental apparatuses are used: (i) FEI setup, and (ii) jet fluid force measurements setup. The FEI test results are used to validate the developed theoretical model. The aim of this study is to formulate a theoretical model for jet flow that can predict the critical instability velocity.

5.2 Stability behavior of rod bundle subjected the jet cross-flow

5.2.1 Test parameters

Rod array vibration is measured with a range of jet velocities covering the rod array behavior from turbulence induced vibration until fluidelastic instability. The effect of an offset between the jet centerline and array centerline (i.e. jet eccentricity ξ as shown in Figure 5.1a) has been investigated by (Gad-el Hak et al., 2021) with a jet-to-rod diameter ratio of 2.3. The authors found experimentally that a jet eccentricity of 0.25P had a lower critical velocity. Thus, FEI experiments and model are developed for more unstable case ($\xi = 0.25$P). Figure 5.1 shows the rod array configuration with the nozzle. The fluidelastic instability tests are done with jet flow parameters:

- $\xi = 0.25P$ that corresponds to the jet flow is offset by a quarter of spacing (P).
- $D_{Jet}/D = 3.0$, as shown in Figure 5.1b.
- $H/D = 0.32$ that corresponds to the gap between the nozzle exit and the first row, as shown in Figure 5.1a.

- $L_{Jet}/L_{Rod} = 0.5$ that identifies the location of the applied jet flow on the array as shown in Figure 5.1c.

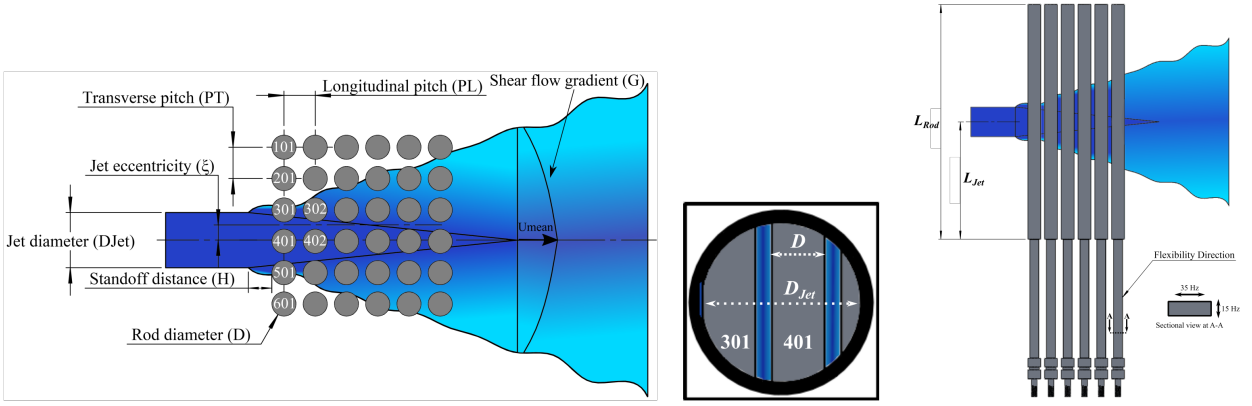

(a) (b) (c)

Figure 5.1 (a) top sectional view of rod array for jet eccentricity of ξ=0.5P, (b) projected view from the nozzle at ξ=0.25P, and (c) side view of rod array with jet flow configuration.

5.2.2 FEI experimental results

FEI experiments are conducted on a unidirectionally flexible normal square rod bundle having pitch-to-diameter ratio of 1.32 as shown in Figure 5.2a. The rods have natural frequency of 15 Hz in air. Figure 5.2b shows the final test loop for the FEI experiments with a 6x6 fully flexible array installed in the test section. Four different array configurations, single rod, 2x1, 3x1, and 6x6 fully flexible rod bundle, are tested to select a minimum number of rods that presents the dynamical behavior of the 6x6 fully flexible rod bundle. Figure 5.3 shows the experimental results for the tested arrays. In the figure, the jet velocity (V_{Jet}) is defined as the average velocity of flow from the nozzle, and the RMS response is expressed as a percentage of the inter-rod gap (g=P-D). In the figure, f_w is the rod frequency in still water. The single rod and the two rods array are stable in jet cross-flow. Their dynamical behavior lie in the turbulence induced vibration region. Moreover, the rods are statically displaced due to the jet momentum. However, the vibrational behavior of 3x1 row exhibits fluidelastic instability behavior as shown in Figure 5.3c. Above $V_{Jet}/(f_w\ D) = 5$, The central rod 401 response increases from 3.5%g reaching to 50%g with an increment of reduced jet velocity of 0.3. Moreover, the response of the neighbouring rods 301 and 501 has a jump above the critical velocity, but, their vibration amplitudes are not the same for the central rod due to their fixed surrounding rods. In the fully flexible array, the same rods 301, 401, and 501 vibrate with a larger amplitude, as shown in Figure 5.3d due to the strong hydrodynamic

coupling. Therefore, the reduced critical jet velocity is reduced from 5 to 4.4. To conclude, the 3x1 array could be used to develop a FEI model that predicts the critical velocity for the rod bundle subjected to jet cross flow.

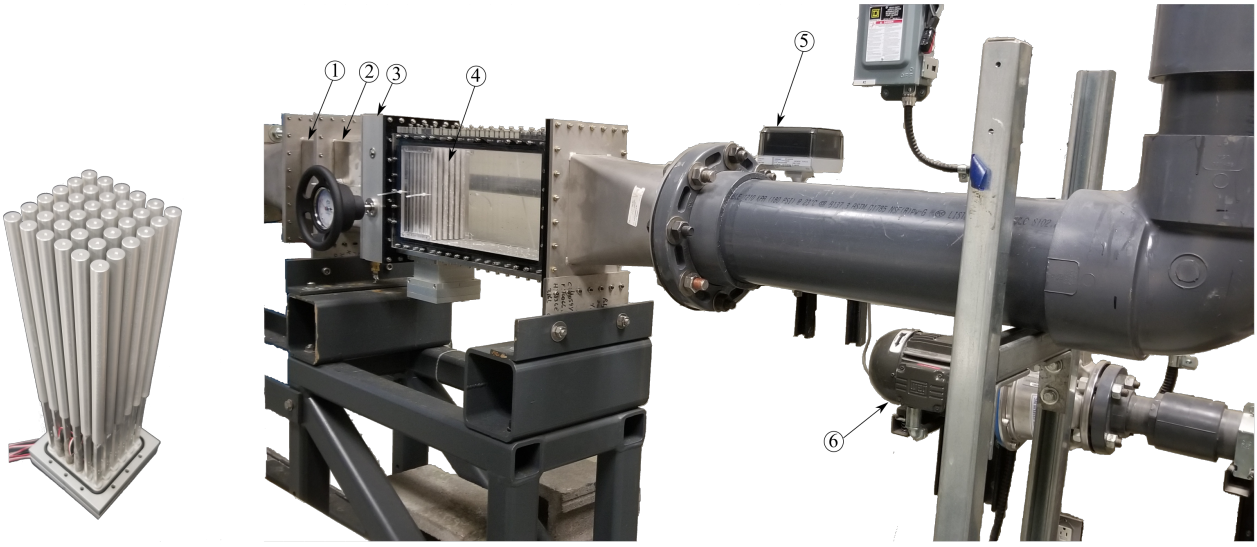

(a) (b)

Figure 5.2 The main components of FEI test loop set-up are labelled: (1) flow straightener, (2) barrel-baffle chamber, (3) displacement jet flow mechanism, (4) rod bundle, (5) water flow meter and (6) centrifugal pump.

5.3 FEI model development

Jet cross-flow induced vibration mainly in the transverse direction to the jet flow, then a theoretical model is developed to model the occurrence of the instability for the transverse vibration. The FEI model is developed to predict the critical velocity for the jet eccentricity case of $\xi = 0.25P$ which is a more unstable case. The initial model development is developed by (Gad-el Hak et al., 2022a). Figure 5.4a shows graphically the relative location of the nozzle to the first row rods for this case. In the figure, the system origin is coincident with the array origin. The injecting jet flow from the nozzle is obstructed by three rods, 301, 401, and 501 as shown in the figure.

Consider the three flexible rods in a rigid in-line square array vibrate in the transverse direction (y) under jet cross flow as shown in Figure 5.4b. The jet fluid forces are coupled with rods motion. The coupled equations of motion of the system can be written as follows:

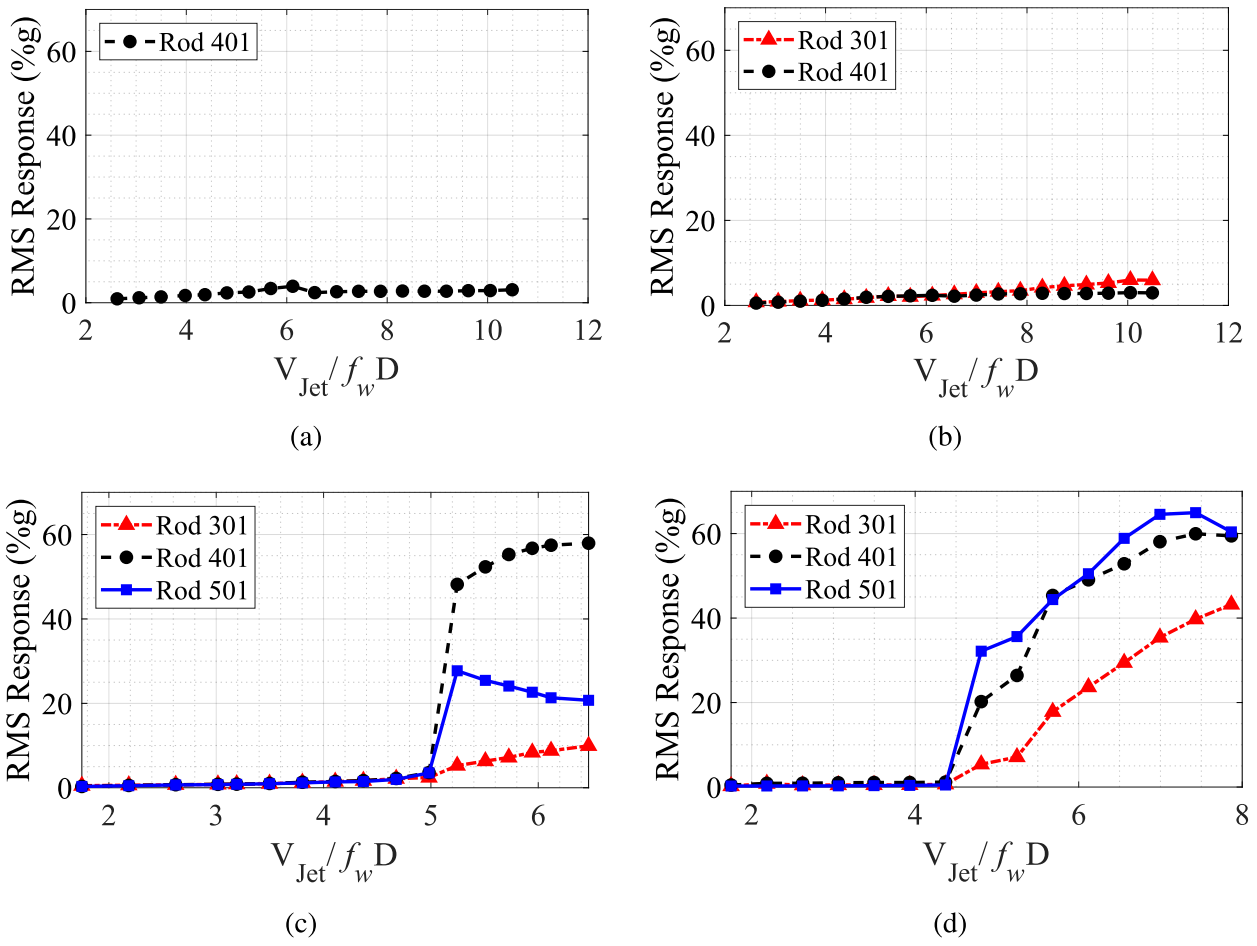

Figure 5.3 FEI results for different arrays: (a) single rod, (b) 2x1 single row, (c) 3x1 single row, and (d) 6x6 fully flexible array.

$$[M_s]\ddot{\vec{y}}_{(t)} + [C_s]\dot{\vec{y}}_{(t)} + [K_s]\vec{y}_{(t)} = \vec{F}_y; \quad \vec{y} = [y_{301}, y_{401}, y_{501}]^T \tag{5.1}$$

where $[M_s]$, $[C_s]$, $[K_s]$ are the mass, damping and stiffness matrices of the structure, respectively, $\ddot{\vec{y}}$ the rods acceleration vector, $\dot{\vec{y}}$ the rods velocity vector, and $\vec{y}$ the rods displacement vector. $\vec{F}_y$ is the jet fluid dynamic force vector in the transverse direction.

For instance, the force components acting on rod 401 in terms of the lift and drag forces are shown in Figure 5.4b. Using a quasi-steady approach, the total transverse direction force component on this rod can be written as follows:

$$F_{y401} = F_L cos(\alpha) - F_D sin(\alpha) = 1/2\rho {V_R}^2 A[C_L cos(\alpha) - C_D sin(\alpha)] \tag{5.2}$$

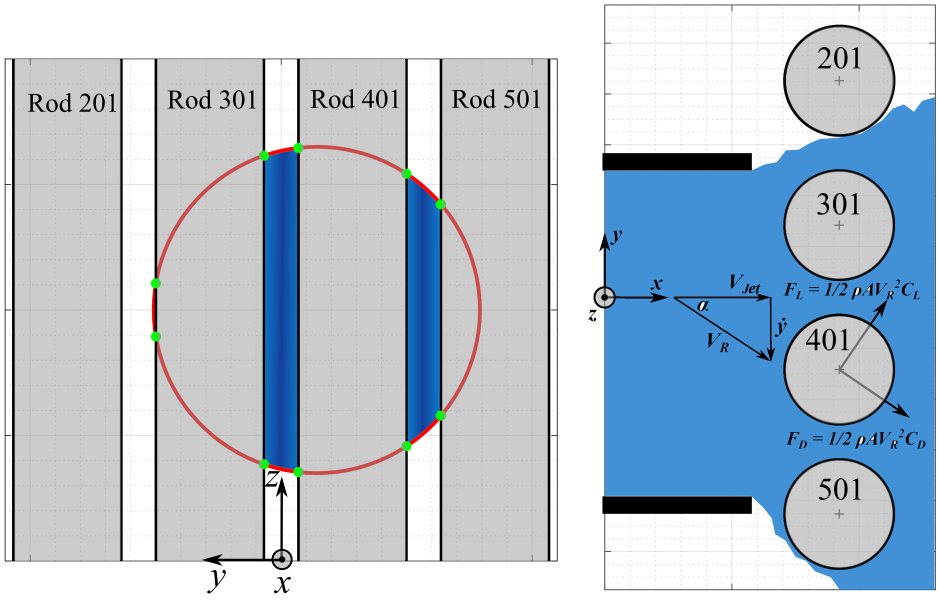

(a) (b)

Figure 5.4 (a) projected view from the nozzle, and (b) top view of the array with the nozzle.

where V_R is the relative flow velocity, and α the angle of attack as defined in Figure 5.4b:

$$V_R = [{V_{Jet}}^2 + \dot{y}^2]^{1/2}; \quad \alpha = \tan^{-1}(\dot{y}/V_{Jet}) \tag{5.3}$$

For small rod vibrations, V_R and α can be formulated as:

$$V_R \approx V_{Jet}; \quad \alpha \approx \dot{y}/V_{Jet} \tag{5.4}$$

The projected area (A) of rod from the nozzle is changed with the transverse rod motion (y) due to the geometrical matching between the circular cross sectional area and the rods (see the intersection points in Figure 5.4a). C_L, C_D, and A for rod 401 can be expressed in linearized form as:

$$\begin{aligned}
C_{L401} &= C_{L401_0} + \frac{\partial C_{L401}}{\partial y_{401}} y_{401} + \frac{\partial C_{L401}}{\partial y_{301}} y_{301} + \frac{\partial C_{L401}}{\partial y_{501}} y_{501} \\
C_{D401} &= C_{D401_0} + \frac{\partial C_{D401}}{\partial y_{401}} y_{401} + \frac{\partial C_{D401}}{\partial y_{301}} y_{301} + \frac{\partial C_{D401}}{\partial y_{501}} y_{501} \\
A_{401} &= A_{401_0} + \frac{\partial A_{401}}{\partial y_{401}} y_{401}
\end{aligned} \tag{5.5}$$

Equation 5.2 can be expanded as follows:

$$F_{y_{401}} = 1/2\rho {V_{Jet}}^2 \left(A_{401_0} + \frac{\partial A_{401}}{\partial y_{401}} y_{401}\right) \left[\left(C_{L401_0} + \frac{\partial C_{L401}}{\partial y_{401}} y_{401} + \frac{\partial C_{L401}}{\partial y_{301}} y_{301} + \frac{\partial C_{L401}}{\partial y_{501}} y_{501}\right) - \left(\frac{\dot{y}_{401}}{V_{Jet}}\right) \left(C_{D401_0} + \frac{\partial C_{D401}}{\partial y_{401}} y_{401} + \frac{\partial C_{D401}}{\partial y_{301}} y_{301} + \frac{\partial C_{D401}}{\partial y_{501}} y_{501}\right)\right] \tag{5.6}$$

In a quasi-steady fluid-dynamic theory, the quasi-static forces are modified to take into account the dynamic feature of the fluid response by introducing a time delay, τ. Simpson and Flower (1977) considered the time lag to be the slowing down effect of the flow as it approaches the tube stagnation point. Following this definition, Price and Paidoussis (1986) introduced a constant time delay as follows:

$$\tau = \frac{\mu D}{V}; \quad \mu \sim O(1) \tag{5.7}$$

where D is the tube diameter, μ is the flow retardation parameter taken to be of order 1, and V is the relevant flow velocity. Price and Paidoussis (1986) used $\mu = 1$ for an in-line square array in uniform flow case. In this paper, V=V_{Jet} because of the model is developed for the upstream row which exposes to V_{Jet}. In addition, the effect of varying μ from 1 to the value that is experimentally extracted, on stability is investigated.

The linearized form of Equation (5.6) is:

$$F_{y401} = 1/2\rho {V_{Jet}}^2 \left[A_{401_0} \left(C_{L401_0} + e^{-i\omega\tau} \frac{\partial C_{L401}}{\partial y_{401}} y_{401} + e^{-i\omega\tau} \frac{\partial C_{L401}}{\partial y_{301}} y_{301} + e^{-i\omega\tau} \frac{\partial C_{L401}}{\partial y_{501}} y_{501}\right) + \left(C_{L401_0} \frac{\partial A_{401}}{\partial y_{401}} y_{401}\right) - \left(A_{401_0} C_{D401_0} \frac{\dot{y}_{401}}{V_{Jet}}\right)\right] \tag{5.8}$$

where ω is the angular frequency ($2\pi f_w$). The first term in Equation 5.8 includes the fluidelastic forces generated due to the rod motion and the cross-coupling forces due to the neighbouring rods motion. The second term ($C_{L0} \frac{\partial A}{\partial y_{401}} y_{401}$) is a new term that introduced in the model to take into account the change in area. The third term is the fluid added damping.

The 3-DOF jet flow-coupled system modelling jet-induced FEI is written as:

$$
\begin{aligned}
&[M_s + M_f]\ddot{\vec{y}_{(t)}} + [C_s]\dot{\vec{y}_{(t)}} + [K_s]\vec{y_{(t)}} = \vec{F}_{y_0} + [K_f]\vec{y_{(t)}} + [C_f]\dot{\vec{y}_{(t)}};\ \ \vec{y} = [y_{301}, y_{401}, y_{501}]^T;\\
&\begin{bmatrix} m_s+m_f & 0 & 0 \\ 0 & m_s+m_f & 0 \\ 0 & 0 & m_s+m_f \end{bmatrix} \begin{Bmatrix} \ddot{y}_{301} \\ \ddot{y}_{401} \\ \ddot{y}_{501} \end{Bmatrix} + \begin{bmatrix} 2m_s\zeta\omega_n & 0 & 0 \\ 0 & 2m_s\zeta\omega_n & 0 \\ 0 & 0 & 2m_s\zeta\omega_n \end{bmatrix} \begin{Bmatrix} \dot{y}_{301} \\ \dot{y}_{401} \\ \dot{y}_{501} \end{Bmatrix}\\
&+ \begin{bmatrix} k_s & 0 & 0 \\ 0 & k_s & 0 \\ 0 & 0 & k_s \end{bmatrix} \begin{Bmatrix} y_{301} \\ y_{401} \\ y_{501} \end{Bmatrix} = \frac{1}{2}\rho(V_{Jet}^2) \left(\begin{bmatrix} A_{301_0} C_{L301_0} \\ A_{401_0} C_{L401_0} \\ A_{501_0} C_{L501_0} \end{bmatrix} + \begin{bmatrix} A_{301_0}\frac{\partial C_{L301}}{\partial y_{301}} e^{-i\omega\tau} + C_{L301_0}\frac{\partial A_{301}}{\partial y_{301}} & .. \\ A_{401_0}\frac{\partial C_{L401}}{\partial y_{301}} e^{-i\omega\tau} & .. \\ 0 & .. \end{bmatrix} \right.\\
&\left. \begin{bmatrix} A_{301_0}\frac{\partial C_{L301}}{\partial y_{401}} e^{-i\omega\tau} & 0 \\ A_{401_0}\frac{\partial C_{L401}}{\partial y_{401}} e^{-i\omega\tau} + C_{L401_0}\frac{\partial A_{401}}{\partial y_{401}} & A_{401_0}\frac{\partial C_{L401}}{\partial y_{501}} e^{-i\omega\tau} \\ A_{501_0}\frac{\partial C_{L501}}{\partial y_{401}} e^{-i\omega\tau} & A_{501_0}\frac{\partial C_{L501}}{\partial y_{501}} e^{-i\omega\tau} + C_{L501_0}\frac{\partial A_{501}}{\partial y_{501}} \end{bmatrix} \begin{Bmatrix} y_{301} \\ y_{401} \\ y_{501} \end{Bmatrix} \right.\\
&\left. + \begin{bmatrix} -A_{301_0}\frac{C_{D301}}{V_{Jet}} & 0 & 0 \\ 0 & -A_{401_0}\frac{C_{D401}}{V_{Jet}} & 0 \\ 0 & 0 & -A_{501_0}\frac{C_{D501}}{V_{Jet}} \end{bmatrix} \begin{Bmatrix} \dot{y}_{301} \\ \dot{y}_{401} \\ \dot{y}_{501} \end{Bmatrix} \right)
\end{aligned}
\tag{5.9}
$$

where $[M_f]$, $[C_f]$, $[K_f]$ are the added-mass, added-damping and added-stiffness matrices of the fluid, respectively. $\vec{F}_{y_0}$ is the remaining constant forces vector because $C_{L0_{301}} \neq C_{L0_{401}} \neq C_{L0_{501}} \neq 0$ due to asymmetric geometrical patterns of the rods with the jet flow as shown in Figure 5.4a. The coefficients of the fluid matrices are needed to be measured, and an experimental setup is detailed in the following section.

5.4 Experimental setup

The main purpose of this research is to understand the fundamental mechanisms underlying rod bundle excitation. This can be achieved by performing a theoretical analysis using the measured jet fluid forces. In the following subsections, test section instrumentation, and test loop are described.

5.4.1 Linear motor design and test section instrumentation

A quasi steady approach is used in the theoretical model development, which assumes that the instantaneous force on the oscillating rod is equal to an equivalent time lagged force on the rod when it is statically displaced. Thus, the quasi-static forces are needed to be measured at a finite steps of the rod motion. A linear motor system is designed to move precisely the rod in jet flow. The linear system consists of positioning slide driven by a stepper motor as

shown in Figure 5.5 using a flexible shaft coupling (labelled 3 in Figure 5.5a). A rigid rod is mounted on a six-axis ATI Nano 17 force/torque sensor to measure the drag and lift forces. In addition, the measured torque is used to determine the location of applied force from the jet flow. A laser optical sensor (label 2 in Figure 5.5b) is pointed on the apparent moving part of the instrumented rod to measure the displacement of rod while the motor moves it.

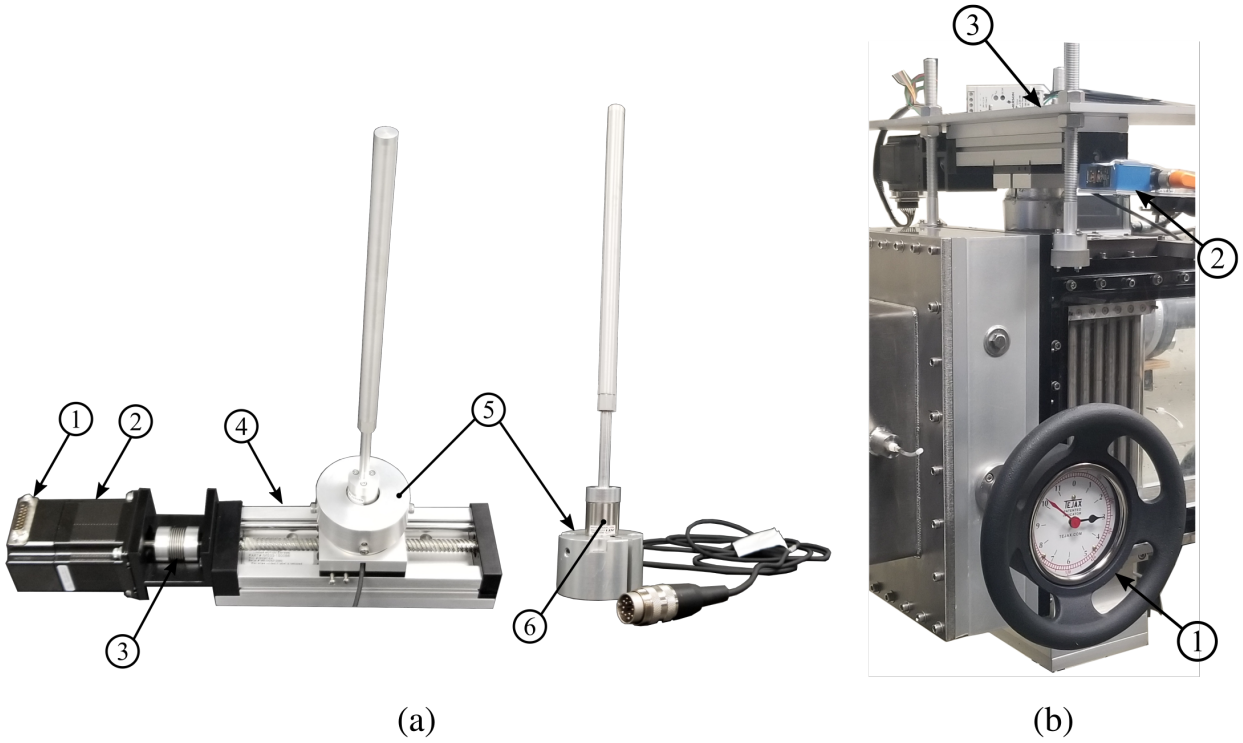

Figure 5.5 (a) liner motor system components, and (b) test section instrumentation.

The hybrid stepper motor with controller and driver with a high micro-step resolution of 256 is selected to move precisely the rod. Microstepping is a method of driving a stepper motor such that every full step of the motor is divided into smaller increments called microsteps, thus, increasing the micro-steps improve the smoothness of the rod response. Figure 5.6a shows graphically the difference between sin wave, full-step square wave, and 1/8 micro-step wave form. A full step increment is another parameter that could use to vibrate the rod close to sin wave, the motor has 1.8° full step increment. The unsteady force measurements are executed using the stepper motor by programming it to vibrate the rod sinusoidally by rotating the shaft clockwise and then anti-clockwise in a time period which defines one-half of the cycle. The frequency of rod oscillation is controlled by setting the motor acceleration. Figure 5.6b shows the measured response from the motor using the lase sensor with a excitation frequency of 8 Hz and 1/128 micro-steps resolution.

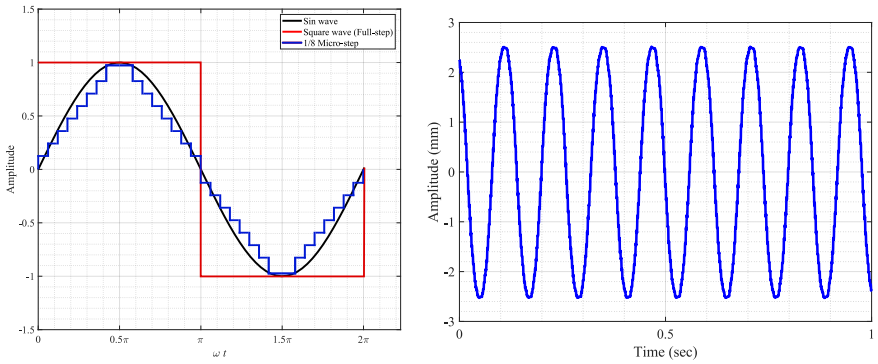

Figure 5.6 (a) comparison between sin wave, square wave, and 1/8 micro-steeping wave form, and (b) the motor response with 1/128 micro-step.

5.4.2 Test loop set-up

The linear motor system and the instrumented neighbouring rods are integrated in the test section. Figure 5.7 shows the test loop used to obtain the quasi-static and unsteady forces of the rod bundle subjected to jet cross-flow. The linear motor is inserted from the top panel and sits on a plate made of Delrin® acetal plastic to reduce the friction and provide a smooth rod motion. The plate has a low friction coefficient of 0.12. The instrumented neighbouring rods with strain gauges are mounted on the bottom panel to measure the cross-coupling components, therefore the array configuration is completed. A 2 horsepower centrifugal pump is used to pump uniformly the water flow through the test loop pipes, then it converts to jet flow using the displacement jet flow mechanism (label 2). The jet flow then enters the instrumented rod array. The average jet flow velocity is calculated using a flow meter (label 6).

5.5 Test results

In this section, two different types of tests: quasi-static fluid force measurements, and unsteady fluid forces, are carried out. The quasi-static/unsteady fluid force measurements are conducted to obtain the input parameters for the theoretical model.

5.5.1 Quasi-static fluid force measurements

The main input parameters for the developed FEI model are the quasi-static force derivatives for the three rods, 301, 401, and 501, in the jet flow due to the motion of each rod individually. In contrast to the uniform flow case, each rod has a specific flow condition relative to the jet

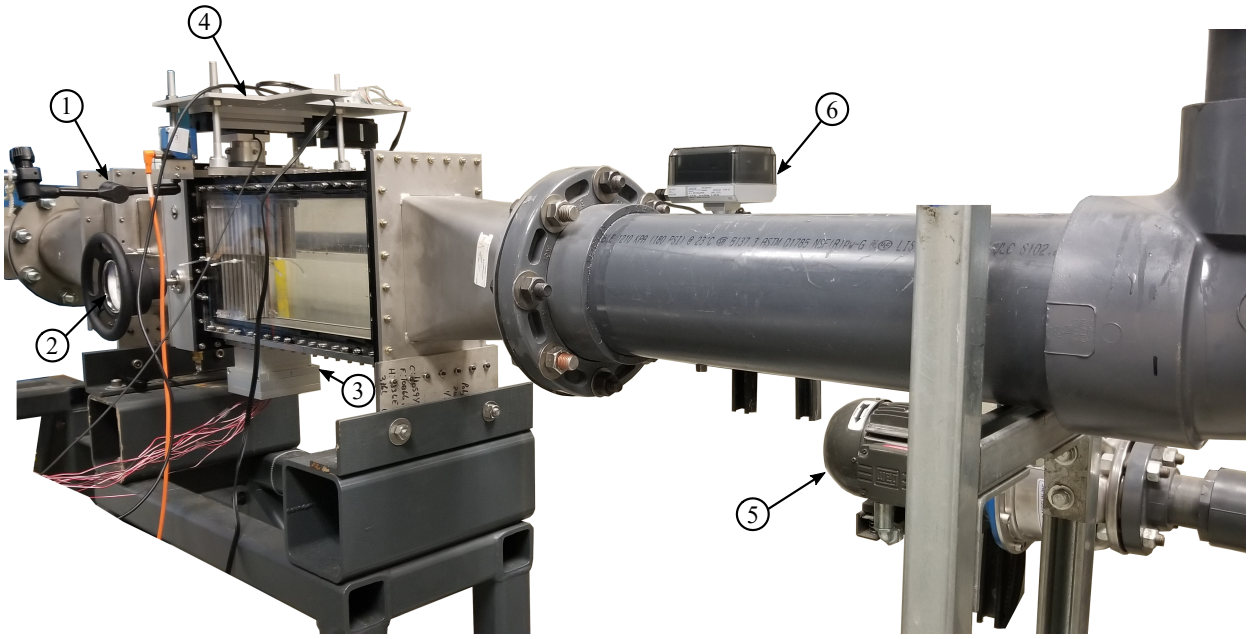

Figure 5.7 The main components of test loop set-up are labelled: (1) laser sensor, (2) displacement jet flow mechanism, (3) instrumented neighbouring rods, (4) linear motor system, (5) centrifugal pump and (6) flow meter.

flow because of asymmetric jet flow conditions in the array. Thus, three different tests are carried out, for each test, one rod is transversely moved and its effect on the surrounding rods is measured in terms of change in lift force. The force measurements of a rod array in jet cross-flow have not been examined previously in the literature, therefore the effect of quasi-static fluid force coefficients varying with the Reynolds numbers ($Re_{Jet} = V_{Jet}D_{Jet}/\nu$) is required to figure out the jet flow behavior in arrays. Five Reynolds numbers: Re_{Jet} = 1.3, 2.0, 2.6, 3.3, and 4 x10^4 are tested to examine the dependence of force coefficient derivatives on Re_{Jet}. The measured forces are normalized based on the projected rod area that corresponds to the rod position relative to the jet flow to determine the lift and drag coefficients. Figure 5.8 shows the variation of area with the non-dimensional displacement (y_k/D) in the lift direction ($\pm 15\%D$). The area derivatives of two rods 301 and 501 are relatively large than the central rod 401 due to their proximity to the nozzle boundary. These area derivatives are used in the stability analysis. Figure 5.9 shows the steady drag and lift coefficients for the central rod 401 with the five tested Reynolds numbers. The results show that the fluidelastic force coefficients do not change significantly in this tested range of jet velocity, which covers the the dynamical behavior of the 3x1 single flexible row from turbulence induce vibration region to fluidelastic instability.

Related to jet flow case, the location of the applied jet fluid force (L_{Jet}/L_{Rod}) is another

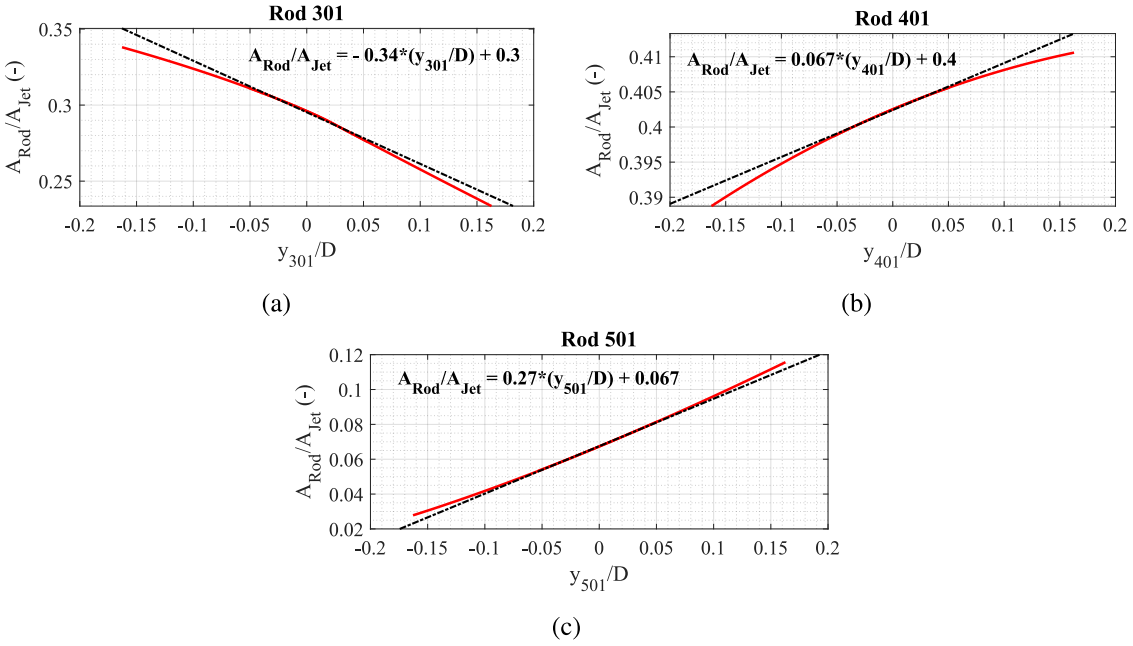

Figure 5.8 Area change (red line) with rod displacement and its linear fitting (black line) for the three rods: (a) rod 301, (b) rod 401, and (c) rod 501.

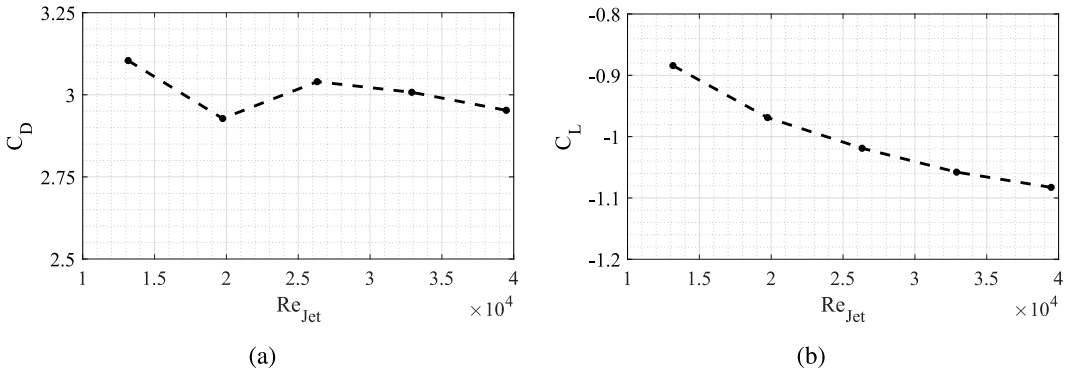

Figure 5.9 Variation of the jet fluid force coefficients for the central rod with jet Reynolds number: (a) C_D, and (b) C_L.

parameter that should be verified versus the jet flow velocity. The measured torque arms in the drag direction are plotted with y_{401}/D and the five Reynolds numbers in Figure 5.10. The location of the applied force is offset within 2.5% from the mid-point of the rod as shown in the figure. Thus, the jet flow path through the array is independent on the jet flow velocity.

The lift coefficient derivative for the rods 301, 401, and 501 with their own non-dimensional displacements are shown in Figures 5.11a, 5.11b, and 5.11c, respectively. The lift coefficient of rod 301 shows a nonlinear variations with rod displacement. This could be attributed

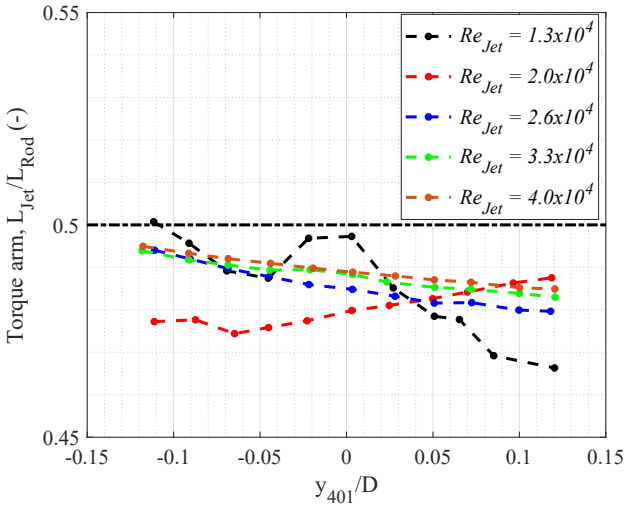

Figure 5.10 Measured torque arm for rod 401 with its non-dimensional displacement.

to flow gaps around this rod changing from two gaps with rod displacement as shown in Figure 5.4a. However, a local linear variation around the rod equilibrium point may be assumed. This variation is captured by extracting a first order term from the quadratic fit shown in Figure 5.11a. Rod 401 has a negative derivative of 2.7 as shown in Figure 5.11b. While the highest negative derivative of -8.3 was observed for rod 501. This could be due to one side of the rod being exposed to the jet flow (see Figure 5.4a), causing a net unbalanced in the lift force. Table 5.1 summarizes all other required input parameter for the stability analysis.

Table 5.1 Steady drag and lift force coefficients (C_{D_0} & C_{L_0}) and derivatives of the lift coefficient ($C_L, y_k/D$) measured at $Re_{Jet} = 4\text{x}10^4$.

Force coefficient	Rod 301	Rod 401	Rod 501
C_{L_0}	-0.026	-1.1	-1.7
C_{D_0}	1.9	2.95	2.26
$C_L, y_{301}/D$	-0.48	-0.16	-
$C_L, y_{401}/D$	-0.29	-2.7	2.2
$C_L, y_{501}/D$	-	4.6	-8.3

5.5.2 Time delay measurement

In addition to measuring the fluidelastic force derivatives and drag forces, the developed model also requires measurement of the time-lag between tube motion and the lift force variations. The designed force measurement system is used in dynamic tests to determine

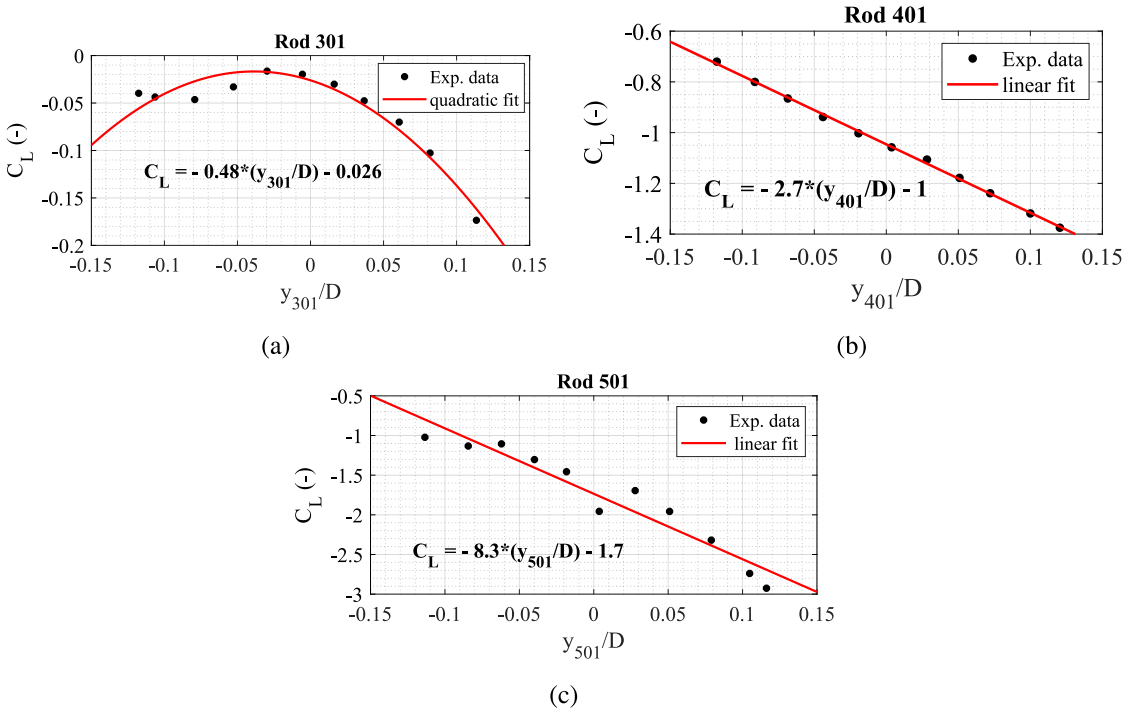

Figure 5.11 Variation of the lift force coefficient of the three rods with their quasi-static displacements in the lift direction at Re_{Jet} = 4x10^4: (a) rod 301, (b) rod 401, and (c) rod 501.

the phase delay. The phase lag is directly associated with the rod velocity. For this reason, the transient behaviour of the lift force coefficient is obtained over a range of jet flow reduced velocities ($V_{Jet}/f\ D$ = 2-10), where f is an excitation frequency. The fluid response time delay (τ) is obtained by calculating the delay between the rod motion (time (t)) and resultant lift force (time (t-τ)) signals to characterize the system dynamics. The fluid response at zero flow is subtracted from the results to calculate accurately the system time delay associated with jet flow. Figure 5.12 shows the unsteady force measurement for a rod excited sinusoidally at a frequency of 7 Hz. The phase lag (φ) between the two signals, tube displacement (Ysin($2\pi ft$)) and fluid force (Fsin($2\pi f(t-\tau)$)), is used to extract the time delay from the simple relation:

$$Fsin(2\pi f(t-\tau)) = Fsin(2\pi ft + \varphi) \tag{5.10}$$

thus φ = (-$2\pi\tau$)f. An example of the measured phase lag (φ) is shown in Figure 5.12b. For each tested point the phase (φ) is extracted to compute the system time delay. Figure 5.13a shows a variation of time delay (τ) with the reduced jet velocity. Consequently, the flow retardation parameter (μ=$\tau/(D/V_{Jet})$) is obtained from the measured time delay as a function of the convection time (D/V_{Jet}) with the reduced jet velocity as shown in Figure 5.13b.

It is varied over the reduced jet velocity, this may be attributed to resulting different jet behavior regimes depending on the excitation frequency as discussed by Rockwell (1972). It is found that $\mu = 1$ at the critical condition, the order of magnitude of μ is consistent with that suggested by Price and Paidoussis (1986).

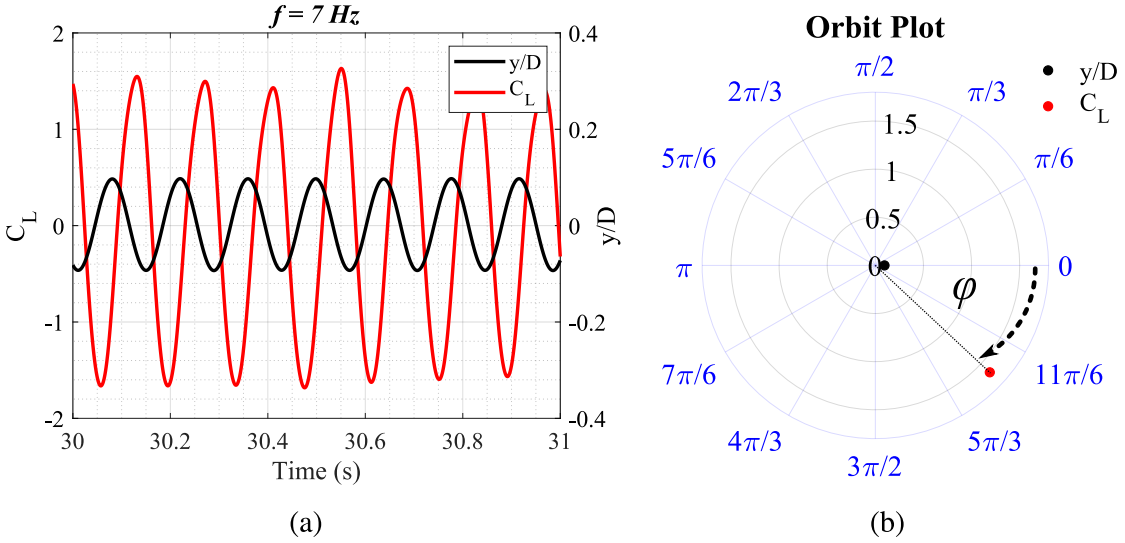

Figure 5.12 (a) Fluid response due to sinusoidal rod motion, and (b) orbit plot showing the phase lag (φ).

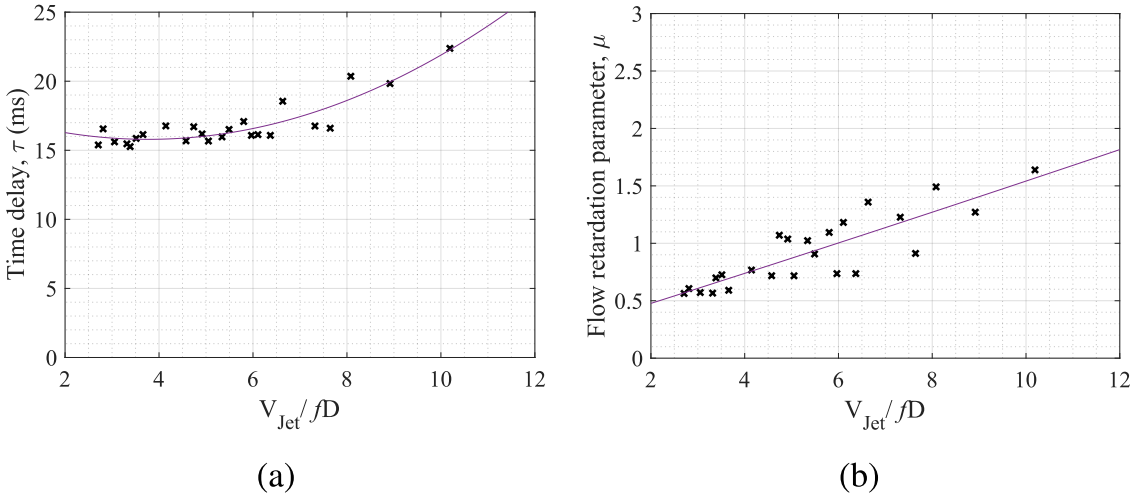

Figure 5.13 (a) Extracted time delay (τ) versus V_{Jet}/fD, and (b) measured flow retardation parameter (μ) versus V_{Jet}/fD.

5.6 FEI model analysis results and model validation

A stability analysis is performed by solving the coupled equation system (Equation 5.9) to obtain the eigenvalues (λ) with the jet velocity. The solution of the equations of motion can be formulated as follows:

$$\vec{y}(t) = \vec{A}e^{\vec{\lambda}t}; \;\; \vec{y} = [y_{301}, y_{401}, y_{501}]^T \tag{5.11}$$

where λ is the eigenvalue. When the real part of λ is positive, the system is unstable and behaves as an unstable oscillator. Thereby, the critical velocity for fluidelastic instability is the lowest velocity at which the real part of any eigenvalue reaches zero and has a tendency to be positive.

5.6.1 Fluidelastic stability analysis

Single flexible rod and 2x1 flexible row stability results

The developed FEI model is first applied to single flexible rod and 2x1 flexible row to demonstrate the stability of these two arrays under jet cross-flow by reducing the number of degrees-of-freedom. The fluidelastic forces and the structural parameters are considered for each rod in the tested arrays (single rod and 2x1 single row) to construct the reduced model. The resulting equation of motion is a function of the jet velocity thus the eigenvalues of the coupled equations are obtained for a wide range of reduced jet velocities. Figures 5.14a and 5.14c show the obtained real and imaginary parts of the eigenvalue, respectively, for the single flexible rod 401. Results for the 2x1 flexible row are plotted in Figures 5.14b and 5.14d. The theoretical results demonstrate that these two arrays are fluidelastically stable because their real parts are negative over the reduced velocity range. The theoretical prediction is confirmed by the experimental test results in Figures 5.3a and 5.3b which show the same rod configuration to be stable. The validation demonstrates that the model is able to predict the array stability in jet cross-flow.

3x1 flexible row stability results

After the developed model is validated with the single flexible rod and the 2x1 flexible row, the coupled equation of motion for the 3x1 row is solved to perform the stability analysis. The eigenvalues of the coupled system are obtained for a wide range of reduced jet velocities starting from near zero until the fluidelastic instability condition (i.e. real part of $\lambda > 0$). Fluidelastic instability is predicted to occur at $V_{Jet}/(f_w\ D) = 5.69$ according to the eigenvalue

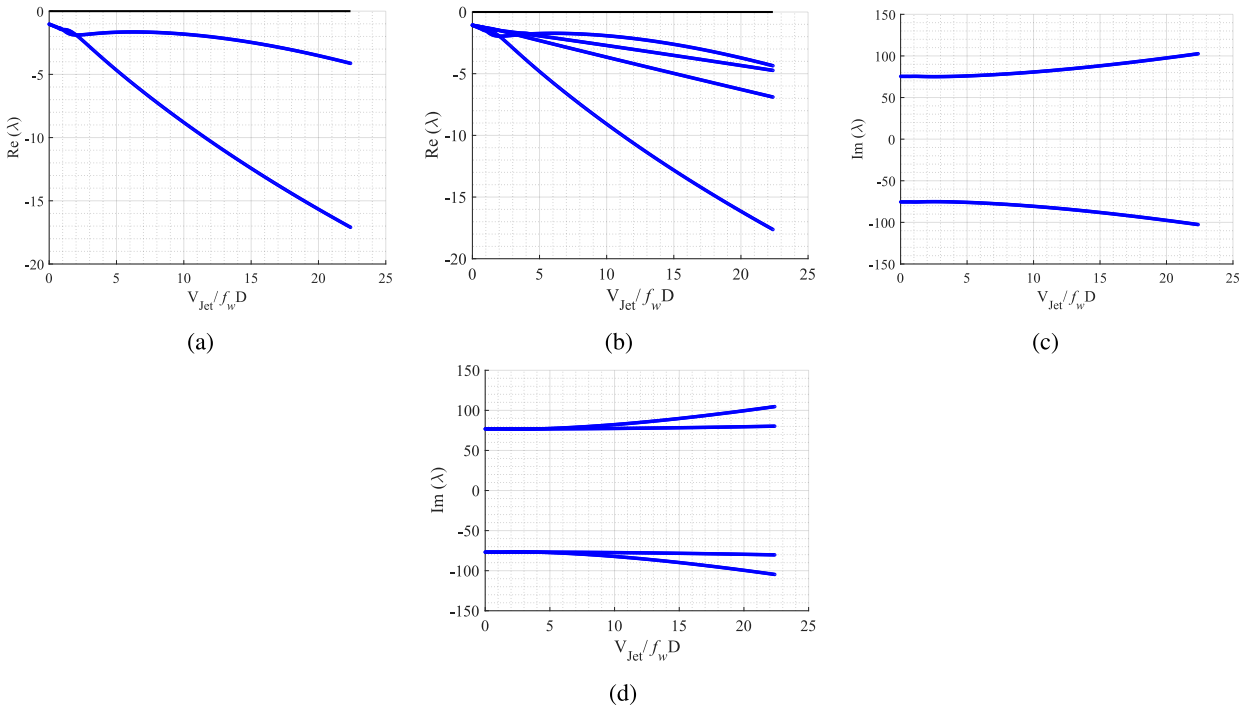

Figure 5.14 Variation of the eigenvalues (Re (λ) and Im (λ)) with reduced jet velocity for the single flexible rod and 2x1 flexible row: (a) and (c) for the single rod 401, and (b) and (d) for the two flexible rods 301 and 401.

results shown in Figure 5.15a. The rod frequency is found to slightly increase with the reduced jet velocities as shown in Figure 5.15b due to the fluid added stiffness as also observed in the FEI experiments. Comparing to the critical reduced jet velocity measured in the FEI tests (see Figure 5.3c), the model results overestimate the critical velocity with an error of approximately 15%.

Direct time domain simulations are also conducted to demonstrate the instability and its growth rate. The responses of the three rods 301, 401, and 501 are calculated at two reduced jet velocities: (i) $V_{Jet}/(f_w\ D) = 5.61$, and (ii) $V_{Jet}/(f_w\ D) = 5.76$. These two reduced jet velocities are near the stability boundary ($V_{Jet}/(f_w\ D) = 5.69$). Figures 5.16a, 5.16b and 5.16c show the responses for rods 301, 401, and 501, respectively at $V_{Jet}/(f_w\ D) = 5.61$ while the responses above the critical reduced velocity are plotted in Figures 5.17a, 5.17b and 5.17c. Although, the responses are obtained from a linear model, the rods response ratios are found to match with the ratios found experimentally. Rod 401 has the highest amplitude, followed by rod 501 and then rod 301.

Figure 5.18 shows the comparison between the trajectories in phase space that obtained below and above the predicted critical reduced jet velocity.

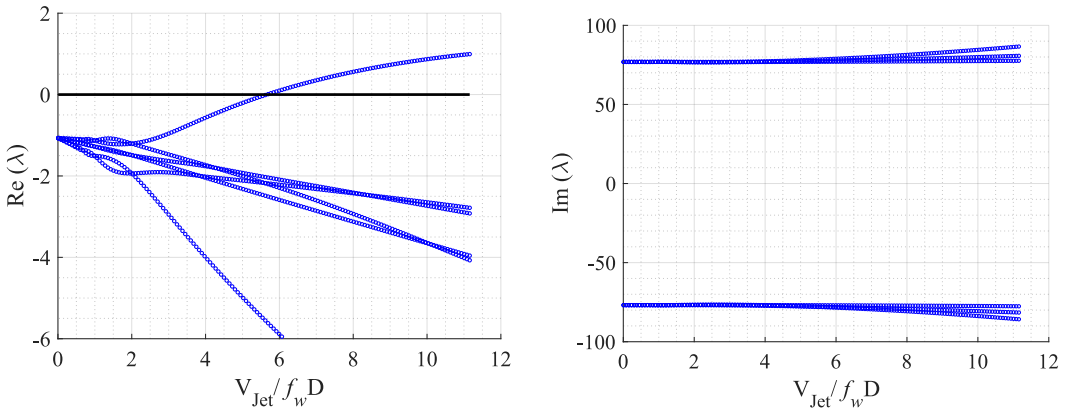

(a) (b)

Figure 5.15 Variation of the eigenvalues with reduced jet velocity for the 3x1 flexible row: (a) Real part of λ, and (b) imaginary part of λ.

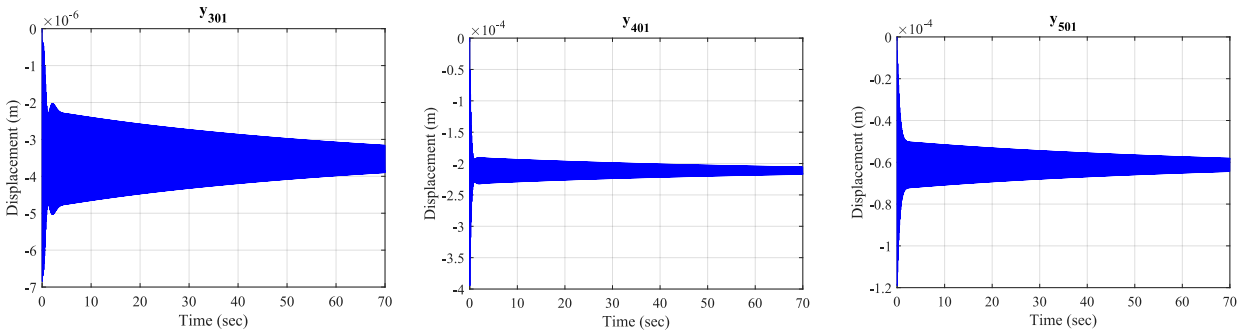

(a) (b) (c)

Figure 5.16 Rods response at $V_{Jet}/(f_w\ D) = 5.61$: (a) rod 301, (b) rod 401, and (c) rod 501.

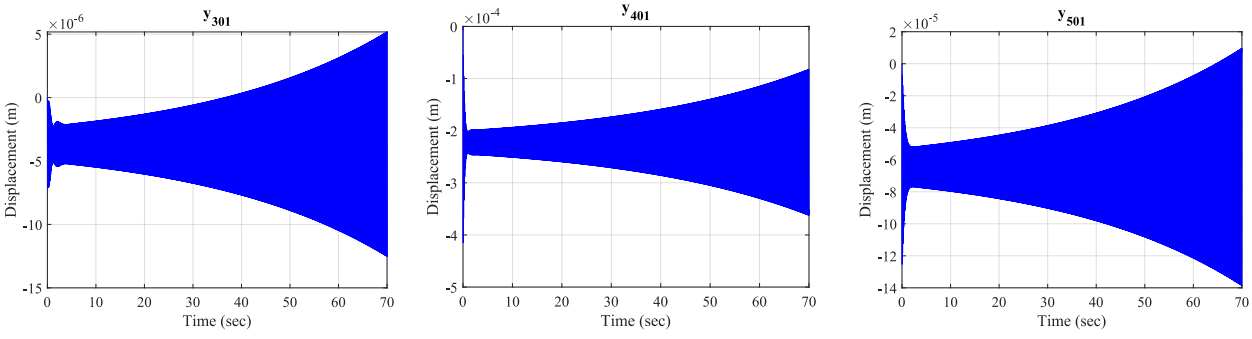

(a) (b) (c)

Figure 5.17 Rods response at $V_{Jet}/(f_w\ D) = 5.76$: (a) rod 301, (b) rod 401, and (c) rod 501.

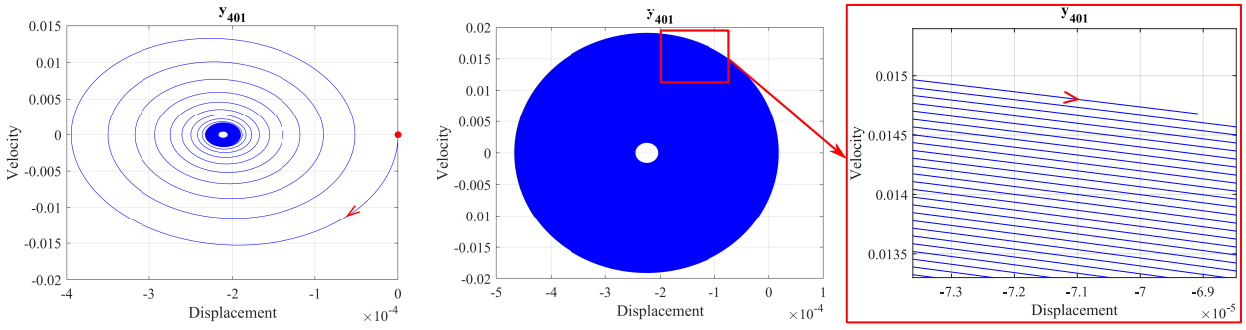

Figure 5.18 Phase portraits for rod 401 at two reduced jet velocities: (a) $V_{Jet}/f_w\ D = 5.61$, and (b) $V_{Jet}/(f_w\ D) = 5.76$.

The stability results for the 3x1 row without including the time delay in the fluidelastic forces show that the array is stable. This means that the fluid-added stiffness does not lead to the instability (i.e. the stiffness controlled mechanism is not the cause of the observed instability). The time delay between the fluid force and rod displacement is the most important parameter to model the instability. Thus, the instability of the array under jet cross-flow is controlled by the damping mechanism.

5.6.2 Stability effect of L_{Jet}/L_{Rod}

PWR fuel rods consists of long small diameter tubes supported at multiple axial locations by spacer grids. The tubes are subjected to external axial coolant flow, however, at certain locations along the span, a flow component transverse to the tube is also existed at proximity of LOCA holes as shown in Figure 5.19a. These locally transverse flows are to be expected where holes have been designed in the baffles. The stability analysis of changing the location of localized jet flow relative to the rod span, on the other hand, would be used to design new reactors with LOCA holes, as well as reconditioning old reactors to make them more safe over their lifespan. A structural analysis of the flexible rod is performed to determine the localized rod stiffness ($K_e = F_{local}/y_{local}$) depending on the location of applied force relative to the rod support (L_{Jet}/L_{Rod}) as shown in Figure 5.19b. A 100 gm weight is applied at different points along the rod span and the local displacement is measured using a laser sensor. Figure 5.20a shows the variation of the normalized effective rod stiffness when the jet fluid force is moved from $L_{Jet}/L_{Rod} = 0.1$ to 0.9.

The stability analysis is performed using the localized rod stiffness in the developed model, since the unstable condition of this parameter is unknown, thus the flow retardation parame-

ter is input in the model as a function of reduced jet velocity (see Figure 5.13). Figure 5.20b shows the variation of the predicted critical reduced jet velocity when the jet flow is moved from the rod root to the rod tip. Because the critical velocity increases with stiffness, it is preferable to place LOCA holes near the spacer grid from a stability aspect. However, the design decision is not straightforward because it should account for the pressure drop across the LOCA hole as well as other design considerations in the thermal-hydraulic analysis of the reactor.

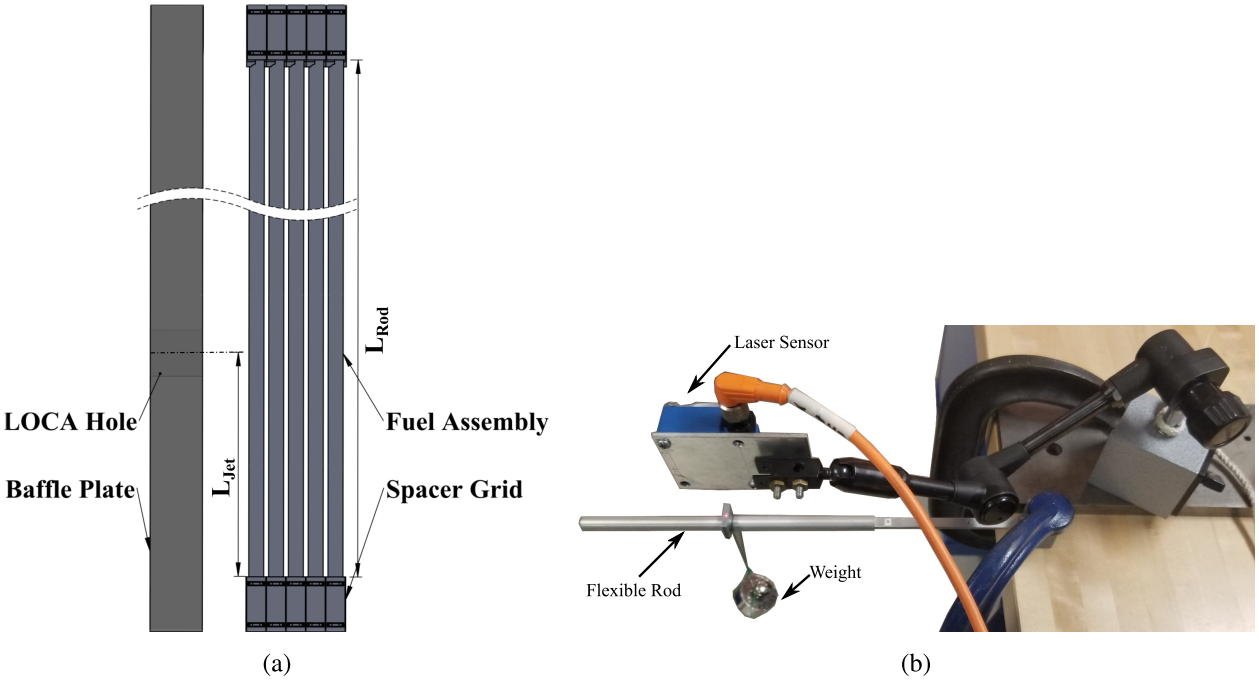

Figure 5.19 (a) schematic showing a single span of fuel rods with LOCA hole, and (b) test rig used to calculate rod stiffness due to jet fluid force.

5.6.3 Stability effect of area derivative

In this section, the effect of the area derivative on rod array stability limit is examined further. Stability analysis is performed for another two cases: (i) constant rod area ($\frac{\partial A}{\partial y}$=0), and (ii) considering the time delay caused by fluid response due to a change in flow area around the rod ($e^{-i\omega\tau}\frac{\partial A}{\partial y}$). The stability results from the two cases are compared with those the experimental critical velocity and with those obtained in the previous section ($\frac{\partial A}{\partial y} \neq 0$). Figure 5.21a shows the variation of the real parts of the eigenvalues with the reduced jet velocity obtained with constant projected rod area. The results show that the fluidelastic instability occurs at $V_{Jet}/(f_w\ D) = 6.0$. This means that neglecting the area derivative

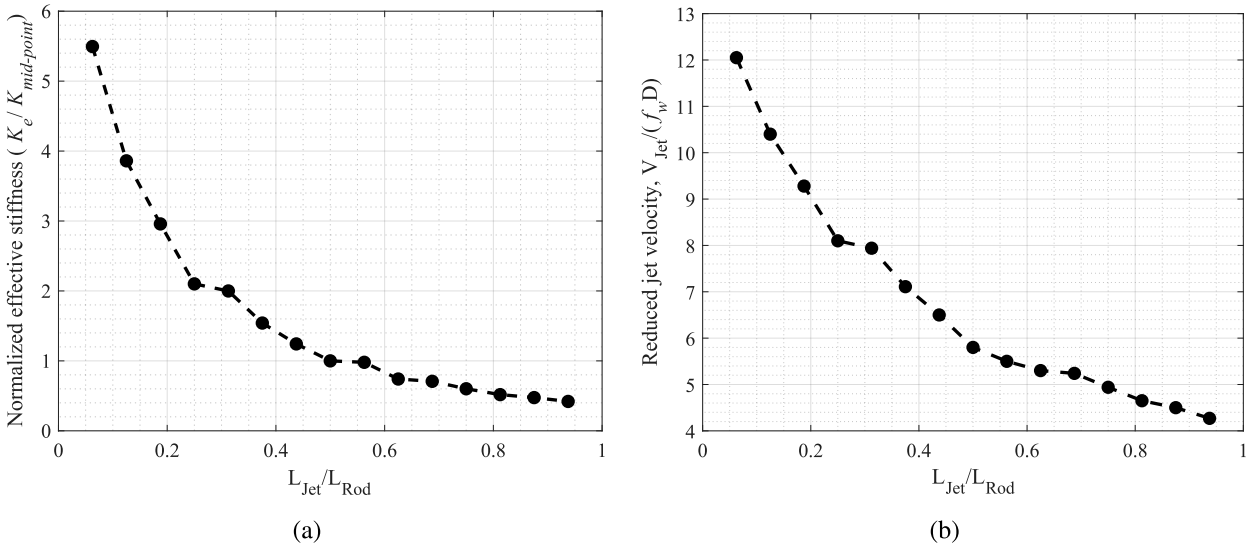

Figure 5.20 (a) variation of normalized rod stiffness ($K_e/K_{mid-point}$) with L_{Jet}/L_{Rod}, and (b) predicted reduced jet velocity as function of L_{Jet}/L_{Rod}.

terms in the equation of motion increases the instability prediction error from 15% to 20%. Moreover, including the fluid response associated with changing area lowers the stability boundary to $V_{Jet}/(f_w\ D) = 4.35$ as shown in Figure 5.21b. Thus, the model underestimates the critical velocity by 13% when the time delay function is multiplied by the rod area derivatives in the model. Considering the area derivative terms in the stability analysis therefore significantly improves model agreement with the experimental results.

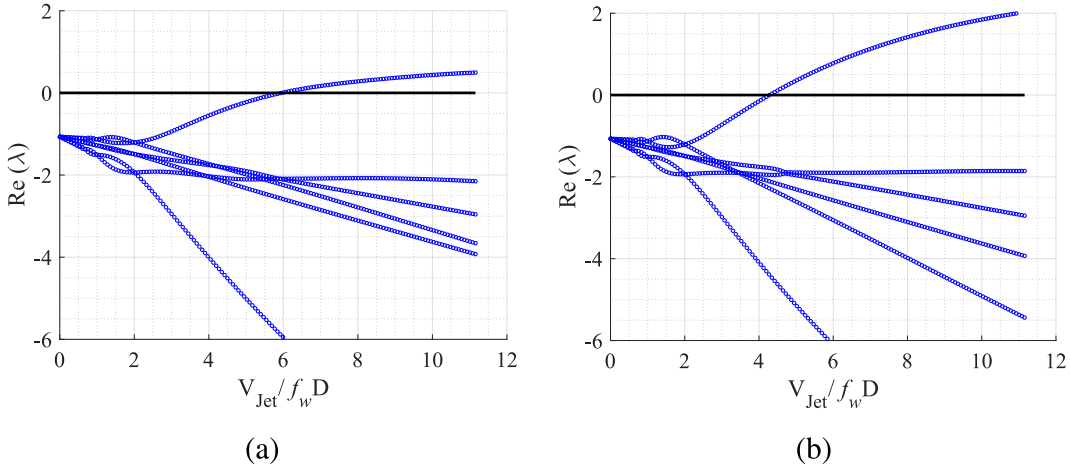

Figure 5.21 Variation of the eigenvalues with reduced jet velocity for two cases: (a) setting $\frac{\partial A}{\partial y}$=0, and (b) $e^{-i\omega\tau}\frac{\partial A}{\partial y}$ in the model.

5.7 Conclusions

The primary aim of this research is to investigate jet cross-flow induced vibration experimentally and theoretically to understand the fundamental mechanisms underlying fuel rod instability in jet cross-flow. Fluidelastic instability (FEI) tests were carried out with four different arrays, single flexible rod, 2x1 flexible row, 3x1 flexible row, and 6x6 fully flexible array. The experiments show that the 3x1 flexible row and 6x6 fully flexible array are fluidelastically unstable.

The development of a dynamic model to predict the critical velocity for the arrays in jet cross-flow case was the main objective of this work. The developed model is based on the quasi-steady approach. However, a new parameter, the rod area derivative, is implemented in the model to capture the dynamic feature of the vibrating rod in jet flow. The fluidelastic forces and time delay are experimentally measured and used as inputs for the developed model.

The main obtained results are summarized as follows:

- The newly developed model accounts for dynamic interactions between rod array vibration with the round jet flow by introducing two terms; the projected rod area and the related rod area derivative due to the rod transverse vibration.
- The time delay of the fluid response demonstrates its dependence on the reduced jet velocity.
- A vibrating rod under circular jet flow changes the rod projected area. As a result, the quasi-static force coefficients are normalized depending on the corresponding projected area. The rod area derivative is found be important and necessary for accurate prediction of the stability boundary of the rod bundle.
- The 3x1 flexible row lost stability at the reduced jet velocity of 5 while the stability threshold of the fully flexible array is reduced to 4.4 due to the flexibility in the array. In comparison to the 2x1 row response, the three rods in the unstable 3x1 row cover the full cross-section of the jet flow emanating from the nozzle, which may result in greater interactions between vibrating rods and the flow boundary causing instability.
- The rod (rod 501) added to the 2x1 row to form the 3x1 row has the highest negative lift derivative compared to the other two rods and thus further contributes to the instability.

- The stability analysis shows agreement between the predicted critical velocity with that obtained experimentally is within an error of 15%. In view of the problem complexity, this is consider quite good for a linear model.

The contributions of the current work are in four areas: (i) accurate measurement the fluidelastic forces in the PWR mock-up array (i.e. closely packed arrays) under jet cross-flow, (ii) experimental determination of the jet fluid response (i.e. time delay) due to the rod response, (iii) introduction of a new term, the rod area derivative, into the governing equations modelling the dynamics of the rod bundle under jet flow condition, which has not before been encountered in the flow induced vibration field, and (iv) development of theoretical model for jet cross-flow induced fluidelastic instability. Future work will focus on the experimental determination of the fluid response associated with changes in the rod area, and whether or not this parameter can lead to instability of a single rod.

CHAPTER 6 ARTICLE 4: PRINCIPAL COMPONENT ANALYSIS (PCA) OF ROD BUNDLE VIBRATION SUBJECTED TO JET CROSS-FLOW

Gad-el-Hak, I, Mureithi, N, Karazis, K, and Williams, G.

This article is under review by "Journal of Sound and Vibration" from 4th August 2022.

Summary

This chapter provides deeper insight into the dynamical behaviour of rod bundles subjected to different jet cross-flows. The axisymmetric rod bundle is tested with three jet-to-rod diameter ratios: $D_{Jet}/D = 1.6$, 2.3, and 3.0. FEI experiments are carried out to collect vibration data for the array in the unstable regime. These data are firstly used to determine the stability limits for the array with the tested nozzles. Then, Singular Value Decomposition (SVD) is applied to the bi-axial vibration data to extract the main features of the rod bundle vibration during instability. Furthermore, Principal Component Analysis (PCA) is employed on the rod bundle vibration in the unstable regime to gain insights into the directionality of rod vibration through rotation angles. A generalized eigenvector model is proposed to predict the directionality of rod bundle vibration under jet-flow excitation. This work is performed to answer the research questions (**Q2** & **Q3**) and to achieve the objective (**O4**).

Graphical Abstract

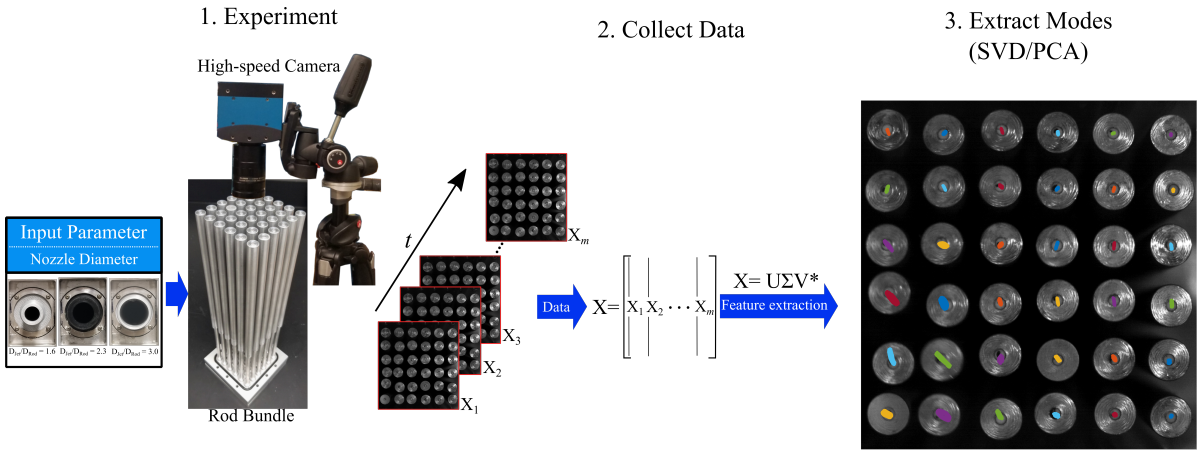

Abstract

In this study, the effect of jet-to-rod diameter ratio on a 6x6 square rod bundle axisymmetric vibration has been experimentally investigated. The dynamical behaviour of the rod bundle is studied for three diameter ratios; 1.6, 2.3 and 3.0. Fluidelastic instability (FEI) tests are performed to obtain the stability threshold of the bundle with the three tested nozzles. A high-speed camera is used to measure the rod bundle vibration. The experiments show that increasing the diameter ratio lowers the critical velocity at which a large vibration amplitude is observed in the bundle (i.e. fluidelastic instability). This is because a larger nozzle diameter generates higher jet flow momentum at the nozzle exit. The maximum vibration amplitude in the bundle, on the other hand, decreases as the diameter ratio increases.

Singular value decomposition (SVD) analysis is applied to extract the main features from the bi-axial vibration data. The results shows that the truncated SVD based of rank of 2 captures the main vibration features of the original data.

Principal component analysis (PCA) is then employed on the rod bundle vibration in the unstable region to gain insights into the directionality of rod vibration through rotation angles. The results show that the derived generalized model could be used to predict the vibration direction angles with different diameter ratio with absolute difference of 10°.

Keywords: Singular value decomposition (SVD), Principal component analysis (PCA), Fluid-structure interaction, Mode shape extraction, Jet cross-flow induced vibrations, Fluidelastic instability, Image processing.

6.1 Introduction

Fluidelastic instability (FEI) is of major concern for tube arrays steam generator and reactor fuel assemblies due to its potential effect. Faster flow velocity improves the thermal performance of heat exchangers. However, the associated fluid forces can produce instability in tube arrays, which can lead to tube-tube impacting, wear fretting failure, tube leakage. FEI analysis serves to ensure the safe operating flow conditions for these heat exchangers.

Uniform cross-flow induced FEI has been extensively studied and reported (see for instance Paidoussis (1981), Price (1995)). Fluidelastic instability is described as a feedback phenomenon between structural motion and the resulting fluid forces. When the feedback is positive, the tube displacement increases, causing fluidelastic instability. The tube array configuration, geometric dimensions and dynamics parameters govern the fluidelastic system dynamics and determine the threshold limit (i.e. *critical velocity*) at which the tube array

becomes unstable. When the critical velocity is exceeded, the tube array vibrates with large amplitudes.

In nuclear reactors, cross-flow induced vibration of fuel rods, due to differences in neighboring assemblies (two or three different fuel assembly designs installed in core), pump flow anomalies, or localized jet cross flow at the core boundaries has been a significant topic of research. The case of the localized circular jet flow is of great importance when the stability of the peripheral fuel rods is evaluated. In contrast with the case of a uniform cross flow the case of the circular jet flow requires that additional parameters are identified and included in the cross flow evaluation (Gad-el Hak et al., 2021). These additional parameters identify the location of the rods in a bundle relative to the jet flow and to specify the jet velocity behavior inside the bundle. Jet eccentricity (ξ) is a jet centerline offset defined with the respect to the array centerline, and the stand-off distance (H) is the gap between the first row to the nozzle exit. Another important parameter is the ratio of the jet diameter to the rod diameter defined by D_{Jet}/D. As a result, studying the contribution of the jet cross-flow parameters to the rod bundle vibration is expected to yield the stability map of the bundle as function of the jet flow parameters. Relatively few studies have addressed the problem of circular jet cross-flow causing FEI compared to the work performed on investigating on the onset of FEI of tube arrays due to uniform cross-flow. Jet-induced FEI has been recently investigated in (Gad-el Hak et al., 2021). The authors performed experiments on a unidirectionally flexible 6x6 normal square rod bundle. Stream-wise and transverse vibrations relative to jet flow were separately investigated. The stability effects of two parameters: jet eccentricity (ξ) and stand-off distance (H) were investigated. The results showed that the vibration was more dominant in the transverse direction. Varying the jet eccentricity ξ changed the flow configuration through the bundle. For $\xi = 0.25$P the resulting asymmetrical flow condition through the bundle reduced the critical velocity compared to the other investigated jet eccentricities. Vortex-induced vibration (VIV) was observed in the stream-wise direction for $\xi = 0$ (jet centered with the middle gap in the bundle). The stability effect of the stand-off distance showed interesting behavior of rod array vibration in the transverse direction. Increasing the H had an initial destabilising and then stabilising effect. This was attributed to the combined effect of two parameters: the jet velocity and the projected area. For larger gaps, the drop in velocity overcomes the increase in the projected area. The stability effect of the third parameter D_{Jet}/D has not been investigated. Evidently, this parameter has a significant effect on the rod array vibration and the threshold stability limit.

The effect of D_{Jet}/D on the rod array dynamics is the focus of the work presented here. During instabilities, rods exhibit orbital motion containing vibration both the stream-wise and transverse vibrations. The orbit plot of rod bundle vibration provides a deeper insight into

the mechanisms underlying the selection of the dominant vibration direction and trajectories of rods vibrating in jet flow. However, it is not possible to separate the purely stream-wise and transverse direction components. Thus, computing an angle of coupled vibrations can be used to identify the vibration direction.

Singular value decomposition (SVD) is the most important matrix factorization method in the theory of linear algebra which has been introduced into signal processing (Brunton and Kutz, 2019). Image processing, applied mathematics, vibration analysis, fluid mechanics, and other fields have all used SVD (Dalpiaz and Rivola, 1997). Furthermore, SVD is used in fault detection and diagnosis for machinery applications to capture the main features of the vibration signals. Different approaches and implementations can be found in the literature including applications to bearings (Ding et al., 2016, Zeng et al., 2019, Zhang et al., 2019, Zhou et al., 2017), gear systems (Wang et al., 2019, Wen et al., 2019), turboprop engines (Ding and Qi, 2016, Li et al., 2017), and denoising application (Zhao et al., 2020). SVD is, however, yet to be applied to rod bundle vibration due to fluidelastic instability.

In the case of axisymmetric rod vibration, it is important to determine the precise angular orientation of rod vibrations. Thus, the original bi-axial vibration data should be rotated to find an optimal direction to present the main vibration direction. Principal component analysis (PCA) has been used in multi-degrees-of-freedom vibration data to determine a linear relation capturing the original data in new coordinate system, i.e. the principal axes. Tumer and Huff (2001a,b) used PCA transformation of vibration data for a helicopter gearboxes to extract the rotation angles and the main principal axis from vibration data measured by triaxial accelerometer. Two angles were defined in the space to present the main vibration direction, then these angles would be used as a reference to diagnose the performance of gearbox.

Ongoing research at Polytechnique Montreal in collaboration with Framatome focuses on understanding the effect of jet flow parameters on rod bundle vibrations. Vibration data collected from a rod bundle subjected to circular jet flow using different nozzle diameters were utilized to study the statistical variations in the mode shape of the rod array, this research aims to answer the following important question. Does there exist a generalized eigenvector model that can predict the rod bundle vibration in jet flows, in addition to characterizing the stability effect of the diameter ratio (D_{Jet}/D). To achieve this, fluidelastic instability tests are conducted on a bundle of axisymmetrically flexible rods, to determine the stability threshold for three jet diameters. These limits are also used to generate a stability map as function of the diameter ratio parameter. This map provides valuable information on safe operation of localized circular jet flows next to fuel arrays. The proposed method uses

standard PCA transformation to compute the rotation angles for each rod for a given nozzle. These angles are then used to propose a generalized eigenvector model based on PCA across the tested diameter ratios.

6.2 Methodology

The main goal of this research is to determine the effect of localized jet cross-flow diameters on rod bundle vibration. For this objective, the rod bundle vibration is obtained for water flow rates incremented up to the condition of FEI, where rod impacting is observed. The FEI tests are conducted in the Fluid-Structure Interaction Laboratory at Polytechnique Montréal. The experimental tests provide the raw data required for the analysis outlined above.

6.2.1 Mathematical formulation

Consider a reduced 2x2 rod bundle vibrating in a jet cross-flow, as shown in Figure 6.1a. The rod axes are perpendicular to the x–y plane and each rod vibrates in this plane with the same frequency. The jet flow is injected from the nozzle and spreads in 3D space through the rod array. The flow velocity at a certain point in the rod bundle is defined by the transverse distance and stream-wise distance relative to the jet flow. The displacement components of a rod (k) in the transverse and stream-wise directions are y_k and x_k, respectively. The jet fluid forces are exerted on the rods in the x and y directions. These called *fluidelastic forces* components are coupled with rod motion. The coupled equation of motion for the 2x2 rod bundle can be expressed as follows:

$$M\ddot{\vec{x}}(t) + C\dot{\vec{x}}(t) + K\vec{x}(t) = 0;\ \vec{x} = [x_1, x_2, x_3, x_4, y_1, y_2, y_3, y_4]^T \tag{6.1}$$

where $M = M_s + M_f$; $C = C_s + C_f$; $K = K_s + K_f$.

M_s is the mass matrix of structure, C_s is the structure damping matrix, K_s is the structure stiffness matrix, M_f is the fluid-added mass matrix, C_f is the fluid-added damping matrix, and K_f is the fluid-added stiffness matrix.

The solution of the coupled equation of motion provides two displacement components for each rod in x and y directions. These displacements can be written as follows:

$$Rod_k response = \begin{bmatrix} x_k \\ y_k \end{bmatrix} = \begin{bmatrix} A_{x_k} e^{i\omega t + \phi_{x_k}} \\ A_{y_k} e^{i\omega t + \phi_{y_k}} \end{bmatrix}; k = 1, 2, 3, 4. \tag{6.2}$$

The response vector can be reduced by introducing a rotation angle (θ) which is an angle

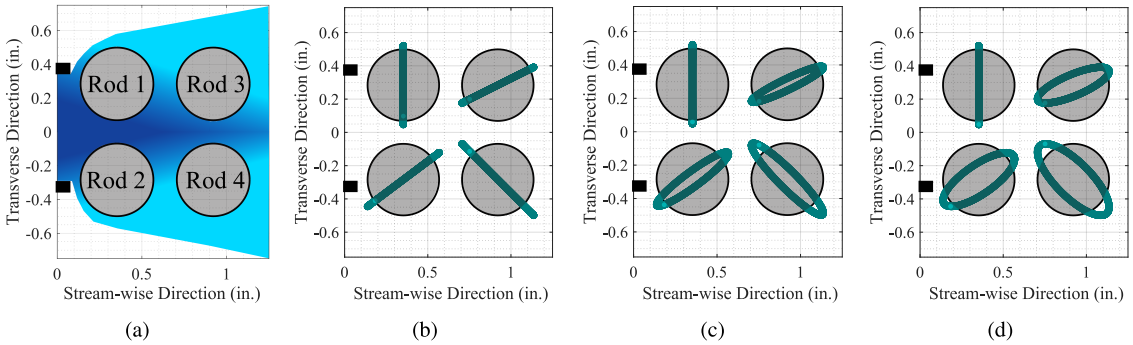

Figure 6.1 (a) 2x2 inline square rod bundle in a jet cross-flow, and the rod bundle response with three phase difference (ψ): (b) $\psi = 0$, (c) $\psi = 20°$, and (d) $\psi = 40°$.

obtained from the amplitude ratio x_k/y_k. The phase difference (ψ) between ϕ_x and ϕ_y is also defined as $\psi_k = \phi_{x_k}$- ϕ_{y_k}. Figure 6.1b is graphically presenting a rod bundle mode shape with different θ for each rod at $\psi = 0$. While Figures 6.1c and 6.1d are presenting the mode shape when $\psi = 20°$ and $40°$, respectively. In this paper, the main features of 6x6 rod bundle mode shape are captured using SVD and PCA from the FEI experimental data.

6.2.2 Experimental setup

Flexible rod bundle

A square array of rods is prepared to perform the FEI tests in the water tunnel at Ecole Polytechnique. The set of flexible rods used in the water experiments are machined from solid aluminum rods with a diameter of 0.43 inches. This main diameter is reduced to 0.27 inches near the rod support to form an axisymmetric "spring" for each rod in the bundle as shown in Figure 6.2a.The rods have axisymmetric flexibility and vibrate in the 2D plane with the same nominal frequency of 35 Hz in air. The flexible rods are mounted as cantilever beams in a square array configuration having a pitch ratio (P/D) of 1.32. In the test section, the full 7.925 inches total rod span is exposed to water flow (i.e jet flow and surrounding fluid). Figure 6.2b shows the fabricated 6x6 flexible rod array.

Measurement system and image processing algorithm

The objective of the experiments is to measure the rod bundle vibrations for a range of jet velocities leading up to the onset of fluid-elastic instability. A full-field rod bundle vibration measurement is preferred when analyzing the square array so as to provide useful insight on how each rod in the bundle behaves for varying the jet flow speed. Since the jet velocity

Figure 6.2 (a) single rods, and (b) 6x6 in-line square flexible rod bundle.

components are not constant through the test section, the vibration is affected by the rod position relative to the jet flow. As a result, it is important to identify locations where the effect of jet flow on rod bundle vibration is reduced. The first step in this study is to design and develop a method for measuring the rod bundle's time-dependent displacement.

Strain gauges are typically used to measure tube array vibration by installing them on the supports of the vibrating tubes. The installation of strain gauges on flat plates is straight forward; however, for small cylindrical surfaces, as in our axisymmetric flexible rods (i.e. 0.27 in. diameter) strain gauge installation is impractical. In addition, the sealing products (M-Coat B + M-Coat F) used to seal the gauges from the water, change the tube damping, hence it is impossible to have uniform damping for all instrumented rods. Thus, selecting a non-intrusive data acquisition system to measure the rod response is strongly recommended.

In the present work, a high-speed digital camera (Motion BLITZ Cube 4, MIKROTRON) is used to capture images of the rod bundle in steady-state response, representing the rod

bundle motion at a specific velocity. The image frame size (880x846 pixels) is extended to capture all the rods. The camera frame rate of 400 frames/sec. is more than ten times the rod frequency in water. The performance of the high-speed camera at this speed is confirmed by Catton et al. (2004). The rod bundle motion for varying jet flow velocities is essentially represented by a series of unprocessed snapshots: 6,000 frames in a single video (about 15 seconds).

The rod motion is extracted from the raw images of the vibrating rod bundle using an image processing algorithm built in MATLAB. Based on the colour contrast between the reflective aluminium rod top surface and the dark background test section, the code detects the rod edges (i.e. red circles) as shown in Figure 6.3a. In the algorithm, the raw image is split into 36 square unit cells (the rods number in the bundle) as shown in Figure 6.3a. The code then searches within each unit cell for the moving rod (circle) to obtain the time-dependent displacement for each rod in the bundle. Figure 6.3b shows the rod bundle vibration on a processed image.

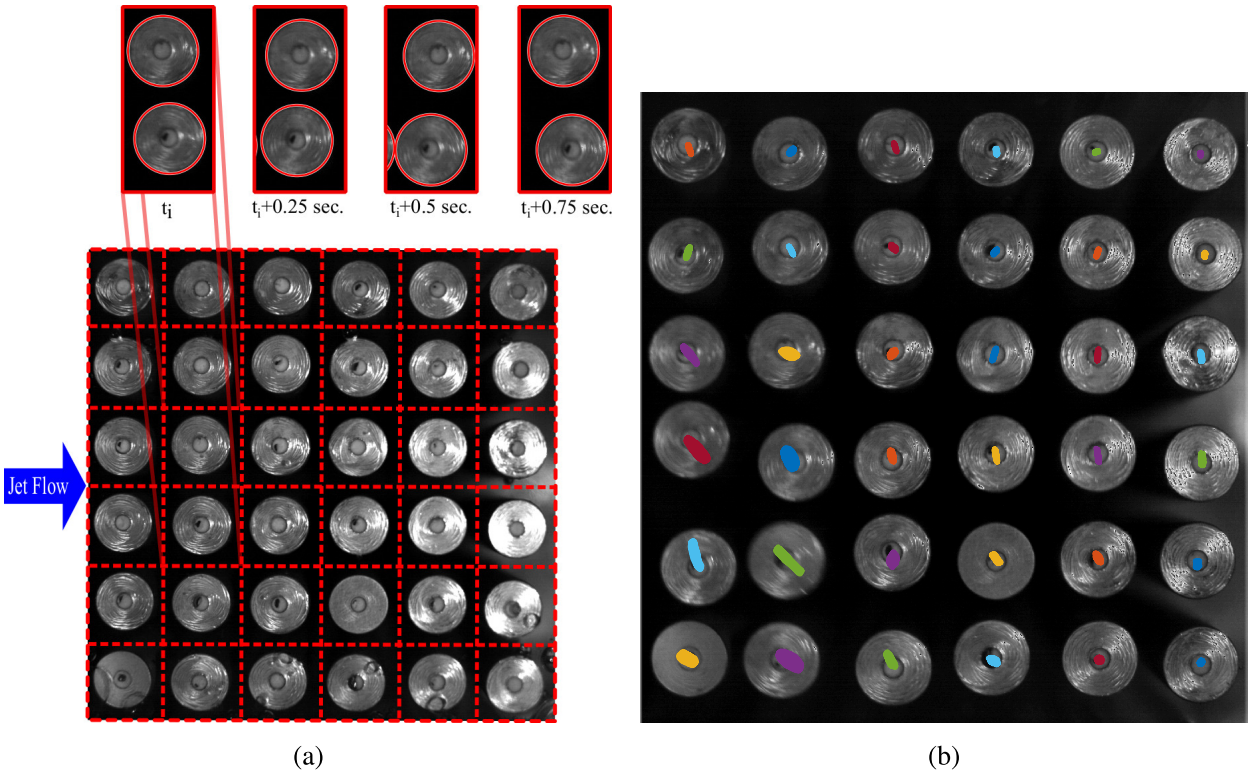

Figure 6.3 (a) Image processing technique, and (b) rod bundle vibration obtained by processing a series of images.

Test loop set-up

The test loop consists of nine main components as labelled in Figure 6.4. The inlet diffuser (labelled 1 in Figure 6.4) expands the water flow from the 3-inch pipe to the rectangular test section area. To minimize induced turbulence, a flow straightener (labelled 2 in Figure 6.4) ensures a more uniform flow in the loop. The uniform flow is delivered to a settling chamber (label 3) prior to conversion to a jet flow. A nozzle is fixed in the jet flow positioning mechanism at the mid-height of the test section to direct the jet flow towards the flexible rod bundle. Polylactic acid (PLA) plastic is used to 3D print three nozzle of diameter, 0.7, 1.0, and 1.3 inches. Rigid acrylic half-tubes are fixed on both sides of the test section to provide the uniformity of the flow around the vibrating tubes. The high-speed camera is positioned in front of the top acrylic panel, so that the viewing plane of the camera is normal to the axis of the tubes as shown in Figure 6.4. Flow is returned to the tank via the transition section (label 6). All test section components are assembled horizontally on a sturdy structure to eliminate any extraneous vibrations that could come from the structure.

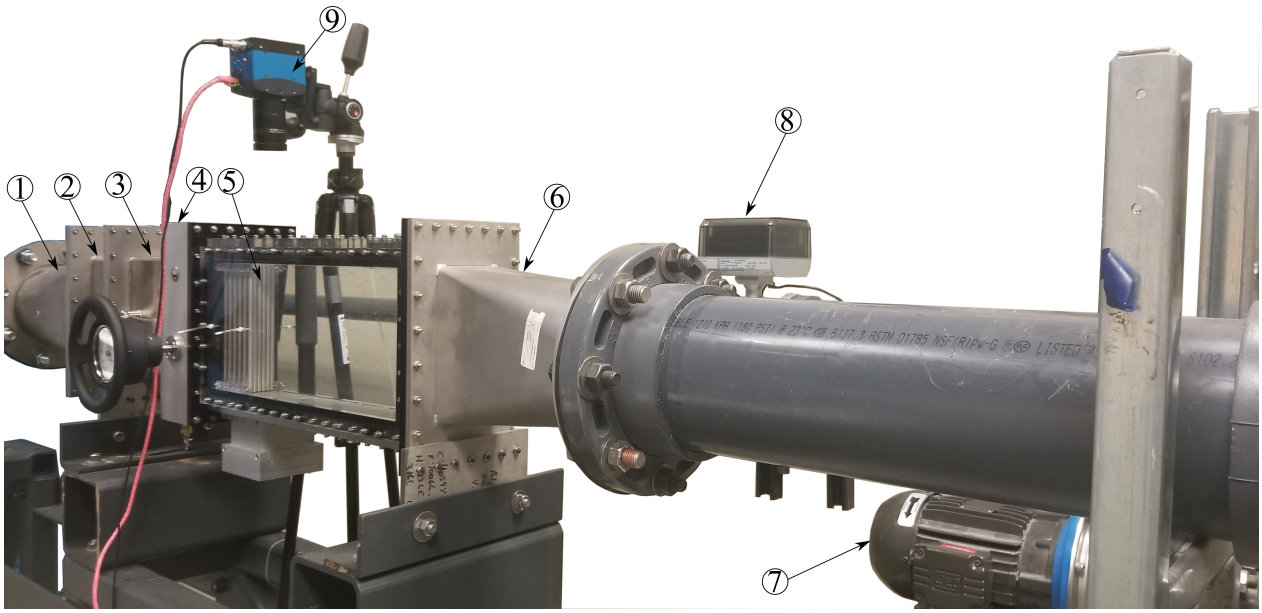

Figure 6.4 The main components of test loop set-up are labelled: (1) diverging rectangular transition section, (2) flow straightener, (3) empty chamber, (4) jet flow positioning mechanism, (5) rod bundle, (6) converging rectangular transition section, (7) centrifugal pump, (8) water flow meter, and (9) high-speed camera.

Test parameters

FIV tests are done for three nozzle diameters, 0.7, 1.0, and 1.3 inches, to determine the effect of nozzle diameter on the critical instability flow velocity. Figure 6.5 shows the three 3D printed nozzles installed inside the test section. For each test, the jet centerline is directed to column 4 in the bundle as shown in Figures 6.6a, 6.6c, and 6.6e to study the effect of jet eccentricity relative to the rod array. The cross-sectional area of the nozzle is the maximum of possible flow area of the jet flow entering the bundle. The jet eccentricity then determines the number of rods exposed to the jet flow as illustrated in the projected views from each nozzle in Figures 6.6b, 6.6d, and 6.6f. The column number and row number of the rods are used as a Cartesian coordinate system to identify the location of each rod. For example, rod 402 is located in column number 4 and row number 2 as shown in Figure 6.6c.

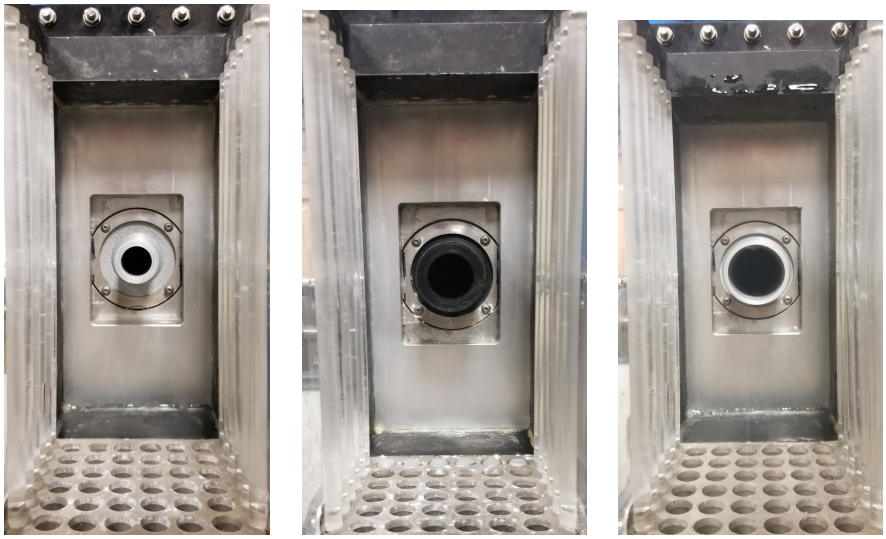

(a) (b) (c)

Figure 6.5 Three tested nozzles: (a) $D_{Jet} = 0.7"$, (b) $D_{Jet} = 1.0"$, and (c) $D_{Jet} = 1.3"$.

6.3 Test results

Three different sized nozzles are investigated with $D_{Jet}/D = 1.6$, 2.3, and 3.0. The fully flexible 6x6 rod bundle is tested using the nozzles to obtain its dynamical behavior when subjected to transverse jet flow. Tracking the rod center motion in the x and y directions provides the axisymmetric rod bundle vibration. The analysis of results is presented in three subsections: response amplitude, singular value decomposition (SVD) analysis, and principal component analysis (PCA).

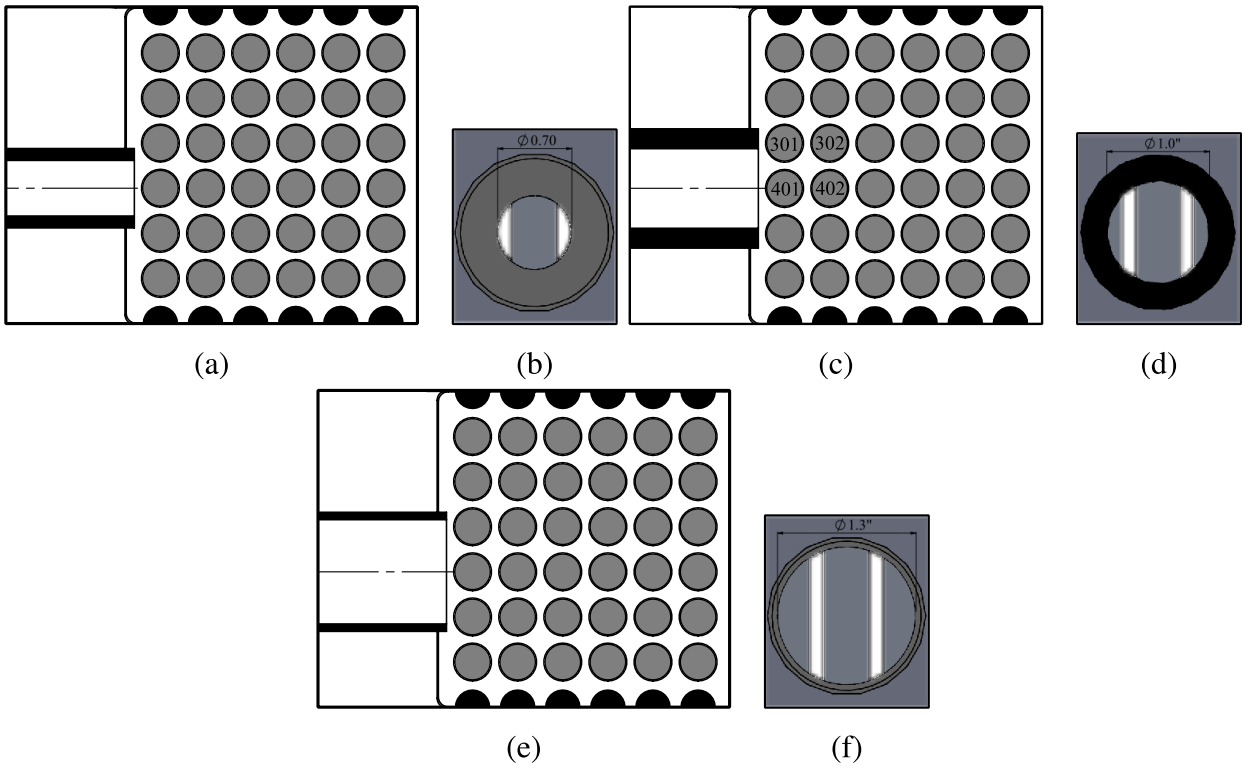

Figure 6.6 Top sectional views and corresponding projected views from the nozzle for the three jet diameters: (a) and (b) for $D_{Jet} = 0.7$", (c) and (d) for $D_{Jet} = 1.0$", (e) and (f) for $D_{Jet} = 1.3$", respectively.

6.3.1 Jet-induced vibration response

In this section, the transverse and stream-wise vibrations are plotted versus average jet velocity individually to highlight the array's most prominent vibration direction. The RMS rod tip displacement is expressed as a percentage of the internal rod gap ($g = P - D$). The jet velocity is calculated as the average flow velocity discharge from the nozzle. The following sub-sections present the rod array vibration with different jet flow diameters.

Dynamical behavior of fully flexible 6x6 rod bundle with $D_{Jet}/D = 1.6$

A full-field rod bundle vibration is extracted from the image processing algorithm. For brevity, we present only the responses for the first three rows, which have the most significant amplitudes in the array. Figure 6.7 shows the vibrational behaviour for the 18 rods with increasing jet flow velocity from 2.5 m/s to 4 m/s. When the flow velocity reaches 3 m/s an unstable vibration with a significant amplitude is observed. For velocity values larger than 3 m/s, the response increases rapidly from 5%g to 20%g for a velocity increment of only 0.1

m/s. In this densely packed bundle, the strong hydrodynamic coupling causes all rods to follow the same vibration rate, with different amplitudes depending on rod location relative to the jet flow.

In the first row, the maximum vibration amplitude occurs in the transverse direction for rod 501. However, for rod 401 the vibration is approximately equal in both directions. The detailed dynamics for rod 401 are shown in Figure 6.8, where time-traces of the response are plotted for two jet velocities: 3.0 m/s, and 3.9 m/s. Corresponding orbit plots, and 3D power spectral density (PSD) plots are also shown. The orbit plot shows the rod vibration axis is inclined by roughly 45° relative to the transverse direction. The rod vibrates around a point shifted from its static center point by the jet momentum. The rod vibration occurs at a single frequency, corresponding to the rod natural frequency in water as seen in the PSD plot.

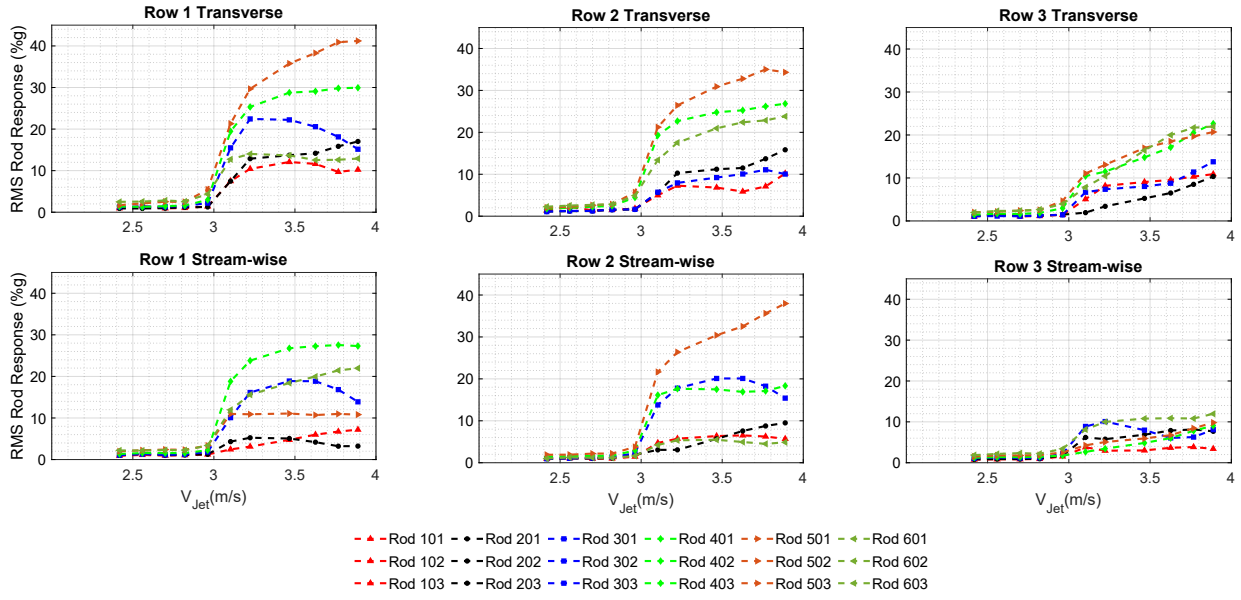

Figure 6.7 Rod bundle vibrations in transverse and stream-wise directions for $D_{Jet}/D = 1.6$.

The dynamics of rod 402, which is located downstream of rod 401 in the same column, is shown in Figure 6.9. Rod 402 vibrates around its static centre as opposed to rod 401 due to the mixing flow from the first row. A small peak at 32.5 Hz observed in the PSD plot, may be due to vortices generated in the first two rows. The rod motion trajectory is an elliptical shape having a major axis close to the transverse direction.

Figure 6.10 shows orbit plots for rod 401 for four jet velocities in the unstable vibration regime, to see how their motion trajectories are changed during the instability. The rod 401 vibrates in a straight line path with zero phase difference for low velocity, but transitions to

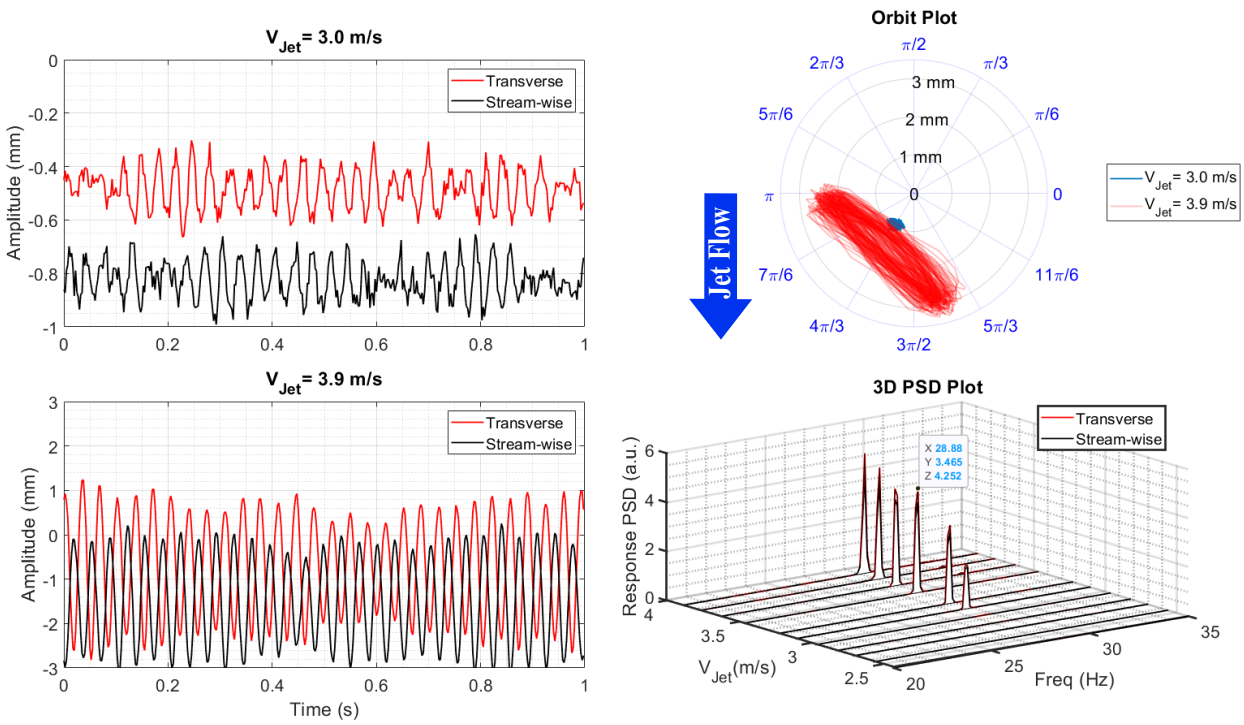

Figure 6.8 Time traces, orbit plot, and PSD plots for Rod 401.

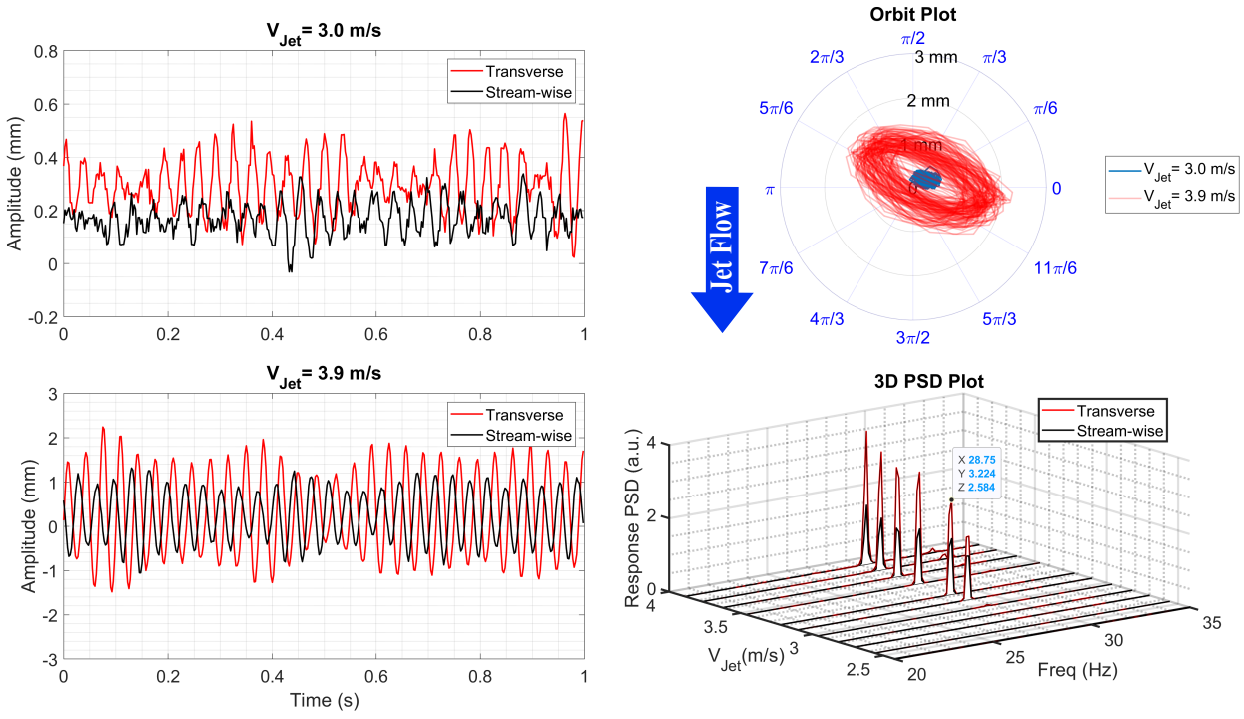

Figure 6.9 Time traces, orbit plot, and PSD plots for Rod 402.

an oval orbit as the jet velocity increased.

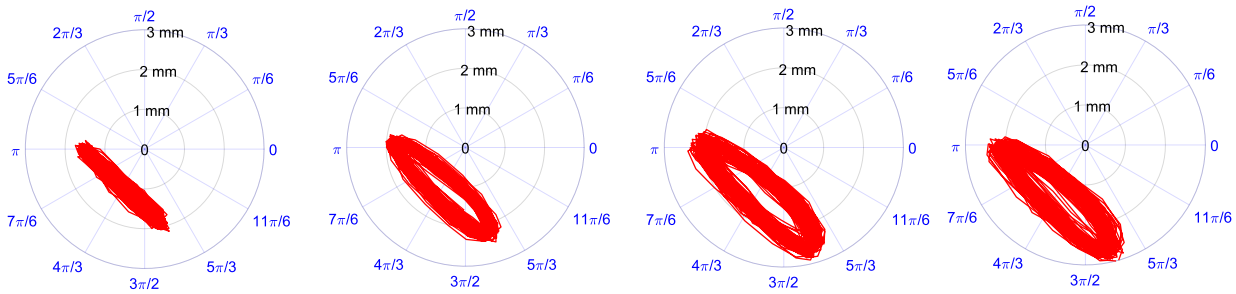

(a) (b) (c) (d)

Figure 6.10 Orbit plots for rod 401 for four jet velocities: (a) V_{Jet} = 3.1 m/s, (b) V_{Jet} = 3.2 m/s, (c) V_{Jet} = 3.46 m/s, and (d) V_{Jet} = 3.6 m/s, respectively.

Dynamical behavior of fully flexible 6x6 rod bundle with D_{Jet}/D = 2.3

Tests for a large nozzle diameter having D_{Jet}/D = 2.3 are presented here. The bundle is tested for velocities V_{Jet} = 1.5 m/s to 2.5 m/s covering the range from turbulence induced vibrations to instability conditions as shown in Figure 6.11. The first small peak in the vibration response is observed at V_{Jet} of 1.85 m/s. However, on increasing the jet velocity, the response is decreased to 5%g. Above V_{Jet} = 2 m/s, large amplitude unstable vibrations occur in the array reaching 30%g in the transverse direction. Compared to the case D_{Jet}/D = 1.6 results, the maximum transverse vibration in the bundle is reduced from 40%g to 30%g. The smaller jet diameter results in a lower drag force emanating from the jet cross sectional area. Figure 6.12 presents more details of the vibrations behavior of rod 402. For low flow velocities, the rod vibrates at 32.25 Hz, the first peak of vibration seen in 3D PSD plot. This frequency is also observed for the case D_{Jet}/D = 1.6 response but for higher velocities; however, in the latter case, it had little effect on the rod bundle vibration (see Figures 6.7 and 6.9). For the larger nozzle a 10%g response is measured; this response is due to vortex induced excitation. Vortex induced vibration (VIV) results from lock-in between shedding frequency on rod natural frequency. The rationale for this response may lie on the matching of the geometrical conditions between the circular nozzle (i.e. flow gap area) and the array producing and intensifying the vortices behind the column facing jet flow, as shown graphically in Figure 6.6.

Orbit plots for rod 402 for four jet velocities covering the VIV and FEI vibration regions are shown in Figure 6.13. At VIV, lock-in condition, the jet Strouhal number Str_{Jet} equals to 0.43. In literature, da Silva and Metais (2002) investigated numerically the dominant

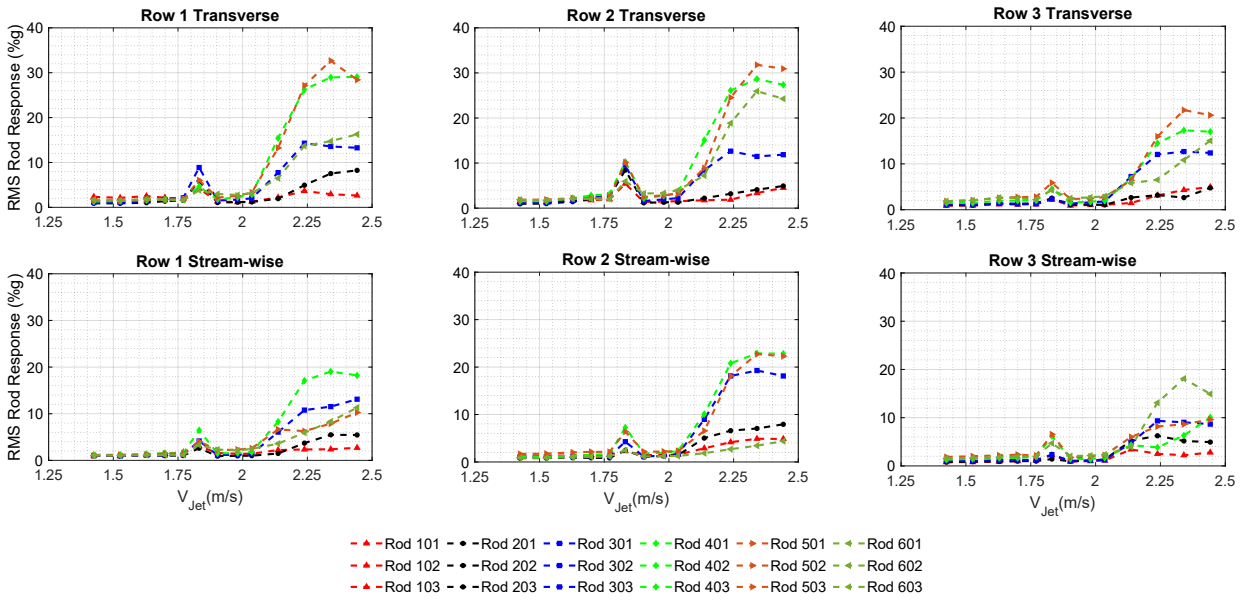

Figure 6.11 Rod bundle vibrations in transverse and stream-wise directions for $D_{Jet}/D = 2.3$.

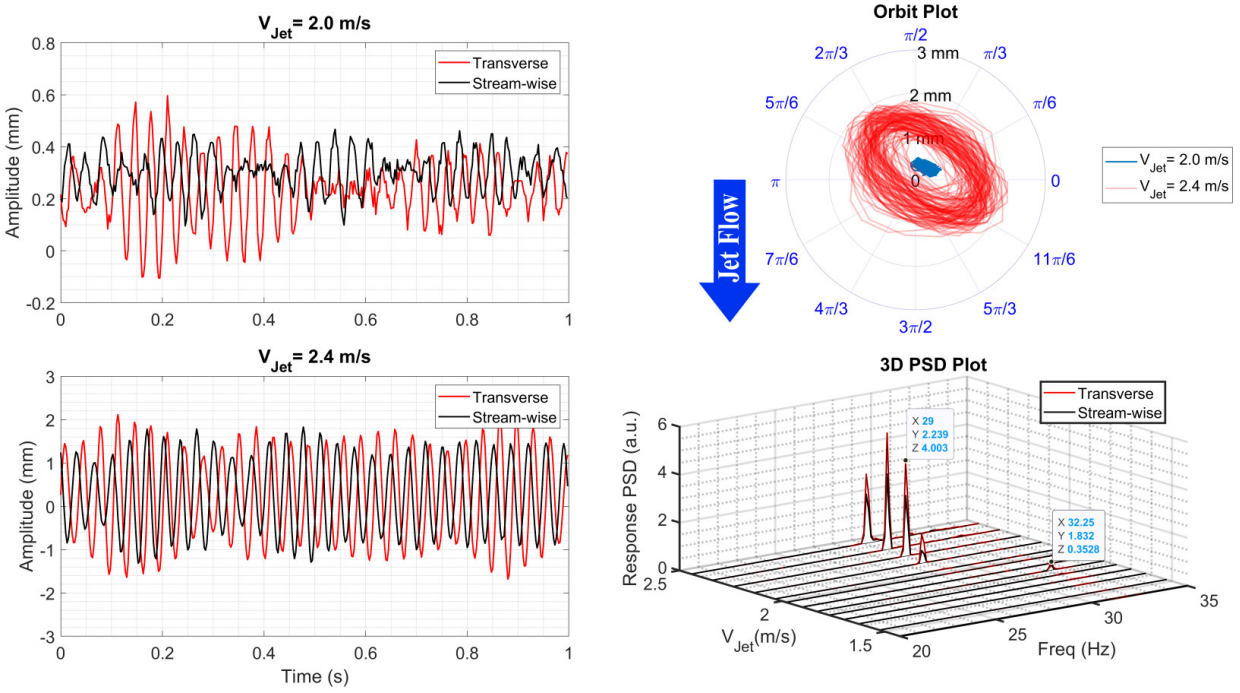

Figure 6.12 Time traces, orbit plot, and PSD plots for Rod 402.

Strouhal number for the vortex dynamics of a forced round jet with variflap excitation (which is a combination of a varicose (axisymmetric) excitation and of a flapping excitation). The accompanying preferred frequency was found to correspond to $Str_{Jet} = 0.38$, which is close

to value obtained here. This could explain what happens with the rod 402 motion. The rod vibrates in a straight line having an inclination angle of 30° as shown in 6.13a, suggesting that the vortices excite the rod in variflap mode. The vibration angle is flipped to 150° in the FEI region as shown in Figure 6.13b. With increasing jet velocity, vibration amplitudes increase resulting in a large orbital motion also having a large minor axis.

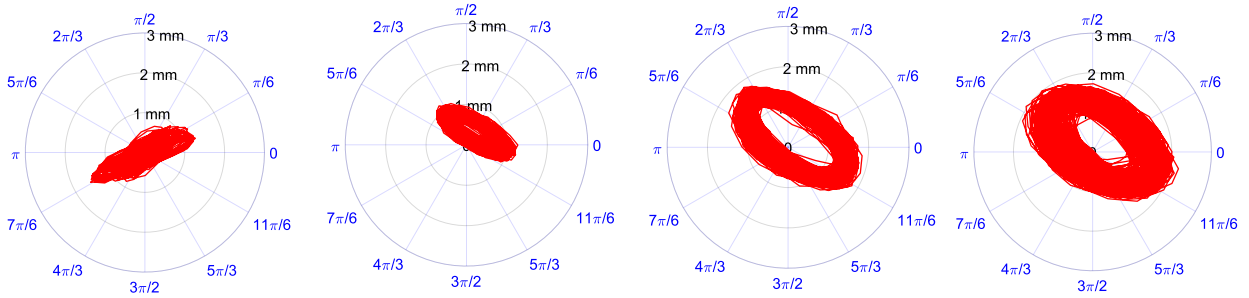

Figure 6.13 Orbit plot of rod 402 with four jet velocities: (a) $V_{Jet} = 1.8$ m/s, (b) $V_{Jet} = 2.14$ m/s, (c) $V_{Jet} = 2.24$ m/s, and (d) $V_{Jet} = 2.34$ m/s, respectively.

Dynamical behavior of fully flexible 6x6 rod bundle with $D_{Jet}/D = 3.0$

Finally, the fully flexible (6x6) rod bundle is tested with the nozzle having $D_{Jet}/D = 3.0$. The first three rows response is plotted for $V_{Jet} = 0.75$ m/s to 1.75 m/s in Figure 6.14. The critical jet velocity decreases to 1.46 m/s, which is lower than the 2.0 m/s for the $D_{Jet}/D = 2.3$, and 3.0 m/s for the $D_{Jet}/D = 1.6$. Moreover, the third row response is seen to monotonically decrease with increasing nozzle diameter (see Figures 6.7, 6.11). This could be attributed to the reduced jet momentum dissipate for the smallest nozzle diameter, resulting in a high jet flow that travels deeper into the bundle. Above the critical velocity, the rods vibrated at a single frequency of 29.25 Hz as shown in Figure 6.15. This frequency corresponds to the natural frequency of rods in water, confirming fluidelastic instability as the excitation mechanism.

The row 1 transverse vibration is higher than the stream-wise vibration, because the first row in the bundle is subjected to higher jet momentum, thus, the rods are deflected in the stream-wise direction. As a result, the rod motion is mostly in the transverse direction, as shown in Figure 6.15 by a narrow elliptical orbit plot. Rod 402 in the array, which is behind rod 401, vibrates in a more wider elliptical orbit as shown in Figure 6.16. Because the flow path is modified when the jet impinges on the rods, it could cause static loads on the rods in the direction of its path, as observed by (Denizou et al., 1985). The vibratory orbit centre

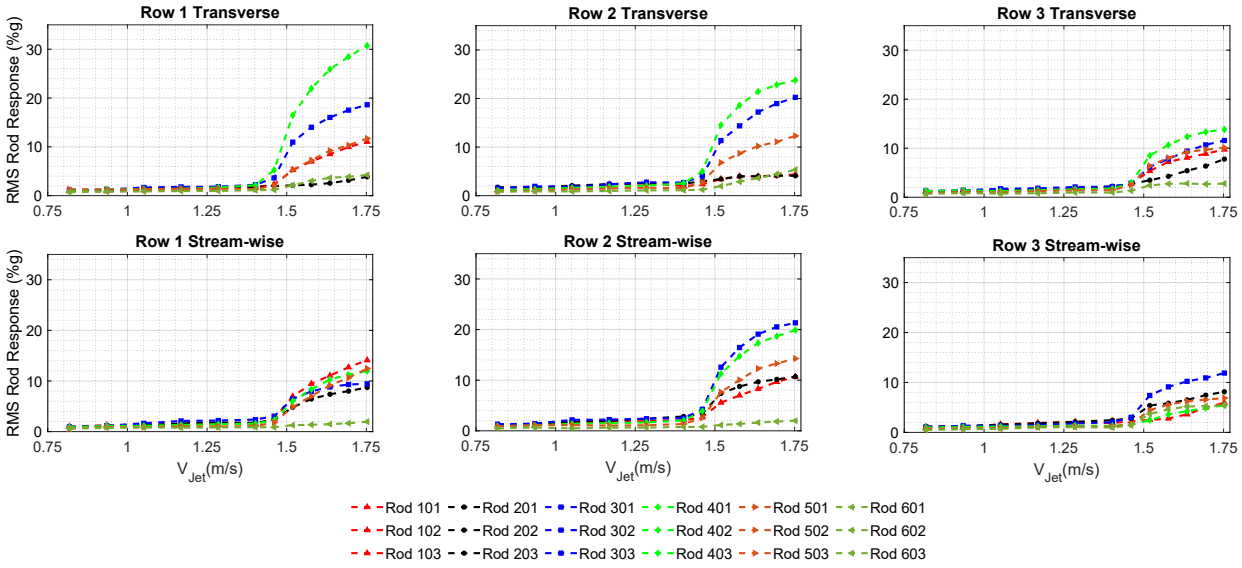

Figure 6.14 Rod bundle vibrations in transverse and stream-wise directions for $D_{Jet}/D = 3.0$.

of rod 402 is opposing to the jet flow direction.

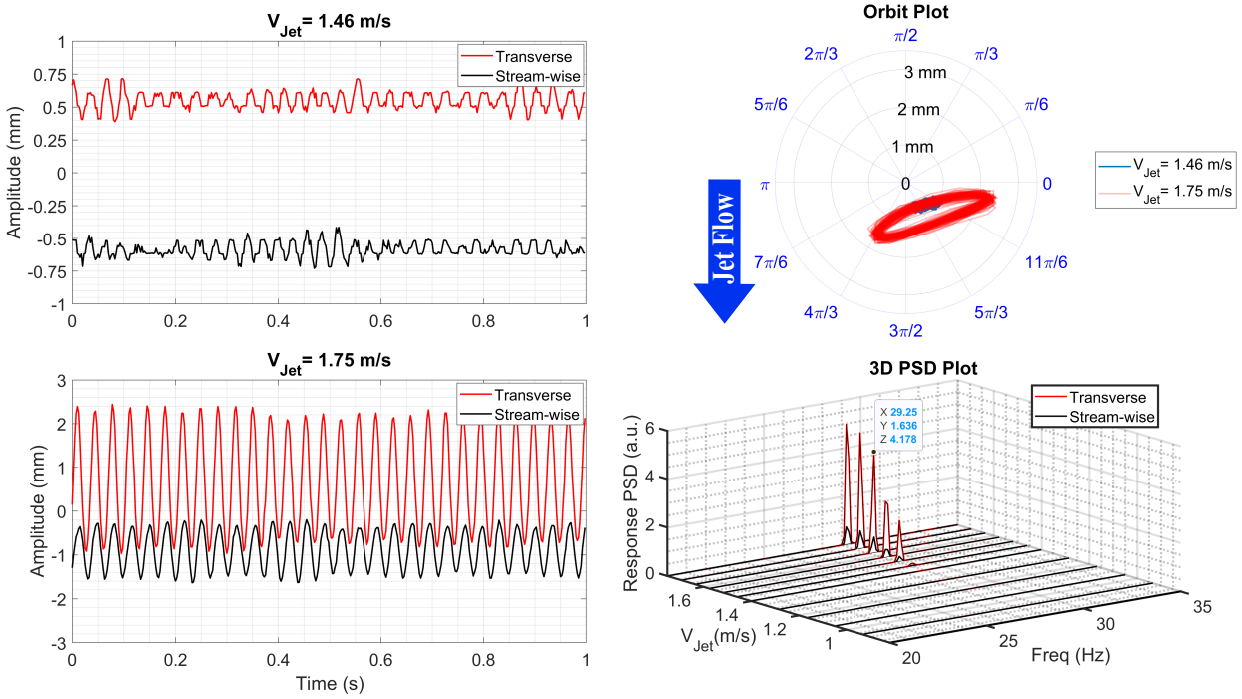

Figure 6.15 Time traces, orbit plot, and PSD plots for Rod 401.

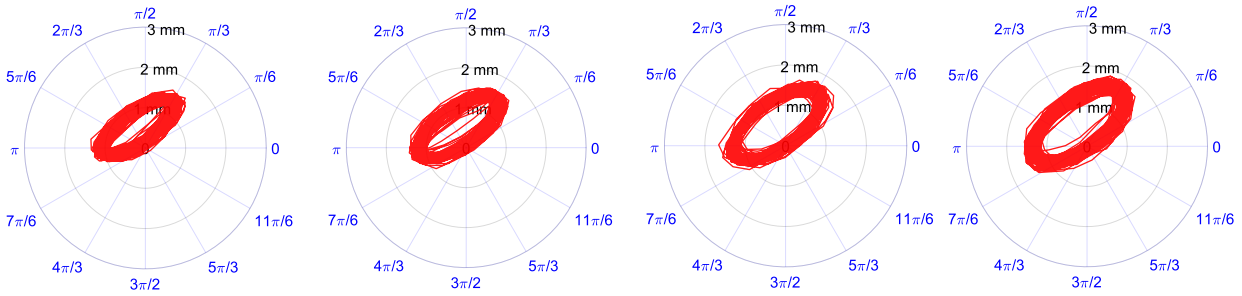

(a) (b) (c) (d)

Figure 6.16 Orbit plot of rod 402 with four jet velocities: (a) V_{Jet} = 1.57 m/s, (b) V_{Jet} = 1.64 m/s, (c) V_{Jet} = 1.7 m/s, and (d) V_{Jet} = 1.75 m/s, respectively.

6.4 Stability boundary

The dynamical behavior of the rod bundle subjected to jet cross-flow has been investigated for three nozzle diameter ratios D_{Jet}/D = 1.6, 2.0, 3.0. Fluidelastic instability of the rod bundle was found to cause large amplitude vibrations. The stability equation for the jet cross-flow induced vibration was previously defined in (Gad-el Hak et al., 2021) as follows:

$$\frac{V_{Jet}}{fD} = K\sqrt{\frac{m\delta_0}{\rho D^2}\frac{D}{D_{Jet}}\frac{L}{D_{Jet}}} \tag{6.3}$$

The non-dimensional parameters, including the reduced velocity V_{Jet}/fD, the mass damping parameter $m\delta_0/\rho D^2$, the reduced jet diameter D/D_{Jet}, and the jet to length ratio L/D_{Jet} are used to construct stability maps that identify the stability threshold as a function of jet diameter ratio (D_{Jet}/D).

The rod frequency (f) and damping ratio (ζ) in water are the input parameters for the stability equation. Free decay tests in air and water for a single flexible rod in the bundle are performed to determine these parameters. These tests are conducted by fixing all rods except one, which is free to vibrate as shown in Figure 6.17a. Figure 6.17b shows the experimental results for the air and water tests. The exponential decay envelope is extracted by a Hilbert function as presented in the figure. The rod frequency is measured to be 35.0 Hz in air and 29 Hz in water. The difference in frequencies is used to compute the added mass. The damping ratio is 0.23% in air and 2.0% in water.

The stability constant (K) in Equation 6.3 is determined to show the stability effect of the diameter ratio on the rod array instability threshold. The threshold boundary for the jet-rod aligned configuration (see Figure 6.6) with the three ratios D_{Jet}/D = 1.6, 2.3, and 3.0 has a

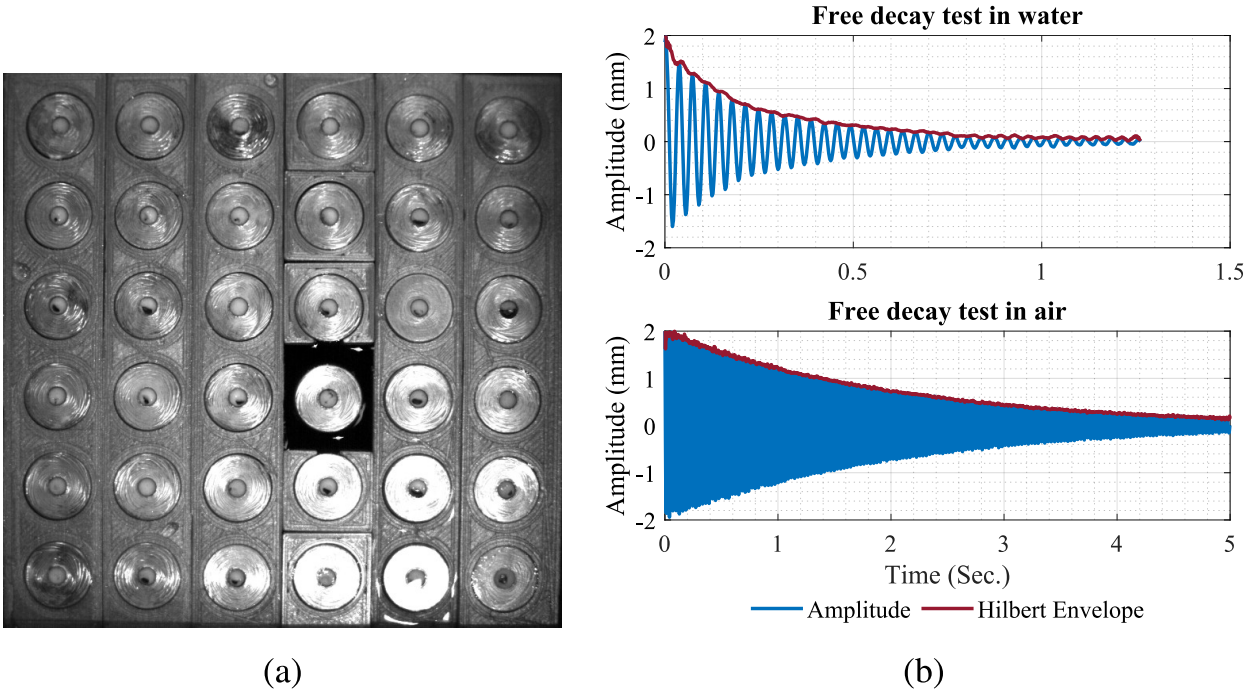

Figure 6.17 (a) test section setup for the free decay test, and (b) experimental results for the free decay tests in air and water.

linear relation with $K = 5.6$ as shown in Figure 6.18.

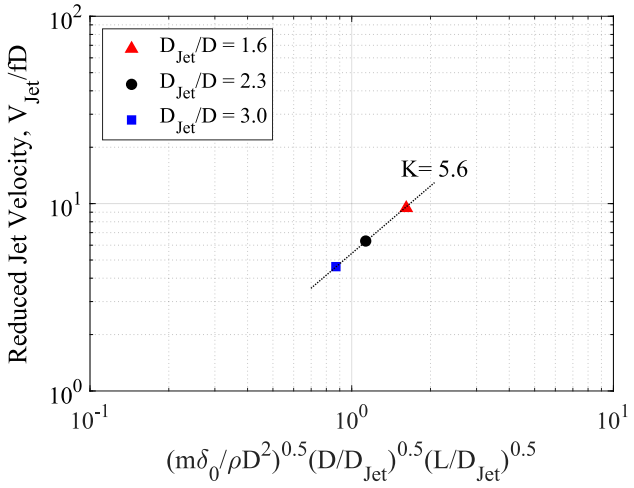

Figure 6.18 Threshold of unstable vibration for the tested bundle 6x6 with the three diameter ratios, D_{Jet}/D.

6.5 Singular value decomposition (SVD) analysis

A key objective of the present work is to gain a general understanding of the complex rod bundle dynamics based on a limited number of tests. In this section, an experimental level data analysis is performed using Singular Value Decomposition (SVD). The analysis aims to discover a generalized (principal) coordinate system, capturing the essential dynamics for the jet-bundle system. Each rod in the bundle vibrates with a specific angle for a given test condition. Extraction of the main features of the rod bundle vibration during instability would give further insight into the dominant vibration configurations (mode shape) of the rod bundle. Singular value decomposition (SVD) analysis is applied to extract the main vibration modal shapes from bi-axial (i.e. stream-wise and transverse directions) vibration data. We defined X a nxm input matrix containing the rod bundle vibration data as presented in Equation 6.4, where n is the number of vibration data from the image (i.e. 2x36), and m is a number of recorded frames from experiments.

$$X = \begin{bmatrix} Rod101(transverse)_1 & ... & Rod101(transverse)_m \\ Rod101(stream-wise)_1 & ... & Rod101(stream-wise)_m \\ Rod201(transverse)_1 & ... & Rod201(transverse)_m \\ . & ... & . \\ . & ... & . \\ Rod606(stream-wise)_1 & ... & Rod606(stream-wise)_m \end{bmatrix} \tag{6.4}$$

In SVD the matrix X is factorized into the product of three matrices as follows:

$$X = U\Sigma V^* \tag{6.5}$$

where U and V are unitary matrices with orthonormal columns, the columns of U are called *left singular vectors* of X and the columns of V are called *right singular vectors* (Brunton and Kutz, 2019). *Singular values* are the diagonal elements of Σ and they are arranged from largest to smallest, where the number of non-zero singular values equals the rank (r) of X. For the rod bundle vibration data, X is a matrix of 72x6000, thereby its rank is equal to 72.

SVD provides an optimal low-rank approximation for the matrix X. The SVD produces a hierarchy of low-rank approximations, from which a rank-r approximation is derived by keeping the leading r singular values and vectors while neglecting the rest. The rank-r SVD approximation is given by the sum of r distinct matrices as follows:

$$\tilde{X} = \tilde{U}\tilde{\Sigma}\tilde{V}^* = \sum_{k=1}^{r} u_k \sigma_k {v_k}^* = u_1\sigma_1{v_1}^* + u_2\sigma_2{v_2}^*.....u_r\sigma_r{v_r}^* \tag{6.6}$$

Choosing a low rank matrix ($\tilde{X}$) which has a good approximation to the data matrix (X) is a crucial key of reducing the size and dimension of large data sets while keeping dominant low-dimensional features in the truncated SVD. The singular values for $D_{Jet}/D = 1.6$ at $V_{Jet} = 3.9$ m/s with the rank, r are presented in Figure 6.19a. The first singular value corresponds to a static mode of the rod bundle displacement which is the mean position for each rod during vibration. Beyond $r = 4$, the singular value is gradually decreased with the rank, r as shown in Figure 6.19a. To determine the most important ranks needed to maintain the main feature of the rod bundle vibration, a cumulative energy of $\sum \sigma_r$ is calculated for each rank as shown in Figure 6.19b. The truncated matrix ($\tilde{X}$) based on the first two ranks preserves 97% of the total energy in the vibration data, whereas the first four ranks preserve 98% of the total energy.

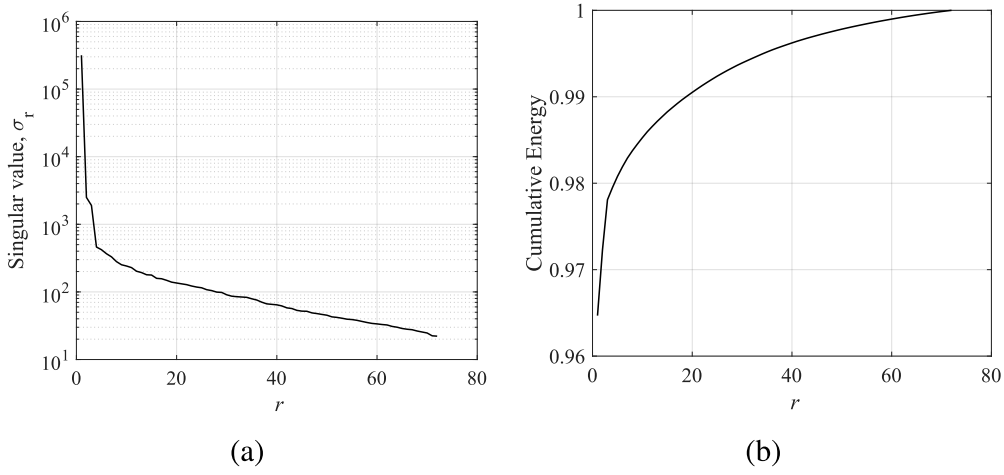

Figure 6.19 (a) Singular values σ_r, and (b) cumulative energy in the r modes for $D_{Jet}/D = 1.6$.

Figure 6.20 shows a comparison between the original vibration data, the truncated SVD vibration data based on $r = 2$, and the truncated SVD vibration data based on $r = 4$. The approximated rod bundle vibration with $r = 2$ clearly captures the main features of the response where compared to the original vibration data. While the approximated rod bundle vibration based on $r = 4$ captures additional characteristics to complete the vibratory profile, considering the changes in the minor axis of vibration. Consequently, the directionality of the rod motion can be clearly identified using only the first two ranks.

The truncated SVD of the rod bundle vibration corresponding to $r = 2$ for the three diameter ratios $D_{Jet}/D = 1.6$, 2.3, 3.0 are compared in Figure 6.21. The black thick lines in these figures present the boundary of the nozzles. Roughly speaking, the rod motion is more dominant in the transverse direction to the jet flow. Furthermore, the vibration angle

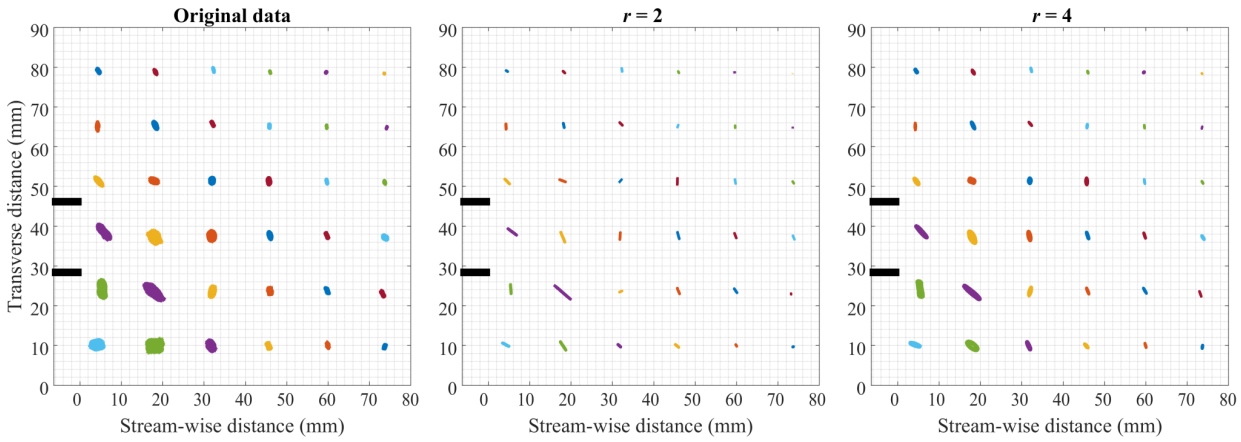

Figure 6.20 Truncated SVD of the rod bundle vibration at two ranks, $r = 2$ and 4 for $D_{Jet}/D = 1.6$.

obtained for some rods is similar for different diameter ratios. The latter observation raises the question whether there exits a generalized eigenvector model that can be used to predict the directionality of rod bundle vibration under jet flows excitation. This leads us to the final analysis in this study which is based on principal component analysis (PCA), as detailed in the following subsection.

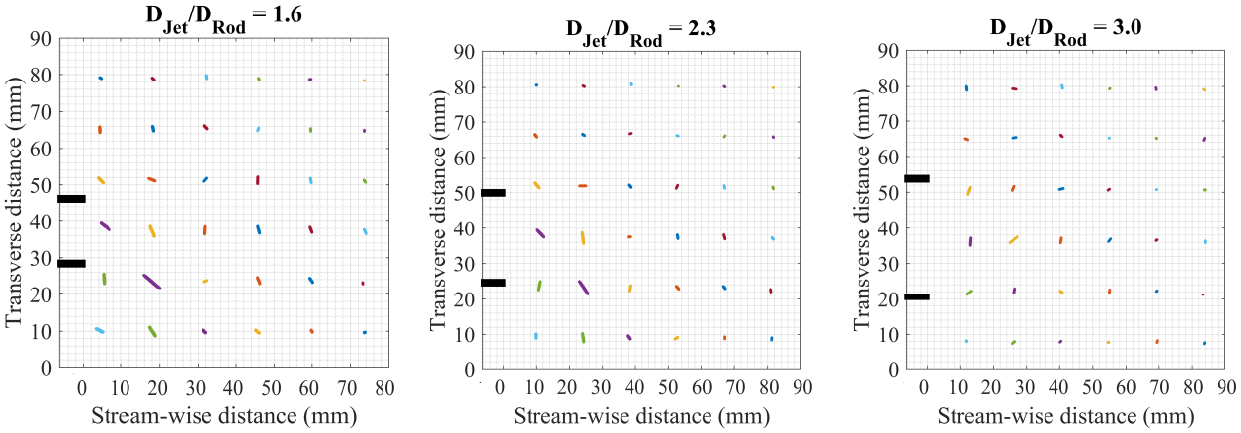

Figure 6.21 Truncated SVD based on $r = 2$ for three diameter ratios: (a) $D_{Jet}/D = 1.6$, (b) $D_{Jet}/D = 2.3$, and (c) $D_{Jet}/D = 3.0$.

6.6 Principal component analysis (PCA)

One of the most common applications of the SVD is principal components analysis (PCA), which provides a data-based, coordinate system for representing correlated data (Brunton and Kutz, 2019). The data from bi-axial rod bundle vibration in jet flows can be analyzed separately in each of the two measuring directions, or merged in a single matrix for analysis. The proposed methodology in this research employs Principal Components Analysis (PCA) on the bi-axial vibration data to combine the two vibration measurement axes into a single "principal axis" with maximum variance as discussed by (Johnson et al., 2014, Tumer and Huff, 2001a). The connection between the physical recording axes is removed using this method of hierarchically reordering orthogonal variations by integrating the two axes of vibration recordings. The fundamentals of this technique are presented in the following sections, which use rod bundle vibration data obtained for three different nozzles. PCA transformation is conducted on a single nozzle vibration data, followed by a transformation employing the experimental vibration data of three tested nozzles to obtain generalized eigenvectors. Next, the generalized eigenvectors are compared to the eigenvectors obtained from individual tested nozzles to see if they can be utilized to predict the vibrational modes for each tested nozzle.

6.6.1 PCA on rod bundle vibration for a single nozzle

The bi-axial vibration data from the image processing method for rod 402 in the bundle for $D_{Jet}/D = 2.3$ is given as an example (Equation 6.7) to demonstrate the mathematical formulation of the proposed technique. X is the n x m input matrix for each rod, where m is the column number corresponding to the transverse (*y-axis*) or stream-wise (*x-axis*) vibration data from the image processing algorithm for one test condition, and n is the number of frames per one testing jet velocity (i.e. 6,000 frames). The mean value of the vibration data is removed to formulate the mean-subtracted data matrix, B according to Equation 6.8.

$$X = \begin{bmatrix} Rod402(y,\mathrm{D}_{Jet} = 1.0 \text{ in.})_1 & Rod402(x,\mathrm{D}_{Jet} = 1.0 \text{ in.})_1 \\ Rod402(y,\mathrm{D}_{Jet} = 1.0 \text{ in.})_2 & Rod402(x,\mathrm{D}_{Jet} = 1.0 \text{ in.})_2 \\ . & . \\ . & . \\ Rod402(y,\mathrm{D}_{Jet} = 1.0 \text{ in.})_n & Rod402(x,\mathrm{D}_{Jet} = 1.0 \text{ in.})_n \end{bmatrix} \tag{6.7}$$

$$B = X - \bar{X} \tag{6.8}$$

where, $\bar{X}$ is the mean matrix.

The covariance matrix of the rows of B is given by (Brunton and Kutz, 2019):

$$C = \frac{1}{n-1} B^* B \tag{6.9}$$

Computing the eigendecomposition of C results in three output matrices, namely PC, SC, and VAR. The mxm PC matrix corresponds to the eigenvectors of the covariance matrix. The matrix nxm SC represents the rotated variables, with each column representing one of the major components. The mx1 vector VAR contains the principal component variances. PCA performed in Matlab for this example: rod 402 with $D_{Jet}/D = 2.3$ at $V_{Jet} = 2.24$ m/s, results in the following matrices: $PC = \begin{bmatrix} -0.57 & 0.82 \\ 0.82 & 0.57 \end{bmatrix}$ $VAR = \begin{bmatrix} 1.12 \\ 0.243 \end{bmatrix}$

Rod 402 has the original coordinate system y (transverse vibration) and x (stream-wise vibration) as presented in Figure 6.22a. Its principal components are linear combinations of the original variables x and y (centered), which represent the selection of a new coordinate system after rotating the original coordinate as shown in Figure 6.22b. The first principal component, is in the first column of the PC matrix, represents the highest variance, as follows: 0.82y-0.57x (using centred variables x, y). The coefficients indicate that the original *y-axis* (0.82 in the PC matrix) gives the greatest weight to the leading principal component. The variance of the first column of the SC matrix is identified by the first element of VAR vector which is 1.12, while the second variance has a small value of 0.243. As a result, the first principal component accounts for 82.35 % of the total variance. Obviously, the first principal component, which accounts for the majority of the variance in the data, is sufficient to capture the main changes in the axisymmetric rod bundle vibration.

By considering of the first principal component as the optimal axis for maximum variance of rods vibration, the rotation angle of the principal coordinate system is calculated as shown in Figure 6.23a. This angle is computed for each test velocity in the unstable vibration region for all tested nozzles. The changes in these angles are analyzed to give a deeper insight on how the jet diameter affects the directionality of rod vibration, and the phase angle between the rods for a given nozzle diameter. In addition, the changes in the vibration direction through the unstable vibration are captured for the same nozzle. Identification of the mode shape based on the rotation angle is graphically presented in Figure 6.23b. The rotation angle (θ) for the first principal axis is obtained as follows:

$$\theta = tan^{-1} \frac{PC1(2,1)}{PC1(1,1)} = tan^{-1} \frac{0.82}{-0.57} \tag{6.10}$$

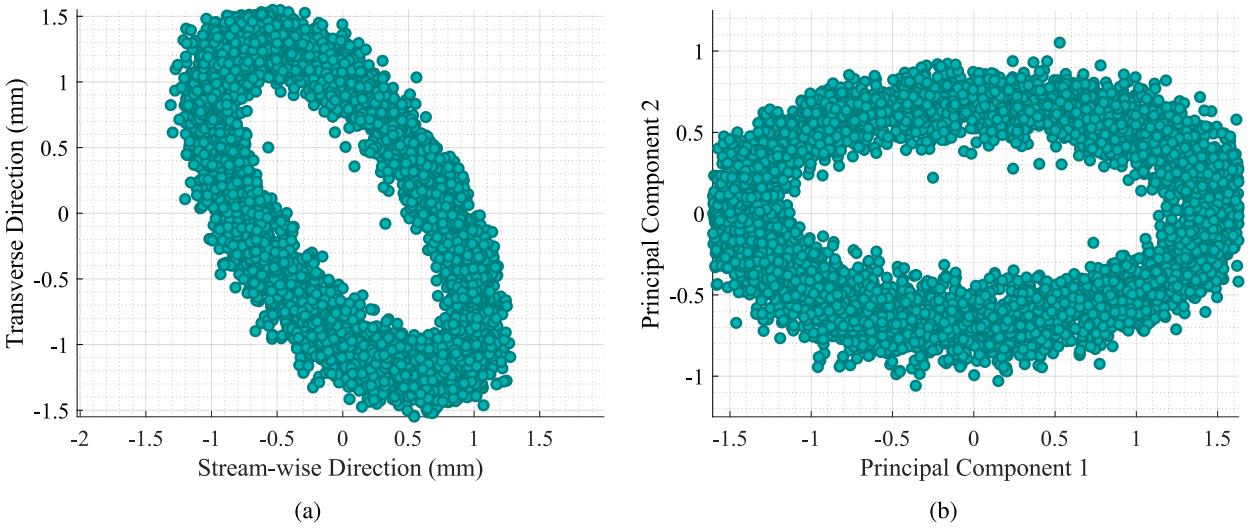

Figure 6.22 (a) Rod 402 vibration data with the original coordinate, and (b) principal component analysis (PCA) of rod 402 at test condition of $V_{Jet} = 2.14$ m/s, and $D_{Jet}/D = 2.3$.

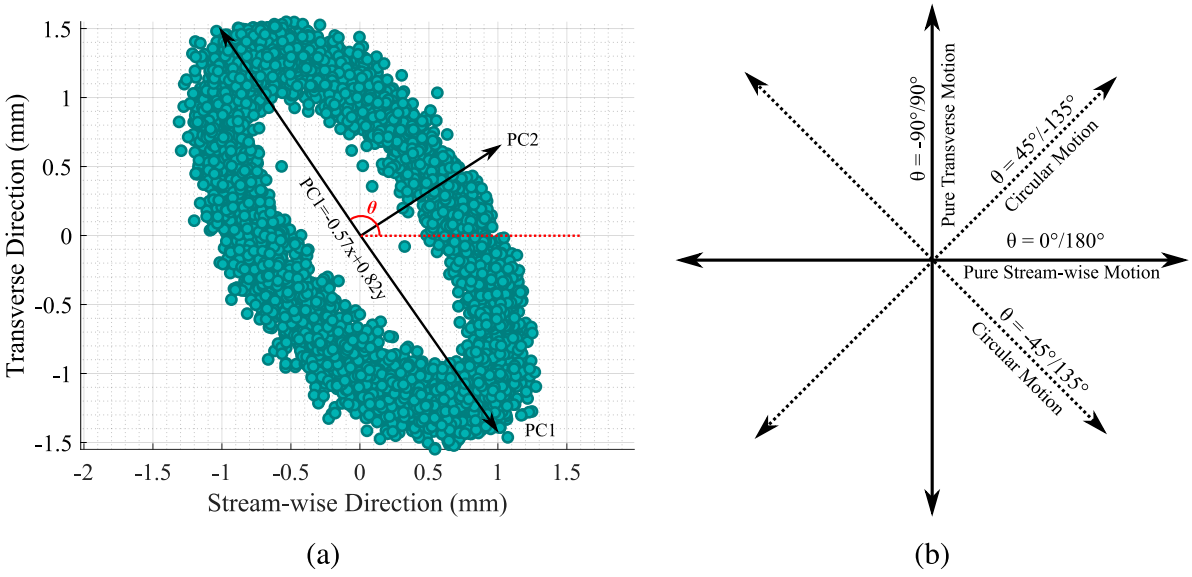

Figure 6.23 (a) a schematic drawing showing the rotation angle, and (b) identification of mode shape based on θ.

Monitoring and quantifying the mode shape of the rod array for each nozzle is performed by calculating the first modal parameter, the angle (θ) based on the first principal axis. Figure 6.23b shows graphically how the angle of the rod motion can be used to identify its orbital motion. Rod motion is purely transverse when the angle is coincided with a vertical axis (90°/-90°). However, pure streamwise rod motion is identified by the angle values 0°/180°,

while circular motion of rods occurs when the rotation angles are equal to 45°/-135° or -45°/135°. Deviation from these specific angles indicate rod motion in elliptical orbits. Table 6.1 shows the numerical results obtained from the PCA transformation for the first three rods. Each PC's contributed energy is determined as a percentage of its eigenvalue over the total sum of the two PC's eigenvalues. PC1 almost fully captures the vibration features, as shown in the table, with energy ranging from 80 % to 96.6 % of the total variance. The x and y coefficients in PC matrix show which axis of the rod vibration is more highly weighted. For rod 301 the original two axis (x & y) have equal weights for the two smallest nozzles. The rod orbit motion depends on the phase difference. For instance, $\psi = 90$ indicates that the rod motion has a circular orbit. For the larger nozzle ($D_{Jet}/D = 3.0$), rod 301 motion changes to one that is strongly coupled in the transverse direction. The transformation angle for rod 401 decreases with increasing jet diameter, from the second quadrant to approach the transverse axis. Rod 501 on the other hand vibrates in the transverse direction for the two smallest jet diameters. For the largest nozzle diameter the rod motion is equally coupled in both directions. To summarize, the rod bundle response is closely linked to the driving fluidelastic forces. As shown in the table, the same rod, under different jet diameter flows has different weighting ratios between x and y motions. This indicates that the fluid forces generated by the jet flow are not constant relative to the jet flow.

The second modal parameter, the phase difference (ψ), is required to complete the rod bundle model parameter identification. Figures 6.24a, 6.24b, and 6.24c show the 3x3 reduced rod bundle mode shape obtained for the three diameter ratios: $D_{Jet}/D = 1.6$, 2.3, and 3.0, respectively. The rod amplitude is scaled up by a factor of 2 for clarity in the figures. Moreover, the highlighted points in the orbits show the staring points for each rod while the arrows show the rod motion direction. For $D_{Jet}/D = 1.6$, rods 301 and 401 have the same rotation angle, however, the phase angles are different, resulting in an elliptical orbit. is not the same, that is why the rod motion path is changed from being in line to elliptical motion. When the rod bundle mode shapes obtained for $D_{Jet}/D = 1.6$ and 2.3 are compared, one clear conclusion emerges: all rods have the same motion direction except rod 501 which switches from anti-clockwise to clockwise motion. This finding leads to the development of a generalized eigenvector model for predicting the rod bundle mode shape in jet flows, for small D_{Jet}/D. The rod bundle mode shape with $D_{Jet}/D = 3.0$ is completely different from that obtained for the smaller ratios. The vibration angle for the column facing incoming jet is flipped from the second quadrant to the first quadrant. In addition, rods in this column move in clockwise paths instead of anti-clockwise paths found for $D_{Jet}/D = 1.6$ and 2.3. The results show that the fluid forces created by the jet flow are not proportional to the nozzle diameter ratio. This supports that further investigation into the effect of diameter ratio on

Table 6.1 PCA details for the five rods in the first row with the three tested jet diameters in the unstable vibration region.

Case		D_{Jet}/D_{Rod}= 1.6		D_{Jet}/D_{Rod}= 2.3		D_{Jet}/D_{Rod}= 3.0	
Rod Number	Variables	VJ = 3.9 m/s		VJ = 2.44 m/s		VJ = 1.75 m/s	
		PC1	PC2	PC1	PC2	PC1	PC2
Rod 301	Eigenvalue contribution (%)	93.47	6.53	90.07	9.93	93.03	6.97
	y coefficient	0.7417	0.6708	0.7124	0.7018	0.9184	-0.3957
	x coefficient	-0.6708	0.7417	-0.7018	0.7124	0.3957	0.9184
	theta based on PC1	132°		135°		67°	
Rod 401	Eigenvalue contribution (%)	95.36	4.64	90.71	9.29	95.87	4.13
	y coefficient	0.742	0.6704	0.8764	0.4817	0.9496	-0.3136
	x coefficient	-0.6704	0.742	-0.4817	0.8764	0.3136	0.9496
	theta based on PC1	132°		119°		72°	
Rod 501	Eigenvalue contribution (%)	94.84	5.16	88.51	11.49	88.31	11.69
	y coefficient	0.9928	0.1197	0.9998	0.0179	0.6782	0.7349
	x coefficient	-0.1197	0.9928	-0.0179	0.9998	0.7349	-0.6782
	theta based on PC1	97°		87°		41°	

the rod bundle dynamics is needed.

6.6.2 PCA of rod bundle vibration and existence of generalized model

Analysis of the main features of the rod bundle vibration data obtained by PCA shows similarity in rod eigenvectors. This section delves into the question of existence of a generalized model for prediction of the rod bundle mode shapes under jet cross-flow excitation. The PCA transformation is used to answer this question by performing an experiment level analysis, where data for all test cases are jointly analyzed. An input matrix that contains all of the different test conditions (i.e. D_{Jet}/D and V_{Jet}) is formed by concatenating all data into one large matrix. Analysis of this matrix yields the average eigenvector for each rod. This average eigenvector from all tests is then compared to the average eigenvector from each individual nozzle to confirm our hypothesis. All of the test conditions are included in the global input matrix X_{Global}, which contains 15 data sets in the unstable vibration region including 6 cases for $D_{Jet}/D = 1.6$, 4 cases for $D_{Jet}/D = 2.3$, and 5 cases for $D_{Jet}/D = 3.0$. X_{Global} matrix has a dimension of $N\ x\ M$, where N = 6000x15 = 90,000, and $M = 2$ (i.e. bi-axial vibration data). Equation 6.11 presents the mathematical formulation of $X_{Overall}$ matrix for rod 402. Instead of subtracting the global mean value, each experimental data for a given jet velocity

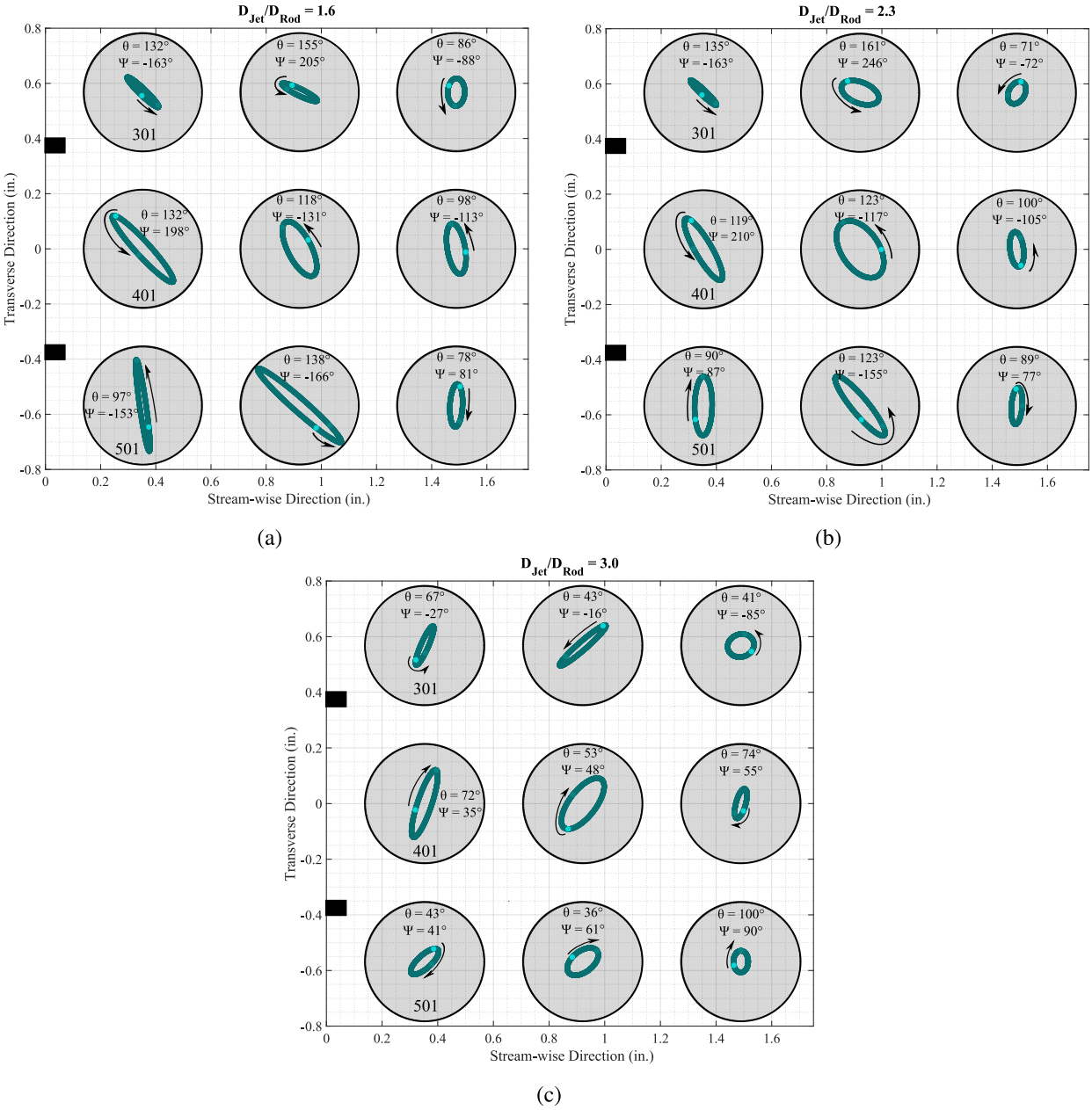

Figure 6.24 3x3 reduced rod bundle mode shape with three diameter ratio (D_{Jet}/D): (a) $D_{Jet}/D = 1.6$, (b) $D_{Jet}/D = 2.3$, and (c) $D_{Jet}/D = 3.0$.

is centred based on its mean value before incorporate into create the 'global' matrix.

$$X_{Global} = \begin{bmatrix} Rod402(x,\mathrm{D}_{Jet}/D_{Rod} = 2.3,\, V_{Jet} = 2.14\ \mathrm{m/s})_1 & Rod402(y,\mathrm{D}_{Jet}/D_{Rod} = 2.3,\, V_{Jet} = 2.14\ \mathrm{m/s})_1 \\ \vdots & \vdots \\ Rod402(x,\mathrm{D}_{Jet}/D_{Rod} = 2.3,\, V_{Jet} = 2.14\ \mathrm{m/s})_{6000} & Rod402(y,\mathrm{D}_{Jet}/D_{Rod} = 2.3,\, V_{Jet} = 2.14\ \mathrm{m/s})_{6000} \\ \vdots & \vdots \\ Rod402(x,\mathrm{D}_{Jet}/D_{Rod} = 2.3,\, V_{Jet} = 2.44\ \mathrm{m/s})_1 & Rod402(y,\mathrm{D}_{Jet}/D_{Rod} = 2.3,\, V_{Jet} = 2.44\ \mathrm{m/s})_1 \\ \vdots & \vdots \\ Rod402(x,\mathrm{D}_{Jet}/D_{Rod} = 2.3,\, V_{Jet} = 2.44\ \mathrm{m/s})_{6000} & Rod402(y,\mathrm{D}_{Jet}/D_{Rod} = 2.3,\, V_{Jet} = 2.44\ \mathrm{m/s})_{6000} \\ \vdots & \vdots \\ \vdots & \vdots \\ Rod402(x,\mathrm{D}_{Jet}/D_{Rod} = 3.0,\, V_{Jet} = 1.75\ \mathrm{m/s})_{6000} & Rod402(y,\mathrm{D}_{Jet}/D_{Rod} = 3.0,\, V_{Jet} = 1.75\ \mathrm{m/s})_{6000} \end{bmatrix} \tag{6.11}$$

The coefficients in the PC_{Global} matrix, as obtained in the individual test conditions, demonstrate which vibration axis for the first principal component is the most weighted. The generalized eigenvector model developed from the complete set of experiments can be used to analyze and demonstrate similarities with that obtained from individual test conditions. The generalized eigenvectors form the baseline case for this comparison. The rotation angles, θ (see Equation 6.10) are calculated using the first principal components of the PC global identify the vibration direction. The difference between the angles derived from the global PCA and each tested nozzle determines whether the results based on each tested nozzle belong to the general eigenvector model or not. Figure 6.25 shows the difference between the individual angles obtained from each nozzle (D_{Jet}/D =1.6, 2.3, and 3.0) and the overall angle for the first principal components, for five columns in the bundle (i.e. 30 rods). In the figure, the x-axis is D_{Jet}/D, and the y-axis is the absolute difference which is computed as follows:

$$Absolute\ difference|\Delta\theta| = Abs(\theta_{Overall} - \theta_{D_{Jet}/D=2.3}) \tag{6.12}$$

It can be seen from the figure, the rotation angles for the two columns 2 and 6 have a large deviation from the baseline case, specifically for the two nozzles, $D_{Jet}/D = 2.3$ and 3.0. These columns are located away from the location of the jet flow. Local shear flow effects can be expected to dominate the flow features (over jet inertia for instance) in these regions. Shear flow parameter as defined by Gad-el Hak et al. (2021) is one of the main jet flow parameters which affect the jet cross-flow induces vibration. Because this parameter is a function of the jet velocity, which varies for each nozzle, the two columns may not follow the generalised eigenvector model. These two columns are therefore excluded in the following discussion. Excluding the two columns, the overall PCA accurately predicts the three columns 3, 4, and 5 (see Figure 6.25) rotation angles for two nozzles $D_{Jet}/D = 1.6$ and 2.3, indicating that the eigenvector for these two nozzles follows the proposed generalized (global) model with a maximum error of 10°. These three columns are symmetrically positioned relative to the jet flow. Rod 302 has an angle difference of 30° because of its lactation in the recirculating zone of the two parallel jets. Due to the alignment of the jet flow with the rod 401 centerline, the main flow passage splits into two symmetric planar jets across the bundle, as demonstrated by Wang et al. (2016).

The larger nozzle diameter ratio, $D_{Jet}/D = 3.0$, has a relatively large difference in the rotation angles relative to those computed from the global eigenvector model. The difference range of column rods 4 and 5 is between 50° to 80° for the first two rows. This range decreases to 20°-40° for the other rows. To explain why the global eigenvector model differs for this nozzle, a deeper understanding of the relationship between increasing the nozzle diameter and the

flow behaviour through the bundle is required. An algorithm has been developed to calculate the flow passage area for each nozzle by integrating the projected area between the nozzle boundary and the interfering rods. The limits of the integration are the intersection points of the two curves, the circle and straight lines, as presented graphically in Figure 6.26. The approximate acceleration ratio of the jet flow through the bundle as a result of transitioning from the circular cross sectional area to the inter-rod gaps is plotted versus with the diameter ratio (D_{Jet}/D) in Figure 6.27. Increasing the nozzle diameter ratio from 1.6 to 2.3 slightly reduces the acceleration ratio from 3.7 to 3.5 from the interfering of the nozzle geometry with the bundle geometry. However, the nozzle diameter ratio $D_{Jet}/D = 3.0$ has a higher acceleration ratio of 4.13, which is likely to significantly change the flow behavior through the bundle. The acceleration ratio is therefore a key factor influencing the efficiency of the proposed global eigenvector model. The proposed model is expected to be most accurate for cases with similar acceleration ratios.

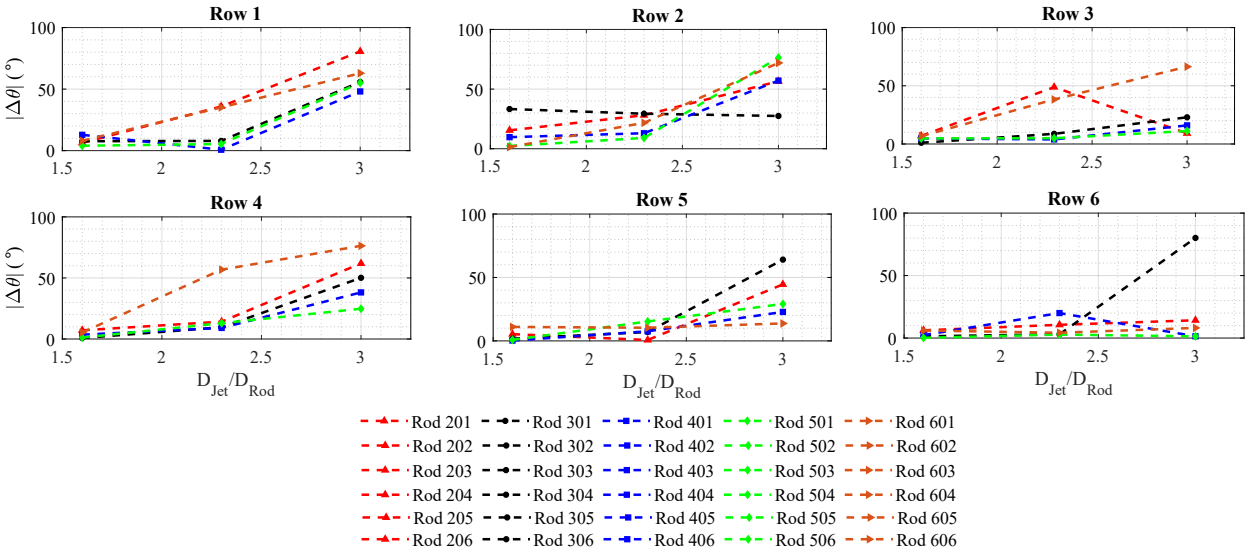

Figure 6.25 Absolute difference of rotation angles based on PC1 between individual and overall PCA eigenvectors.

6.7 Conclusions

Jet cross-flow induced instability of a rod bundle has been investigated in this work. The jet diameter is the most important input parameter that can influence the dynamical behavior of the rod bundle. FEI tests are conducted on an axisymmetric rod bundle with three nozzles having diameter ratios (D_{Jet}/D) of 1.6, 2.3, and 3.0. For each diameter ratio, the rod bundle

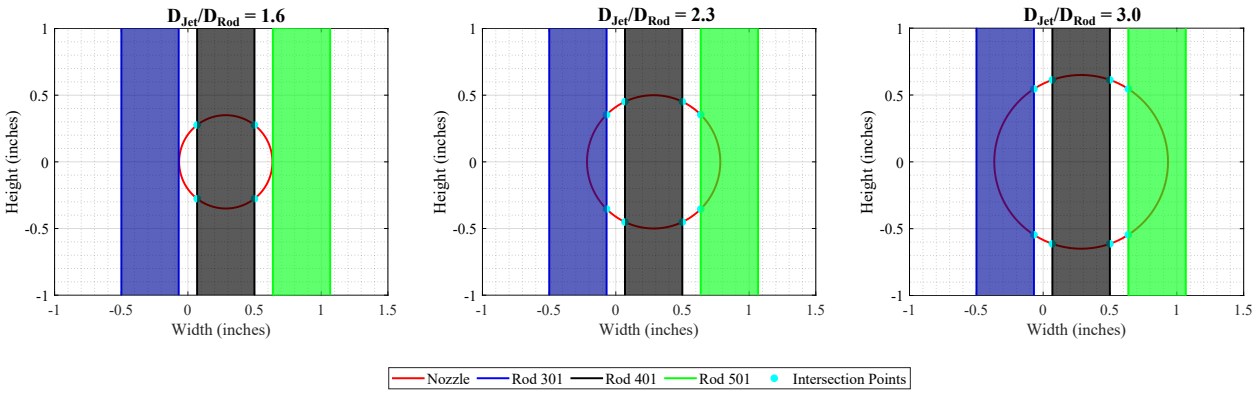

Figure 6.26 Intersection regions between the three nozzles and the rod bundle.

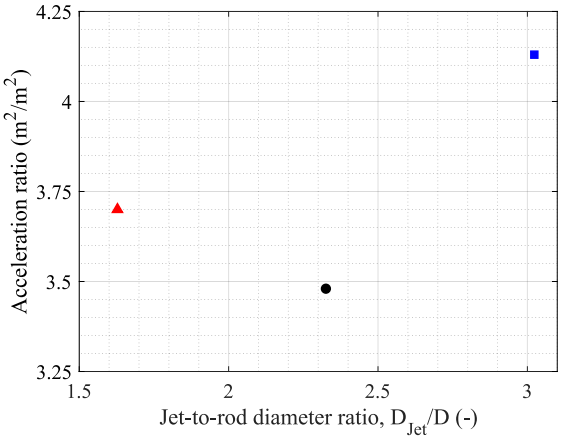

Figure 6.27 Acceleration ratio of the jet flow associated with increasing the diameter ratio, D_{Jet}/D.

was tested in the range of jet velocity that covered the array behavior from turbulence induced vibration until fluidelastic instability. A bi-axial rods vibration, stream-wise and transverse directions, is tracked using a high-speed camera. A stability map is generated using the critical velocity obtained for each test condition. The map showed that this 6x6 in-line bundle for the jet-rod aligning case has a stability constant of 5.6.

Singular value decomposition (SVD) analysis shows that the truncated SVD based on the rank of 2 accurately captures the main vibration features of the original data.

A PCA transformation is used to compute the rotation angles of the principal directions for each diameter ratio in order to discover the optimal direction of vibration that has the highest variance. For each rod, the angles difference between PCA based on all diameter ratios and that based on each diameter ratio is used to evaluate the performance of the generalized

eigenvector model. The main findings are:

- The flow gap areas across the bundle change as the nozzle diameter increases, but the changes are not linear due to geometrical matching between the nozzle location with the rods facing the jet flow.
- The acceleration ratio is a key parameter that could be used to quantify the effect of diameter ratio (D_{Jet}/D) on the rod bundle vibration induced by jet cross-flow.
- The generalized eigenvector model can be used to predict the mode shape of a rod bundle that is subjected to jet cross-flows from nozzles with the same acceleration ratio.

The primary aim of this research is to provide deeper insight into the dynamical behaviour of rod bundles subjected to jet cross-flows. The global eigenvector model develops here could be used to predict the mode shape of the rod bundle for nozzles having nearly the same acceleration ratio. In addition, the stability map provides detailed and accurate instructions for the operating jet flow condition as function of jet flow parameters.

Further tests with different nozzle diameters are required to investigate the effect of projecting new test results onto the global eigenvectors model for mode shape prediction of rod bundles subjected to jet cross-flow. In addition the effect of jet eccentricity on the rod bundle vibration needs further studying in order to incorporate its effect in a single model jet cross-flow induces vibration.

CHAPTER 7 ARTICLE 5: MITIGATION OF JET CROSS-FLOW INDUCED VIBRATIONS USING AN INNOVATIVE BIOMIMETIC NOZZLE DESIGN INSPIRED BY SHARK GILL GEOMETRY

Gad-el-Hak, I. and Mureithi, N.
Published in Scientific Reports - Nature on 30th June 2022.
DOI: https://doi.org/10.1038/s41598-022-15026-8

Summary

This chapter presents a solution to mitigate the rod bundle vibration by increasing the mixing rate between the jet flow and surrounding fluid, and consequently increasing the decay rate of the jet velocity. A new nozzle inspired by sharks is proposed. The nozzle concept takes advantage of the high efficiency capacity of shark gill slits. Three nozzles, circular nozzle, 10 fin shark-inspired nozzle, and 15 fin shark-inspired nozzle, are experimentally tested to evaluate the performance of the new design on jet cross-flow induced vibrations. Tests are performed on the axisymmetric rod bundle vibration at $\xi = 0$. This work is performed to answer the research question (**Q6**) and to achieve the objective (**O5**).

Graphical Abstract

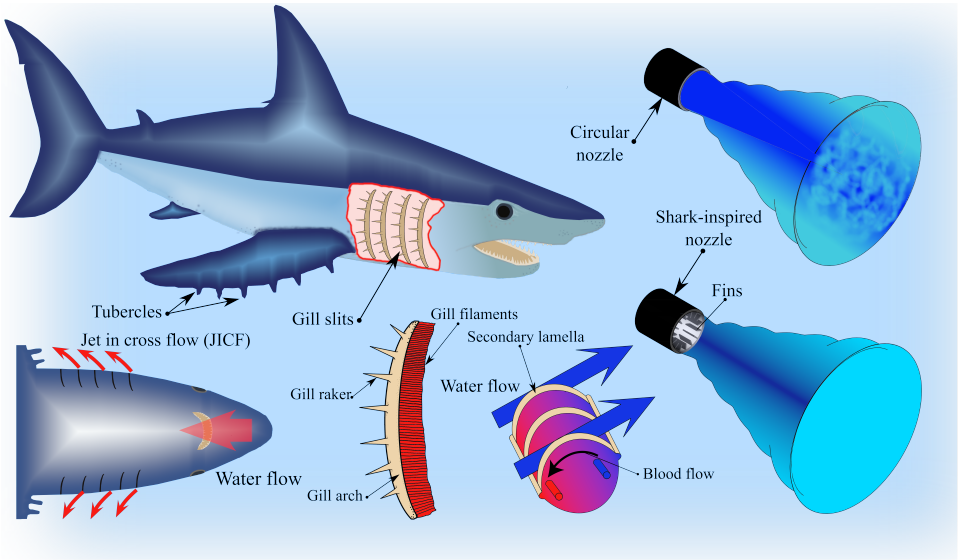

Abstract

Shark gill slits enable sharks to eject the water after the oxygen has been removed in ram ventilation. The reduced effect of jet flow from the gill slits gives sharks smooth maneuverability. A biomimetic "shark nozzle" is proposed to improve mixing between the jet flow and surrounding fluid. Jet flow systems are an essential component of many industrial applications. The key characteristic of jet flow is the mixing process that occurs between two fluid streams to allow heat and/or mass transfer between them. Many industrial and propulsion devices that use jet flows need rapid mixing for effective and environmentally friendly operation. Fuel-injection systems, chemical reactors, and heating and air conditioning systems are examples of devices where a mixing process takes place. Recently, jet flow plays an important role in design and operation of specialized nuclear pressurized water reactors (PWRs). The loss-of-coolant accident (LOCA) holes and slots machined in the core periphery baffle plates are designed to mitigate the effects of a severe LOCA event. However, in normal operation, the holes are a source of a jet flow that can induced vibrations in the fuel assemblies near the baffle before being mixed with the surrounding fluid. This may cause wear and fretting in fuel rods with their supports. The ultimate solution to prevent the fuel assembly vibrations from LOCA hole jetting in a reactor is enhancing mixing of a jet flow with ambient flow in order to rapidly reduce jet momentum. This work proposes a new shark-inspired nozzle design that exploits the observed high efficiency capacity of shark gill slits. Tests are conducted to evaluate the performance of the new design. The obtained results show that the shark-inspired biomimetic nozzle has a greater effect on the rod bundle vibration, and the critical velocity at which the unstable vibration occurs in the rod bundle is delayed by 20% using the biomimetic nozzle. In addition to delaying instability, a vibration amplitude reduction of 85% was obtained by using the proposed shark-inspired nozzle instead of the circular nozzle.

7.1 Introduction

Over the last few decades, jet flows have received much attention (Crow and Champagne, 1971, Gutmark and Ho, 1983, Ho and Huerre, 1984, Yule, 1978). A jet's flow field can be described as follows. At the jet centerline, the flow is uniform while a shear layer is generated near the nozzle wall, which is defined as a top-hat velocity profile. As a result of generating the shear layer with thickness (θ), small disturbances, normally described by their Strouhal number ($St_\theta = f\theta/U$), are amplified and eventually roll-up into a coherent structure and periodic sets of vortices, making it subject to the Kelvin-Helmholtz, or the

shear-layer instability (Becker and Massaro, 1968). The dynamics of these vortices dominate shear layer growth, which is defined by phenomenon such as vortex pairing. The dominant jet instability mode, which is described by the Strouhal number based on the nozzle diameter (St_{Jet}=fD_{Jet}/V_{Jet}), becomes the preferred mode as the vortices grow and develop towards the end of the potential core. The interaction of vortices beyond the end of the potential core causes complex non-linear motion, which breaks the flow's coherent structure and results in transition to turbulent flow. One of the most important aspects of a turbulent jet is its ability to entrain more fluid from its surroundings due to the presence of the shear-layer flow at the jet boundary.

Turbulent mixing is used in many industrial components to transfer heat and mass between two or more fluid streams as in gas burners, chemical reactors, liquid mixers, gas mixers, heat exchangers, and atomizers. Efficient and rapid mixing is a particularly important to the performance of these components. Passive flow control techniques for increasing the rate of jet mixing in circular nozzle flows have been investigated by a large number of researchers (Krishnaraj and Ganesan, 2021, Phanindra and Rathakrishnan, 2010, Reeder and Samimy, 1996, Thangaraj et al., 2022, Zaman et al., 1991). One of the most effective passive control techniques is the application of mechanical tabs at the exit plane of the nozzle. Tab-controlled jets have received serious consideration due to their practical applications. Tabs have been discovered to have a considerable impact on entrainment and jet mixing rate due to their ability to generate streamwise vortex pairs. However, the key parameters of tab-controlled jets include the effect of tab geometry, tab number, tab orientation, tab size, and tab position relative to nozzle outlet (Krishnaraj and Ganesan, 2021). These parameters are still under investigation. The most commonly used tab in the literature is the delta tab (triangular shape). The tab number is varied from one tab to four tabs. Tab shape and number are the most important parameters that affect the mixing rate, thus they should be designed with care.

In addition to the conventional jet flow applications, some nuclear reactor vessel designs employ holes that are machined into the core baffle plates to relieve pressure differentials during a Loss of Coolant Accident (LOCA). A Loss of Coolant Accident (LOCA) is a mode of failure for reactor cores that is caused by a break in the reactor coolant pressure boundary. As a result of this failure scenario, the pressure difference across the baffle plates inside the reactor core is increased. During normal operation, the fluid flow though the LOCA holes has a small effect on the core average flow field, but it is a source of jet flow that can result in fretting failures of fuel assemblies, as reported by the IAEA (2015). A similar failure mode involved defective joints between baffle plates that allow high jet flows through narrow gaps. This phenomenon is called *baffle jetting* and may induce fuel rod vibrations that cause

fretting and wear of the fuel cladding that contain the fission products. This type of failure has been observed since the 1970s (U.S. NRC, 1980) and more recently at the North Anna power plant in 2014 (Bischof, G.T., 2014) involving damage to two fuel rods. While baffle jetting is caused by a degradation of the baffle plate bolts, and LOCA hole flow jetting is a result of design choices, both phenomena underscore the importance of understanding jet cross-flow induced vibrations.

Current reactors have a significant difficulty in reducing the resulting vibrations in their fuel assemblies due to circular jet cross-flow. From a manufacturing prospective, a circular nozzle shape for LOCA holes was proposed as it is easier to drill holes in the baffle plates. However, the mixing rate between the jet flow and the surrounding fluid, on the other hand, is a key factor in rod bundle vibration; switching from linear momentum into angular momentum (i.e vortices) would reduce the resulting vibrations. Changes to the nozzle shape are used in passive jet control to improve mixing. It is also feasible to boost the swirl flow at the exit jet boundary and improve the flow condition at the rod bundle with appropriately designed jet nozzles. Thus, using a biomimicry design approach, a new nozzle shape inspired by shark gill slits is proposed. As a result, a LOCA hole shape with adequate mixing enhancement capabilities will represent a step forward from circular nozzles.

Nowadays and in the future, engineers and designers will do well to pay attention to specific detail and systems design in nature so as to draw inspiration for efficient, renewable, self-sustaining, and ultimate solutions to many engineering problems. Biomimicry, biomimetics, and bio-inspired design are alternative terms for an innovative approach to design and engineering, inspired by design in nature. Nature-inspired innovation can lead to new paths of exploration and problem-solving opportunities that have previously been ignored. Nature is the prime example of 'eco-design,' and it demands the full attention of those working on renewable energy, materials, medical engineering, and technical advancement issues. An example of applied biomimicry from the seas is humpback whales. Humpback whale flippers feature non-smooth leading edges (i.e. tubercles), which showed fluid dynamic improvements as compared to the smooth leading edges of our turbines and fans. Tubercles reduce drag by 32%, increase lift by 8%, and increase angle of attack by 40% over smooth flippers before stalling in wind tunnel testing of model humpback whale flippers with and without tubercles (Miklosovic et al., 2004). There is also much to learn from birds. The composite turbine blade of a turboexpander was designed using biomimicry of bird flight wings, with fibre orientations that mimicked the structure of the bird's feathers by Gad-el Hak (2019). The author found that the same barb angle inspired by the flight feather was used to produce the smallest tip deflection of the rotor blades, resulting in an 80% weight reduction of biomimetic blades over stainless steel rotor blades.

Inspired by sharks, a new biomimicry nozzle design is proposed as shown in Figure 7.1. Efficient and rapid mixing is a key factor to mitigate vibrations from jet cross-flow in pressurized water reactor cores. Sharks breathe through a series of five to seven gill slits behind their heads on both sides of their bodies, which absorb oxygen from the water as it flows over them and is then flushed out. This respiration process, which involves forcing of water over the gills by swimming motions, is known as "*ram ventilation*" (Muir and Kendall, 1968). The water emanating through the gills into the ocean corresponds to jet in cross-flow (JICF) from an engineering perspective. However, this jet flow is ejected with little effect on the sharks to provide them with greater maneuvering and swimming capability. That means that the design of the gill slits enhances mixing between the jet flow and the surrounding water in the oceans. The jet velocity decays faster and the flow exits the slits with minimum effect on the shark.

Gills mainly consist of gill arches (*branchial arches*), gill rakers and gill filaments. Gill arches are a series of bony "loops" to support the gills. At their base are gill rakers, which protect the gills from mechanical damage. Each gill arch has filaments (protein structures) which perform gas exchange through a capillary network that provides a large surface area for the exchange process. In addition, the gill filaments are extended with the secondary gill lamellae to create inter-filament water channels, which help increase their surface area for gas exchange. The spacing and height of the secondary lamellae control the cross-section area of the water flow (Hughes, 1966). Furthermore, an efficient countercurrent gas exchange at the secondary gill lamellae further increases oxygen uptake and carbon dioxide release (Benz, 1984). Gill rakers and filaments have an important effect on the fluid dynamics of the exiting water. Thus, simulating their effects in the jet flow will help us to design an efficient nozzle, and thereby eliminate or reduce the rod bundle vibrations.

The goal of the paper is to propose a biomimetic nozzle design based on the shark gill slits to develop more rapidly the mixing layer between the jet flow and the surrounding flow. Our proposed biomimicry approach is to attach equally spaced thin fins circumferentially at the circular nozzle base to enhance the mixing process by rapidly entraining the still fluid in the jet flow. The resulting jet cross-flow induced vibrations is investigated experimentally for three nozzle designs, (*i*) a basic circular nozzle, (*ii*) a shark-inspired nozzle with 10 fins, and (*iii*) a shark-inspired nozzle with 15 fins. The paper compares the ability of the proposed biomimetic nozzle to delay the critical velocity at which unstable vibrations occur and to damp the post-instability vibration amplitudes of the rod bundle. Comparison is made with the reference case of the circular nozzle. A high-speed camera is used to obtain full-field rod array vibrations by capturing a sequence of images for a specific duration with the image frame size including all rods in the bundle. An image processing algorithm determines the

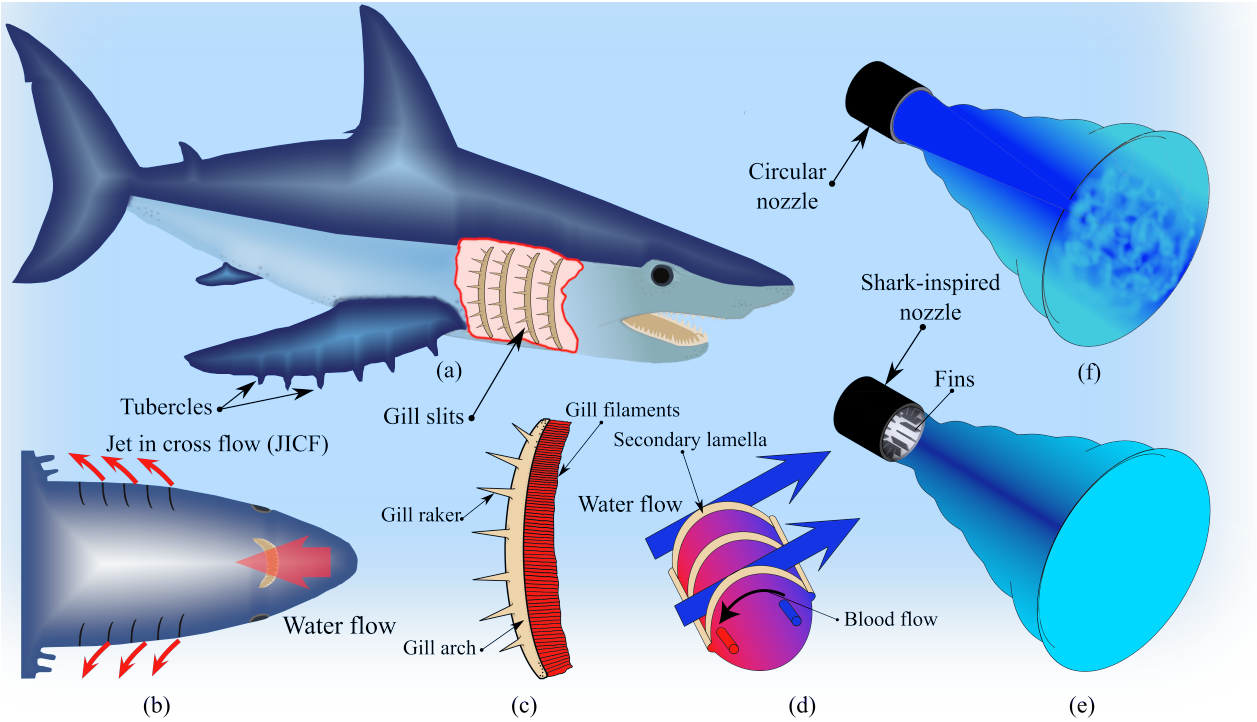

Figure 7.1 Modelling of bio–inspired nozzle. (a) shark anatomy, (b) ram ventilation concept corresponding to jet in cross flow, (c) drawing of a gill showing gill filaments (oxygen absorption), gill arch (supporting structure), and gill rakers, (d) schematic drawing of a portion of filaments and their secondary lamellae and also the countercurrent exchange system, (e) schematic drawing of shark-inspired nozzle, and (f) circular jet flow.

rod tip displacements fields by tracking the rod tip centers when the array is subjected to a specific jet velocity. The dynamical behavior of the rod bundle is obtained by increasing the jet velocity up to the unstable condition.

7.2 Experimental design concept

7.2.1 Shark-inspired nozzle design

The aim of the experiments is to look at how the rod bundle vibrates under flow conditions that cause fluid-elastic instability. Since the jet flow velocity in the test section is not constant; it is function of stream-wise and transverse direction related to jet centerline, the time-dependent displacement for each rod in the tube bundle will give us a deeper understanding about how the rods vibration is affected by the nozzle shape. Figure 7.2 shows the three tested nozzles, the base nozzle diameter is the same in three cases. However, very thin fins

(1 mm thickness) are attached circumferentially at the circular nozzle base simulating the secondary lamella in sharks. Fin thickness should be kept to a minimum to avoid increasing the pressure drop across nozzle due to the added blockage effect. The 1 mm fin thickness is selected because it is the minimum thickness (possible for a printed nozzle) that ensured the structural integrity for fins during the testing. The fin length is 12.7 mm inside the nozzle simulating the shark's secondary lamellae (Hughes, 1966). Furthermore, the effect of the number of fins on the rod bundle vibrations is investigated for two values, 10 and 15 fins.

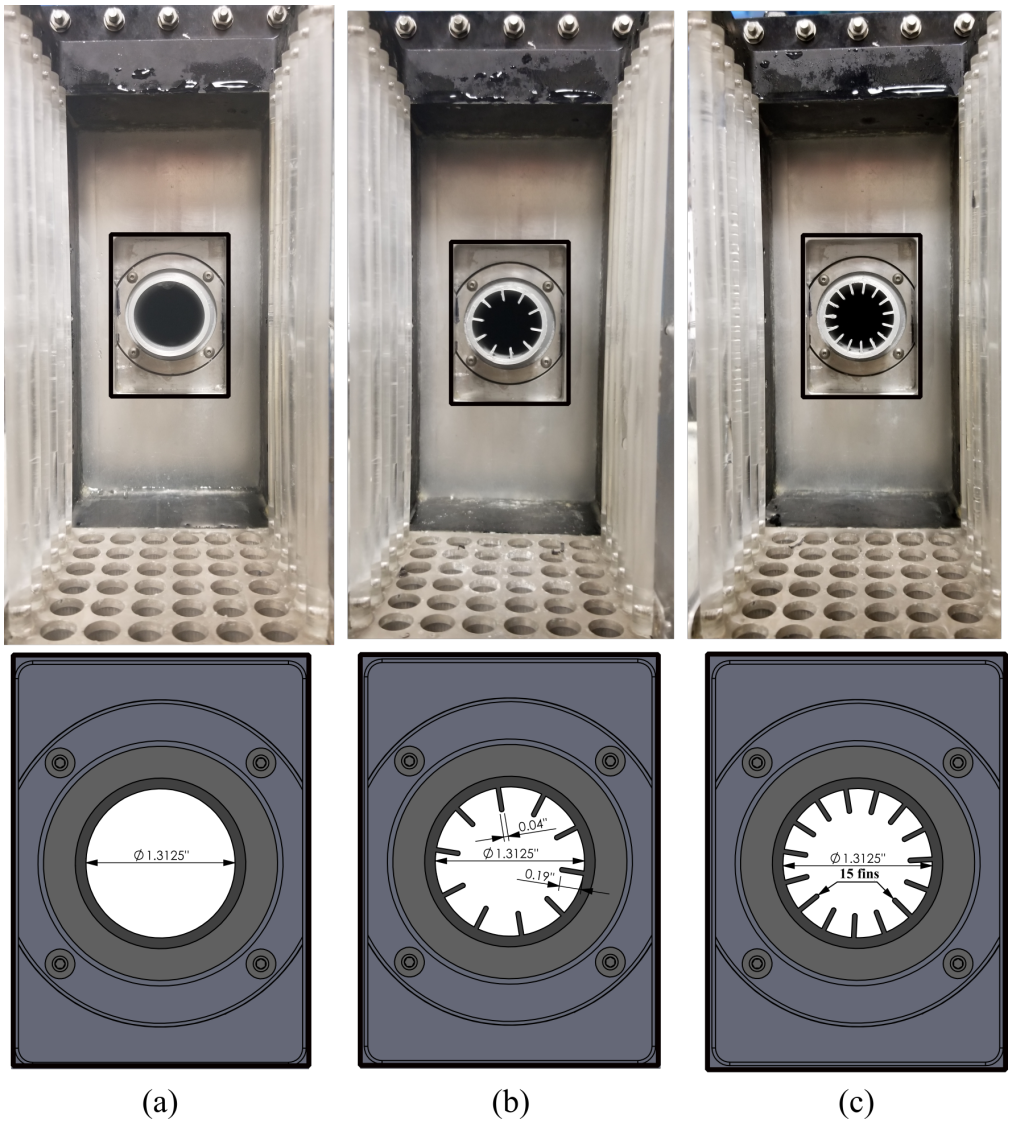

Figure 7.2 Three tested nozzle: (a) circular nozzle, (b) 10 fins shark-inspired nozzle, and (c) 15 fins shark-inspired nozzle.

7.2.2 Experimental set up

Experiments were conducted to see how the proposed biomimetic nozzle affected jet cross-flow induced vibrations. A reduced fully flexible rod bundle 6x6 is selected to investigate its dynamical behavior due to transverse jet flow. The axisymmetric rod bundle vibration has frequency of 29 Hz in still water for all rods. To form a 6x6 configuration, the flexible rods are arranged in a normal square array with a pitch-to-diameter ratio (P/D) of 1.32 as in the fuel assembly. Figure 7.3 shows the top sectional view of the designed tested section including the other designed components simulating what happens in the nuclear reactor cores. The uniform flow from the rectangular cross section duct is squeezed and converted to jet flow when it passes through the nozzle. The rods are exposed at their mid-span to a developed jet cross-flow. Figure 7.4 shows the water test loop.

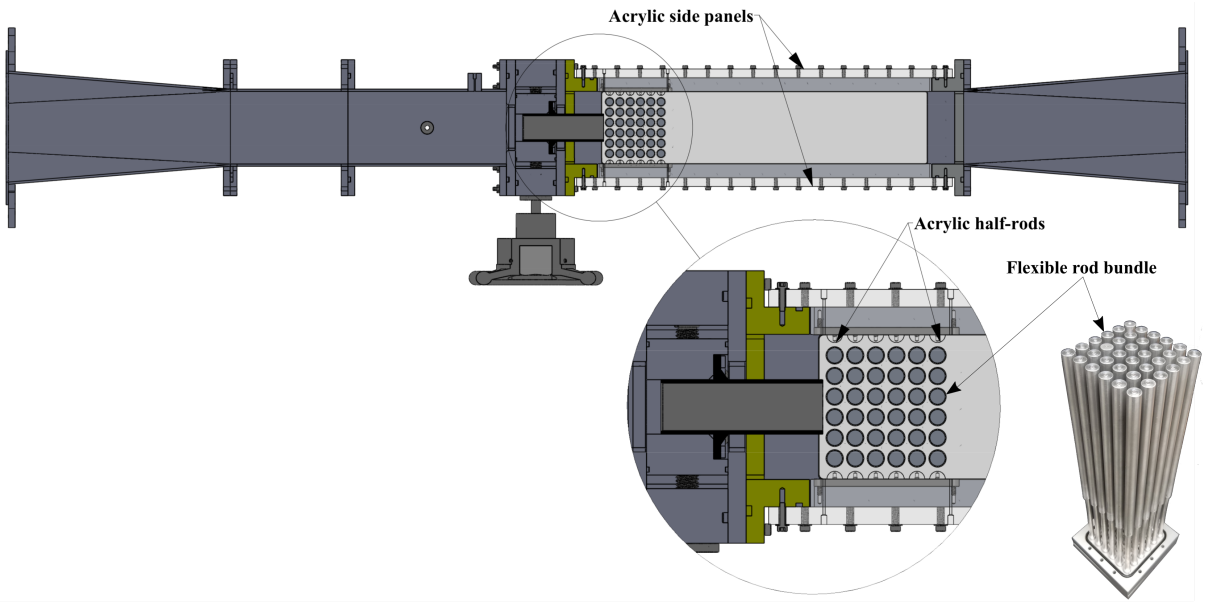

Figure 7.3 Experimental set-up.

7.2.3 Measurement system and image processing

A high-speed imaging technique is considered the best solution to capture the vibration response of the rod bundle; this data acquisition method system is completely non-intrusive; no sensors (such as strain gauges) are needed on the rod surfaces, and wires are not required to be fed through the test section. Sequential images of the rod bundle vibration, during which the rods are excited by the jet cross-flow at a particular velocity, are captured using

a high-speed digital camera (Motion BLITZ Cube 4, MIKROTRON). The image frame size is large enough to capture all of the rods in the tested bundle. The camera is positioned on the top panel of the test section such that its viewing plane is normal to the rods' axis as shown in Figure 7.5.

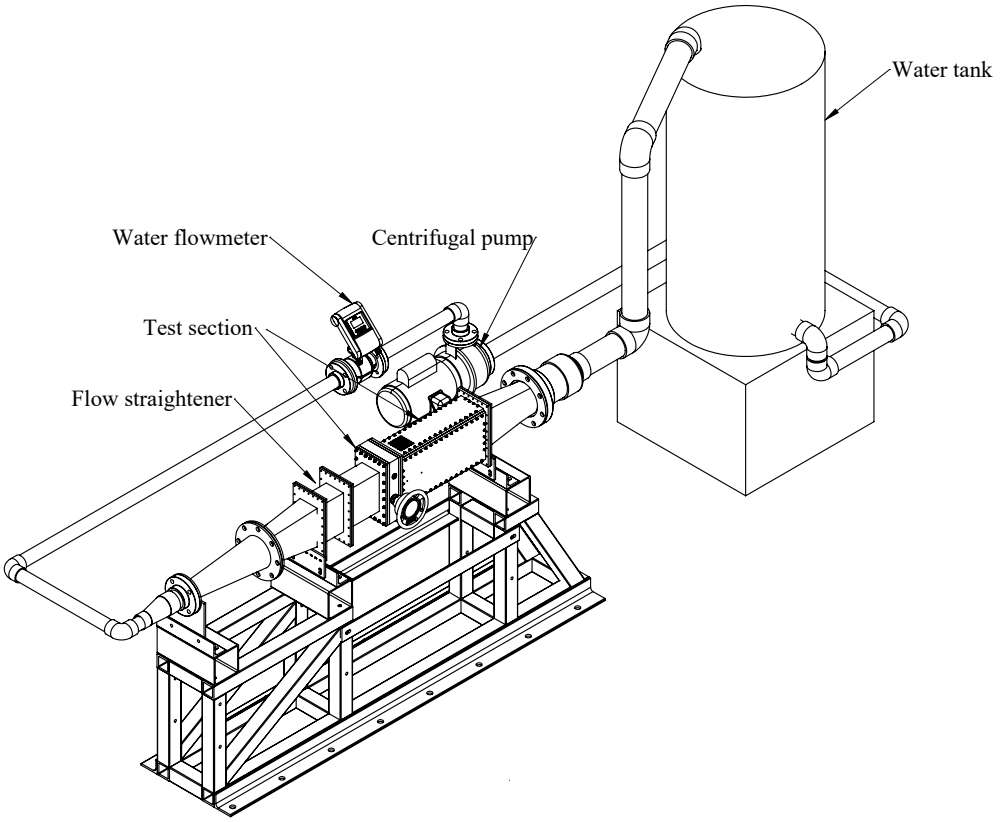

Figure 7.4 Test loop setup.

7.2.4 Image processing algorithm

To determine the rod bundle vibration at each jet flow velocity, a MATLAB image processing algorithm is generated to detect the centre of each rod in the bundle. The developed code detects the edges of rods based on the colour difference between the shiny aluminum top rod surface and the dark background test section. Thus, the image size is divided into 36 square unit cells (the rods number in the bundle), each identified by a four-point boundary in the code as shown in Figure 7.6a. Figure 7.6b shows the vibrations that occurred for one second from rods 302 and 402. Processing 5,600 images would give us the rod bundle vibrations that occurred for 15 seconds at each velocity.

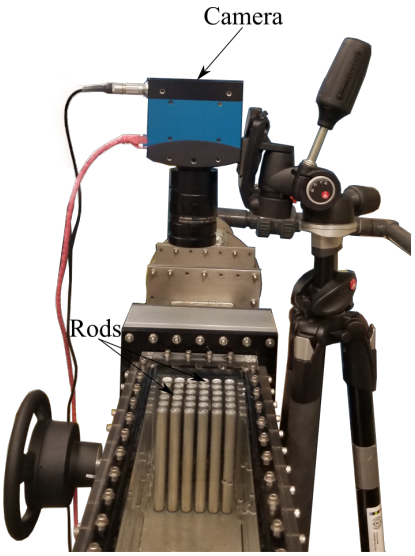

Figure 7.5 Camera set-up.

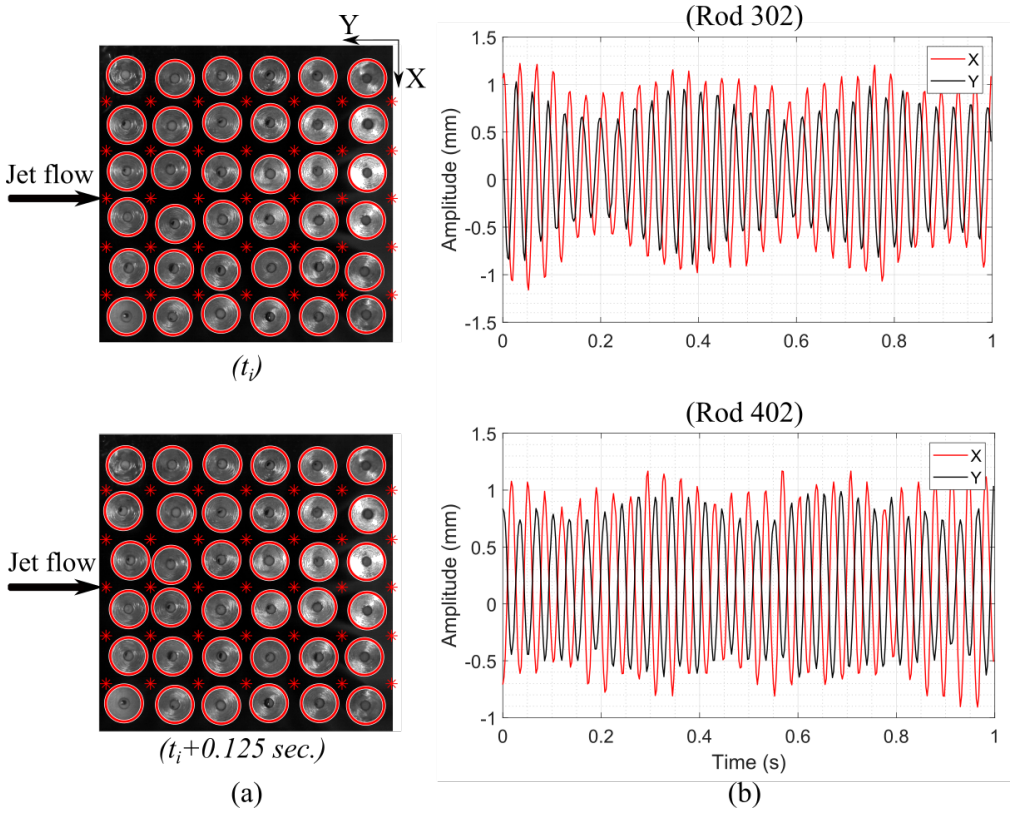

Figure 7.6 (a) processed images showing the detected circles by the code and the four-point boundary for each rod in the bundle, and (b) the time signals for two rods 302 and 402 during one second at V_{Jet}= 2 m/s for 15 fins shark-inspired nozzle.

7.3 Results

Jet cross-flow induced vibration is experimentally investigated for in-line square 6x6 rod bundle simulating a reduced fuel bundle to determine its dynamical behavior. The vibratory response of the tested bundle is obtained by increasing the jet cross-flow velocity up to the onset of an unstable vibration condition (*fluidelastic instability*). The use of a high-speed camera has the significant advantage of capturing the full-field rod bundle vibration while being completely non-intrusive. The measurements are obtained at frame-rate of 400 Hz while the rods vibrated at 29 Hz in water. The 6x6 rod bundle is first tested with the circular jet as a reference case for the comparison with the shark-inspired nozzles to show their effects on the rod bundle vibration.

7.3.1 Circular nozzle jet cross- flow induced vibrations of rod bundle

Figure 7.7 illustrates the behavior of the rod bundle subjected to the circular jet cross-flow. The RMS vibration response normalized by the inter-rod gap (*gap=Pitch-rod diameter*) is obtained in a jet velocity range from 0.93 to 1.75 m/s for each rod in the bundle. The rod responses for rows 1-3 are arranged in Figure 7.7 by three sub-figures, each one included the six rods in the same row. The rods in the bundle are identified by their column number followed by their row number. For example, rod 502 is located in column number 5 and row number 2. The row number is in the direction perpendicular to the jet flow. The dynamical behavior of the rod bundle can be divided into two regions based on the jet velocity: (*i*) V_{Jet} from 0.93 to 1.5 m/s and (*ii*) V_{Jet} from 1.5 to 1.75 m/s. In the first region, the rods are excited by the turbulence in the jet flow as confirmed by the wide band power spectral density (PSD) plot (see Figure 7.8a). The flow velocity $V_{Jet} = 1.5$ m/s marks the stability boundary for the rod bundle. Above the critical velocity (1.5 m/s), the response amplitude is increased sharply. This corresponds to the phenomenon of fluidelastic instability (FEI), where rods vibrate sinusoidally at the single natural frequency of the rod bundle as shown in Figure 7.8b. The maximum vibration amplitude in the first two rows reaches up to 30% of the gap within a jet velocity interval of 0.25 m/s. While the third row response is decreased to 18%gap. The downstream rows are less affected by the jet flow due to the spreading and mixing rate of the jet.

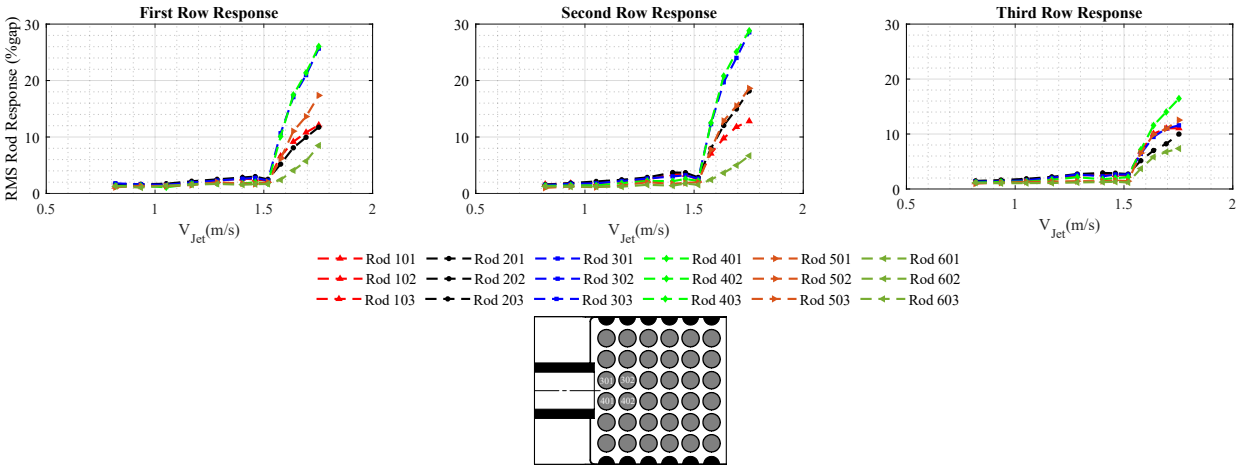

Figure 7.7 Rod bundle vibrations using the circular nozzle.

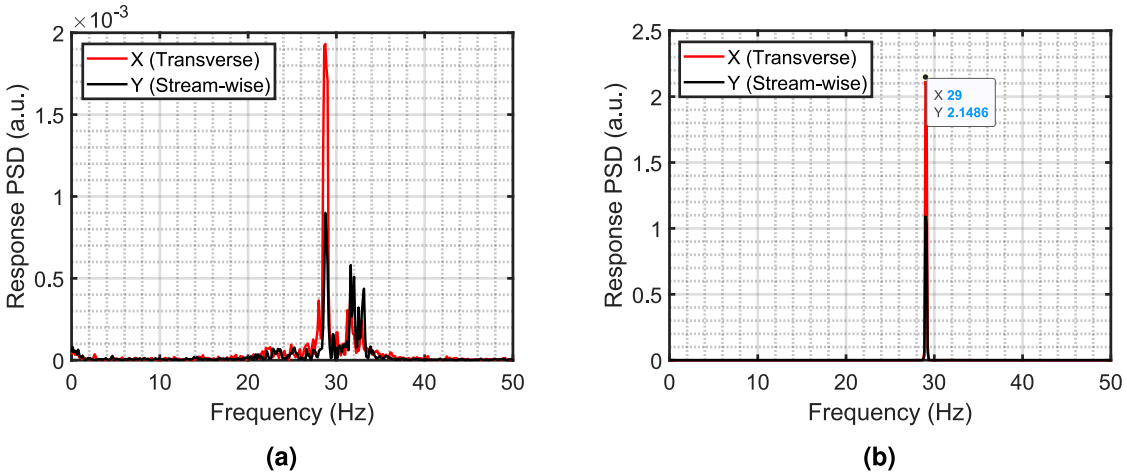

Figure 7.8 (a) PSD plot for Rod 401 at V_{Jet} = 1.45 m/s, and (b) PSD plot for Rod 401 at V_{Jet} = 1.75 m/s.

7.3.2 Jet cross-flow induced vibrations of rod bundle for 10-fin shark-inspired nozzle

The rod bundle vibrations with the circular jet flow provides a reference basis for the performance evaluation of the shark-inspired nozzles. The biomimicry design is investigated first with the 10 fins shark-inspired nozzle. Fluidelastic behavior of the rod bundle is obtained by increasing the jet velocity from 0.87 m/s to 1.92 m/s. Figure 7.9 presents the rod bundle vibration results for the biomimetic nozzle. The attached fins showed their influence by delaying the critical velocity from 1.5 m/s in the circular nozzle case to 1.55 m/s. Furthermore, the maximum response in the first row (rod 401) is reduced by 10% while the reduction

percentage is increased 20% and 26% for second row and third row rods, respectively. The interesting results of the 10 fins shark-inspired nozzle on mitigation of jet cross-flow induced vibrations lead us to investigate another biomimetic nozzle with higher number of fins to show its effect on the mixing process.

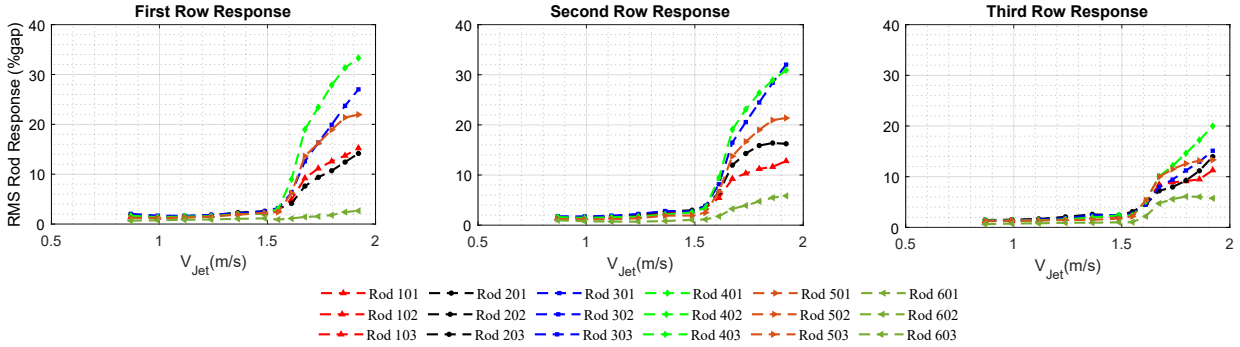

Figure 7.9 Rod bundle vibrations using 10 fins shark-inspired nozzle.

7.3.3 Jet cross-flow induced vibrations in rod bundle due to the shark-inspired nozzle with 15 fins

A second shark-inspired nozzle with 15 fins is tested to investigate the effect of the number of flow channels on the rod array vibration, increasing number of fins corresponds increasing the mixing rate of the jet flow. Figure 7.10 shows the RMS rod response obtained with 15 fins shark-inspired nozzle. As seen from this figure, the fin number has a major impact on the dynamical behavior of the rod bundle. The jet velocity at which instability occurred is significantly delayed, from 1.5 m/s to 1.75 m/s. Compared with the test conducted with the circular jet, the maximum response in the first row (rod 401) is mitigated by 85%, and the mitigation percentage for the second row (rod 402) response is almost the same at 81% while, this percentage became 75% for the third row response (rod 403). Furthermore, unlike with the circular jet cross-flow induced vibrations, the increasing rate in the unstable vibration response is not as sharp as shown in Figure 7.11. Compared with the results obtained with the 10 fins shark-inspired nozzle, rod 401 vibration is mitigated by 53%, while the vibration of rods 402 and 403 is eliminated by 32% and 46%, respectively. Consequently, the comparison between the results obtained with the three nozzle designs lead to the conclusion that the biomimetic nozzle design has a significant effect on the mixing rate of the jet flow. This results in a major reduction in the rod bundle vibration. In addition, the number of fins is important parameter when considering the mixing rate and water flow resistance through the nozzle. Increasing the number of fins shows an interesting effect on the percentage reduction

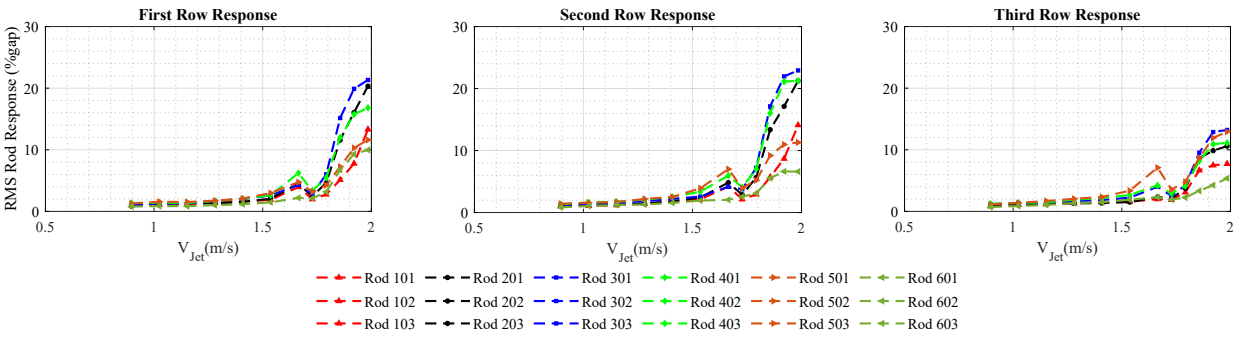

Figure 7.10 Rod bundle vibrations using 15 fins shark-inspired nozzle.

in the rod bundle vibrations. However the reduction in effective nozzle diameter should be carefully considered as fin number increases due to associated increase in pressure drop. The 10 fins shark-inspired nozzle reduces the base diameter by 3.5% due to the fins volume. Moreover, this reduction in diameter increases to 5% for the 15 fin nozzle. However, the results with the 15 fins shark-inspired nozzle show a significant mixing efficiency compared to the other tested nozzles. Thus, the mixing rate and pressure drop across the biomimetic nozzle with 15 fins is optimal.

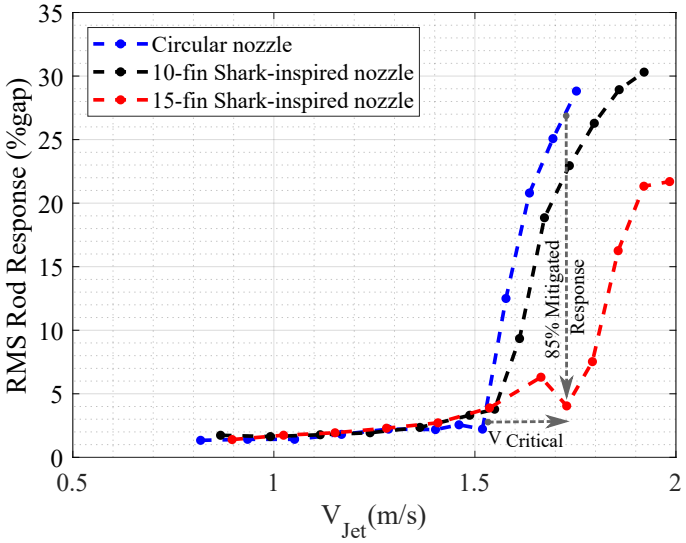

Figure 7.11 Comparison of rod 402 response with three different nozzles.

7.4 Discussion

In this paper, a new biomimetic nozzle based on the shark gill slits is designed to mitigate the jet cross-flow induced vibrations by providing efficient and rapid mixing between the jet

flow and surrounding fluid. The effect of the proposed shark-inspired nozzle is evaluated versus the circular nozzle in the rod bundle vibrations. The experimental results show a significant vibration amplitude reduction (85%) obtained by replacing the circular nozzle with the shark-inspired nozzle. An early study by Fujita et al. (1990) that identified the planar jet flow induced instability showed that the instability threshold is quantified by the jet momentum. Thus, the reduction in the area due to the attached fins should be considered together with jet critical velocity by introducing the critical jet momentum. Equation (7.1) is used to calculate the jet momentum at the stability threshold.

$$M_{Critical} = A_{Exit} V_{Critical}^2 \tag{7.1}$$

where $M_{Critical}$ is the critical jet momentum, A_{Exit} the cross-sectional area of the nozzle, and $V_{Critical}$ the jet velocity at the instability threshold. Figure 7.12 shows the critical jet velocities and the corresponding jet critical momentum plotted versus the diameter ratio between the nozzle and the rod. For the shark-inspired nozzles, an equivalent diameter is calculated from the exit cross-sectional area of the nozzle. The stabilizing effect of the 10 fin shark-inspired nozzle may come from the blockage effect of the fins, as a result of equal momentum value with that obtained with the circular nozzle. However, increasing the number of fins to 15 affects the fluid dynamics of the jet flow; the critical momentum is increased by 20% meaning that the rod bundle is safe from instability with this biomimetic nozzle. Increasing the fin number channels the main flow into more streams which appears to enhance mixing.

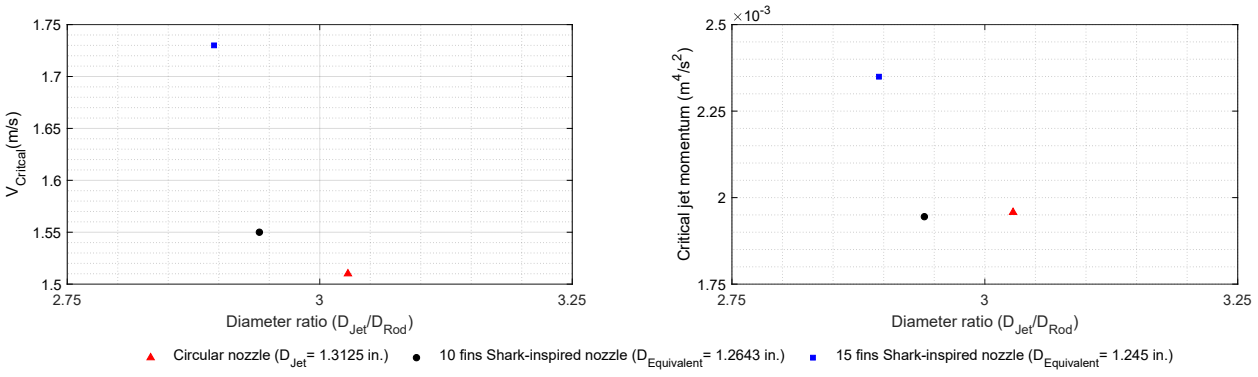

Figure 7.12 Comparison of critical jet velocity and momentum from the three tested nozzles.

7.5 Conclusions

This study is conducted to propose a solution to grid-to-rod fretting of fuel assemblies proximity to the loss-of-coolant accident (LOCA) holes that has been observed in some nuclear reactors. The injected flow from LOCA holes causes fuel rod vibration, which can lead to wear and fretting with their supports (spacer grids). The most effective way to reduce vibration caused by jet cross flow is to improve mixing between the jet potential core and the surrounding fluid, which causes the jet velocity to decay faster and its impact on the rods to be reduced.

Biomimicry of shark gill slits configuration can be incorporated to design a biomimetic nozzle by attaching very thin fins mimicking the shark's secondary lamellae. After the gas exchange process, the exit flow behaviour from the gill slits is of interest due to its steadiness and smoothness. Following the biomimciry design approach that proven through experiments on the rod bundle vibration with two shark-mimetic nozzles; 10 and 15 fins, we found that:

- The shark-inspired nozzle has a significant effect on the vibration amplitude and the stability threshold of the jet cross-flow induced vibrations. The minimum vibration response was obtained with 15 fins which is consistent with very confined flow channels of the shark's secondary lamellae. However, the blockage effect of fins should be carefully considered with increasing the fin number.

- The 15 fin shark-inspired nozzle increased the critical jet velocity from 1.5 m/s to 1.75 m/s in the case of the circular nozzle, which mitigates the rod bundle vibration by 85%. This vibration amplitude reduction can contribute to an increased the safety limit for reactors during normal operation.

- FEI occurs when the jet momentum exceeds the critical limit. Experiments with the 15 fin shark-inspired nozzle confirmed that the critical jet momentum is increased by 20% when the circular nozzle is replaced by proposed biomimetic nozzle.

Highly efficient mixing nozzles are of great interest for a variety of applications. The shark-inspired nozzles can be integrated into fuel injection systems, atomizers and gas mixers to improve the mixing rate. The number of the attached fins will directly affect the jet flow dynamics and mixing efficiency. The fin number and pressure drop around the nozzle must be optimised.

CHAPTER 8 ARTICLE 6: FLUIDELASTIC INSTABILITY OF A FUEL ROD BUNDLE SUBJECTED TO COMBINED AXIAL FLOW AND JET CROSS-FLOW

Gad-el-Hak, I, Mureithi, N, and Karazis, K.

This article has been submitted to "Journal of Fluids and Structures" on 10th October 2022.

Summary

This chapter presents an experimental apparatus to study a dynamical behavior of a mock-up PWR assembly under combined axial and jet cross-flow. To investigate the effect of axial flow on rod bundles subjected to jet cross-flow, single-span 6x5 rod bundles and a 3x1 array are tested in combined transverse/axial flow and pure axial flow. In combined flow tests, FEI experiments are carried out with three axial flow velocities to determine how the critical jet cross-flow velocity changes. Furthermore, axial flow induced damping tests are performed to measure the variation of damping ratio with increasing axial flow velocity. The model developed for pure jet cross-flow induced FEI in Chapter 5 is adopted to take into account the effect of axial flow by introducing the incidence angle of the jet cross-flow. The model developed to predict the instability in combined flow is validated using the experimental results. This work is performed to answer the research questions (**Q4** and **Q5**) and to achieve the objective (**O6**).

Graphical Abstract

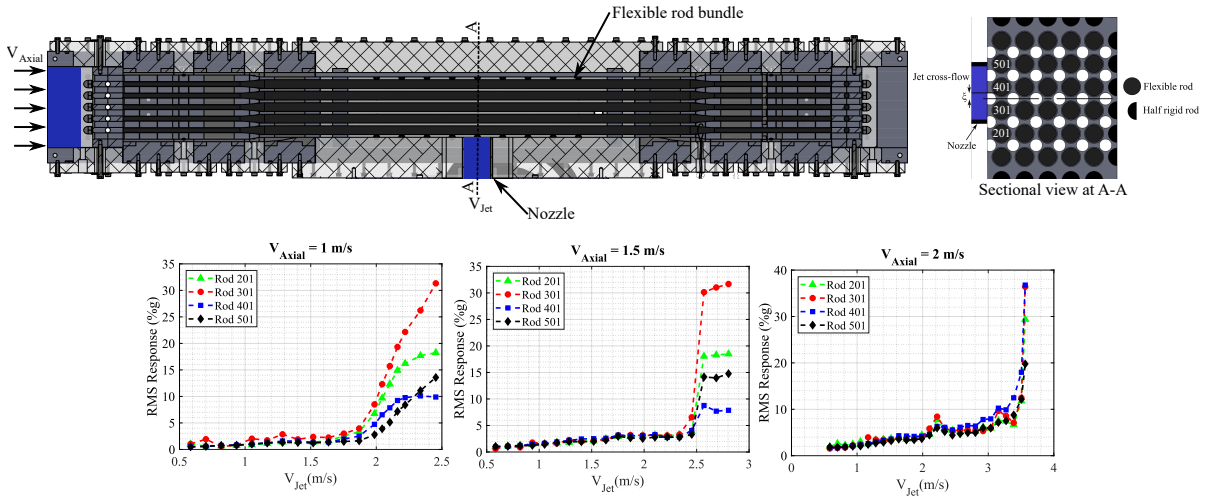

Abstract

Nuclear fuel bundles are subjected to axial coolant flow in addition to jet cross-flow in a specific design of pressurized water reactors (PWRs). The combined axial flow and jet cross-flow was found to induce fretting wear of the fuel rods at the spacer grid position. Investigating a reduced fuel rod bundle under jet-in-transverse-flow (JITF) condition is necessary to determine safe vibration free operation conditions for these reactors.

This paper presents an experimental and theoretical framework to understand the fluidelastic behavior of a rod bundle subjected to axial flow and localized jet cross-flow. A 6x5 axisymmetric flexible single-span rod bundle is used to simulate a part of a fuel assembly under combined flow. Two working flow conditions, pure axial flow, and JITF, are studied on a mock-up PWR assembly. The experiments show that the arrays are stable under pure axial flow as expected. Then, the responses of the rod bundles under combined flows (i.e. JITF) are measured at three test axial flow velocities, V_{Axial}= 1 m/s, 1.5 m/s, and 2.0 m/s. The results show that the critical jet cross-flow velocity increases linearly with the axial flow velocity with a velocity ratio (VR = V_{Jet}/V_{Axial}) of 1.3.

The second part of the work is the development of a fluidelastic instability model to predict the stability boundary for rod bundles under combined axial flow and jet cross-flow. The effect of axial flow on the jet cross-flow is introduced by implementing an incidence angle (θ) of jet flow with respect to the rods. The fluid added damping terms in the developed mode are shown to be functions of θ. The fluidelastic forces are expressed as functions of the projected rod area derivative to account for rod vibration. The stability analysis shows the capability of the model to predict the trend of critical jet cross-flow velocity with the axial flow velocity. The model validation shows the predicted critical velocities to be within an absolute error range from 7% to 12.5% when compared to experiments. The theoretical analysis highlights the importance of the cross-coupling fluidelastic forces in predicting the instability of the mock-up PWR assembly.

Keywords: PWR fuel assembly, Loss-of-Coolant Accident (LOCA), Fluidelastic instability model, Jet in cross-flow (JICF), Axial flow, Jet in cross-flow induced vibrations, Quasi-steady model.

8.1 Introduction

Flow-induced vibration (FIV) is an important concern in the design and operation of nuclear power plants components, heat exchangers and nuclear cores. Fluid flow rate should be high for better thermal performance and efficiency of these components; however, fluid flow induces

vibrations, which could limit plant life span. In nuclear reactor cores, the fuel is cooled by axial flow (parallel to the fuel rods), whereas in the steam generator, tubes are subjected to cross-flow. Cross-flow generally induces higher vibrations than purely axial flow owing to the higher turbulence pressure exerted on the surface of the fuel rods (Paidoussis, 1981). In nuclear reactors, cross-flow combined with axial flow exists in certain conditions and locations in the reactor. A cross-flow may occur between neighboring fuel assemblies when these assemblies have differing designs (resulting in pressure difference between the assemblies). Pump flow anomalies and core boundary imperfections may also lead to transverse flow. In the latter, a localized high speed jet cross-flow may result. Reactor fuel rods are designed to operate in axial flow (parallel to the rod axis). Axial flow induces minimal vibration of the fuel rods. Flow transverse to the rod axes (cross-flow) can potentially result in unacceptably large amplitude vibrations; in the extreme, flow-induced instability could potentially occur. In light of this a deep understanding of the flow-induced dynamics of fuel rod arrays subjected to combined axial and transverse flows is of fundamental and practical importance.

PWR fuel rods are arranged in square lattice arrays, called fuel assemblies. The assemblies are surrounded by baffle plates which guide the coolant flow through the core and establish a new flow boundary around the fuel assemblies (U.S. NRC, 2016). A small portion of the coolant flow is bypassed between the core barrel and the core baffle. In the hypothetical case of a loss of coolant (LOCA) event in the reactor, the hydrodynamic pressure would increase significantly across the baffle plates. Some PWRs include safety features such as loss of coolant accident (LOCA) holes and slots in the core periphery baffles enclosing the fuel assemblies, which relieve pressure build-up in the case of LOCA as shown in Figure 8.1. During normal operation, some of these reactors have experienced grid-to-rod fretting fuel rods due to injected flows from LOCA holes as reported in (IAEA, 2015). Near LOCA holes, PWR fuel assemblies are subjected to the resulting combined axial and localized transverse jet flow conditions at multiple axial positions where LOCA holes are located. There is presently limited knowledge on the effect of combined flow on the dynamical behavior of fuel rod arrays.

Uniform cross-flow induced vibrations in tube bundles have been extensively investigated in the literature. Research on fluidelastic instability has led to an in-depth understanding of the fundamental mechanisms governing it (Chen, 1984, Price, 1995). Among the excitation mechanisms in cross flow, fluidelastic instability is the most destructive mechanism and can potentially lead to fuel rod leakage. The instability is of self-excited type in that it results from the feedback coupling between the rod motion and fluid dynamic forces. Several theoretical models have been developed to predict fluidelastic instability. The complexity of the models ranges from the purely analytical (Yetisir and Weaver, 1993a,b) and the semi-analytical flow

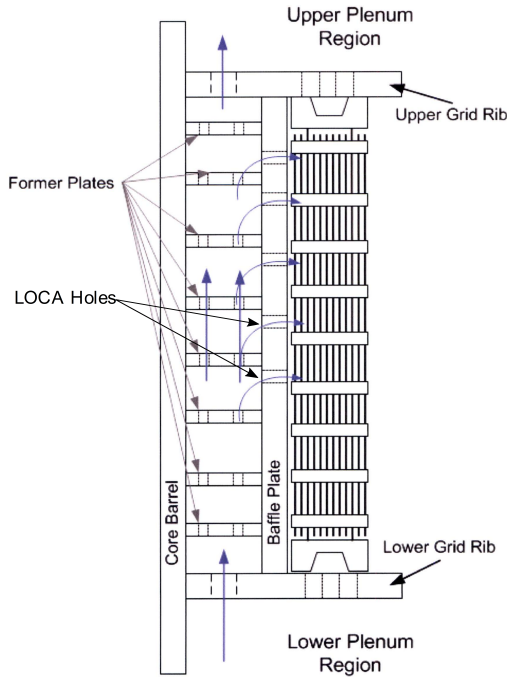

Figure 8.1 Baffle-barrel design including LOCA holes,(AREVA, 2017).

channel model (Lever and Weaver, 1986) to the semi-empirical unsteady models (Chen, 1987, Tanaka and Takahara, 1981). Connors (1970) developed a semi-empirical quasi-static model to determine the stability of tube rows in cross-flow. The stability boundary was defined by a stability constant (K) defined by the ratio between two parameters, reduced critical velocity and mass damping parameter. The class of quasi-steady models (Price and Paidoussis, 1986) that are based on experimentally measured stability derivatives and drag coefficients is our focus in this study. The implementation of a time delay or phase lag component into the quasi-steady model accounts for fluid force velocity dependence. According to the aforementioned, fluidelastic instability of tube arrays subjected to uniform flow is well known, and existing models function reasonably well.

A circular jet has been found to induce instability as demonstrated in (Gad-el Hak and Mureithi, 2022, Gad-el Hak et al., 2021, 2022a). Square rod arrays, of size 2x1, 2x2, 6x6, having pitch-to-diameter (P/D) ratio of 1.32 were tested. The authors investigated the effect jet cross-flow on transverse and stream-wise vibrations, separately. It was found that the instability mainly occurred in the transverse direction. The critical velocity was shown to be dependent on the offset between the jet centerline and array centerline (i.e. jet eccentricity, ξ). The tested arrays were most unstable for a jet eccentricity $\xi = 0.25P$. The effect of jet cross-flow on axisymmetric rod bundle vibration was also investigated by Gad-el Hak and Mureithi (2022) for two different nozzles; a circular nozzle, and a newly proposed shark-inspired nozzle.

The latter nozzle is designed to mitigate the rod bundle vibration by increasing the mixing rate of the jet flow with the surrounding fluid. It was found that the critical velocity could be delayed by 20% using the biomimetic nozzle. In addition to delaying instability, a vibration rod amplitude reduction of 85% was obtained. Gad-el Hak et al. (2022a) also developed a theoretical model based on the quasi-steady approach to predict the critical jet velocity for instability. A new formulation of the fluidelastic forces as a function of the rod area derivative was derived to account variation of the projected area through LOCA holes. The stability boundary prediction was shown to be within 15% of experimental result. This work provides a valuable starting point for the case of combined axial and jet cross-flow induced fluidelastic instability.

Combined axial flow and localized jet cross-flow, here referred to as jet in transverse flow (JITF), describes a jet of fluid that emanates from a nozzle and interacts with the flow transverse to the jet. In the fluid mechanics literature this combined flow configuration is normally referred to as jet in cross-flow (JICF). However, in the present work cross-flow is defined relative to the rods. The term "jet in transverse flow (JITF)" is preferred. The main flow features of JITF have been addressed by numerous experiments and simulations as reviewed by (Margason, 1993). Mixing is induced and accompanied by a complex three-dimensional flow topology and entrainment phenomena as shown in the schematic of Figure 8.2a. The resulting interaction that occurs between the two flows creates a complex set of coherent flow structures and vortex systems. Based upon the experimental observations by Fric and Roshko (1994), four principal types of vortical structures are created due to interaction between the jet and transverse flow. These structures can be classified as: shear layer vortices, counter-rotating vortex pair (CVP), horseshoe vortex system and wake vortices as shown in Figure 8.2a. The jet trajectory is considered as one of the major characteristics of the transverse jet. It is defined by the deflection of the jet in the transverse flow direction as shown in Figure 8.2b. The prediction of the jet trajectory is critically important information on the flow configuration in a reactor core under a LOCA event. The jet trajectory determines how far the jet can penetrate before being deflected by the axial flow. The jet trajectory has long been the subject of many experimental measurements and analytical studies (Broadwell and Breidenthal, 1984, Keffer and Baines, 1963, Smith and Mungal, 1998). The jet centerline trajectory is defined by the locus of the maximum velocity measured in the plane of symmetry. It is clearly recognised that the penetration of the jet into the transverse flow is mainly correlated with the flow velocity ratio. Experimental data can be scaled by using the power-law form (Broadwell and Breidenthal, 1984):

$$\frac{x}{VR.D_{Jet}} = A(\frac{z}{VR.D_{Jet}})^B \tag{8.1}$$

where A and B are constants determined from experiments and VR = V_{Jet}/V_{Axial} is the velocity ratio. Pratte and Baines (1967) found that A = 2.05 and B = 0.28 for VR from 5 to 35. In the present work, the presence of a rod array may affect the parameters of Equation 8.1. However, as a first approximation, Equation 8.1 will be used to estimate the jet trajectory.

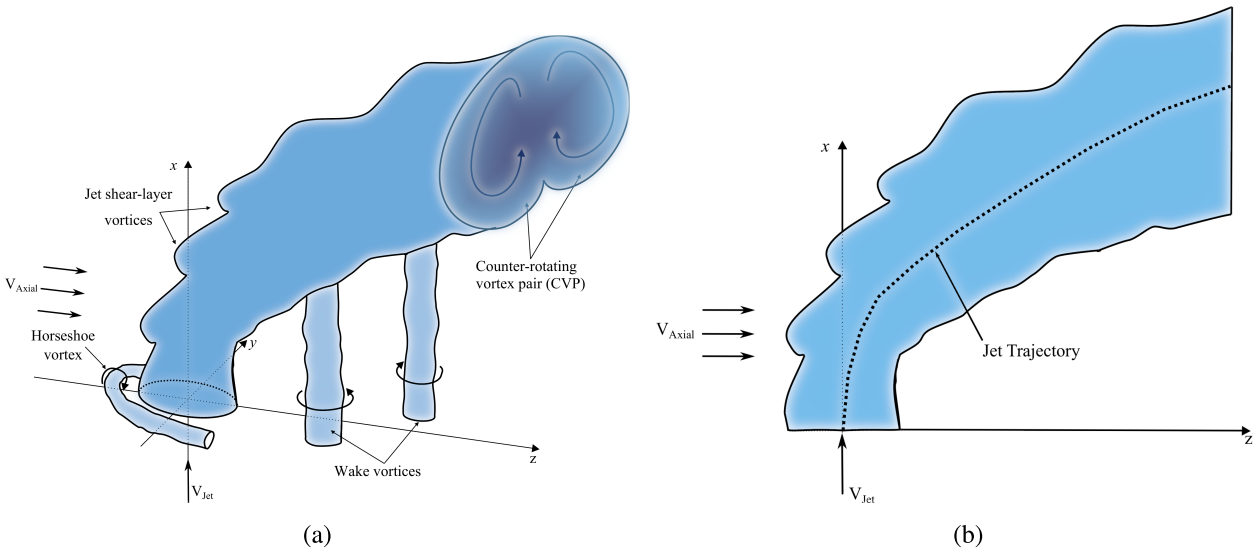

Figure 8.2 (a) schematic drawing of jet in cross-flow (JITF), (b) sectional view of the JITF showing the jet trajectory.

The work reported here addresses the problem of fluidelastic instability in a mock-up PWR fuel assembly subjected to jet in transverse flow (JITF). The study is prompted by the requirement to evaluate the probability of fluidelastic instability excitations occurring in reactor fuel assemblies near LOCA holes. The work reported here consists of experimental measurements and theoretical model development. A single-span PWR mock-up array is designed and fabricated to evaluate its dynamical behavior under JITF for different axial flow velocities. The aim of the flow-induced vibration test is to understand the stability behavior of the array and collect critical jet flow velocity data. The experimental critical jet velocities are also used to validate the theoretical model.

8.2 Experimental setup

8.2.1 Design and test parameters

The purpose of the experimental tests is to measure the effect of primary coolant axial flow as well as mixed jet cross-flow and axial flow on a PWR fuel assembly model. Special attention was given to design a mock-up having dimensions as close as possible to the actual dimensions in nuclear reactor cores. The mock-up bundle is designed to be a 6x5 square array of rods with a pitch-to-diameter ratio of 1.32, identical to the fuel rod arrangement in a PWR. Two rod array configurations are investigated, a 3x1 flexible row, and a 6x5 fully flexible bundle as shown in Figures 8.3a and 8.3b, respectively. A single-span rod bundle setup mimics one span of the fuel assembly supported between two clamping grids as shown in Figure 8.3c. The main geometry parameters for the test apparatus are:

- ξ, the jet centerline offset relative to rod array centerline, as shown in Figure 8.3a.
- D_{Jet}/D, the jet-to-rod diameter ratio.
- H, the nozzle exit distance to the first row of the rod array, as shown in Figure 8.3a.
- L_{Jet}, the axial location of the applied jet flow along the rod bundle span.

The test apparatus is designed for the following set of parameters:

- $0 \leq \xi/P \leq 0.5$, where P is the rod pitch spacing in the array,
- $D_{Jet}/D = 3.0$,
- $H/D = 0.32$,
- $L_{Jet}/L_{Rod} = 0.5$, where L_{Rod} is the rod length.

8.2.2 Flexible rod bundle and instrumentation

The rod bundle consists of axisymmetrically flexible rods having a first mode frequency of 35 Hz in air. The flexible rods are machined from solid aluminum rods to the diameter of reactor fuel rods. The boundary condition of the single-span rod bundle is clamped at both rod ends as shown in Figure 8.4. The rod diameter is reduced near the clamping point to achieve the desired flexibility (frequency) and to make the rod behaves as a rigid body motion. However, the diameter change occurs gradually with a transition angle $\leq 5^\circ$ to avoid flow separation over the transition section of the rod.

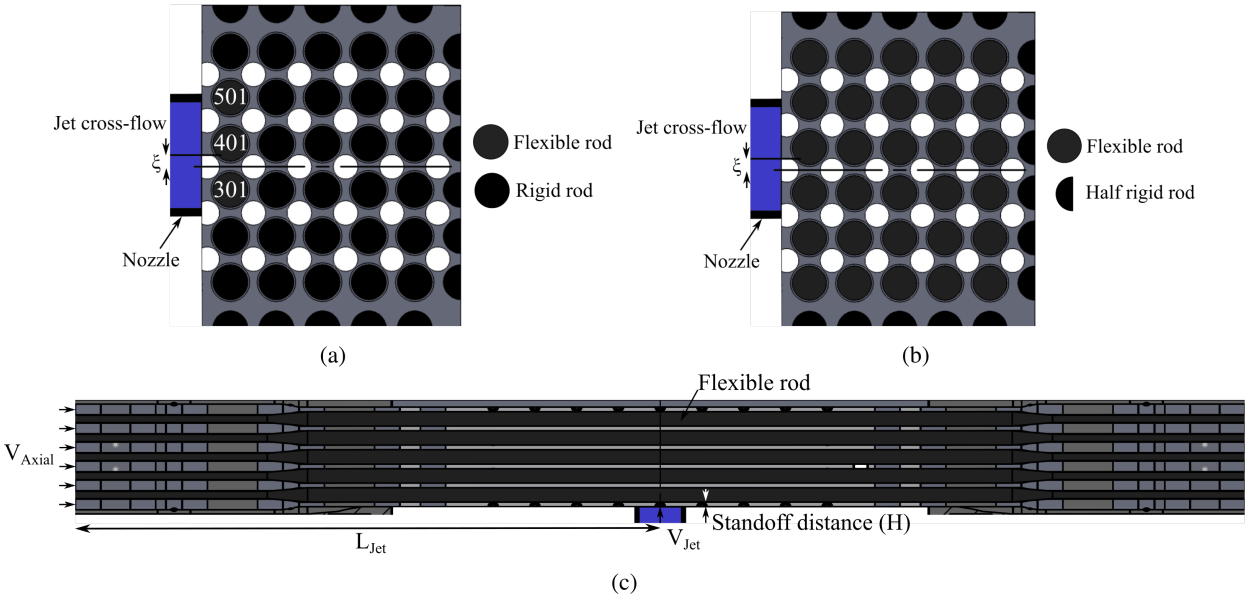

Figure 8.3 (a) sectional view of 3x1 flexible row configuration for jet eccentricity of ξ=0.25P, (b) sectional view of 6x5 fully flexible bundle configuration for jet eccentricity of ξ=0.25P, and (c) top view of rod array.

The compact rod bundle is fully submerged in axial flow, thus measuring the array vibration is a challenge. Vibration amplitude, damping, and frequencies of five rods in the first row are measured under the various flow rate conditions by the strain gauges installed on the rod support near the clamping location. Each rod is instrumented with four strain gauges. Two strain gauges are connected to form a half bridge to measure the stream-wise vibration, while the second half bridge measures the transverse vibration. The instrumented rods are immersed in high velocity axial flow, so sealing the strain gauges is imperative. The sealing products M-Coat B and M-Coat F are used to protect the strain gauges. The instrumented rods are calibrated to determine the conversion factor from strain to rod mid-span displacement for first mode bending vibrations.

Figure 8.4 6x5 fully flexible rod bundle setup.

8.2.3 Test section setup

A test section frame structure is designed and fabricated to create a confined flow channel for the mock-up bundle by providing a direct support to the test section panels. The frame structure also serves to prevent bending vibrations of the test section during the experiments. In addition the frame structure supports the jet flow displacement mechanism as shown in Figure 8.5a. The test section frame is semi-modular. It is assembled from the five main parts; a total of 52 parts make the complete assembly. The modular design concept simplifies that fabrication of the parts while also reducing the material waste that would be produced by machining a single large component. The modular design can be easily expanded to accommodate long multi-span fuel rods. Figure 8.5b shows the fully assembled test section frame.

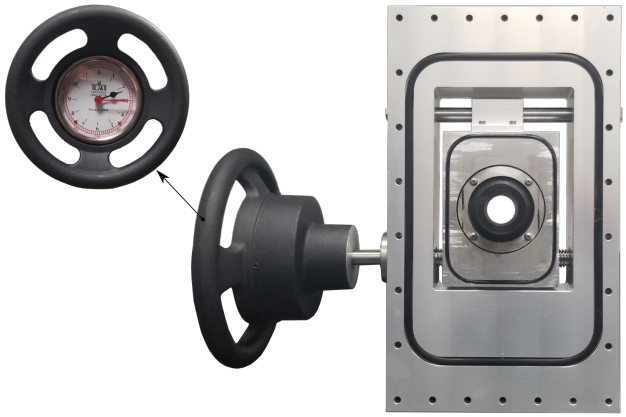

(a)

(b)

Figure 8.5 (a) jet flow displacement mechanism, (b) assembled test section frame.

Acrylic panels are mounted on the frame to provide a confined flow channel around the rod bundle. These test section panels have half rigid rods to ensure flow uniformity and correct boundary conditions in the test section. The fourth side where jet is injected has a smooth

wall. This matches the actual configuration inside reactors (i.e. LOCA holes in baffle plates) as shown in Figure 8.6a. The fuel assembly mock-up is installed inside the test section as shown in Figure 8.6b.

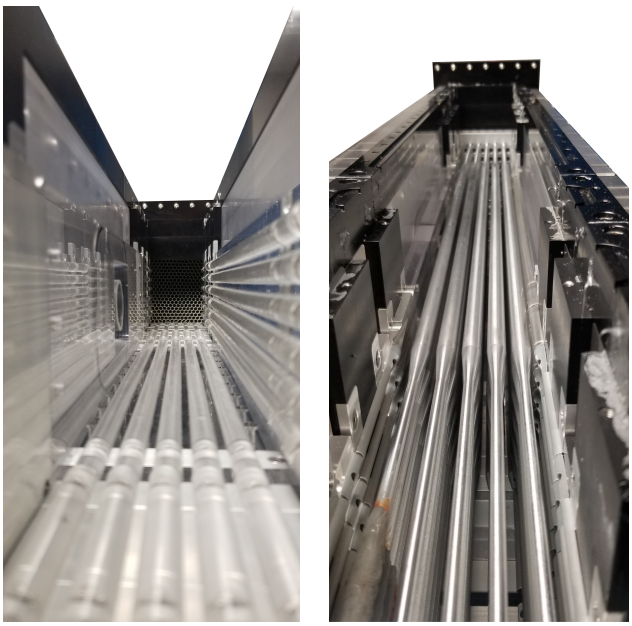

(a) (b)

Figure 8.6 (a) assembled test section with panels, (b) setup of the rod bundle inside the test section.

8.2.4 Test loop setup

The assembled test section is mounted on a sturdy support structure to eliminate any extraneous vibrations, and connected to the rest of the flow loop. Figure 8.7 shows the final test loop for the study of jet in transverse flow induced vibration of the PWR assembly mock-up. It consists of two sub-loops: (i) the axial flow loop branch, and (ii) the jet transverse flow loop branch. Two different pumps are used, one for each sub-loop. A 25 HP centrifugal pump is used to pump the axial water flow up to flow velocities matching in-core operating conditions. Before the flow enters parallel to the rods, it first passes through a flow straightener (labelled 5 in Figure 8.7) to reduce any turbulence caused by pipe connections. A 2 HP centrifugal pump is employed for the jet transverse flow. Uniform water flow from the pump is converted to a jet flow via a nozzle in the jet flow displacement mechanism (labelled 7 in Figure 8.7). Each pump is connected to a flow meter to measure the average flow rate in the branch. Ball valves installed in the test apparatus can adjust the flow in the test section from pure axial flow to mixed axial and jet cross-flow.

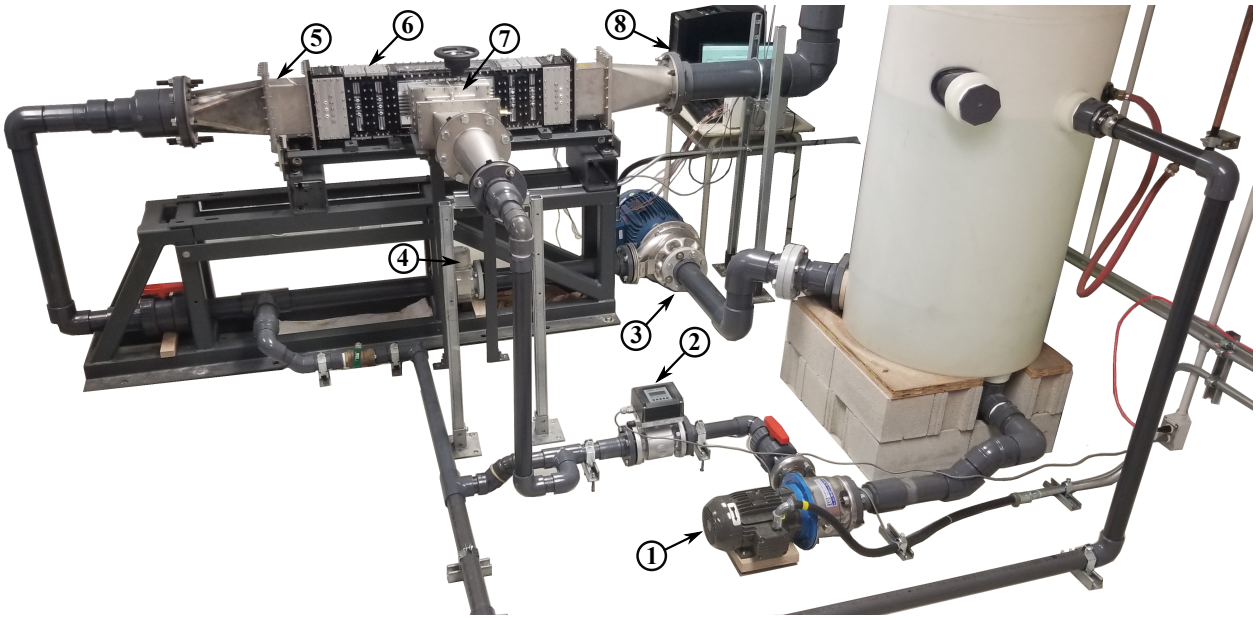

Figure 8.7 The main components of test loop setup are labelled: (1) cross-flow pump, (2) cross-flow meter, (3) axial flow pump, (4) axial flow meter, (5) flow straightener, (6) main test section, (7) displacement jet flow mechanism, (8) data acquisition system.

8.3 Test results

Three different types of tests were carried out; axial flow induced vibration, axial flow induced damping, and jet in transverse flow (JITF) induced fluidelastic instability tests. The experimental results are presented in this section.

8.3.1 Flow-induced vibration response of rod bundle subjected to purely axial flow

The rod array response is first measured in pure axial flow as a reference case to be compared with the effect of a jet cross-flow. Two different arrays, a 3x1 flexible row, and a fully flexible array, are tested in axial flow of velocity ranging from 0.5 m/s to 3 m/s. This range of flow velocity is selected to cover the test cases of jet in transverse flow. Figures 8.8a and 8.8b present the RMS vibration response of the 3x1 flexible row, and the fully flexible array, respectively. The two arrays are stable in the tested range of flow velocities (as expected, Paidoussis (1998)). The resultant RMS response is less than 5% of the inter-rod gap. The vibrations are attributed to flow turbulence excitation. Figures 8.9a and 8.9b show 3D power spectral densities (PSDs) plots for rod 401 in the two arrays: 3x1 flexible row, and 6x5 fully

flexible bundle, respectively. The wide band power spectral densities (PSDs) confirm the purely turbulence excitation mechanism for the bundle in axial flow. As shown in Figure 8.9b, the turbulence intensity increases in the 6x5 flexible array due to the increased flexibility of this array.

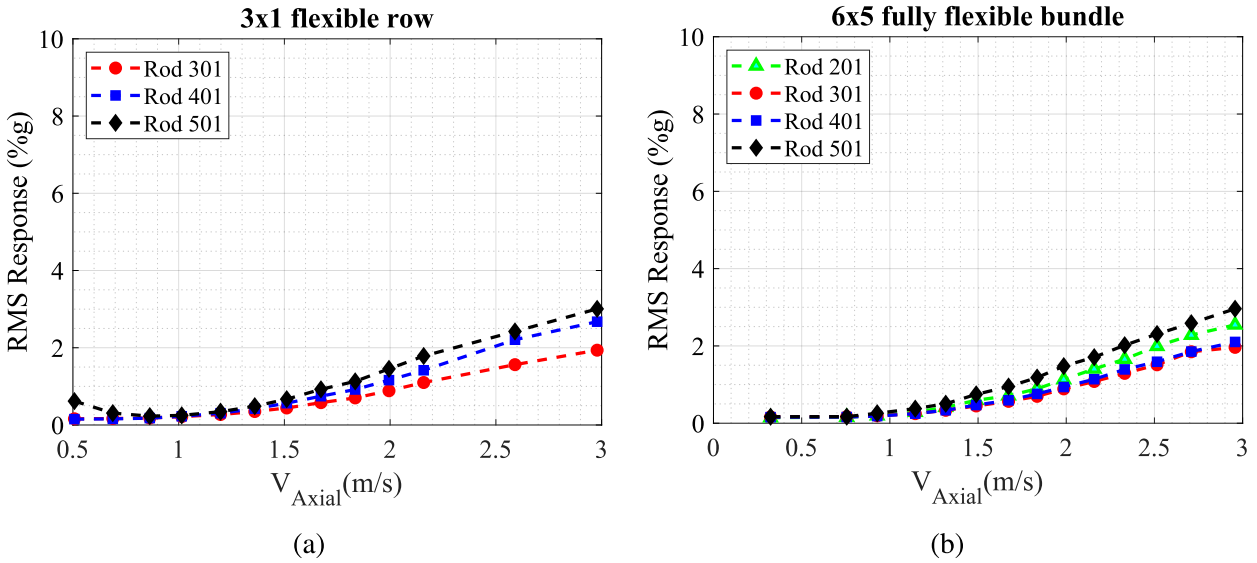

Figure 8.8 Axial flow induced vibrations for two arrays: (a) 3x1 flexible row, (b) 6x5 fully flexible bundle.

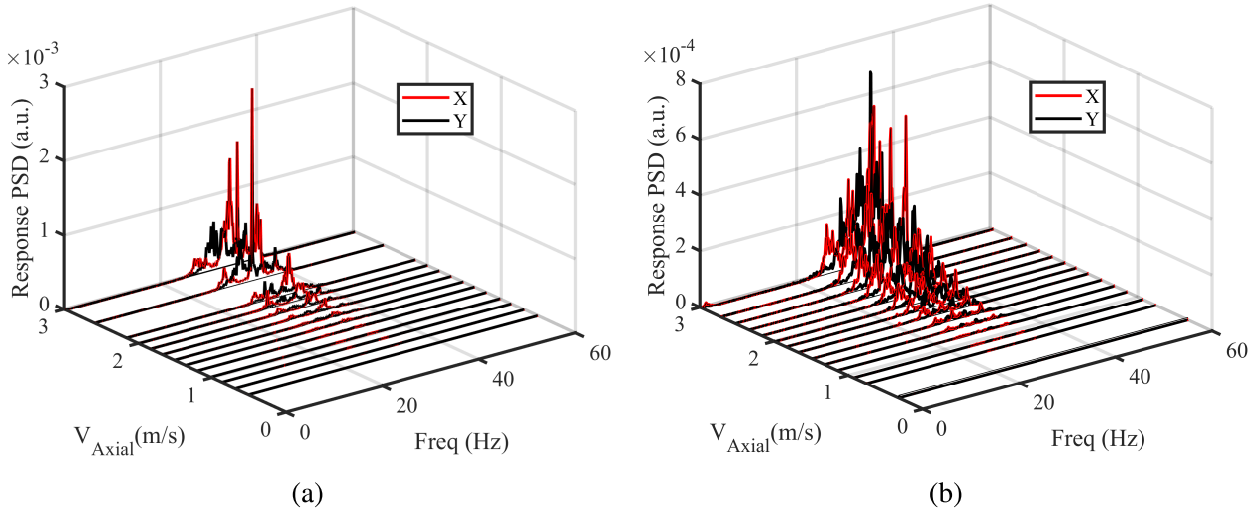

Figure 8.9 3D power spectral densities (PSDs) plots for rod 401 in the stream-wise direction (x), and the transverse direction (y): (a) 3x1 flexible row, (b) 6x5 fully flexible bundle.

8.3.2 Dynamics of rod bundle subjected to combined axial flow and jet cross-flow

After examining the influence of pure axial flow on rod bundle vibration, the effect of combined axial and jet cross-flow is studied next. Fluidelastic instability (FEI) experiments are carried out by increasing the jet cross-flow velocity while keeping the axial flow velocity constant until the onset of instability. The stability boundary of the mock-up array is measured varying two parameters: the number of flexible rods, and axial flow velocity. The identical arrays used in the axial flow tests, the 3x1 flexible row and the 6x5 fully flexible array, are tested to investigate the stability effect of transverse jet flow on the axial flow-induced vibration results. The arrays are tested for three axial flow velocities, V_{Axial} = 1 m/s, 1.5 m/s, 2.0 m/s.

Figures 8.10a, 8.10c, and 8.10e show the RMS responses of the three flexible rods in the 3x1 flexible row configuration. Test results are presented for three axial flow velocities: V_{Axial} = 1 m/s, 1.5 m/s, and 2.0 m/s, respectively. The RMS response is normalized by the inter-rod gap (g). The corresponding dominant response frequencies are shown in Figures 8.10b, 8.10d, and 8.10f, respectively. For V_{Axial} = 1 m/s, fluidelastic instability-induced large amplitude vibrations occur starting at V_{Jet} = 2.2 m/s (Figure 8.10a). The rod 401 response increases by 23%g with an increment of the jet velocity of 0.12 m/s, followed by the rod 301 response with 12%g increase in amplitude and 7%g increase in the rod 501 response. For V_{Axial} = 1.5 m/s case, the critical jet cross-flow velocity is delayed to 2.35 m/s. Due to the stabilizing effect of the axial flow, the stability limit of the jet flow is moved up further to 3.0 m/s for V_{Axial} = 2.0 m/s case. From Figure 8.10, it is evident that the rod 401 has the largest vibration amplitudes in the array for the three axial flow cases. This could be attributed to the rod 401 being coupled to two neighboring flexible rods 301 and 501.

In the instability-induced large amplitude vibrations, the three rods vibrate with the same frequency as seen in Figures 8.10b and 8.10d for the two cases V_{Axial} = 1.0 m/s and 1.5 m/s. At the higher jet flow velocities the rods become fully coupled thus vibrate at the identical frequency. While the intermittent fluidelastic instability occurs in the case of V_{Axial} = 2.0 m/s as shown in Figure 8.10f due to strong turbulence excitation (V_{Jet} through the gap equals 12 m/s). Figures 8.11 and 8.12 compare 3D power spectral densities (PSDs) for rod 401 in the stream-wise direction and transverse direction, respectively, for the three axial flow velocities. For the two cases: V_{Axial} = 1.0 m/s and 1.5 m/s, a single frequency peak is seen at the rod natural frequency. While the rod vibrates with combined frequencies in the case of V_{Axial} = 2.0 m/s, as shown in Figure 8.11c, confirming the intermittent nature of the instability in this case.

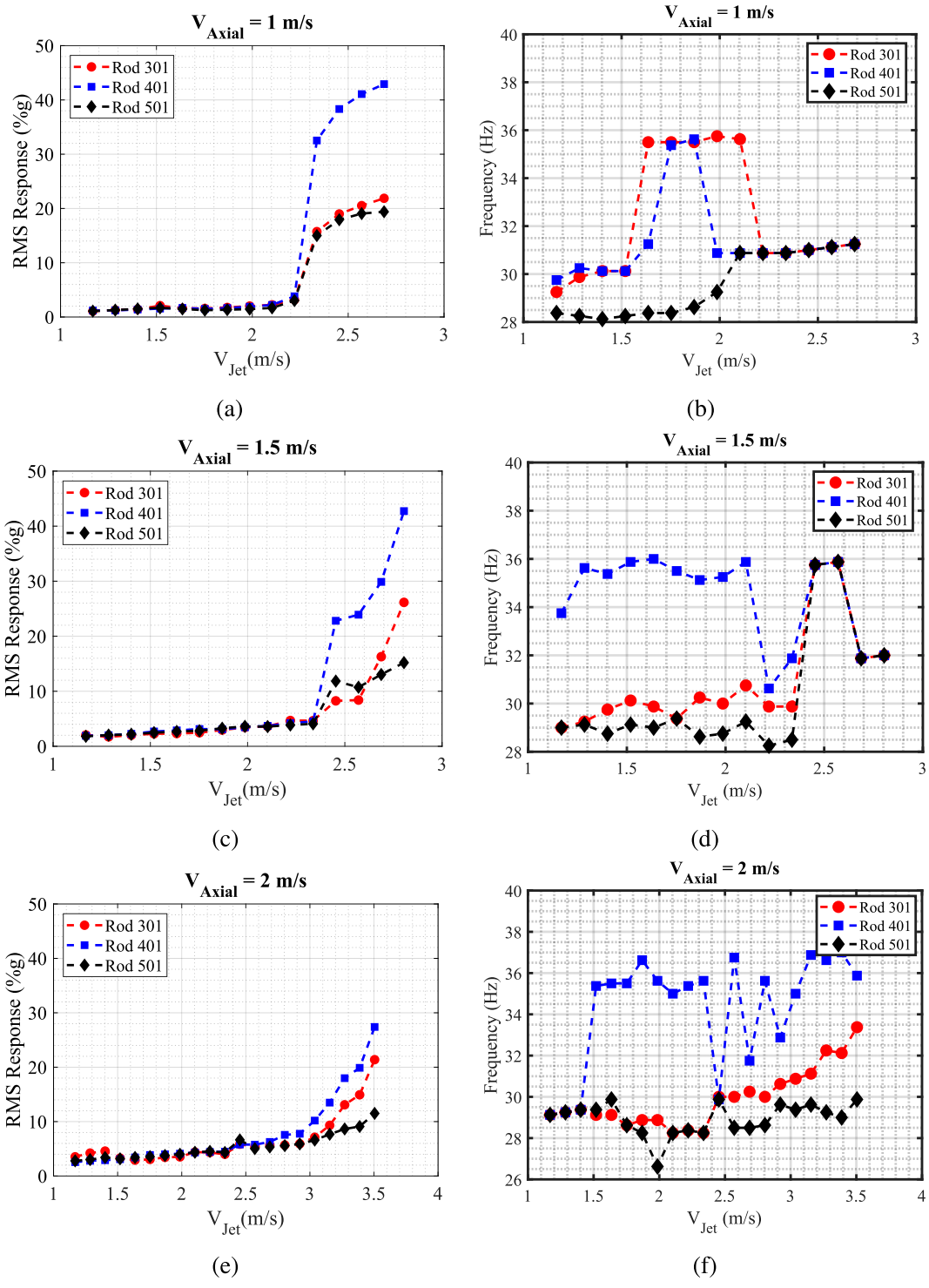

Figure 8.10 RMS response and dominant response frequencies of 3x1 rod bundle for three tested axial flow velocities: (a) and (b) for V_{Axial} = 1 m/s, (c) and (d) for V_{Axial} = 1.5 m/s, and (e) and (f) for V_{Axial} = 2.0 m/s.

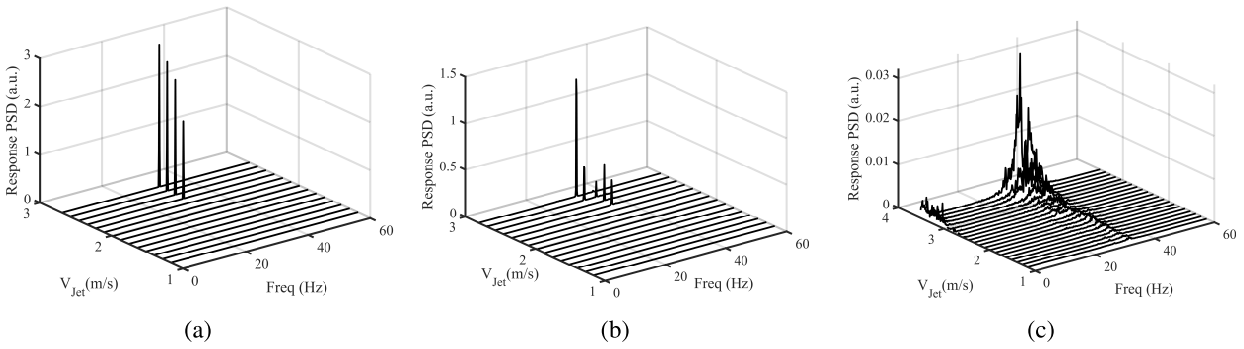

Figure 8.11 3D PSD plots in the stream-wise direction of rod 401 with the three axial flow velocities cases: (a) V_{Axial} = 1.0 m/s , (b) V_{Axial} = 1.5 m/s, and (c) V_{Axial} = 2.0 m/s.

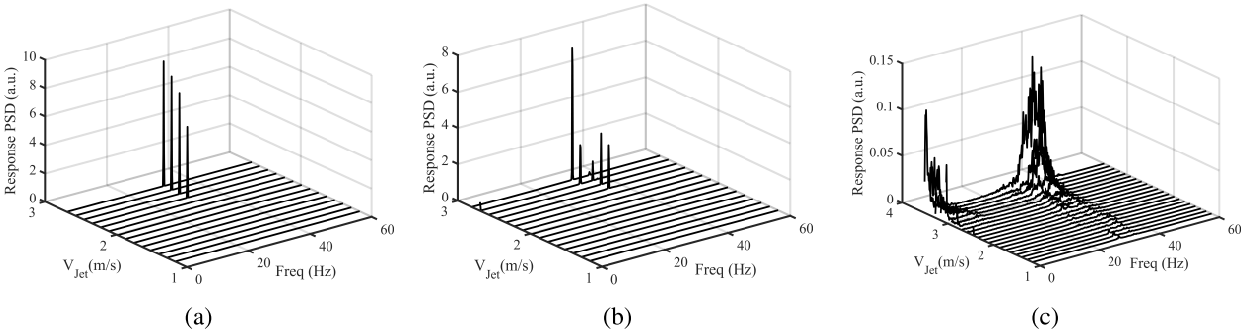

Figure 8.12 3D PSD plots in the transverse direction of rod 401 with the three axial flow velocities cases: (a) V_{Axial} = 1.0 m/s , (b) V_{Axial} = 1.5 m/s, and (c) V_{Axial} = 2.0 m/s.

During fluidelastic instabilities, the rods exhibit orbital motion containing vibrations in both the stream-wise and transverse directions relative to the jet flow. The orbit plot of rod bundle vibration provides information on the dominant vibration direction and trajectories of rods vibrating in combined axial and jet cross-flow. Figure 8.13 shows orbit plots for the three vibrating rods in the combined flow for the V_{Axial} = 1.0 m/s case. The rods vibrate in a straight line path transversely to the jet flow with zero phase difference between the transverse and stream-wise directions. It is clear that the most dominant vibration direction is the transverse direction. Importantly, the orbital dynamics show that the destabilizing fluidelastic forces are predominantly in the direction transverse to the jet flow.

To see the effect of the axial flow velocity on rod motion trajectories, the orbit plots for the V_{Axial} = 1.5 m/s case are plotted in Figure 8.14. The rods 301 and 401 have a phase difference between the transverse and stream-wise directions leading to an oval orbit motion. However, the vibration remains predominantly in the transverse direction. Figure 8.15 shows the rod trajectories for the V_{Axial} = 2.0 m/s case. The rod motion is mainly in the transverse

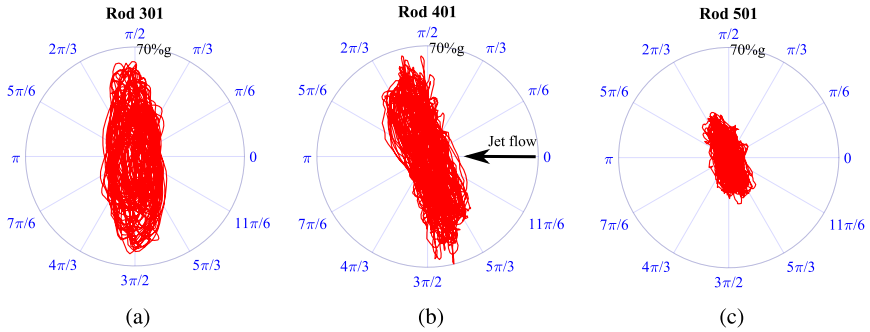

Figure 8.13 Orbit plots for three rods for the V_{Axial} = 1.0 m/s case at V_{Jet} = 2.6 m/s: (a) rod 301, (b) rod 401, and (c) rod 501.

direction, but it is more random. The foregoing results suggest that a theoretical model could be developed based purely on the transverse direction motion to predict the critical instability velocity of the bundle subjected to jet in transverse flow (JITF).

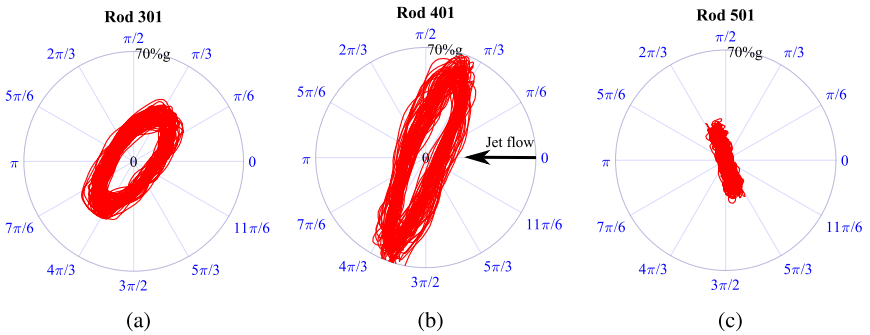

Figure 8.14 Orbit plots for three rods for the V_{Axial} = 1.5 m/s case at V_{Jet} = 2.8 m/s: (a) rod 301, (b) rod 401, and (c) rod 501.

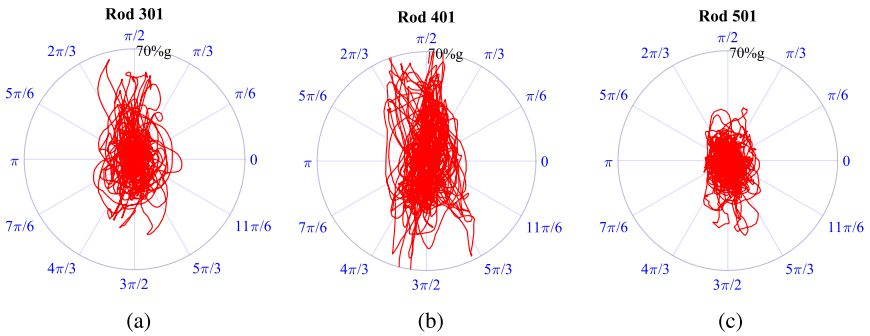

Figure 8.15 Orbit plots for three rods for the V_{Axial} = 2 m/s case at V_{Jet} = 3.5 m/s: (a) rod 301, (b) rod 401, and (c) rod 501.

Having investigated the effect of combined axial and jet cross-flow on the simple 3x1 flexible row configuration, the fluidelastic excitation behavior of the 6x5 fully flexible rod array was studied next. The critical jet cross-flow velocity is determined for the same three axial flow velocities, as in the 3x1 flexible row case, to compare the dynamics of the two arrays. The fully flexible array vibration response is measured for jet cross-flow velocities ranging from 0.5 m/s to the onset of fluidelastic instability. Figures 8.16a, 8.17a, and 8.18a present the RMS responses of the four first row flexible rods, rod 201, rod 301, rod 401, and rod 501, in the 6x5 fully flexible array configuration. The results are for the same three axial flow velocities: V_{Axial} = 1 m/s, 1.5 m/s, and 2.0 m/s, respectively. The corresponding 3D PSD plots in the stream-wise direction for rod 401 in the three cases are presented in Figures 8.16b, 8.17b, and 8.18b. While the corresponding 3D PSD plots in the transverse direction for rod 401 in the three cases are presented in Figures 8.16c, 8.17c, and 8.18c. For V_{Axial} = 1 m/s, the critical jet cross-flow velocity is 1.9 m/s. This velocity is less than that observed in the 3x1 row case ($V_{Jet,critical}$ = 2.2 m/s). This reduction in the stability limit is attributed to the increase in the flexibility of the array which increases rod cross-coupling. This is further investigated in the theoretical modeling part of the paper. Fluidelastic instability is clearly observed in the two cases having V_{Axial} = 1 m/s and 1.5 m/s as confirmed in Figures 8.16b, 8.16c, 8.17b and 8.17c by the large amplitude response at a single frequency vibration. The instability of the fully flexible array for V_{Axial} = 2 m/s is clearly stronger than that observed in the 3x1 flexible row response (see Figure 8.10e and Figure 8.18a). The stabilizing effect of axial flow is also observed for the fully flexible array. Interestingly, the stability boundaries for the tests with V_{Axial} = 1.5 m/s, and 2.0 m/s, are approximately the same as those for the flexible array and the 3x1 flexible row. This may be explained by the jet/rod-bundle configuration. The jet flow entering the array directly interacts with the three first row rods (301, 401, 501) which are part of the 3x1 row array tested. On entering the rod bundle, the jet flow spreads and dissipates (rapidly for high axial flow velocities). The nearly identical critical velocities for the fully flexible array and the 3x1 row of rods suggests that the three rods (301, 401, 501) are responsible for causing array instability. This was also experimentally found to be the case in Gad-el Hak et al. (2022a).

Figure 8.19a summarizes the critical jet cross-flow velocity versus axial flow velocity relation for the two tested arrays. It is seen from the figure that the stability threshold, $V_{Jet,critical}$, increases approximately linearly with V_{Axial}. The linear variation corresponds to the velocity ratio VR (= V_{Jet}/V_{Axial}) equal to 1.3. This parameter (VR) could be used to characterize the stability limit of rod arrays subjected to combined axial flow and jet cross-flow. Figure 8.19b shows schematically the flow regimes of a jet in transverse flow (JITF) with respect to VR. The ratio VR = 1.25 is a transition value between detached and deformed JITF or fully

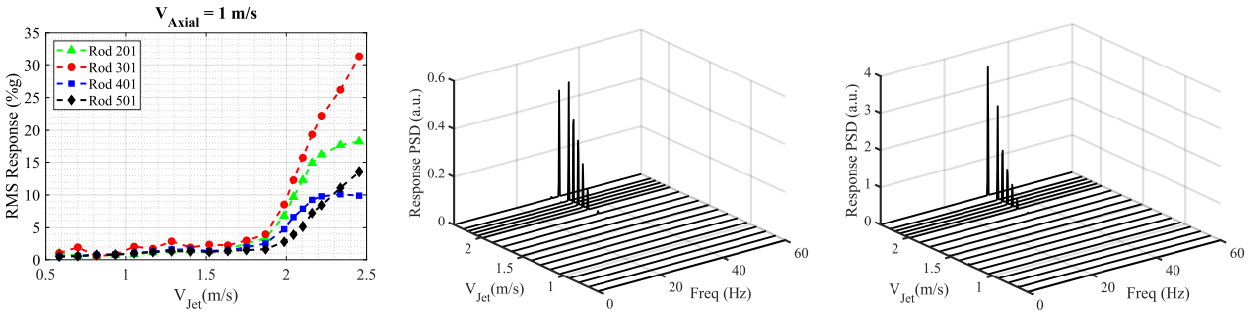

(a) (b) (c)

Figure 8.16 RMS response for four rods in 6x5 fully flexible rod bundle for $V_{Axial} = 1.0$ m/s, (b) corresponding 3D PSD plots in the stream-wise direction of rod 401, and (c) corresponding 3D PSD plots in the transverse direction of rod 401.

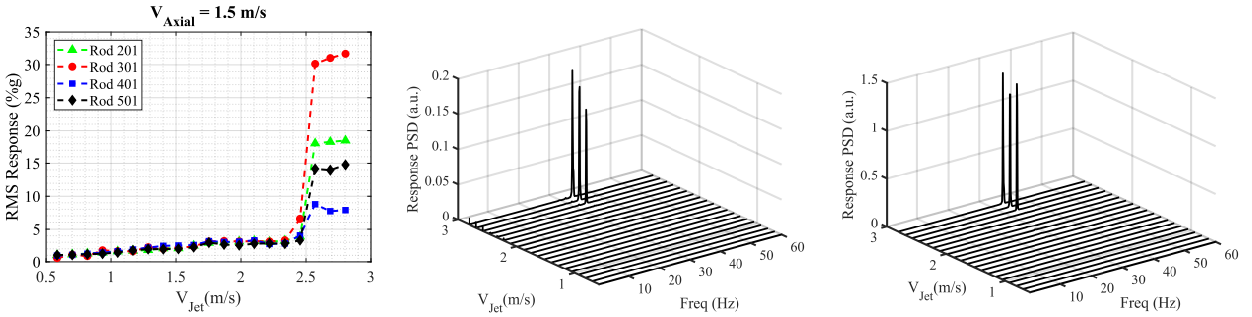

(a) (b) (c)

Figure 8.17 RMS response for four rods in 6x5 fully flexible rod bundle for $V_{Axial} = 1.5$ m/s, (b) corresponding 3D PSD plots in the stream-wise direction of rod 401, and (c) corresponding 3D PSD plots in the transverse direction of rod 401.

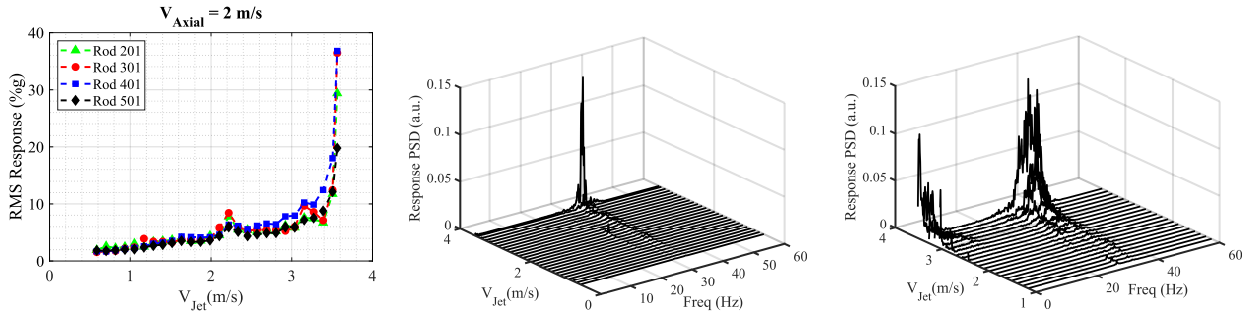

(a) (b) (c)

Figure 8.18 RMS response for four rods in 6x5 fully flexible rod bundle for $V_{Axial} = 2$ m/s, (b) corresponding 3D PSD plots in the stream-wise direction of rod 401, and (c) corresponding 3D PSD plots in the transverse direction of rod 401.

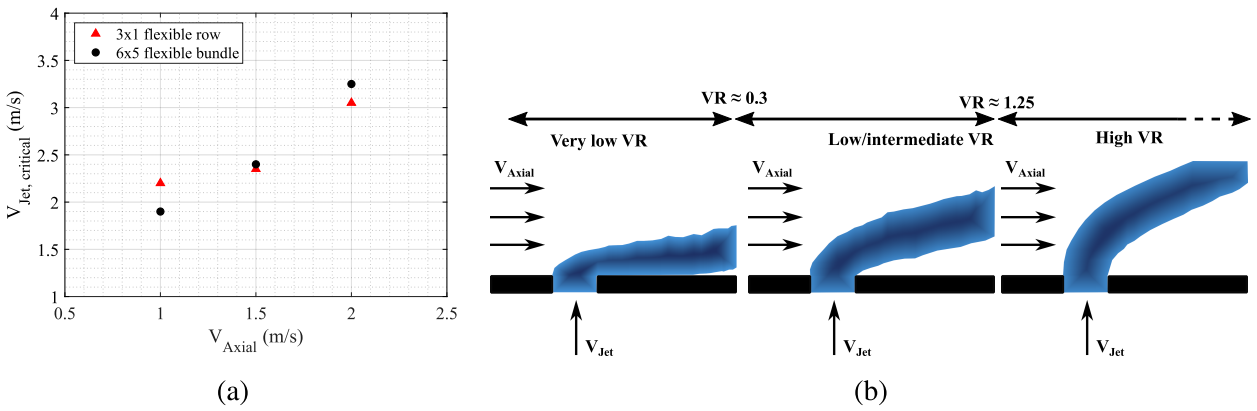

Figure 8.19 (a) Stability boundaries of jet cross-flow velocity with axial flow velocity for the two tested arrays, and (b) jet in transverse flow (JITF) flow regimes with respect to velocity ratio (VR= V_{Jet}/V_{Axial}).

detached JITF (Cambonie and Aider, 2014). From the test results presented here it could be concluded that when the jet flow is fully detached from the wall, the effect of jet flow is significant enough to induce instability in rod arrays.

8.3.3 Axial flow damping tests

The objective of the axial flow damping test is to identify the vibration characteristics (damping ratio (ζ) and frequency (f)) of a flexible rod when axial flow is introduced. These modal parameters of the flexible rod will be used in a theoretical model to perform the stability analysis. To measure the flexible rod frequency and damping characteristics, free decay tests are performed. However, performing a free decay test under axial flow conditions is a challenging task requiring a specialized test setup. In the setup, a vented set screw is fixed on a panel near the flexible rod in the downstream region as shown in Figure 8.20. A very thin (0.01 inch) flexible cable is passed through a small hole in the set screw and knotted on the rod support.

The rod is initially statically displaced and then released to vibrate freely in water flow conditions. To ensure repeatability, the test is done three times for each flow condition. The damping test is performed for five test conditions, still water, and for axial velocities (V_{Axial}) in the range 0.5 m/s - 2.0 m/s, as listed in Table 8.1. Figures 8.21a and 8.21c show example time traces for free decay tests performed in still water, and for the case V_{Axial} = 1.5 m/s, respectively. The damping ratio (ζ) is calculated by fitting a 1 dof frequency response function (FRF) to the Fourier transform of the response as shown in Figures 8.21b

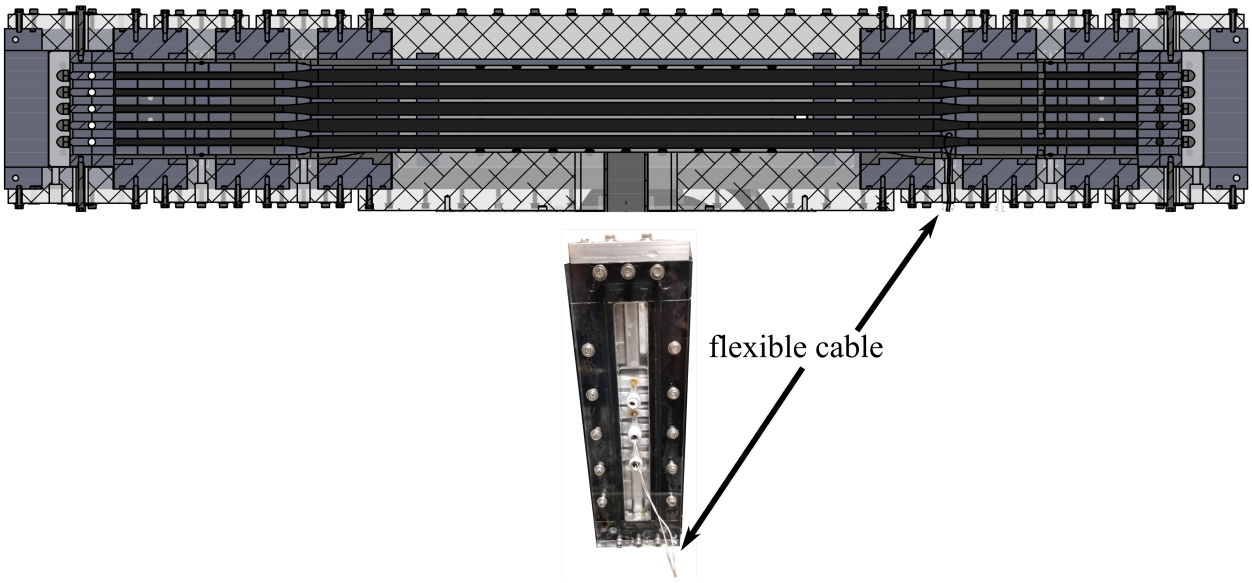

Figure 8.20 Free decay test setup.

and 8.21d. The calculated rod damping ratio includes the contributions of both structural damping and axial flow-induced damping. Table 8.1 shows the rod frequency and damping ratio for each test condition. The damping ratio increases slightly between the still water case and the V_{Axial} = 1.0 m/s case. As the axial flow velocities increase from 1.0 m/s to 2.0 m/s, the damping ratio increases by approximately 50%. The increase is not linear. A large jump in damping occurs between V_{Axial} = 1.0 m/s and V_{Axial} = 1.5 m/s. The rod frequency increases only slightly with increasing axial flow velocity. Collard et al. (2005) studied the effect of axial flow on the modal characteristics of a PWR fuel assembly. They found that the damping term increased linearly with the axial flow velocity. In addition, the equivalent modal mass decreased with the axial flow rate, which agrees with our findings.

Table 8.1 Damping ratio and frequency values of a single flexible rod versus axial flow velocity.

Case	frequency (Hz)	damping ratio, ζ
Still water	27.9	0.0202
$V_{Axial} = 0.5m/s$	27.98	0.0204
$V_{Axial} = 1.0m/s$	28.06	0.0207
$V_{Axial} = 1.5m/s$	28.4	0.0275
$V_{Axial} = 2.0m/s$	28.6	0.03

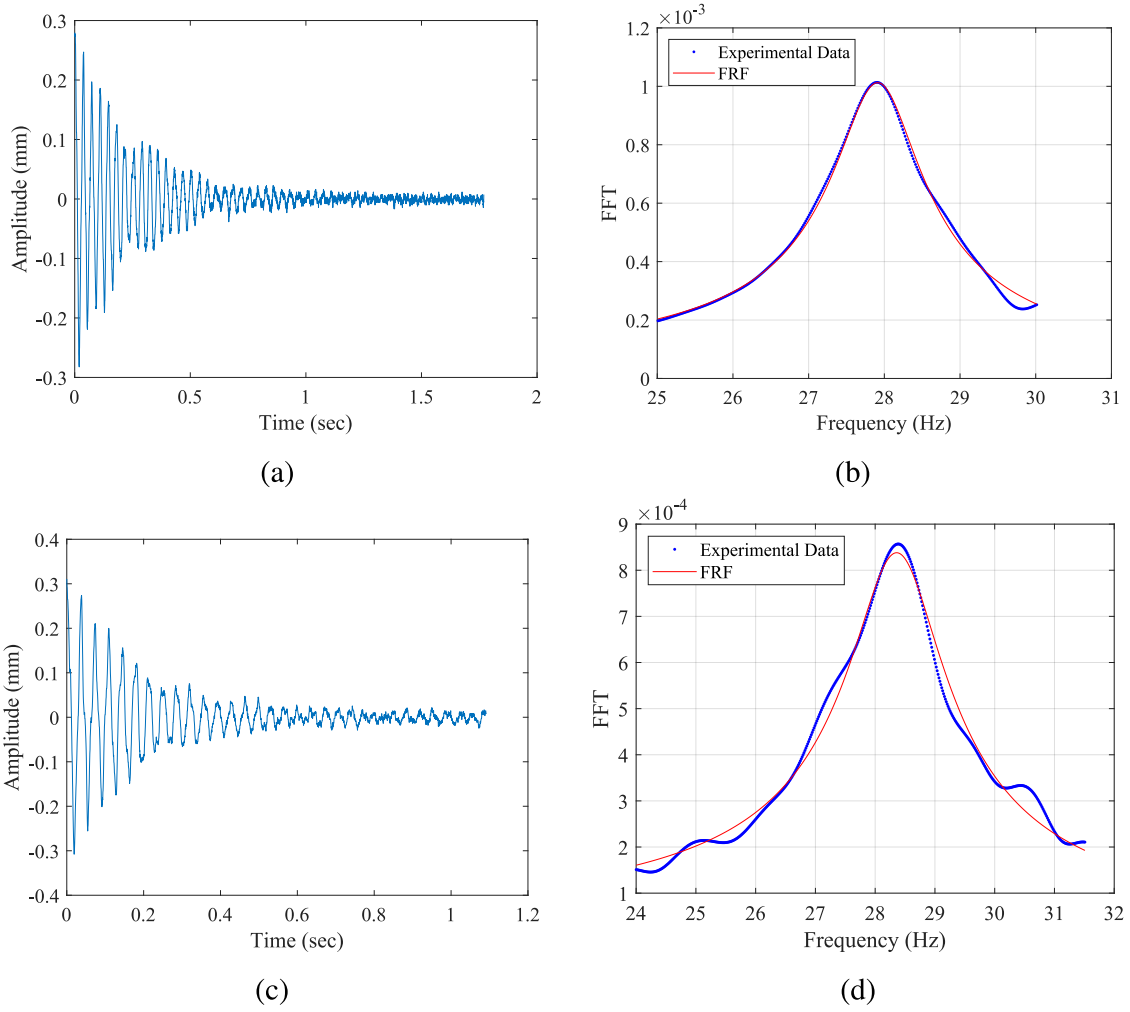

Figure 8.21 Free decay tests: (a) in still water, (c) at V_{Axial} = 1.5 m/s, and FRF fit of experimental data: (b) in still water, and (d) at V_{Axial} = 1.5 m/s.

8.4 JITF induced FEI model development

The dynamical behaviour of the single span mock-up PWR assembly in a pure axial flow was found to be limited to low amplitude turbulence-induced vibrations. Tests with combined axial flow and jet cross-flow induced strong self-excited vibrations attributed to fluidelastic instability. The jet in transverse flow induced vibration was mainly in the direction transverse to the jet flow. The stability threshold of the 3x1 flexible row was found to be close to that obtained for the 6x5 fully flexible array (see Figure 8.19a). The experimental results suggest that a theoretical model based on the 3x1 row configuration may provide insight into the stability behavior of a rod bundle subjected to JITF.

Figure 8.22a shows graphically the location of the nozzle relative to the first row rods for the

3x1 configuration. In the figure, the system origin is coincident with the array centerline. The jet flow direction is along the x-axis, and the axial flow is parallel to the z-axis. The jet flow from the nozzle is obstructed by the three rods, 301, 401, and 501 as seen in the figure.

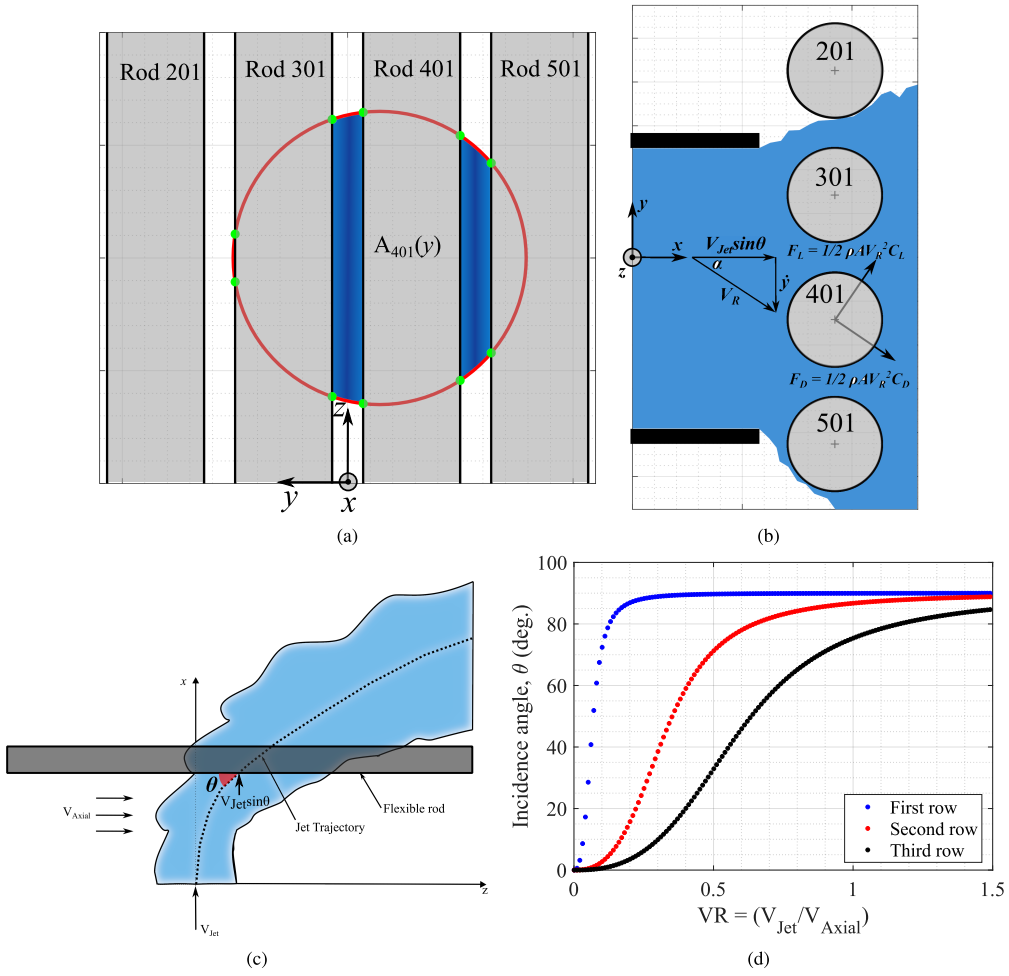

Figure 8.22 (a) projected view from the nozzle, (b) top view of the array with the nozzle, (c) schematic drawing showing the JITF with the array, and (d) variation of the incidence angle with the velocity ratio (VR).

In the proposed model, we consider the three flexible rods (in the otherwise rigid array) vibrating purely in the transverse direction (y) under JITF as shown in Figures 8.22b. The rods are exposed to localized jet fluid forces at the mid-span location. Thus, the rods are modeled as point masses where the effective rod mass and stiffness are measured by putting a weight at the mid-point (location of jet flow) and measuring the mid-point displacement. The jet flow is deflected by the effect of the axial flow momentum, thus the jet trajectory intersects with the rods at an incidence angle (θ) as shown in Figure 8.22c. This angle is a function of the stand-off distance (H), velocity ratio (VR), and jet diameter (D_{Jet}) as shown

in Figure 8.22d. A model for the dynamical behavior of a rod bundle subjected to jet cross-flow was recently developed by Gad-el Hak et al. (2022b). This model is extended here to account for the important and non-trivial effect of the axial flow on the jet cross-flow. The jet-induced fluid forces are coupled with the rod motion. The coupled equations of motion of the system can be written in the following general form:

$$[M_s]\ddot{\vec{y}_{(t)}} + [C_s]\dot{\vec{y}_{(t)}} + [K_s]\vec{y_{(t)}} = \vec{F_y}; \;\; \vec{y} = [y_{301}, y_{401}, y_{501}]^T \tag{8.2}$$

where $[M_s]$, $[C_s]$, $[K_s]$ are, respectively, the mass, damping and stiffness matrices of the structure, and $\vec{y}$ the rod displacement vector considering only the first vibration mode for each rod. $\vec{F_y}$ is the jet fluid dynamic force vector in the direction transverse to the jet flow. Consider for instance, the force components acting on rod 401. These force components, expressed in terms of the lift and drag forces are shown in Figure 8.22b. Using a quasi-steady approach, the total transverse direction force component on this rod can be written as follows:

$$F_{y401} = F_L cos(\alpha) - F_D sin(\alpha) = 1/2\rho {V_R}^2 A[C_L cos(\alpha) - C_D sin(\alpha)] \tag{8.3}$$

where V_R is the relative flow velocity, and α the angle of attack as defined in Figure 8.22b:

$$V_R = [(V_{Jet} sin\theta)^2 + \dot{y}^2]^{1/2}; \;\; \alpha = \tan^{-1}(\dot{y}/V_{Jet} sin\theta) \tag{8.4}$$

For small rod vibrations, V_R and α can be approximated as:

$$V_R \approx V_{Jet} sin\theta; \;\; \alpha \approx \dot{y}/V_{Jet} sin\theta \tag{8.5}$$

The projected area (A) of the rod relative to the nozzle changes with the transverse rod motion (y) due to the change in geometrical matching between the circular jet cross-sectional area and the rods (see the intersection points in Figure 8.22a). As an example the projected area for rod 401 is related to the displacement y by $A = A_{Jet} * (0.067 * (y_{401}/D) + 0.4)$. C_L, C_D, and A for rod 401 can be expressed in linearized form as:

$$\begin{aligned}
C_{L401} &= C_{L0} + \frac{\partial C_L}{\partial y_{401}} y_{401} + \frac{\partial C_L}{\partial y_{301}} y_{301} + \frac{\partial C_L}{\partial y_{501}} y_{501} \\
C_{D401} &= C_{D0} + \frac{\partial C_D}{\partial y_{401}} y_{401} + \frac{\partial C_D}{\partial y_{301}} y_{301} + \frac{\partial C_D}{\partial y_{501}} y_{501} \\
A_{401} &= A_0 + \frac{\partial A}{\partial y_{401}} y_{401}
\end{aligned} \tag{8.6}$$

Equation 8.3 can thus be linearized as follows:

$$F_{y_{401}} = 1/2\rho(V_{Jet}sin\theta)^2 \left(A_{401_0} + \frac{\partial A_{401}}{\partial y_{401}} y_{401}\right) \left[\left(C_{L401_0} + \frac{\partial C_{L401}}{\partial y_{401}} y_{401} + \frac{\partial C_{L401}}{\partial y_{301}} y_{301} + \frac{\partial C_{L401}}{\partial y_{501}} y_{501}\right) - \left(\frac{\dot{y}_{401}}{V_{Jet}sin\theta}\right) \left(C_{D401_0} + \frac{\partial C_{D401}}{\partial y_{401}} y_{401} + \frac{\partial C_{D401}}{\partial y_{301}} y_{301} + \frac{\partial C_{D401}}{\partial y_{501}} y_{501}\right)\right] \tag{8.7}$$

In the quasi-steady fluid-dynamic theory, the quasi-static forces are modified to take into account the dynamic feature of the fluid response by introducing a time delay, τ. Simpson and Flower (1977) considered a time lag associated with the deceleration of the flow as it approaches the tube stagnation point. Following this definition, Price and Paidoussis (1986) introduced a constant time delay in the form:

$$\tau = \frac{\mu D}{V}; \quad \mu \sim O(1) \tag{8.8}$$

where D is the tube diameter, μ is the flow retardation parameter (taken to be of order 1), and V is the relevant flow velocity. Price and Paidoussis (1986) used $\mu = 1$ for an in-line square array in uniform flow. In this paper, V=V_{Jet}sinθ since the model is developed for the upstream row which is exposed to the jet velocity component V_{Jet}sinθ.

Introducing the time delay effect, the fluid force Equation (8.7) becomes:

$$F_{y401} = 1/2\rho(V_{Jet}sin\theta)^2 \left[A_{401_0} \left(C_{L401_0} + e^{-i\omega\tau}\frac{\partial C_{L401}}{\partial y_{401}} y_{401} + e^{-i\omega\tau}\frac{\partial C_{L401}}{\partial y_{301}} y_{301} + e^{-i\omega\tau}\frac{\partial C_{L401}}{\partial y_{501}} y_{501}\right) + \left(C_{L401_0}\frac{\partial A_{401}}{\partial y_{401}} y_{401}\right) - \left(A_{401_0} C_{D401_0}\frac{\dot{y}_{401}}{V_{Jet}sin\theta}\right)\right] \tag{8.9}$$

where ω is the angular vibration frequency. The first term in Equation 8.9 includes the fluidelastic forces generated due to the rod motion and the cross-coupling forces due to the motion of the neighbouring rods. The second term ($C_{L401_0}\frac{\partial A_{401}}{\partial y_{401}} y_{401}$) is introduced in the model to take into account the change in projected area. The third term is the component of the fluid added damping which is a function of the jet incidence angle (θ).

The 3-DOF jet flow-coupled system modelling jet-induced vibrations is written as:

$$
\begin{aligned}
&[M_s + M_f]\ddot{\vec{y_{(t)}}} + [C_s]\dot{\vec{y_{(t)}}} + [K_s]\vec{y_{(t)}}(t) = \vec{F}_{y_0} + [K_f]\vec{y_{(t)}} + [C_f]\dot{\vec{y_{(t)}}};\ \ \vec{y} = [y_{301}, y_{401}, y_{501}]^T; \\
&\begin{bmatrix} m_s + m_{f_{301301}} & m_{f_{301401}} & 0 \\ m_{f_{401301}} & m_s + m_{f_{401401}} & m_{f_{401501}} \\ 0 & m_{f_{501401}} & m_s + m_{f_{501501}} \end{bmatrix} \begin{Bmatrix} \ddot{y}_{301} \\ \ddot{y}_{401} \\ \ddot{y}_{501} \end{Bmatrix} + \begin{bmatrix} 2m_s\zeta\omega_n & 0 & 0 \\ 0 & 2m_s\zeta\omega_n & 0 \\ 0 & 0 & 2m_s\zeta\omega_n \end{bmatrix} \begin{Bmatrix} \dot{y}_{301} \\ \dot{y}_{401} \\ \dot{y}_{501} \end{Bmatrix} \\
&+ \begin{bmatrix} k_s & 0 & 0 \\ 0 & k_s & 0 \\ 0 & 0 & k_s \end{bmatrix} \begin{Bmatrix} y_{301} \\ y_{401} \\ y_{501} \end{Bmatrix} = \frac{1}{2}\rho(V_{Jet}sin\theta)^2 \left(\begin{bmatrix} A_{301_0}C_{L301_0} \\ A_{401_0}C_{L401_0} \\ A_{501_0}C_{L501_0} \end{bmatrix} + \begin{bmatrix} A_{301_0}\frac{\partial C_{L301}}{\partial y_{301}}e^{-i\omega\tau} + C_{L301_0}\frac{\partial A_{301}}{\partial y_{301}} & .. \\ A_{401_0}\frac{\partial C_{L401}}{\partial y_{301}}e^{-i\omega\tau} & .. \\ 0 & .. \end{bmatrix} \right. \\
&\left. \begin{bmatrix} A_{301_0}\frac{\partial C_{L301}}{\partial y_{401}}e^{-i\omega\tau} & 0 \\ A_{401_0}\frac{\partial C_{L401}}{\partial y_{401}}e^{-i\omega\tau} + C_{L401_0}\frac{\partial A_{401}}{\partial y_{401}} & A_{401_0}\frac{\partial C_{L401}}{\partial y_{501}}e^{-i\omega\tau} \\ A_{501_0}\frac{\partial C_{L501}}{\partial y_{401}}e^{-i\omega\tau} & A_{501_0}\frac{\partial C_{L501}}{\partial y_{501}}e^{-i\omega\tau} + C_{L501_0}\frac{\partial A_{501}}{\partial y_{501}} \end{bmatrix} \begin{Bmatrix} y_{301} \\ y_{401} \\ y_{501} \end{Bmatrix} \right. \\
&\left. + \begin{bmatrix} -A_{301_0}\frac{C_{D301}}{V_{Jet}sin\theta} & 0 & 0 \\ 0 & -A_{401_0}\frac{C_{D401}}{V_{Jet}sin\theta} & 0 \\ 0 & 0 & -A_{501_0}\frac{C_{D501}}{V_{Jet}sin\theta} \end{bmatrix} \begin{Bmatrix} \dot{y}_{301} \\ \dot{y}_{401} \\ \dot{y}_{501} \end{Bmatrix} \right)
\end{aligned}
\tag{8.10}
$$

where $[M_f]$, $[C_f]$, $[K_f]$ are the added-mass, added-damping and added-stiffness matrices of the fluid, respectively. m_{ii} is the added-mass of the rod i due to its own displacement, while m_{ij} (i $\neq$ j) are inter-rod coupling-related added mass terms. Chen (1975) calculated analytically the self-added (m_{ii}) and cross coupled (off diagonal terms (m_{ij}, i $\neq$ j)) mass coefficients for a row of cylinders. It was found that these terms are dependent on the gap-to-cylinder radius ratio and number of cylinders. Corresponding to our array geometry, the added mass cross-coupling coefficients could be estimated from Chen's study as 20% of the direct-added mass term. These off-diagonal terms (in the mass matrix of Equation 8.10) are assumed negligible compared to the diagonal terms ($m_s + m_{f_{ii}}$) in the total mass matrix. $\vec{F}_{y_0}$ is the remaining constant forces vector.

The coefficients of the fluid matrices need to be measured experimentally. The quasi-static and unsteady force measurements are challenging due to the array compactness, the JITF complexity, and the rod bundle boundary conditions (i.e. array fully immersed in high speed water flow). The fluidelastic force coefficients were previously measured on the same array and nozzle configuration by Gad-el Hak et al. (2022b) in pure jet cross-flow. The test results are shown in Table 8.2. These coefficients will be used in the stability analysis considering the effect of axial flow.

The fluid response time delay (τ) is needed in developed model for the JITF induced instability. Since the first row in the mock-up array is close to the LOCA hole and the instability

source comes from the jet cross-flow, we could approximately use the same time delay in the JITF as in a pure jet cross-flow case. Gad-el Hak et al. (2022b) measured experimentally the phase difference between the rod motion (in time (t)) and resultant lift force (time (t-τ)) signals for a range of reduced jet velocities as shown in Figure 8.23a. The time delay (τ) was then computed from the phases (φ) as $\tau = -\varphi/2\pi f$ as presented in Figure 8.23b. The flow retardation parameter (μ=$\tau/(D/V_{Jet})$) is obtained from the measured time delay as function of the convection time (D/V_{Jet}) with the reduced jet velocity as shown in Figure 8.24. The effect of considering the flow retardation parameter as a function or a constant value at the critical condition is discussed in the next section.

Table 8.2 Steady drag and lift force coefficients (C_{D_0} & C_{L_0}) and derivatives of the lift coefficient ($C_L, y_k/D$) measured at Re_{Jet} = 4x10^4, Gad-el Hak et al. (2022b).

Force coefficient	Rod 301	Rod 401	Rod 501
C_{L_0}	-0.026	-1.1	-1.7
C_{D_0}	1.9	2.95	2.26
$C_L, y_{301}/D$	-0.48	-0.16	-
$C_L, y_{401}/D$	-0.29	-2.7	2.2
$C_L, y_{501}/D$	-	4.6	-8.3

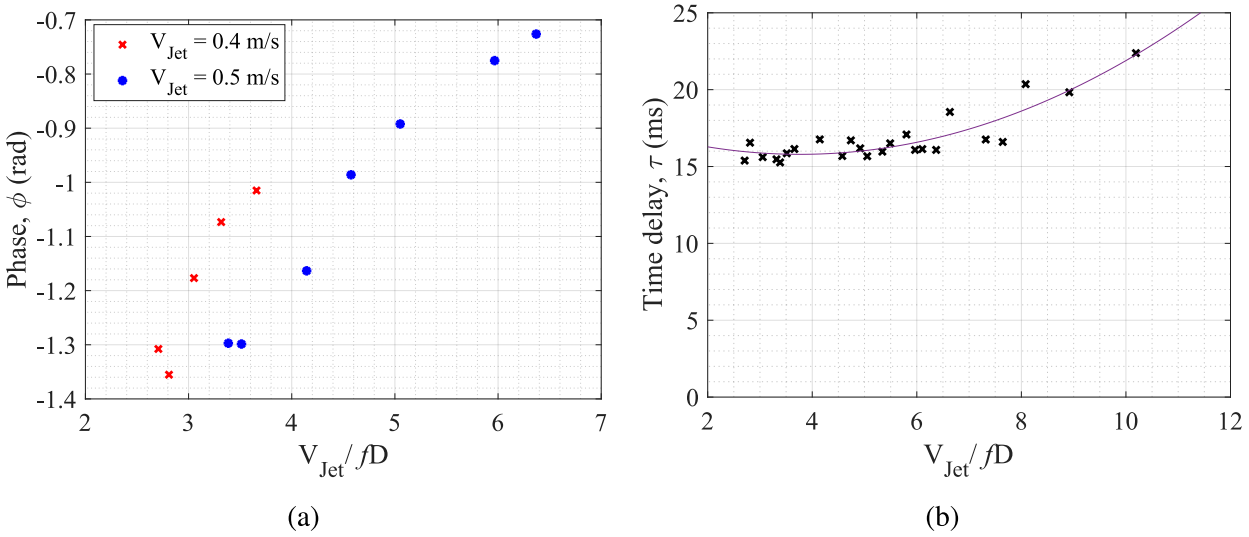

Figure 8.23 (a) Measured phase difference (φ) between the rod motion and the lift force, and (b) extracted time delay (τ) versus V_{Jet}/fD, (Gad-el Hak et al., 2022b).

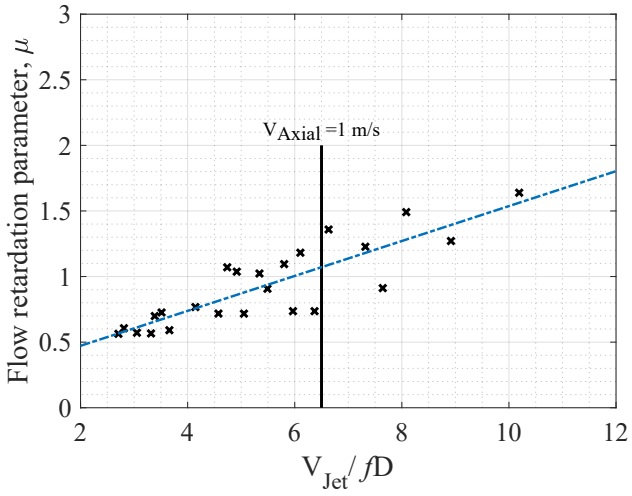

Figure 8.24 Extracted flow retardation parameter (μ) versus V_{Jet}/fD, (Gad-el Hak et al., 2022a).

8.5 FEI model analysis results and model validation

A stability analysis of the rod row is carried out for the three axial flow velocity cases: V_{Axial} = 1.0 m/s, 1.5 m/s, and 2.0 m/s. The resulting equation of motion (Equation 8.10) is a function of the jet velocity. For each case, the corresponding damping at V_{Axial} is used in the analysis, and the jet cross-flow velocity is increased from $V_{Jet} = 0$ to the instability condition. At each V_{Jet} value, the incidence angle is calculated using Equation 8.1 as function of the velocity ratio (VR = V_{Jet}/V_{Axial}), and the stand-off distance as shown in Figure 8.22d. The critical jet velocity is determined by solving the coupled equation system (Equation 8.10) to obtain the eigenvalues (λ) for a wide range of the jet velocities. The solution of the equations of motion can be formulated as follows:

$$\vec{y}(t) = \vec{A}e^{\vec{\lambda}t}; \quad \vec{y} = [y_{301}, y_{401}, y_{501}]^T \tag{8.11}$$

where λ is the eigenvalue. When the real part of λ is positive, the response grows exponentially and the system behaves as an unstable oscillator (if Im(λ) $\neq$ 0). The critical jet velocity for fluidelastic instability is the lowest velocity at which the real part of any eigenvalue reaches zero and with a positive slope versus V_{Jet}. Figures 8.25a and 8.25d show the real and imaginary parts of the eigenvalue, respectively, obtained for V_{Axial} = 1.0 m/s. Fluidelastic instability is predicted to occur at V_{Jet} = 2.35 m/s according to the eigenvalue results shown in the figure. Comparing to the critical jet velocity measured in the FEI tests (see Figure 8.10a), the model results overestimate the critical jet velocity with an error of

approximately 7%. The rod frequency is found to slightly increase with the jet velocities as shown in Figure 8.25d due to the fluid added stiffness as also observed in the FEI experiments. For the $V_{Axial} = 1.5$ m/s case, the predicted critical jet velocity is 2.65 m/s as shown in Figure 8.25b. This velocity exceeds the experimental stability limit velocity by 12.5%. The final stability analysis is carried out for the $V_{Axial} = 2.0$ m/s case as shown in Figures 8.25c and 8.25f. The model predicts the instability threshold at $V_{Jet} = 2.8$ m/s while the instability occurs in experiments at $V_{Jet} = 3.05$ m/s. Figure 8.26 shows the model validation versus the experimental stability threshold for the three axial flow velocity cases. The effects of the flow retardation parameter and the cross-coupling fluidelastic forces are demonstrated by performing two different analyses sets for each axial flow case. The first analysis evaluates the effect of the flow retardation parameter (μ) by inputting μ as a function of the reduced jet velocity in the model, and comparing the theoretical results with μ = constant value at the experimental critical reduced jet velocity as shown in Figure 8.26a. The second analysis demonstrates the effect of the cross-coupling forces between the rods in predicting the instability. The stability limits from the two cases (cross-coupling forces $\neq 0$ & cross-coupling forces $= 0$) are presented in Figure 8.26b with the experimental critical jet velocities. The model accuracy is improved by 7% by including the flow retardation parameter as a function of the reduced jet velocity as shown in Figure 8.26a. The results confirm the important parameters in modeling the instability is the cross-coupling fluid forces between the rods. Neglecting these forces increases the error by up to 50% in predicting the critical jet velocity as shown in Figure 8.26b.

8.6 Conclusions

The primary aim of this work was to investigate combined axial flow and jet transverse flow induced vibration experimentally and theoretically in order to understand the fundamental mechanisms underlying fuel assembly instability induced by a jet transverse flow (JITF). A single-span mock-up PWR assembly was designed and fabricated to study the effect of the mixed flow on the dynamical behavior of the mock-up array. Two different flows, a pure axial flow, and a combined jet in transverse flow, were investigated in this study. The experiments show that the tested arrays are fluidelastically stable under pure axial flow. However, the mock-up arrays become unstable and large vibration amplitudes are observed in the arrays when it is subjected to localized jet cross-flow and axial flow. Moreover, the effect of three axial flow velocities, $V_{Axial} = 1.0$ m/s, 1.5 m/s, and 2.0 m/s, are studied on the stability threshold of the two arrays. The results show that the critical jet cross-flow velocity increases linearly with the axial flow velocity with a ratio of 1.3. Thus, it is found that the

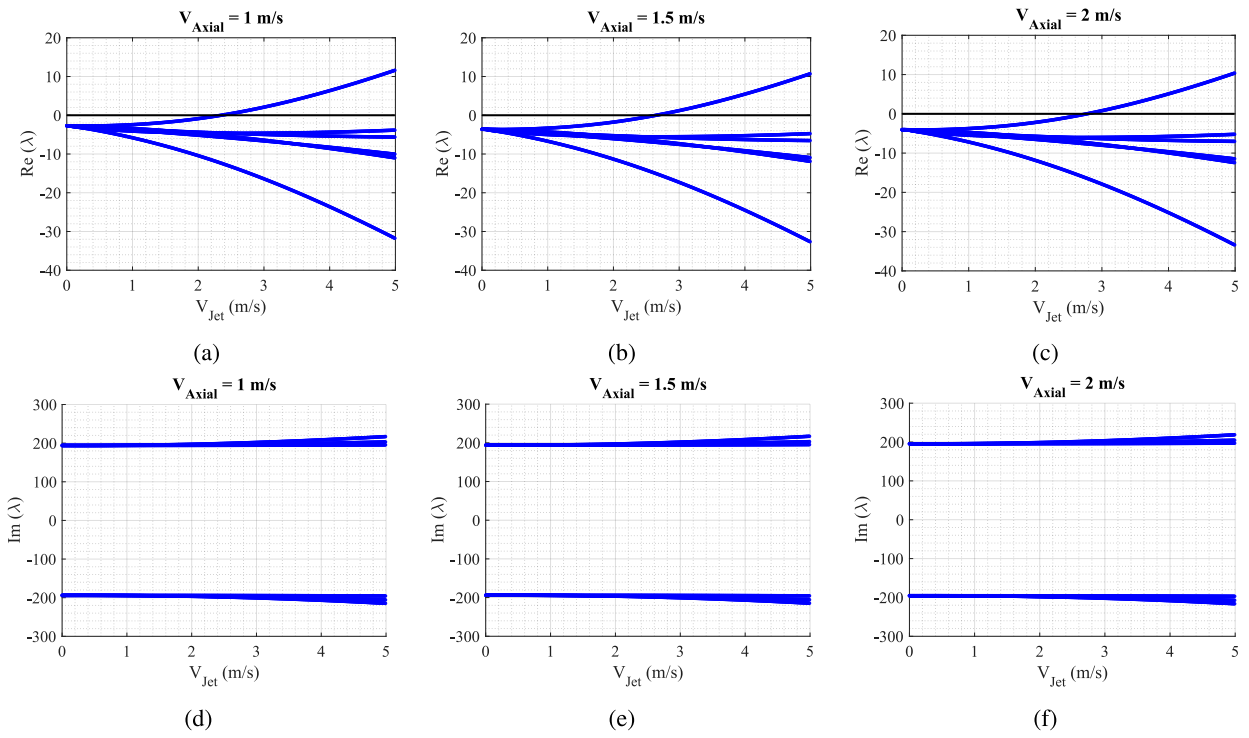

Figure 8.25 Variation of the eigenvalues (Re (λ) and Im (λ)) with jet velocity for the three axial velocities cases: (a) and (d) for V_{Axial} = 1.0 m/s, and (b) and (e) for V_{Axial} = 1.5 m/s, (C) and (f) for V_{Axial} = 2.0 m/s.

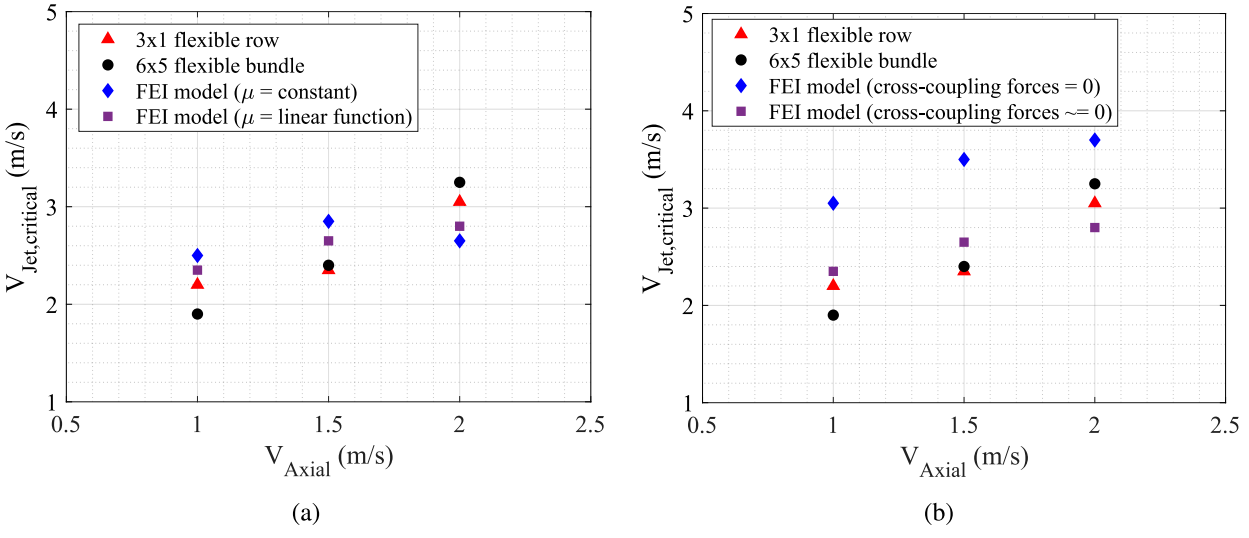

Figure 8.26 JITF induced FEI model validation for the three axial flow cases: (a) effect of the flow retardation parameter (μ) on the stability limits, and (b) effect of the cross-coupling force terms on the stability limits.

velocity ratio (VR=V_{Jet}/V_{Axial}) is the best parameter to characterize the stability boundary of arrays subjected to combined axial flow and jet cross-flow.

The JITF induced instability model development to predict the critical jet velocity for the arrays was the second objective of this work. The arrays tested in pure axial flow found to be stable and their responses are in the turbulence induced vibration range. However, the axial flow effects on the array dynamics are: (i) increase the rod damping, and (ii) deflect the jet cross-flow. Thus, the model includes the "bending" effect of the jet cross-flow by projecting the normal component of the jet flow on the rod. When the rod vibrates in the transverse direction relative to the circular jet flow, the projected area of the rod changes. Consequently, two new parameters, the rod area derivative and the jet-rod incidence angle, are implemented in the model to capture the dynamic features of the vibrating rod in combined axial flow and jet cross-flow.

A stability analysis was performed for the three axial flow velocities cases, V_{Axial} = 1.0 m/s, 1.5 m/s, and 2.0 m/s to validate the developed model with the experiments. The theoretical results show agreement between the predicted critical velocities with those obtained experimentally within an error range of 7% to 12.5% over the axial velocity range above. The theoretical analysis shows the importance of the cross-coupling forces between the rods in predicting the instability, the model results are improved by 50% with considering these forces. Moreover, introducing the flow retardation parameter as a function of the reduced jet velocity in the model gives a better prediction of the stability boundaries of the arrays under combined axial flow and jet cross-flow. Increase in the stability limit with the axial flow velocity is governed by two main parameters, the incidence angle of the jet flow and the damping induced by axial flow. Because the fuel assembly is located close to the baffle plates, the jet is approximately normal to the first row (as in the pure jet cross-flow case) at the critical velocity ratio. This suggests that the increase in stability threshold is related to an increase in the damping by the axial flow. Further experiments and theoretical analysis of arrays having larger stand-off distance of the jet flow are needed to generalize the developed model.

CHAPTER 9 GENERAL DISCUSSION

The research work presented in this thesis was motivated by the need to investigate and quantify the problem of fluidelastic instability of rod bundles subjected to a jet cross-flow and parallel axial flow using experimental and modelling approaches. A research program comprising experimental work and analytical modelling is carried out. In the experimental work, a series of increasingly complex rod bundle-flow configurations are tested. The starting point is a study of the stability behaviour of a rod bundle mounted elastically under a pure jet cross-flow (in the absence of axial flow). A rod bundle with 1-DOF supports is first investigated. This same bundle dimension is then replaced with axisymmetric supports (having 2-DOF). Thereafter, a mock-up PWR fuel assembly is fluidelastically evaluated under conditions of combined axial flow and jet cross-flow. The stabilizing effect of the axial flow on the jet induced instability is studied in detail with the goal of determining the underlying stabilization mechanism. Equally important, the parameters governing the fluidelastic instability (FEI) of rod bundles subjected to both pure jet cross-flow and combined flow are determined with the goal of extending existing fluidelastic instability models to the transverse jet flow case and the combined axial and jet-cross flow case.

As a reminder, the objectives of this research project were: **O1** characterize experimentally the dynamical behavior of a rod bundle subjected to pure jet cross-flow, **O2** perform fluidelastic stability derivatives and time delay measurements, **O3** develop a semi-empirical quasi-steady model for FEI induced by jet cross-flow, **O4** develop a generalized eigenvector model to predict the mode shape of the array under jet cross-flows, **O5** proposed a passive mitigation method for jet cross-flow induced vibrations, and **O6** characterize experimentally and model analytically the dynamics of a single-span flexible rod bundle subjected to a jet in transverse flow (JITF). The flow chart of Figure 9.1 summarizes the research work conducted in the research project.

In the two-part paper (Chapters 3 and 4), a series of flow induced vibration (FIV) experiments were carried out to achieve **O1**. Rod bundles, 6x6 and 6x5, were tested under pure jet cross-flow to measure their responses in the stream-wise direction. The dynamical behavior of the arrays was evaluated for three jet eccentricities (ξ) = 0, $0.25P$, and $0.5P$. The jet eccentricity was varied in the experiments using a specially designed mechanism as described in detail in Chapter 3. The stream-wise tests showed the complex effects of ξ on the excitation mechanisms. The jet-array aligned case ($\xi = 0$) had an excitation mechanism similar to a lock-in/synchronization phenomenon, where a resonant peak is observed. When the jet

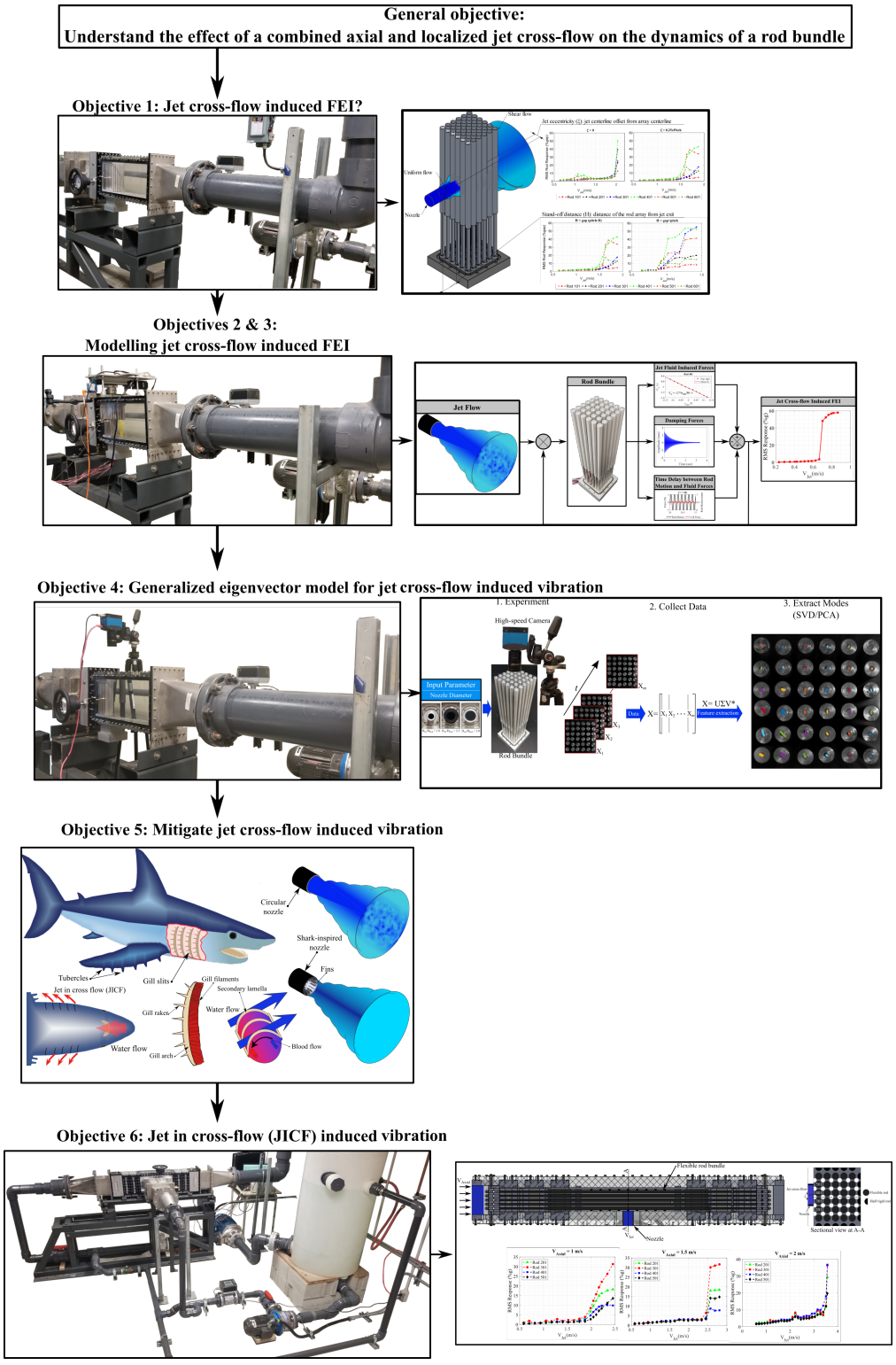

Figure 9.1 Flowchart of the research conducted.

flow is displaced by 0.25 pitch, the excitation mechanism changes to turbulence-induced vibrations (TIV). However, the aligned jet-rod case showed a fluidelastic instability (FEI) phenomenon at relatively high jet velocity. Our explanation for this dependence of the rod array response on ξ is the flow configuration variation through the rod gaps as shown in Figures 3.15, 3.18, and 3.23. Changing ξ from 0 to $0.5P$ changes the flow gap from a single gap into a pair of symmetrical flow gaps. On the other hand, the two resonant peaks are obtained when the rod bundle is displaced away from the jet flow (i.e larger stand-off distance). This could be attributed to a switch in the excitation mode from the varicose to the jet flapping excitation mode which occurs in the larger gap before the jet exits the rod bundle.

The second paper (Chapter 4) presented transverse vibration results for the same rod bundle dimensions used in the work of the first paper (Chapter 3) identifying the direction in which the instability is most critical. Three rod bundles, 6x6, 6x5, and 6x4, were tested with the same three jet eccentricities $\xi = = 0$, $0.25P$, and $0.5P$ as in Chapter 3. The fluidelastic instability (FEI) experiments showed that jet cross-flow induces FEI in the transverse direction in all tested cases. However, the stability limit depends strongly on the jet eccentricity (ξ) and stand-off distance (H). The case of $\xi = 0.25P$ had the lowest critical jet velocities. Rod motion in an asymmetric velocity field (see Figure 3.18) might have a large effect on fluidelastic forces, resulting in instability at low jet velocity. Another important finding is the decrease in the critical jet velocity with increasing stand-off distance which then reverses beyond a certain distance. This stand-off distance behavior could be explained by two contradicting jet flow mechanisms: (i) decreasing V_{Jet} with increasing H, and (ii) increasing A_{Rod} with increasing H. However, when the rods vibrate, the jet cross-section is amplified as shown in Figure 4.12 due to excitation of the large eddies in a round jet which increases the effective projected area on the exposed rods.

Summarizing the experimental results in stability maps is important to provide guidelines for the design of fuel assemblies in proximity to LOCA holes. The Connors model is used to define the stability boundary for uniform flow cases thus a stability equation based on jet flow should be formulated instead. The output from **O1** is the stability equation for jet flow induced FEI as a function of four non-dimensional parameters; the reduced velocity (V_{Jet}/fD), the mass damping parameter ($m\delta_0/\rho D^2$), the reduced jet diameter (D/D_{Jet}) and the jet to length ratio (L/D_{Jet}). All experiments in two Chapters 3 and 4 are conducted at $D_{Jet}/D = 2.3$ and the jet is centred at the mid-point of rod span.

Fundamentally the most important result in the two-part paper is the clear confirmation of the occurrence of transverse fluidelastic instability in rod bundles due to jet cross-flow. This

led to the development of a theoretical model for jet cross-flow induced FEI as described in objectives **O2** and **O3**. In the third paper (Chapter 5), an experimental and theoretical framework were carried out to develop and validate a theoretical model for jet cross-flow induced FEI. The experimental work is divided into two parts: (i) FEI tests for $D_{Jet}/D = 3.0$ as the same in the reactor cores and $\xi = 0.25P$ (i.e. more unstable case), and (ii) measure model input parameters which are quasi-static/unsteady fluid force measurements. In the first part, four different array configurations, single rod, 2x1, 3x1, and 6x6 fully flexible rod bundle, are tested to determine the smallest number of rods that exhibits the dynamical behaviour of the 6x6 fully flexible rod bundle. The experiments showed single rod and 2x1 flexible row were stable under the tested range of jet velocity. However, it was found that the 3x1 flexible row is fluidelastically unstable at the reduced critical jet velocity of 5 near to that obtained in the fully flexible rod bundle ($V_{Jet,critical} = 4.4$). This 3x1 row covers the jet flow from the nozzle. Thus, the model was developed based on 3-DOF jet flow-coupled system. The model input parameters were: the lift force coefficient derivative for each rod due to its own motion which would not be the same as in the uniform flow case, and their cross-coupling terms with neighbouring rods. Also considered was the time delay of the fluid response relative to the rod vibration. In addition, a new parameter, the rod area derivative for each rod takes into account the dynamics of vibrating rods under localized jet cross-flow.

In the second part of the experimental work, the steady drag and lift coefficients (C_D & C_L) for the three rods were measured for a range of jet Reynolds numbers. The measured C_L and C_D showed only slight dependence on jet Reynolds number. The time delay between the rod displacement and the generated unsteady forces was also measured for various jet flow velocities and excitation frequencies. The flow retardation parameter (μ) was found to vary with the reduced jet velocity. This may be attributed to resulting different jet behavior regimes depending on the excitation frequency as discussed by Rockwell (1972). It was, however, found that the order of magnitude of μ is 1. The steady drag and lift coefficients together with their derivatives were used to complete the quasi-steady model.

The newly developed model was first validated with a single rod and 2x1 flexible row to demonstrate their fluidelastic behaviour. The stability results showed that these two arrays were stable as observed in the experiments. Next, a stability analysis was performed for the 3x1 flexible row. The predicted jet critical velocity was found to be within 15% of the experimental stability limit.

After understanding the instability mechanism underlying a rod bundle unidirectionally flexible in the transverse direction, an axisymmetric rod bundle, with the same dimensions considered in Chapters 3, 4, and 5, was tested for different jet cross-flow diameters (D_{Jet}).

The fourth paper (Chapter 6) achieved the objective (**O4**) by performing an experimental level data analysis using singular value decomposition (SVD) and principal component analysis (PCA) to discover a generalized (principal) coordinate system, capturing the essential dynamics for the jet-bundle system. Three nozzles having jet-to-diameter ratios $D_{Jet}/D =$ 1.6, 2.3, and 3.0, were tested at jet eccentricity $\xi = 0.5P$. A high-speed camera was used to capture the rod bundle vibration. Thousands of images were captured for a given test condition, then these raw images were processed using an in-house image processing algorithm to track each rod displacement in the stream-wise and transverse directions. To determine generalized eigenvectors, a PCA transformation was performed on a single nozzle bi-axial vibration data, followed by a transformation using the experimental vibration data of the three tested nozzles. The generalized eigenvectors were then compared to the eigenvectors obtained from individual tested nozzles to determine whether they can be used to identify the vibrational modes for each tested nozzle. The derived model predicted the vibration direction angles for the two diameter ratios $D_{Jet}/D = 1.6$ and 2.3, with absolute difference of 10°, while the difference for the $D_{Jet}/D = 3.0$ ranged from 20° to 40°. These results led to vital insight into the relationship between nozzle diameter and the flow behaviour through the bundle. An acceleration ratio of the jet flow through the bundle as a result of transitioning from the circular cross sectional area to the inter-rod gaps was introduced in this study to explain why the model differs for the nozzle having $D_{Jet}/D = 3.0$. Interestingly, the effect of D_{Jet}/D is not linear due to geometrical matching between the nozzle location with the rods facing the jet flow. Consequently, the acceleration ratio is a key parameter that could be used to quantify the effect of the diameter ratio on the rod bundle vibration induced by jet cross-flow.

Suppressing flow induced vibration is at the core many research effort driven by industrial applications. This is the case for the present work. In the fifth paper (Chapter 7), a design solution to prevent jet cross-flow induced FEI is proposed. The solution involves enhancing mixing of the jet flow with the ambient flow in order to rapidly reduce jet momentum or convert it into angular momentum (i.e vorticity) which would in turn reduce the resulting vibrations. Inspired by *"ram ventilation"* in sharks, a new biomimetic nozzle design is proposed to mitigate jet cross-flow induced vibrations. Our proposed biomimicry approach is to attach equally spaced thin fins circumferentially at the circular nozzle base to simulate the effect of gill rakers in the gill slits. Three nozzles, a basic circular nozzle, a shark-inspired nozzle with 10 fins, and a shark-inspired nozzle with 15 fins, were tested at $\xi = 0$ in this paper. The resulting jet cross-flow induced vibrations from the shark-inspired nozzles are compared with the reference case of the circular nozzle. The experimental results showed the ability of the proposed biomimetic nozzle to delay the critical velocity by 20% at which unstable

vibrations occur and, to furthermore, damp the post-instability vibration amplitudes of the rod bundle by 85%.

A final stage of the research was to study the complex rod bundle-flow configurations by testing a single-span mock-up array under combined axial flow and jet cross-flow. A new test loop was built to achieve the objective (**O6**) as shown in Figure 9.1. The sixth paper (Chapter 8) presented experimental and modelling work for arrays under jet in transverse flow (JITF) excitation. The 6x5 mock-up array was tested at jet eccentricity $\xi = 0.25P$, including investigation of the effect of the number of flexible rods on the stability threshold. The 3x1 row and 6x5 fully flexible array were tested under pure axial flow and JITF to determine the effect of the axial flow on the dynamical behavior of arrays subjected to jet cross-flow.

In the JITF experiments, three axial flow velocities, V_{Axial} = 1.0 m/s, 1.5 m/s, and 2.0 m/s, were tested. The experiments showed that the bundles were stable under pure axial flow, however, injecting the transverse jet flow in the axial flow domain induced FEI in the arrays. The instability velocity was found to increase with increasing the axial flow velocity. The increase in critical jet velocity is nearly linear. The velocity ratio (VR = V_{Jet}/V_{Axial}) was found to be the best parameter quantify the instability threshold of arrays subjected to combined axial and jet cross-flow. Furthermore, a modelling approach was used to predict this trend of the stability threshold with the axial flow velocity.

The model developed for pure jet cross-flow in the third paper used as a base case to build a JITF model induced FEI. The effect of axial flow was considered in the model by introducing a jet flow incidence angle relative to the rods. Stability analysis results showed that the model could predict the stability limit within a maximum absolute error of 12.5% over the three tested axial flow velocities.

The comprehensive study on jet cross-flow induced vibrations presented in this Thesis addressed the fundamental dynamics of the problem and has experimentally uncovered rod array stability behavior. The key mechanism governing jet cross-flow induced instability are well predicted by the theoretical model presented. Further study and experiments on this problem may, however, be required, as indicated in the following section.

CHAPTER 10 CONCLUSIONS AND RECOMMENDATIONS FOR FUTURE WORK

The core of this research project is to address the fundamental problem of the dynamics of rod bundles subjected to combined axial and transverse jet flow. Of particular interest is the case where the transverse (cross-) flow takes the form of a circular jet, corresponding to flow through LOCA holes at the core baffle plates in some designs of pressurized water reactors (PWRs). Research outputs could be highlighted in the following items: (i) contributions, (ii) limitations and challenges, (iii) recommendations for future work, and (iv) research project deliverables. Each item will be presented in the following subsections.

10.1 Contributions

The following are the main contributions from this work:

- The design and building of a high precision specialized test facility to investigate the stability behaviour of rod bundles mimicking the fuel assembly under jet cross-flow. It has been shown in Chapter 3 that changing jet eccentricity (ξ) in tests leads us to design a specialized mechanism to move the jet flow across the arrays. Furthermore, the setup and instrumentation of these densely packed arrays is a difficult task, thus a precise measurement of the gaps between rods in the setup arrays is performed prior to performing FEI experiments.

- Measurement and comprehensive study of variation stability limits with the jet flow parameters on flexible rod bundles in the stream-wise and transverse directions. The FEI experiments confirmed the predominance of the transverse fluidelastic instability of the in-line square arrays subjected to jet cross-flow. A new stability boundary considering jet momentum based on the Connors equation was proposed for arrays in jet cross-flow. The FEI study showed that the stability constant has a strong dependence on the jet flow parameters H and ξ. The stability constant (K) varies approximately linearly with the jet-to-rod diameter ratio (D_{Jet}/D).

- Measurement and comprehensive study of the transverse quasi-steady and the unsteady fluid forces on a 3x1 in the first row in the square array subjected to jet cross-flow. The measured quasi-steady forces confirmed that the rod stability derivatives are strongly influenced by flow asymmetry. An important finding is that the rod projected area is

not constant when the rod vibrates in LOCA hole jetting. This dynamic area variation plays an important role in jet flow-induced fluidelastic instability.

- The present work was the first attempt to measure the quasi-steady and the unsteady fluid forces in a highly compact rod bundle having prototypical reactor fuel bundle geometry and dimension and subjected to localized jet cross-flow. This was also the first attempt to develop a theoretical model based on a quasi-steady approach to predict the stability boundary of an array under pure jet cross-flow. A new formulation of the fluidelastic forces as functions of the projected rod area derivative is another important finding in this research. The validation of the developed model for jet cross-flow induced FEI shows the potential of the model in predicting the stability of the array within an error of 15%.

- Extraction of bundle mode shapes, using SVD and PCA, under different jet flows is another outcome from this thesis. The analysis shows that the mode shape obtained from two different nozzles is almost the same. A deeper investigation of these two nozzles shows that the nozzles have almost the same acceleration ratio (A_{Jet}/A_{Gap}). This points out that the nozzle diameter changes are not linear due to geometrical matching between the nozzle location with the rods facing the jet flow. The generalized mode shapes, obtained across a range of flow and geometry (nozzle diameter) parameter spaces, provide an efficient basis for model order reduction.

- Another significant and practical contribution of the study is the mitigation of jet cross-flow induced FEI. A new shark-inspired nozzle is proposed by attaching a very thin fin inside a circular nozzle to simulate the effect of the shark gill slits structure. The effect of the biomimetic nozzle on the rod array vibration is evaluated versus a circular nozzle. The comparison shows a 85% amplitude reduction and 20% delay in the stability limit by using the shark-inspired nozzle.

- Investigation a stabilizing effect of the axial flow on the jet induced instability of the rod bundle. Three different axial flow tests show that the critical jet cross-flow velocity is changed linearly with the axial flow, resulting in a velocity ratio (V_{Jet}/V_{Axial}) ≈ 1.3. Another important outcome of the tests is that this velocity ratio corresponds to a fully detached JITF topology.

- The present research was the first attempt to adopt a jet cross-flow induced FEI model to take into account the effect of axial flow. The JITF induced FEI model is developed by introducing an incidence angle of jet flow on the first row while being deflected by the axial flow. The model validation shows agreement with the experimental critical

jet flow velocity within an absolute maximum error of 12.5% over the tested three axial flow velocities cases.

All of these contributions helped in understanding the research topic and accomplishing all of the research objectives. However, some challenges remain.

10.2 Limitations and Challenges

A number of challenges and limitation were experienced in the course of the project:

- Changing the location of applied jet fluid force (L_{Jet}) on rod array is practically limited because the nozzle is already driven by a lead screw to move it in the transverse direction with respect to the array. While, including the radial direction change, along the rod span, in the jet flow displacement mechanism would increase the design and sealing complexity. However, the effect of changing L_{Jet} could be predicted from the stability analysis.
- The rod bundle assembly in each FIV test for pure jet cross-flow took a few days to mount the cantilevered rods in the mounting plate because the error in the inter-rod gap is very sensitive to the rod alignment in the array, if there is a 0.15° very small inclination angle of rod, this is resulting 25% error in the gap.
- The model analysis led to the discovery of the acceleration ratio (A_{Jet}/A_{Rod}) as a key parameter normalizing nozzle geometry changes.
- The maximum tested jet velocity in the quasi-static and unsteady fluid force measurements is restricted by the maximum torque value of the force sensor. The measured force values on the rod are small compared to the maximum values of the force sensor due to the partial projection of jet flow on the rod. However, the torque exerted on the rod is a function of the location of applied jet force. It is necessary to check the measured torque and force values to be below the maximum values of the force sensor during the tests.

It is consequently proposed that future research investigate the following aspects.

10.3 Recommendations for Future Work

- Adding an alignment feature to adjust and verify the rod alignment will be helpful to assemble the rod array easily.

- Change the jet flow displacement mechanism to test larger nozzle diameters than 1.3 inches to complete the stability map generalization.
- Examine the jet flow structure in stagnant fluid and moving fluid through the rod bundle to provide insight on the array-jet interaction behavior.
- Measure the fluidelastic forces in the stream-wise direction to provide complete data for fluidelastic instability of a mock-up PWR array.
- Measure the time delay associated with changing the rod area to simulate a vibrating rod in the circular jet flow (i.e. LOCA holes) and also investigate deeper the effect of the rod area derivative on the instability mechanism of arrays subjected to localized circular jet cross-flow.
- Increase the pump capacity of jet flow in the combined axial and jet cross-flow experiments to test the in-core operating condition.

10.4 Research Project Deliverables

This PhD project has led to six journal articles and four conference papers.

Conference Papers

1. I. Gad-el-Hak, N. Mureithi, K. Karazis, and G. Williams. "Experimental Investigation of Jet Cross-Flow Induced Vibration of a Rod Bundle." *In Pressure Vessels and Piping Conference* (Vol. 85338, p. V003T04A014), American Society of Mechanical Engineers, July 2021.
2. I. Gad-el-Hak, N. Mureithi, and K. Karazis. "Theoretical and Experimental Study on The Fluidelastic Instability of Rod Bundle Subjected To Jet Cross-flow." *In FIV2022 Conference*, 2022.
3. I. Gad-el-Hak, N. Mureithi, and K. Karazis. "Mitigating Jet Cross-flow Induced Vibrations Using a Bio-inspired Nozzle." *In FIV2022 Conference*, 2022.
4. I. Gad-el-Hak, N. Mureithi, and K. Karazis. "Evaluation of Fuel Rod Response Using Principal Component Analysis." *ASME International Mechanical Engineering Congress and Exposition*. American Society of Mechanical Engineers, 2022.

Journal Papers

1. I. Gad-el-Hak, and N. Mureithi. "Mitigation of jet cross-flow induced vibrations using an innovative biomimetic nozzle design inspired by shark gill geometry." *Scientific Reports* 12.1 (2022): 1-11.

2. I. Gad-el-Hak, N. Mureithi, K. Karazis, and G. Williams. "Jet cross-flow induced vibrations in rod bundles. Part I: Experimental apparatus and stream-wise vibration results." Accepted for publication in *Nuclear Engineering and Design*.

3. I. Gad-el-Hak, N. Mureithi, K. Karazis, and G. Williams. "Jet cross-flow induced vibrations in rod bundles. Part II: Transverse vibration results and excitation mechanisms." Accepted for publication in *Nuclear Engineering and Design*.

4. I. Gad-el-Hak, N. Mureithi, and K. Karazis. "Fluidelastic instability (FEI) model for a rod bundle subjected to jet cross-flow." Submitted to *Journal of Fluids and Structures* on 28th June 2022, Under review.

5. I. Gad-el-Hak, N. Mureithi, K. Karazis and G. Williams. "Principal component analysis (PCA) of rod bundle vibration subjected to jet cross-flow." Submitted to *Journal of Sound and Vibration* on 29th June 2022, Under review.

6. I. Gad-el-Hak, N. Mureithi, and K. Karazis. "Fluidelastic instability of a fuel rod bundle in combined axial flow and jet cross-flow." has been submitted to *Journal of Fluids and Structures* on 10th October 2022.

REFERENCES

G. N. Abramovich, T. Girshovich, S. I. Krasheninnikov, A. Sekundov, and I. Smirnova. The theory of turbulent jets. *Moscow Izdatel Nauka*, 1984.

M. Albertson, Y. Dai, R. A. Jensen, and H. Rouse. Diffusion of submerged jets. *Transactions of the American Society of Civil Engineers*, 115(1):639–664, 1950.

AREVA. Response to RAls on WCAP-17788 Volume 4 - B&W plants. 2017.

H. A. Becker and T. Massaro. Vortex evolution in a round jet. *Journal of Fluid Mechanics*, 31(3):435–448, 1968.

G. W. Benz. On the conservative nature of the gill filaments of sharks. *Environmental Biology of Fishes*, 10(1):111–116, 1984.

Bischof, G.T. Report No. 50-339/2014-002-00, Virginia Electric and Power Company, North Anna Power Station. `https://www.nrc.gov/docs/ML1432/ML14325A692.pdf`, 2014.

R. D. Blevins. Flow-induced vibration. *New York*, 1977.

P. Boulanger, P. Fardeau, and J. Rigaudeau. FIV of PWR fuel rods under local jets: instability threshold and influence of jet configuration. In *Transactions of the 14th International Conference on Structural Mechanics, Reactor Technology (SMiRT 14), Lyon, France*, 1997.

J. Broadwell and R. Breidenthal. Structure and mixing of a transverse jet in incompressible flow. *Journal of Fluid Mechanics*, 148:405–412, 1984.

S. L. Brunton and J. N. Kutz. *Data-driven science and engineering: Machine learning, dynamical systems, and control*. Cambridge University Press, 2019.

D. Burgreen, J. Byrnes, and D. Benforado. Vibration of rods induced by water in parallel flow. *Transactions of the American Society of Mechanical Engineers*, 80(5):991–1001, 1958.

E. E. Callaghan. *Investigation of the penetration of an air jet directed perpendicularly to an air stream*. Number 1615. National Advisory Committee for Aeronautics, 1948.

T. Cambonie and J.-L. Aider. Transition scenario of the round jet in crossflow topology at low velocity ratios. *Physics of Fluids*, 26(8):084101, 2014.

I. Catton, V. K. Dhir, O. Alquaddoomi, D. Mitra, and P. Adinolfi. Development of design criteria for fluid induced structural vibration in steam generators and heat exchangers. Technical report, University of California, Los Angeles (US), 2004.

S. Chen. Design guide for calculating the instability flow velocity of tube arrays in crossflow. Technical report, Argonne National Lab.(ANL), Argonne, IL (United States), 1981.

S. Chen. Instability mechanisms and stability criteria of a group of circular cylinders subjected to cross-flow. Part I: theory. *Journal of Vibration and Acoustics*, 1983a.

S. Chen. Instability mechanisms and stability criteria of a group of circular cylinders subjected to cross-flow. Part 2: Numerical Results and Discussions. *Journal of Vibration and Acoustics*, 1983b.

S. Chen. Guidelines for the instability flow velocity of tube arrays in crossflow. *Journal of Sound and Vibration*, 93(3):439–455, 1984.

S. Chen. A general theory for dynamic instability of tube arrays in crossflow. *Journal of Fluids and Structures*, 1:35–53, 1987.

S.-S. Chen. Vibrations of a row of circular cylinders in a liquid. 1975.

S.-S. Chen. Flow-induced vibration of circular cylindrical structures. Technical report, Argonne National Lab.(ANL), Argonne, IL (United States), 1985.

S. L. Coelho and J. Hunt. The dynamics of the near field of strong jets in crossflows. *Journal of Fluid Mechanics*, 200:95–120, 1989.

B. Collard, S. Pisapia, D. Broc, and S. Bellizzi. Flow induced damping of a PWR fuel assembly. In *Structural behaviour of fuel assemblies for water cooled reactors: proceedings of technical meeting. Vienna*, pages 279–288, 2005.

H. Connors. Fluid elastic vibration of tube arrays excited by cross flow. In *ASME Symposium on Flow-Induced Vibration in Heat Exchanger, Winter Annual Meeting*, pages 42–47, 1970.

S. C. Crow and F. Champagne. Orderly structure in jet turbulence. *Journal of Fluid Mechanics*, 48(3):547–591, 1971.

C. B. da Silva and O. Metais. Vortex control of bifurcating jets: a numerical study. *Physics of fluids*, 14(11):3798–3819, 2002.

G. Dalpiaz and A. Rivola. Condition monitoring and diagnostics in automatic machines: comparison of vibration analysis techniques. *Mechanical Systems and Signal Processing*, 11 (1):53–73, 1997.

J.-P. Denizou, J.-M. Dubief, and P. Bouchard. Experimental study of the fuel rod behaviour under baffle jetting. 1985.

B. Ding, X. Chen, X. Zhang, Y. Zhang, and R. Yan. SVD-based dictionary learning for bearing fault diagnosis. In *2016 International Symposium on Flexible Automation (ISFA)*, pages 1–4. IEEE, 2016.

F. Ding and Z. Qi. Turboprop engine fault diagnosis based on hilbert spectrum and singular value decomposition. In *2016 6th International Conference on Mechatronics, Computer and Education Informationization (MCEI 2016)*, pages 1300–1304. Atlantis Press, 2016.

T. Fric and A. Roshko. Vortical structure in the wake of a transverse jet. *Journal of Fluid Mechanics*, 279:1–47, 1994.

K. Fujita, T. Ito, and N. Kohno. Experimental study on the vibration of circular cylinders subjected to cross-flow jetted from a narrow gap. *Journal of Fluids and Structures*, 4(1): 99–124, 1990. doi: https://doi.org/10.1016/0889-9746(90)90057-C.

I. Gad-el Hak. Fluid-structure interaction for biomimetic design of an innovative lightweight turboexpander. *Biomimetics*, 4(1):27, 2019. doi: https://doi.org/10.3390/biomimetics4010027.

I. Gad-el Hak and N. Mureithi. Mitigation of jet cross-flow induced vibrations using an innovative biomimetic nozzle design inspired by shark gill geometry. *Scientific Reports*, 12 (1):1–11, 2022.

I. Gad-el Hak, N. Mureithi, K. Karazis, and G. Williams. Experimental investigation of jet cross-flow induced vibration of a rod bundle. In *Pressure Vessels and Piping Conference*, volume 85338, page V003T04A014. American Society of Mechanical Engineers, 2021.

I. Gad-el Hak, N. Mureithi, and K. Karazis. Theoretical and experimental study on the fluidelastic instability of rod bundle subjected to jet cross-flow. In *Submitted to FIV2022 Conference*, 2022a.

I. Gad-el Hak, N. Mureithi, and K. Karazis. Fluidelastic instability (FEI) model for a rod bundle subjected to jet cross-flow. *Submitted to Journal of Fluids and Structures*, 2022b.

S. Granger and M. Paidoussis. An improvement to the quasi-steady model with application to cross-flow-induced vibration of tube arrays. *Journal of Fluid Mechanics*, 320:163–184, 1996.

E. Gutmark and C.-M. Ho. Preferred modes and the spreading rates of jets. *The Physics of Fluids*, 26(10):2932–2938, 1983. doi: https://doi.org/10.1063/1.864058.

A. Hertrick, R. Riddell, R. Schwirian, G. Dorogy, W. Bryan, and R. Hopkins. Comparison of calculated and measured fluid jet impingement velocities in a simulated reactor geometry. *Nuclear science and engineering*, 88(3):396–403, 1984.

C.-M. Ho and P. Huerre. Perturbed free shear layers. *Annual Review of Fluid Mechanics*, 16:365–424, 1984.

J.-M. Huang and F.-B. Hsiao. On the mode development in the developing region of a plane jet. *Physics of fluids*, 11(7):1847–1857, 1999.

G. Hughes. The dimensions of fish gills in relation to their function. *Journal of Experimental Biology*, 45(1):177–195, 1966. doi: https://doi.org/10.1242/jeb.45.1.177.

IAEA. Review of fuel failures in water cooled reactors. `https://www.iaea.org/publications/8259/review-of-fuel-failures-in-water-cooled-reactors`, 2015.

R. A. Johnson, D. W. Wichern, et al. *Applied multivariate statistical analysis*, volume 6. Pearson London, UK:, 2014.

J. Keffer and W. Baines. The round turbulent jet in a cross-wind. *Journal of Fluid Mechanics*, 15(4):481–496, 1963.

M. Kitlan Jr, A. McClenny Jr, and D. Culp. Upflow conversion-eliminating the potential for baffle jetting at mcguire. *Transactions of the American Nuclear Society;(United States)*, 63(CONF-910603-), 1991.

A. Krishnaraj and V. Ganesan. Investigation of jet mixing characteristics using slotted rectangular tabs. *Journal of Aerospace Technology and Management*, 13, 2021. doi: https://doi.org/10.1590/jatm.v13.1188.

A. M. Kuethe. Investigations of the turbulent mixing regions formed by jets. 1935.

H. Lee and Y. Chang. Flow-induced vibration of rod arrays in a jet flow. *Journal of Pressure Vessel Technology*, pages 46–49, 1990.

J. H.-w. Lee, V. Chu, and V. H. Chu. *Turbulent jets and plumes: a Lagrangian approach*, volume 1. Springer Science & Business Media, 2003.

J. Lever and D. Weaver. On the stability of heat exchanger tube bundles, part i: Modified theoretical model. *Journal of Sound and vibration*, 107(3):375–392, 1986.

C. Li, C. Lishun, L. Tao, G. Li, C. Ming, and Z. Lin. Features of singular value decomposition and its application to the vibration monitoring of turboprop engine. In *International Conference in Communications, Signal Processing, and Systems*, pages 1495–1506. Springer, 2017.

R. J. Margason. Fifty years of jet in cross flow research. *In AGARD*, 1993.

D. Miklosovic, M. Murray, L. Howle, and F. Fish. Leading-edge tubercles delay stall on humpback whale (megaptera novaeangliae) flippers. *Physics of Fluids*, 16(5):L39–L42, 2004. doi: https://doi.org/10.1063/1.1688341.

B. Muir and J. Kendall. Structural modifications in the gills of tunas and some other oceanic fishes. *Copeia*, pages 388–398, 1968. doi: https://doi.org/10.2307/1441767.

T. Nakamura and N. Mureithi. Recent findings on stream-wise fluidelastic instability and its application. In *title JAXA Special Publication: Proceedings of the First International Symposium on Flutter and its Application*, page 565, 2017.

T. Nakamura, S. Kaneko, F. Inada, M. Kato, K. Ishihara, T. Nishihara, N. W. Mureithi, and M. A. Langthjem. *Flow-induced vibrations: classifications and lessons from practical experiences*. Butterworth-Heinemann, 2013.

M. B. Narayanan. The behaviour of excited plane jets. *Sadhana*, 12(1-2):31–43, 1988.

T. New, T. Lim, and S. Luo. Effects of jet velocity profiles on a round jet in cross-flow. *Experiments in Fluids*, 40(6):859–875, 2006.

M. Paidoussis. The amplitude of fluid-induced vibration of cylinders in axial flow. Technical report, Atomic Energy of Canada Ltd., Chalk River, Ontario (Canada), 1965.

M. Paidoussis. Dynamics of flexible slender cylinders in axial flow part 1. theory. *Journal of Fluid Mechanics*, 26(4):717–736, 1966a.

M. Paidoussis. Dynamics of flexible slender cylinders in axial flow part 2. experiments. *Journal of Fluid Mechanics*, 26(4):737–751, 1966b.

M. Paidoussis. Dynamics of cylindrical structures subjected to axial flow. *Journal of sound and vibration*, 29(3):365–385, 1973.

M. Paidoussis. Fluidelastic vibration of cylinder arrays in axial and cross flow: state of the art. *Journal of Sound and Vibration*, 76(3):329–360, 1981.

M. Paidoussis and L. R. Curling. An analytical model for vibration of clusters of flexible cylinders in turbulent axial flow. *Journal of Sound and Vibration*, 98(4):493–517, 1985.

M. P. Paidoussis. *Fluid-structure interactions: slender structures and axial flow*, volume 1. Academic press, 1998.

M. P. Paidoussis, S. J. Price, and E. De Langre. *Fluid-structure interactions: cross-flow-induced instabilities*. Cambridge University Press, 2010.

P. N. Papanicolaou and E. J. List. Investigations of round vertical turbulent buoyant jets. *Journal of Fluid Mechanics*, 195:341–391, 1988.

R. Pavlica and R. Marshall. An experimental study of fuel assembly vibrations induced by coolant flow. *Nuclear Engineering and Design*, 4(1):54–60, 1966.

B. C. Phanindra and E. Rathakrishnan. Corrugated tabs for supersonic jet control. *AIAA Journal*, 48(2):453–465, 2010. doi: https://doi.org/10.2514/1.44896.

B. D. Pratte and W. D. Baines. Profiles of the round turbulent jet in a cross flow. *Journal of the Hydraulics Division*, 93(6):53–64, 1967.

S. Price. A review of theoretical models for fluidelastic instability of cylinder arrays in cross-flow. *Journal of Fluids and Structures*, 9(5):463–518, 1995.

S. Price and M. Paidoussis. Fluidelastic instability of an infinite double row of circular cylinders subject to a uniform cross-flow. *Journal of Vibration, Acoustics, Stress, and Reliability in Design*, 1983.

S. Price and M. Paidoussis. An improved mathematical model for the stability of cylinder rows subject to cross-flow. *Journal of Sound and Vibration*, 97(4):615–640, 1984.

S. Price and M. Paidoussis. A single-flexible-cylinder analysis for the fluidelastic instability of an array of flexible cylinders in cross-flow. *Journal of Fluids Engineering*, 1986.

S. Price, B. Mark, and M. Paidoussis. An experimental stability analysis of a single flexible cylinder positioned in an array of rigid cylinders and subject to cross-flow. *Journal of Pressure Vessel Technology*, 1986.

E. Quinn. Vibration of fuel rods in parallel flow. Technical report, General Electric Co. Atomic Power Equipment Dept., San Jose, Calif., 1962.

N. Rajaratnam. *Turbulent jets*. Elsevier, 1976.

M. Reeder and M. Samimy. The evolution of a jet with vortex-generating tabs: real-time visualization and quantitative measurements. *Journal of Fluid mechanics*, 311:73–118, 1996. doi: https://doi.org/10.1017/S0022112096002510.

B. W. Roberts. *Low frequency, self-excited vibration in a row of circular cylinders mounted in an airstream*. PhD thesis, University of Cambridge, Eng., 1962.

D. Rockwell. External excitation of planar jets. *Journal of Applied Mechanics*, 1972.

K. Rostrom. Seven-rod fuel element vibration tests. *Ab. Atomenergi (Stockholm), Arbetsrapport RRL-726*, 1964.

K. Seki, S. Kuwabara, K. Tanimura, S. Matsumoto, and M. Toba. A study on fuel rod vibration induced by baffle jet flow. *Nuclear Technology*, 74(1):27–37, 1986.

V. Shinde, E. Longatte, F. Baj, and M. Braza. A theoretical model of fluidelastic instability in tube arrays. *Nuclear Engineering and Design*, 337:406–418, 2018.

A. Simpson and J. Flower. An improved mathematical model for the aerodynamic forces on tandem cylinders in motion with aeroelastic applications. *Journal of Sound and Vibration*, 51(2):183–217, 1977.

S. Smith and M. Mungal. Mixing, structure and scaling of the jet in crossflow. *Journal of fluid mechanics*, 357:83–122, 1998.

H. Tanaka and S. Takahara. Fluid elastic vibration of tube array in cross flow. *Journal of sound and vibration*, 77(1):19–37, 1981.

T. Thangaraj, M. Kaushik, D. Deb, M. Unguresan, and V. Muresan. Survey on vortex shedding tabs as supersonic jet control. *Frontiers in Physics*, page 842, 2022. doi: https://doi.org/10.3389/fphy.2021.789742.

I. Y. Tumer and E. M. Huff. Principal components analysis of triaxial vibration data from helicopter transmissions. In *56th Meeting of the Society for Machinery Failure Prevention Technology*, 2001a.

I. Y. Tumer and E. M. Huff. Using triaxial accelerometer data for vibration monitoring of helicopter gearboxes. In *International Design Engineering Technical Conferences and Computers and Information in Engineering Conference*, volume 80296, pages 3161–3171. American Society of Mechanical Engineers, 2001b.

U.S. NRC. Fuel pin damage due to water jet from baffle plate corner. `https://www.nrc.gov/reading-rm/doc-collections/gen-comm/circulars/1980/cr80017.html`, 1980.

U.S. NRC. *Westinghouse Technology Systems Manual*. 2016.

C. Wang, H. Li, G. Huang, and J. Ou. Early fault diagnosis for planetary gearbox based on adaptive parameter optimized vmd and singular kurtosis difference spectrum. *IEEE Access*, 7:31501–31516, 2019.

H. Wang, S. Lee, and Y. A. Hassan. Particle image velocimetry measurements of the flow in the converging region of two parallel jets. *Nuclear Engineering and Design*, 306:89–97, 2016.

D. Weaver. On flow induced vibrations in hydraulic structures and their alleviation. *Canadian Journal of Civil Engineering*, 3(1):126–137, 1976.

D. Weaver and M. El-Kashlan. On the number of tube rows required to study cross-flow induced vibrations in tube banks. *Journal of Sound and Vibration*, 75(2):265–273, 1981.

X. Wen, G. Lu, and P. Yan. Vibration feature extraction via graph-modeled SVD for running stability assessment of industrial machine. In *2019 International Conference on Sensing, Diagnostics, Prognostics, and Control (SDPC)*, pages 35–39. IEEE, 2019.

I. Wygnanski and H. Fiedler. Some measurements in the self-preserving jet. *Journal of Fluid Mechanics*, 38(3):577–612, 1969.

M. Yetisir and D. Weaver. An unsteady theory for fluidelastic instability in an array of flexible tubes in cross-flow. Part I: Theory. *Journal of Fluids and Structures*, 7(7):751–766, 1993a.

M. Yetisir and D. Weaver. An unsteady theory for fluidelastic instability in an array of flexible tubes in cross-flow. Part II: Results and comparison with experiments. *Journal of Fluids and Structures*, 7(7):767–782, 1993b.

M.-h. Yu, C.-m. Yu, and K.-h. Chen. Fluid elastic instability of a small circular cylinder in the shear layer of a two-dimensional jet. *Physics of Fluids*, 16(7):2357–2370, 2004.

L. L. Yuan, R. L. Street, and J. H. Ferziger. Large-eddy simulations of a round jet in crossflow. *Journal of Fluid Mechanics*, 379:71–104, 1999.

A. Yule. Large-scale structure in the mixing layer of a round jet. *Journal of Fluid Mechanics*, 89(3):413–432, 1978. doi: https://doi.org/10.1017/S0022112078002670.

K. B. Zaman, M. Samimy, and M. Reeder. Effect of tabs on the evolution of an axisymmetric jet. In *Symposium on Turbulent Shear Flows*, number NASA-TM-104472, 1991.

M. Zeng, W. Zhang, and Z. Chen. Group-based k-svd denoising for bearing fault diagnosis. *IEEE Sensors Journal*, 19(15):6335–6343, 2019.

Q. Zhang, Y. Fan, and Y. Gao. Rolling bearing fault feature extraction method based on mckd combined with sensitive svd. In *2019 IEEE 8th Data Driven Control and Learning Systems Conference (DDCLS)*, pages 776–781. IEEE, 2019.

M. Zhao, L. Cheng, H. An, and F. Tong. Flow and flow-induced vibration of a square array of cylinders in steady currents. *Fluid Dynamics Research*, 47(4):045505, 2015.

Z. Zhao, S. Wang, D. Wong, Y. Guo, and X. Chen. The sparse and low-rank interpretation of svd-based denoising for vibration signals. In *2020 IEEE International Instrumentation and Measurement Technology Conference (I2MTC)*, pages 1–6. IEEE, 2020.

Q. Zhou, Y. Qin, Z. Wang, and L. Jia. Study on fault diagnosis for bearing based on vmd-svd and extreme learning machine. In *International Conference on Electrical and Information Technologies for Rail Transportation*, pages 87–97. Springer, 2017.